The Flow Behaviour of Elemental Mercury DNAPL in Porous Media

Andrea D'Aniello

Dipartimento di Ingegneria Civile, Edile e Ambientale

Università degli Studi di Napoli Federico II

Thesis submitted for the degree of PhD in Civil Systems Engineering
Napoli, April 2017

Supervisors

Prof. Domenico Pianese, Università degli Studi di Napoli Federico II

Dr. Niels Hartog, Universiteit Utrecht

Co-Supervisors

Dr. Luigi Cimorelli, Università degli Studi di Napoli Federico II

Dr. Luca Cozzolino, Università degli Studi di Napoli Parthenope

PhD Programme Coordinators - XXIX Cycle

Prof. Dr. Andrea Papola, Università degli Studi di Napoli Federico II

Prof. Elvira Petroncelli, Università degli Studi di Napoli Federico II

The Reading Committee

Prof. Dr. Vittorio Di Federico, Alma Mater Studiorum Università di Bologna

Dr. Vahid J. Niasar, The University of Manchester

Dr. Hamid M. Nick, Danmarks Tekniske Universitet

Prof. Dr. Paolo Salandin, Università degli Studi di Padova

This research was financially supported by the P.O.R. Campania FSE 2007/2013-2014/2020.

Abstract

This thesis focuses on the characterization of the flow behaviour of elemental mercury (Hg^0) DNAPL (Dense NonAqueous Phase Liquid) in porous media. In the subsurface, Hg^0 DNAPL can act as a long lasting source of contamination, causing detrimental consequences for the human health and the environment. Therefore, insight into the flow behaviour of elemental mercury in porous media is needed and is critical in assessing the control of contaminant spreading as well as remediation approaches. However, the scientific literature on Hg^0 DNAPL is still very limited and, to date, it remains unclear to what extent the validity of the classical constitutive relations, used to describe DNAPLs flow behaviour, as well as the scaling theory, holds for elemental mercury. These issues become crucial in partially water saturated porous media, where liquid Hg^0 is likely to behave as a nonwetting phase with respect to both air and water. To address these knowledge gaps, experimental and numerical analysis were performed. In particular, the properties affecting the constitutive relations governing liquid Hg^0 infiltration behaviour were explored first, using capillary pressure-saturation, $P_c(S)$, experiments in different granular porous media, and in two- and three-phase fluid systems. Then, the infiltration and (re)distribution behaviour of Hg^0 DNAPL was studied in variably water saturated stratified porous media with flow container experiments and dual gamma ray measurements of porosity and fluid saturations. Experimental results indicated that elemental mercury infiltration is strongly controlled by the porous medium water content and can be triggered by its changes due to, for example, rain events. Finally, a new theoretical formulation of elemental mercury retention properties in variably water saturated porous media was proposed and, to assess to what extent numerical modelling can predict elemental mercury migration in porous media, the flow container experiments were simulated using GDAn, the code developed by the Author.

Keywords: elemental mercury; DNAPL; variably water saturated; multiphase flow; constitutive theory; Leverett scaling; PCE; gamma radiation; GDAn.

Abstract

Il presente elaborato è volto alla caratterizzazione del comportamento fluidodinamico del mercurio elementale (Hg^0) in forma separata dalla fase acquosa (DNAPL – Dense NonAqueous Phase Liquid). Nel sottosuolo, il mercurio elementale liquido può costituire una fonte di contaminazione a lungo termine, producendo conseguenze deleterie per gli esseri umani e l'ambiente. Pertanto, si palesa la necessità di approfondire il comportamento fluidodinamico del mercurio liquido nei mezzi porosi. Approfondimento, questo, fondamentale per definire la capacità di tale contaminante di diffondersi, nonché i relativi approcci di bonifica. Ciò nonostante, ad oggi, la letteratura scientifica sul mercurio elementale DNAPL è ancora limitata, e non è chiaro fino a che punto si possa estendere a tale contaminante la validità delle teorie costitutive classiche, adottate per i DNAPLs, nonché della teoria di scala. Questi interrogativi divengono altresì cruciali in mezzi porosi parzialmente saturi, dove si prevede che il mercurio elementale si comporti come una fase non-bagnabile nei confronti sia dell'aria che dell'acqua. Al fine di colmare queste lacune, sono state condotte sia analisi sperimentali che numeriche. In primo luogo, si è proceduto con la caratterizzazione, in mezzi porosi granulari ed in sistemi bi- e tri-fase, delle proprietà che influenzano i legami costitutivi che governano la propagazione del mercurio elementale liquido. Successivamente, a mezzo di prove in acquiferi sperimentali, saturi e parzialmente saturi, e con l'ausilio di un sistema duale a raggi gamma, si è analizzato il processo di infiltrazione e (re)distribuzione del mercurio elementale liquido. I risultati sperimentali hanno mostrato che l'infiltrazione del mercurio liquido nei mezzi porosi è fortemente controllata dal contenuto d'acqua e che può innescarsi a seguito di variazioni dello stesso, dovute, ad esempio, ad eventi meteorici. Infine, è stata proposta una nuova formulazione teorica dei legami costitutivi del mercurio elementale in mezzi parzialmente saturi e, per valutare fino a che punto la modellazione numerica sia in grado di riprodurre la propagazione del mercurio elementale liquido nei mezzi porosi, gli esperimenti sono stati riprodotti con GDAn, il codice numerico sviluppato dall'Autore.

Acknowledgements

During these three years I luckily crossed my path with a lot of great people, and it is a pleasure to thank them.

First, I want to express my gratitude to Prof. Domenico Pianese, who gave me the chance to join the PhD programme and to discover the fascinating world of research. Since the very beginning, he supported me and had faith in my capabilities, motivating me to do my best. Even though my research topic was completely new for his group, he allowed me to lead my research autonomously and independently, thus giving me a challenging opportunity of scientific and personal growth.

My deepest gratitude goes to Dr. Niels Hartog, the person who mostly contributed to my growth as a researcher. Our collaboration started randomly, more like a bet I would say. Nevertheless, it soon became more than this, leading to an intense and satisfying research activity. His scrupulous eye, his dedication to work, and his broad and fresh view on practical and theoretical problems are of inspiration. He is a great researcher and, most of all, he is an outstanding human being. I am honoured of having had the opportunity to meet him.

I wish to thank Prof. Dr. Majid Hassanizadeh, who kindly welcomed me in the Hydrogeology Group at Utrecht University. Despite his numerous international commitments, he found some time to discuss together, giving me precious hints and suggestions. He treated me as a member of his group, and this had a great value to me.

A special thank goes to Tony, Thom, and Dominika, who were always there when I needed something in the lab, bearing my demanding load of (sometimes weird and ineffective) requests.

I sincerely thank the reading committee for the time spent reviewing this thesis and for the encouraging comments about my research.

Inevitable thanks go to all the Italian colleagues. Some of them I can really call friends.

The nine months spent in Utrecht were among the most beautiful of my life. I owe a lot to this experience and to the people I met. Some of them made my stay in the Netherlands unique and unforgettable, and I will always be grateful for this.
Infine, voglio ringraziare i miei amici più cari e la mia famiglia. Ognuno di voi, in maniera unica ed irripetibile, mi ha dato fiducia, ispirazione e amore, risollevandomi dalle mediocrità quotidiane e mostrandomi che c'è tanto altro per cui valga la pena vivere e lottare.

Andrea

Napoli, 7th April 2017

a mia Madre e mio Padre

Table of Contents

List of Figures

List of Tables

Chapter 1

Mercury Pollution: Environmental Fate and Transport in the Subsurface

A general overview of mercury occurrence in the subsurface is presented throughout this chapter, aiming to describe the characteristics of this hazardous contaminant, especially in its metallic form. The first part of the chapter is devoted to describe the several sources of mercury contamination together with its environmental and toxicological risks. Then, the current insights into mercury fate and transport in soil and groundwater systems are addressed, from the description of the typical sources and forms of mercury contamination to the definition of the several species into which mercury can transform once in the subsurface. Thereafter, a detailed and up to date overview of the limited scientific literature existing on elemental mercury DNAPL (Dense NonAqueous Phase Liquid) flow behaviour in porous media is presented. In the end, the scope of the research work and the outline of the thesis are pointed out.

1.1 Sources of Mercury in the Environment

Mercury can either occur in the environment as a result of natural processes, like volcanic activity, fires, movement of rivers, lakes, streams, oceanic upwelling, and biological processes, or as a result of anthropogenic activities, which considerably contributed to its distribution since the industrial revolution (Risher, 2003). Mercury exists in various forms and substances, mainly falling in three categories, namely: i) elemental mercury, Hg^0, both in liquid and gaseous state; ii) inorganic mercury compounds, such as mercuric chloride,

$HgCl_2$, mercurous chloride, Hg_2Cl_2, mercuric sulphide, HgS, mercuric acetate, $HgC_4H_6O_4$; iii) organic mercury compounds, like methylmercury, CH_3Hg^+, and dimethylmercury, $(CH_3)_2Hg$.

Typical anthropogenic sources of mercury release in the environment are associated to mercury mining (UNEP, 2002), mercury amalgamation for gold and silver mining (Lechler et al., 2000; UNEP, 2002; Hylander and Meili, 2003), and to industrial activities, such as wood preservation (Bollen et al., 2008), chlor-alkali and thermometer manufacturing plants (Biester et al., 2002; Hylander and Meili, 2003; Bernaus et al., 2006; Arbestain et al., 2009; Brooks and Southworth, 2011; Miller et al., 2013). Actually, among the principal consumers of mercury, the chlor-alkali industry has a major role. As a matter of fact, in 1996, almost the 40% of the mercury world production was due to the chlor-alkali industry (Sznopek and Goonan, 2000). Most of the chlor-alkali plants using liquid Hg^0 cells are located in Western Europe and, according to Euro Chlor (1999), the Hg^0 consumption was of about 100 tons per year in 1999. According to Lindley (1997), almost 12000 tons of liquid Hg^0 were in use as electrodes in European chlor-alkali plants. Furthermore, the fate of the 90% of liquid Hg^0 bought by Western European chlor-alkali plants is not reported (Euro Chlor, 1999) and, most probably, considerable amounts of liquid Hg^0 are still stored in wastes in proximity of the chlor-alkali facilities (Hylander and Meili, 2003).

Mercury can also be found in products of commercial use, like batteries, switches, lights, cosmetics, pesticides, dental amalgams, and explosives (Hylander and Meili, 2003; Risher, 2003).

1.2 Human and Toxicological Risks of Mercury Exposure

Mercury is globally recognised for its harmful effects on human health and for the detrimental consequences of its release in the environment (US EPA, 2007a; World Chlorine Council, 2011). Human exposure to mercury can occur in a variety of ways (Risher, 2003) like: i) eating methylmercury contaminated fish (Salonen et al., 1995); ii) walking on a contaminated soil; iii) playing with liquid mercury from broken electrical switches, thermometers, barometers, blood pressure monitors, etc.; iv) bringing any liquid mercury or broken mercury device into the home, where vapours might build up in indoor air; v) drinking contaminated water and breathing ambient air (usually minor). An

additional relevant cause is occupational exposure. Workers in fluorescent tubes manufacturing (Fawer et al., 1983), chlor-alkali facilities (Levine et al., 1982; Fawer et al., 1983; Piikivi and Tolonen, 1989), thermometers plants (Ehrenberg et al., 1991), gold miners (Risher, 2003), and dentists (Ngim et al., 1992; Echeverria et al., 1995) reported symptoms of mercury neurotoxicity after long term exposure.

In recent years, efforts have been made to control and reduce mercury emissions into the environment, and legislative texts and government policies are restricting its industrial use. As a matter of fact, recent policies like the United Nations Environmental Programme (UNEP) Global Mercury Convention (Minamata Convention on Mercury), a multilateral environmental treaty agreed by over 140 countries on 19th January 2013, requires signatory nations to (NICOLE, 2015): i) phase out mercury in acetaldehyde (by 2018) and chlor-alkali (by 2025) manufacturing processes and restrict its use elsewhere; ii) reduce and eliminate the use of mercury in other industries, such as artisanal gold mining, and also reduce air emissions from point sources such as coal burning, cement production, smelting of non-ferrous metals and waste incineration; iii) phase out or reduce mercury in products, such as batteries, switches, lights, cosmetics, pesticides, measuring devices, and dental amalgams.

Reported symptoms following mercury exposure may include: behavioural changes, tremors, pulmonary toxicity, respiratory failure, hypertension, renal toxicity, skin rashes, and even death (US EPA, 2007b).

Particularly sensitive to mercury exposure is the central nervous system, and several cognitive, personality and motor disturbances have been reported. As a matter of fact, mercury is a neurotoxicant, and the major symptoms of its neurotoxicity include tremors, emotional lability, insomnia, memory loss, neuromuscular changes, headaches, polyneuropathy and performance deficits in tests of cognitive functions (Risher, 2003). Long term exposure to elemental mercury vapours enhances these effects, which may persist for years after the end of the exposure. Organic forms of mercury, like methylmercury, instead, interfere with the growth and migration of neurons and may induce irreversible damages to the developing central nervous system of the foetus (US EPA 1997).

Short term exposure to high concentrations of elemental mercury vapours may induce respiratory symptoms (Risher, 2003) such as cough, dysponea, chest tightness, haemoptysis, pulmonary function impairment, and in the most severe cases, respiratory distress, pulmonary oedema, lobar pneumonia, fibrosis, and desquamation of the bronchiolar epithelium (ATSDR, 1999). Inorganic mercury compounds may also affect the respiratory system (Murphy et al., 1979; Samuels et al., 1982; Kang-Yum and Oransky, 1992).

Increased blood pressure and palpitations, as a result of short term inhalation exposure to high levels of elemental mercury vapour, have been reported in several cases (ATSDR, 1999). Ingestion of mercuric chloride and mercurous chloride may also result in cardiovascular toxicity (Warkany and Hubbard, 1953; Chugh et al., 1978), while the ingestion of methylmercury contaminated fish may increase the risk of myocardial infarction (Salonen et al., 1995).

Elemental mercury vapours may cause a series of gastrointestinal effects such as stomatitis, abdominal pains, nausea and diarrhoea (Risher, 2003). Ingestion of mercuric chloride causes vomiting, diarrhoea, severe abdominal pain, oropharyngeal pain, ulceration and haemorrhages of the gastrointestinal tract (Afonso and deAlvarez, 1960; Chugh et al., 1978; Murphy et al., 1979). In addition, hepatic effects, like jaundice, may be provoked by the ingestion of mercuric chloride (Murphy et al., 1979).

In general, all mercury forms are also known to produce toxic effects on renal activity. Short term exposure to high concentrations of mercury vapour, as well as ingestion of mercuric chloride, may cause acute renal failure (ATSDR, 1999; Risher, 2003), while organic forms of mercury may induce polyuria and albuminuria (Jalili and Abbasi, 1961; Cinca et al., 1980).

Skin rashes, irritation, and other dermal reactions, like acrodynia, may be the result of inhalation, oral or dermal exposure to elemental mercury vapours or inorganic mercury (ATSDR, 1999; Risher, 2003). High concentrations of elemental mercury vapours may also induce red and burning eyes, and conjunctivitis (Sexton et al., 1978; Foulds et al., 1987; Karpathios et al., 1991; Bluhm et al., 1992; Schwartz et al., 1992).

1.3 Mercury Fate and Transport in the Subsurface

1.3.1 Sources of Mercury Contamination

The presence of mercury in soil systems is mainly due to (Leterme and Jacques, 2013): i) atmospheric wet and dry deposition and litterfall; ii) lithogenic phenomena; iii) anthropogenic contamination.

Over the 90% of the atmospheric mercury is elemental mercury vapour (Risher, 2003; Zhang et al., 2009). In the atmosphere, mercury can cover large distances in a relatively small amount of time, of about 2500 km in 72 hours according to Glass et al. (1991), and the aerial residence time may vary in a range from 6 days (Andren and Nriagu, 1979) to 6 years (US EPA, 1984) before its redistribution in air or water, mostly in the form of inorganic mercury (Zhang et al., 2009). The redistribution of mercury is usually due to wet deposition, which contributes approximately to the 66% of the atmospheric mercury removal (Fitzgerald et al., 1991; Lindqvist, 1991a,b), even though, during the summer months, dry deposition may result in the 70% of the atmospheric mercury removal (Lindberg et al., 1991). Over the 97% of the gaseous mercury that dissolves in groundwater is elemental mercury (Vandal et al., 1991), but, usually, it does not remain in this form for long, as it preferentially combines to form other compounds or enters again in the atmosphere (Risher, 2003). Atmospheric sources are also primarily responsible for the presence of mercury in the vegetation, especially on leaves, and once they fall on the ground a further mercury release in soils can occur (Obrist et al., 2011).

As a result of natural processes, like volcanic activity, mercury can be found in ore deposits, mainly in the form of cinnabar ores (HgS), and in bedrocks. Oxidation and weathering of these formations are responsible of further release of mercury in soils, which is then transported via Hg^0 degassing or via speciation in groundwater (Leterme and Jacques, 2013).

Mercury soil contamination may also occur from several sources directly related to anthropogenic activities like spilling, mine tailing, landfills, polluted sewage sludge, or indirectly as a result of the deposition of prior atmospheric emissions (Leterme and Jacques, 2013). Liquid elemental mercury is used in several industrial processes and human activities (sec. 1.1), and its occurrence in the subsurface as DNAPL (Dense

NonAqueous Phase Liquid) is reported worldwide. As a matter of fact, liquid elemental mercury has been observed in the subsurface in proximity of several chlor-alkali plants like in Lavaca Bay, Texas (USA), (Scanlon et al., 2005), at the industrial area in Bussi sul Tirino, Italy, (Di Molfetta and Fracassi, 2008), near the Onodaga Lake, New York (USA), (Deeb et al., 2011; ITRC, 2012), at the Oak Ridge Y-12 National Security Complex, Tennessee (USA), where the estimated loss of liquid Hg^0 to the soil is about 193000 kg (Brooks and Southworth, 2011), and at the Botany Industrial Park, Sidney (Australia), (Golder Associates, 2011). Once liquid Hg^0 infiltrates in the subsurface and immobilizes, it acts as a long lasting source of contamination. Thanks to its low aqueous solubility, 0.07 mg/l (Eichholz et al., 1986), it takes a considerable amount of time before the DNAPL source depletes, and liquid Hg^0 can be found in soil and groundwater systems even after decades (Davis et al., 1997). Furthermore, once in the subsurface, liquid mercury is subjected to speciation (sec. 1.3.2), thus releasing in the water phase organic and inorganic mercury compounds that are more toxic, mobile and soluble than Hg^0 itself, like dimethylmercury (C_2H_6Hg) and mercuric chloride ($HgCl_2$), which exhibit an aqueous solubility of 1 g/l (National Research Council, 2000) and of 28.6 g/l (Risher, 2003), respectively. In addition, due to its high vapour pressure, 0.07 Pa (CRC, 2014), it can further release contaminants through volatilization (Walvoord et al., 2008).

1.3.2 Mercury Speciation

Mercury can occur in different phases in the subsurface (Leterme and Jacques, 2013): i) dissolved in the aqueous phase as a free ion (Hg^{2+}) or complexed with inorganic and organic ligands; ii) elemental mercury as a dense nonaqueous phase liquid (DNAPL); iii) sorbed on soil minerals and insoluble organic matter; iv) in the gas phase; v) in solid precipitated phase. As a result of anaerobic microbial processes in anoxic sediments, methylation of inorganic mercury may also occur (Compeau and Bartha, 1985; Gilmour et al., 1992).

The valence state in which mercury exists in the environment (Hg^0, Hg^+, Hg^{2+}) is determined by multiple factors, including pH, ionic strength, redox potential, concentrations of dissolved organic matter, dissolved oxygen, sulphide and suspended solids in solution (Risher, 2003; Leterme and Jacques, 2013). Usually, in soils, the

presence of monovalent mercury is negligible (Schlüter, 2000), and the typical reaction occurring is the reduction of Hg^{2+} to Hg^0 (Gabriel and Williamson, 2004), which is the first step of mercury volatilization from soil. This reaction can be biotic or abiotic, and occurs easily in saturated horizons, which are usually reducing environments (Schlüter, 2000). Both reduction types are influenced by adsorption, because free Hg^{2+} in solution has a higher potential for reduction than an adsorbed mercury compound (Schuster, 1991; Schlüter, 2000; Mishra et al., 2011), and an increase in dissolved organic matter may inhibit reduction due to the unavailability of adsorbed mercury compounds (Leterme and Jacques, 2013). In reduced conditions mercury usually complexes with sulphides, while, in oxidized conditions, the predominant inorganic mercury species are $Hg(OH)_2$, $HgCl_2$, $HgOH^+$, HgS, and Hg^0 (Ullrich et al., 2001; Gabriel and Williamson, 2004; Skyllberg, 2012; Leterme and Jacques, 2013).

Strong interactions between mercury and organic matter are also observed (Leterme and Jacques, 2013), mainly with sulphur-containing functional groups, especially thiol groups (Gabriel and Williamson, 2004; Ravichandran, 2004; Skyllberg, 2012).

In soils, mercury binds strongly to humic materials and sesquioxides, even at soil pH values greater than 4 (Blume and Brummer, 1991), although mercury sorption to soils generally decreases with increasing pH (Schuster, 1991). The sorption of mercury to soil depends on the soil organic content (Blume and Brummer, 1991), and the dominant sorption mechanism is the formation of stable insoluble inorganic and organic complexes rather than ion exchange (Schuster, 1991). Inorganic mercury may be adsorbed onto soil particles, where it is likely to remain bound unless consumed by organisms (Risher, 2003), thus providing the substrate for mercury methylation (Han et al., 2006). As a matter of fact, consumption of elemental or inorganic mercury by microorganisms results in the biotransformation into methylmercury forms, which tend to bioaccumulate due to their lipophilic and proteinbinding properties (Schlüter, 2000; Ullrich et al., 2001). In particular, in aquatic species, bioaccumulation is influenced by the pH (Ponce and Bloom, 1991) and the dissolved oxygen content (Wren, 1992). Methylation of mercury can occur in both oxic and anoxic environments, and the efficiency of microbial methylation depends also on microbial activity, which in turn is influenced by temperature, pH, and redox potential (Leterme and Jacques, 2013).

1.4 Hg^0 DNAPL Flow Behaviour in Porous Media

Research into the flow behaviour of liquid elemental mercury in soil and groundwater systems is still very limited. However, in petroleum engineering, liquid elemental mercury is extensively used as a nonwetting fluid for the analysis of the pore structure of geological formations under vacuum conditions (mercury porosimetry), and the Hg^0-air retention curves are usually used to scale hydrocarbon-brine retention properties (Wardlaw and Taylor, 1976; Vavra et al., 1992; Pittman, 1992; Smith et al., 2002; Newsham et al., 2004; Ruth et al., 2013).

Due to its remarkable density, of about 13.52 times higher than water, (CRC, 2014), and its low aqueous solubility (sec. 1.3.1), elemental mercury behaves like a DNAPL in the subsurface, but its physical properties strongly differ from well-known DNAPLs. For example, elemental mercury has an 8 times higher density, an almost 2 times higher viscosity, and an approximately 15 times higher surface tension than PCE (Schwille, 1988; CRC, 2014). Hence, liquid Hg^0 flow behaviour in porous media is expected to deviate, but, to date, it is unknown how these different properties affect its infiltration and distribution in the subsurface. Other than extensively studied DNAPLs, such as creosote, carbon tetrachloride, trichloroethylene (TCE) and tetrachloroethylene (PCE), (Schwille, 1988; Busby et al., 1995; Hofstee et al., 1998a; Hofstee et al., 1998b; Oostrom et al., 1999; Wu et al., 2000; Oostrom et al., 2003), only few studies have addressed liquid Hg^0 flow behaviour in porous media under environmental conditions.

Eichholz et al. (1986) analysed the potential migration of metallic mercury from shallow land burial sites into groundwater, and observed that standing metallic mercury may penetrate into the ground under its own head. By means of seepage column tests, in dry soils, they observed penetrations of the order of 3-4 cm under 1 mm Hg^0 head and atmospheric pressure. In soils wet to the minimum residual moisture content, liquid Hg^0 moved further where the wet soil was allowed to dry and crack. They concluded that metallic mercury would not migrate much further unless higher hydrostatic pressures were applied, and that the mercury present in typical disposal trenches would have constituted a negligible health hazard unless mercury speciation occurred. However, as lately observed in sites affected by Hg^0 DNAPL contamination (sec. 1.3.1), metallic mercury can reach

greater depths, like near the Onodaga Lake, where it was found 17 m below the ground level (Deeb et al., 2011; ITRC, 2012), or in the site described in Sweijen et al. (2014), where mercury DNAPL presence was confirmed to at least 9 m depth.

The experiments by Devasena and Nambi (2010) showed that liquid Hg^0 acts as a nonwetting fluid, requiring to overcome an entry head to infiltrate in water saturated granular porous media. By means of capillary pressure-saturation curves of two-phase systems of Hg^0-water, TCE-water and PCE-water, they investigated mercury entrapment in water saturated porous media. Mercury entrapment was observed in homogeneous porous media, and, due to the intrinsic differences in the fluids physical properties, their experiments resulted in much lower residual saturation for Hg^0 (0.04) than for TCE (0.14) and PCE (0.17). They argued that this significant variation in residual saturation was probably due to the high interfacial tension of mercury with water, and to its high density and viscosity. As a matter of fact, according to Powers (1992), fluids with a high density and viscosity form unconditionally stable interfaces and result in minimum residual saturations, so they concluded that mercury, being denser and more viscous than water, forms an unconditionally stable interface both during drainage and imbibition. Hence, the pressure exerted by water does not alter the Hg^0 interface, and water flows from the pore throat to the pore body, thus resulting in minimum residual mercury saturation. Conversely, since TCE and PCE have a lower viscosity than water, they form an unstable interface with water, hence their interface becomes highly curved as water enters the pore throat during imbibition, thus separating the interface formed in the pore throat and resulting in higher residual saturations. Furthermore, their results highlighted that mercury DNAPL flow behaviour is governed by gravitational and capillary forces, and is practically independent of viscous forces, as confirmed by the high Bond numbers (ratio of gravitational to capillary forces) and low Capillary numbers (ratio of viscous to interfacial forces) observed in mercury-water systems.

Supported by field site characterisation and two-phase flow modelling, Sweijen et al. (2014) made a first attempt to analyse the transport behaviour of elemental mercury DNAPL in water saturated porous media. By means of an innovative CPT-probe equipped with a camera, they analysed a soil section surrounding a former chlor-alkali plant and found mercury DNAPL at saturations up to 13.2%. One-dimensional two-phase flow

modelling proved to be able to reasonably reproduce Hg^0 DNAPL migration through this section, despite the uncertainty of the values assumed for the flow model parameters, related to the limited scientific literature information. They also performed a numerical comparison between Hg^0 and PCE DNAPLs flow behaviour by means of two-dimensional two-phase flow modelling. This comparison indicated that Hg^0 had a higher capacity to penetrate to greater depths than PCE, further enhanced in presence of a horizontally layered heterogeneity.

1.5 Scope of the Research

This thesis focuses on the characterization of the flow behaviour of elemental mercury DNAPL in porous media. In the subsurface, Hg^0 DNAPL can act as a long lasting source of contamination (sec. 1.3.1), causing detrimental consequences for the human health and the environment (sec. 1.1). Therefore, insight into the flow behaviour of elemental mercury in porous media is needed and is critical in assessing the control of contaminant spreading as well as remediation approaches. As previously shown, the scientific literature on Hg^0 DNAPL is still very limited and, to date, it remains unclear to what extent the validity of the classical constitutive relations (Parker et al., 1987), used to describe DNAPLs flow behaviour, as well as the scaling theory (Lenhard and Parker, 1987), holds for elemental mercury. These issues become crucial in partially water saturated porous media, where liquid Hg^0 is likely to behave as a nonwetting phase with respect to both air and water. To address these knowledge gaps, experimental and numerical analysis were performed. In particular, the properties affecting the constitutive relations governing liquid Hg^0 infiltration behaviour were explored first, using capillary pressure-saturation, $P_c(S)$, experiments in different granular porous media, and in two- and three-phase fluid systems. Then, the infiltration and (re)distribution behaviour of Hg^0 DNAPL was studied in variably water saturated stratified porous media with flow container experiments and dual gamma ray measurements of porosity and fluid saturations.

1.6 Outline of the Thesis

This chapter serves as an introduction of the research work.

In *Chapter 2*, the mathematical and numerical framework of GDAn, the code developed entirely by the Author, is presented and described. Here, a series of analytical, numerical, and experimental benchmark problems, taken from the scientific literature, are used to verify and validate the code.

Chapter 3 describes the analysis of the attenuation behaviour of gamma radiation exhibited by the substances and the materials used within this research, with particular emphasis on liquid Hg^0. Calibration process and operating principles of the dual gamma ray system are also pointed out.

In *Chapter 4*, the analysis of the properties affecting the constitutive relations governing Hg^0 DNAPL infiltration behaviour in different granular porous media is described. To assess the role played by porous media characteristics on Hg^0 DNAPL infiltration behaviour, the results of the two- and three-phase $P_c(S)$ experiments are discussed in relation to the samples intrinsic permeability and porosity. Then, the infiltration behaviour of elemental mercury in water saturated systems is compared with that of PCE, aiming to verify the applicability of the traditional scaling theory. The Hg^0 infiltration behaviour and the scaling of its retention properties in variably water saturated porous media are finally addressed.

In *Chapter 5*, the infiltration and distribution behaviour of Hg^0 DNAPL in water saturated stratified granular porous media is analysed and compared to that of PCE by means of two-dimensional flow container experiments. Dual gamma ray measurements of porosity fields and DNAPL saturation profiles allowed a quantitative comparison of the flow behaviour of the two DNAPLs. Then, to assess to what extent numerical modelling can predict elemental mercury migration in water saturated porous media, a selected flow container experiment was simulated using GDAn.

Chapter 6 deals with the analysis of Hg^0 DNAPL infiltration and (re)distribution behaviour in variably water saturated porous media. First, a new theoretical formulation of elemental mercury retention properties is presented, and the new constitutive relationship is enforced within the GDAn code. Then, a two-dimensional flow container experiment in a partially

water saturated stratified granular porous medium is described and analysed. Dual gamma ray measurements of porosity, water and Hg^0 saturations allowed a quantitative analysis of the flow behaviour of elemental mercury. Finally, to assess to what extent the new constitutive formulation is able to cope with elemental mercury migration in variably water saturated porous media, the flow container experiment was simulated with the modified GDAn code.

In the end, *Chapter 7* provides a synthesis of the research work, in which the main findings are highlighted and discussed together with the implications for future research.

References

Afonso J, deAlvarez R (1960). *Effects of mercury on human gestation*. American Journal of Obstetrics and Gynecology, 80, 145–154.

Andren AW, Nriagu JO (1979). *The global cycle of mercury*. In: Nriagu JO, ed. The biogeochemistry of mercury in the environment. New York, NY, Elsevier/North Holland Biomedical Press, pp. 1–22.

Arbestain MC, Rodriguez-Lado L, Bao M, Macias F (2009). *Assessment of mercury-polluted soils adjacent to an old mercury-fulminate production plant*. Applied and Environmental Soil Science.

ATSDR (1999). *Toxicological profile for mercury (update)*. Atlanta, GA, US Department of Health and Human Services, Public Health Service, Agency for Toxic Substances and Disease Registry, March.

Bernaus A, Gaona X, van Ree D, Valiente M (2006). *Determination of mercury in polluted soils surrounding a chlor-alkali plant: direct speciation by X-ray absorption spectroscopy techniques and preliminary geochemical characterisation of the area*. Analytica Chimica Acta, 565(1), 73–80.

Biester H, Müller G, Schöler HF (2002). *Estimating distribution and retention of mercury in three different soils contaminated by emissions from chlor-alkali plants: part I.* Science of the Total Environment, 284(1), 177–189.

Bluhm RE, Bobbitt RG, Welch LW, Wood AJ, Bonfiglio JF, Sarzen C, Heath AJ, Branch RA (1992). *Elemental mercury vapour toxicity, treatment, and prognosis after acute, intensive exposure in chloralkali plant workers: Part I. History, neuropsychological findings and chelator effects*. Human and Experimental Toxicology, 11(3), 201–210.

Blume HP, Brummer G (1991). *Prediction of heavy metal behavior in soil by means of simple field tests*. Ecotoxicology and Environmental Safety, 22, 164–174.

Bollen A, Wenke A, Biester H (2008). *Mercury speciation analyses in $HgCl_2$-contaminated soils and groundwater - implications for risk assessment and remediation strategies*. Water Research, 42(1), 91-100.

Brooks SC, Southworth GR (2011). *History of mercury use and environmental contamination at the Oak Ridge Y-12 Plant*. Environmental Pollution, 159(1), 219–228.

Busby RD, Lenhard RJ, Rolston DE (1995). *An Investigation of Saturation-Capillary Pressure Relations in Two-and Three-Fluid Systems for Several NAPLS in Different Porous Media*. Ground Water, 33(4), 570-578.

Chugh KS, Singhal PC, Uberoi HS (1978). *Rhabdomyolysis and renal failure in acute mercuric chloride poisoning*. Medical Journal of Australia, 2, 125–126.

Cinca I, Dumitrescu I., Onaca P, Serbänescu A, Nestorescu B (1980). *Accidental ethyl mercury poisoning with nervous system, skeletal muscle, and myocardium injury*. Journal of Neurology, Neurosurgery & Psychiatry, 43(2), 143-149.

Compeau GC, Bartha R (1985). *Sulfate-reducing bacteria: principal methylators of mercury in anoxic estuarine sediment*. Applied and Environmental Microbiology, 50(2), 498-502.

CRC (2014). *Handbook of Chemistry and Physics*. 94th ed. (Internet Version 2014).

Davis A, Bloom NS, Que Hee SS (1997). *The Environmental Geochemistry and Bioaccessibility of Mercury in Soils and Sediments: A Review*. Risk Analysis 17(5), 557-569.

Deeb R, Hawley E, Kell L, O'Laskey R (2011). *Assessing alternative endpoints for groundwater remediation at contaminated sites*. ESTCP-Project ER-200832.

Devasena M, Nambi IM (2010). *Migration and entrapment of mercury in porous media*. Journal of Contaminant Hydrology, 117, 60–70.

Di Molfetta A, Fracassi F (2008). *Consulenza tecnica sulla contaminazione in atto nell'area del polo industriale di Bussi*. Procura della Repubblica presso il Tribunale di Pescara, procedimento n. 12/2006 R.G.N.R. mod. U.

Echeverria D, Heyer NJ, Martin MD, Naleway CA, Woods JS, Bittner AC Jr (1995). *Behavioral effects of low-level exposure to elemental Hg among dentists*. Neurotoxicology and Teratology, 17(2), 161–168.

Ehrenberg RL, Vogt RL, Smith AB, Brondum J, Brightwell WS, Hudson PJ, McManus KP, Hannon WP, Phipps FC (1991). *Effects of elemental mercury exposure at a thermometer plant*. American Journal of Industrial Medicine, 19(4), 495–507.

Eichholz GG, Petelka MF, Kury RL (1988). *Migration of elemental mercury through soil from simulated burial sites*. Water Research, 22(1), 15-20.

Euro Chlor (1999). *The mercury cell technology in Western Europe*. Presentation at the OSPAR Workshop on the Chlor-Alkali Industry, 27–29 September 1999, Brussels.

Fawer RF, de Ribaupierre Y, Guillemin M, Berode M, Lob M (1983). *Measurement of hand tremor induced by industrial exposure to metallic mercury*. British Journal of Industrial Medicine, 40, 204–208.

Fitzgerald WF, Mason RP, Vandal GM (1991). *Atmospheric cycling and air–water exchange of mercury over midcontinental lacustrine regions*. Water, Air, and Soil Pollution, 56, 745–767.

Foulds D, Copeland K, Franks R (1987). *Mercury poisoning and acrodynia*. American Journal of Diseases of Children, 141, 124–125.

Gabriel M, Williamson D (2004). *Principal Biogeochemical Factors Affecting the Speciation And Transport of Mercury through the terrestrial environment*. Environmental Geochemistry and Health, 26(3), 421-434.

Gilmour CC, Henry EA, Mitchell R (1992). *Sulfate stimulation of mercury methylation in freshwater sediments*. Environmental Science & Technology, 26(11), 2281-2287.

Golder Associates (2011). *2010 Conceptual Site Model - Botany*. Report No. 107623162_001_R_Rev0.

Han FX, Su Y, Monts DL, Waggoner CA, Plodinec MJ (2006). *Binding, distribution, and plant uptake of mercury in a soil from Oak Ridge, Tennessee, USA*. Science of The Total Environment, 368(2), 753-768.

Hofstee C, Dane JH, Walker RC (1998a). *Infiltration and redistribution of perchloroethylene in stratified water-saturated porous media*. Soil Science Society of America Journal, 62(1), 13-22.

Hofstee C, Oostrom M, Dane JH, Walker RC (1998b). *Infiltration and redistribution of perchloroethylene in partially saturated, stratified porous media*. Journal of Contaminant Hydrology, 34(4), 293-313.

Hylander LD, Meili M (2003). *500 years of mercury production: global annual inventory by region until 2000 and associated emissions*. Science of the Total Environment, 304(1), 13-27.

ITRC (2012). *Using Remediation Risk Management to Address Groundwater Cleanup Challenges at Complex Sites*. p 31.

Jalili MA, Abbasi AH (1961). *Poisoning by ethyl mercury toluene sulphonanilide*. British Journal of Industrial Medicine, 18(4), 303-308.

Kang-Yum E, Oransky SH (1992). *Chinese patent medicine as a potential source of mercury poisoning*. Veterinary and Human Toxicology, 34(3), 235–238.

Karpathios T, Zervoudakis A, Thodoridis C, Vlachos P, Apostolopoulou E, Fretzayas A (1991). *Mercury vapor poisoning associated with hyperthyroidism in a child*. Acta Paediatrica Scandinavica, 80(5):551–552.

Lechler PJ, Miller JR, Lacerda LD, Vinson D, Bonzongo JC, Lyons WB, Warwick JJ (2000). *Elevated mercury concentrations in soils, sediments, water, and fish of the Madeira River basin, Brazilian Amazon: a function of natural enrichments?*. Science of the Total Environment, 260(1), 87-96.

Lenhard RJ, Parker JC (1987). *Measurement and prediction of saturation-pressure relationships in three-phase porous media systems*. Journal of Contaminant Hydrology, 1, 407–424.

Leterme B, Jacques D (2013). *Literature Review on Mercury Speciation Soil Systems Under Oxidizing Conditions*. Snowman Network, IMaHG Report, Project No. SN-03/08.

Levine SP, Cavender GD, Langolf GD, Albers JW (1982). *Elemental mercury exposure: Peripheral neurotoxicity*. British Journal of Industrial Medicine, 39, 136–139.

Lindberg SE, Turner RR, Meyers TP, Taylor GE, Schroeder WH (1991). *Atmospheric concentrations and deposition of mercury to a deciduous forest at Walker Branch Watershed, Tennessee, USA*. Water, Air, and Soil Pollution, 56, 577–594.

Lindley AA (1997). *An economic and environmental analysis of the chlor-alkali production process: mercury cells and alternative technologies.* European Commission, Directorate-General III Industry, C-4, Chemicals, plastics, rubber, Brussels, Belgium.

Lindqvist O (1991a). *Mercury in the Swedish environment: 9. Mercury in terrestrial ecosystems bioavailability and effects*. Water, Air, and Soil Pollution, 55(1–2), 101–108.

Lindqvist O (1991b). *Mercury in the Swedish environment: 4. Emissions of mercury to the atmosphere*. Water, Air, and Soil Pollution, 55(1–2), 23–32.

Miller CL, Watson DB, Lester BP, Lowe KA, Pierce EM, Liang L (2013). *Characterization of soils from an industrial complex contaminated with elemental mercury*. Environmental Research, 125, 20–29.

Mishra B, O'Loughlin EJ, Boyanov MI, Kemner KM (2011). *Binding of HgII to High-Affinity Sites on Bacteria Inhibits Reduction to Hg0 by Mixed FeII/III Phases*. Environmental Science & Technology, 45(22), 9597-9603.

Murphy MJ, Culliford EJ, Parsons V (1979). *A case of poisoning with mercuric chloride*. Resuscitation, 7, 35–44.

National Research Council (2000). *Toxicological effects of methylmercury*. Committee on the Toxicological Effects of Methylmercury, Board on Environmental Studies and Toxicology Commission on Life Sciences, National Research Council, Washington, DC.

Newsham KE, Rushing JA, Lasswell PM, Cox JC, Blasingame TA (2004). *A comparative study of laboratory techniques for measuring capillary pressures in tight gas sands*. In SPE Annual Technical Conference and Exhibition. Society of Petroleum Engineers.

Ngim CH, Foo SC, Boey KW, Jeyaratnam J (1992). *Chronic neurobehavioural effects of elemental mercury in dentists*. British Journal of Industrial Medicine, 49(11), 782–790.

NICOLE (2015). *Risk-Based Management of Mercury-Impacted Sites*. Network for Industrially Contaminated Land in Europe.

Obrist D, Johnson DW, Lindberg SE, Luo Y, Hararuk O, Bracho R, Battles JJ, Dail DB, Edmonds RL, Monson RK, Ollinger SV, Pallardy SG, Pregitzer KS, Todd DE (2011). *Mercury Distribution Across 14 U.S. Forests. Part I: Spatial Patterns of Concentrations in Biomass, Litter, and Soils.* Environmental Science & Technology 45(9), 3974-3981.

Oostrom M, Hofstee C, Walker RC, Dane JH (1999). *Movement and remediation of trichloroethylene in a saturated heterogeneous porous medium: 1. Spill behavior and initial dissolution*. Journal of Contaminant Hydrology, 37(1), 159-178.

Oostrom M, Hofstee C, Lenhard RJ, Wietsma TW (2003). *Flow behavior and residual saturation formation of liquid carbon tetrachloride in unsaturated heterogeneous porous media*. Journal of Contaminant Hydrology, 64(1), 93-112.

Parker JC, Lenhard RJ, Kuppusamy T (1987). *A parametric model for constitutive properties governing multiphase flow in porous media*. Water Resources Research, 23(4), 618-624.

Piikivi L, Tolonen U (1989). *EEG findings in chlor-alkali workers subjected to low long term exposure to mercury vapour*. British Journal of Industrial Medicine, 46(6), 370–375.

Pittman ED (1992). *Relationship of porosity and permeability to various parameters derived from mercury injection-capillary pressure curves for sandstone*. The American Association of Petroleum Geologist Bulletin, 76(2), 191-198.

Ponce RA, Bloom NS (1991). *Effect of pH on the bioaccumulation of low level, dissolved methylmercury by rainbow trout (Oncorhynchus mykiss)*. Water, Air, & Soil Pollution, 56, 631–640.

Powers SE (1992). *Dissolution of non aqueous phase liquids in saturated subsurface systems*. Ph.D Dissertation, University of Michigan.

Ravichandran M (2004). *Interactions between mercury and dissolved organic matter: a review*. Chemosphere, 55(3), 319-331.

Risher JF (2003). *Elemental mercury and inorganic mercury compounds: human health aspects*. Concise International Chemical Assessment Document, World Health Organization, Geneva.

Ruth D, Lindsay C, Allen M (2013). *Combining electrical measurements and mercury porosimetry to predict permeability*. Petrophysics, 54(06), 531-537.

Salonen JT, Seppänen K, Nyyssönen K, Korpela H, Kauhanen J, Kantola M, Tuomilehto J, Esterbauer H, Tatzber F, Salonen R (1995). *Intake of mercury from fish, lipid peroxidation, and the risk of myocardial infarction and coronary, cardiovascular, and any death in Eastern Finnish men*. Circulation, 91(3), 645-655.

Samuels ER, Heick HM, McLaine PN, Farant JP (1982). *A case of accidental inorganic mercury poisoning*. Journal of Analytical Toxicology, 6, 120–122.

Scanlon BR, Tachovsky JA, Reedy R, Nicot JP, Keese K, Slade RM, Merwad V, Howard MT, Wells GL, Mullins GJ, Ortiz DM (2005). *Groundwater–surface water interactions in Texas*. Implications for Water Resources and Contaminant Transport (TCEQ), Bureau of Economic Geology, the University of Texas at Austin, 129–131.

Schlüter K (2000). *Review: evaporation of mercury from soils. An integration and synthesis of current knowledge*. Environmental Geology, 39(3), 249-271.

Schuster E (1991). *The behavior of mercury in the soil with special emphasis on complexation and adsorption processes - A review of the literature*. Water, Air, & Soil Pollution, 56, 667-680.

Schwartz JG, Snider TE, Montiel MM (1992). *Toxicity of a family from vacuumed mercury*. American Journal of Emergency Medicine, 10(3), 258–261.

Schwille F (1988). *Dense Chlorinated Solvents in Porous and Fractured Media - Model Experiments*. Lewis Publishers, Chelsea, MI.

Sexton DJ, Powell KE, Liddle J, Smrek A, Smith JC, Clarkson TW (1978). *A nonoccupational outbreak of inorganic mercury vapor poisoning*. Archives of Environmental Health, 33, 186–191.

Skyllberg U (2012). *Chemical Speciation of Mercury in Soil and Sediment. Environmental Chemistry and Toxicology of Mercury*. John Wiley & Sons, Inc., 219-258.

Smith JD, Chatzis I, Ioannidis MA (2002). *A new technique for measuring the breakthrough capillary pressure*. Society of Core Analysis, 40, 2002.

Sweijen T, Hartog N, Marsman A, Keijzer TJ (2014). *The transport behaviour of elemental mercury DNAPL in saturated porous media: Analysis of field observations and two-phase flow modelling*. Journal of Contaminant Hydrology, 161, 24-34.

Sznopek JL, Goonan TG (2000). *The materials flow of mercury in the economies of the United States and the world*. US Geological Survey, Circular 1197.

Ullrich SM, Tanton TW, Abdrashitova SA (2001). *Mercury in the Aquatic Environment: A Review of Factors Affecting Methylation*. Critical Reviews in Environmental Science and Technology, 31(3), 241-293.

UNEP (2002). *Global Mercury Assessment*. Geneva, Switzerland.

US EPA (1984). *Mercury health effects updates: Health issue assessment. Final report*. EPA 600/8-84-019F. US Environmental Protection Agency, Office of Health and Environmental Assessment, Washington, DC.

US EPA (1997). *Mercury Study for Congress. Volume I: Executive Summary*. EPA-452/R-97-003. US Environmental Protection Agency, Office of Air Quality Planning and Standards and Office of Research and Development.

US EPA (2007a). *Treatment Technologies for Mercury in Soil, Waste, and Water*. EPA Report 542-R-07-003. US Environmental Protection Agency, Office of Superfund Remediation and Technology Innovation.

US EPA (2007b). *Elemental Mercury*. EPA Archive Document, www.epa.gov/mercury.

Vandal GM, Mason RP, Fitzgerald WF (1991). *Cycling of volatile mercury in temperate lakes*. Water, Air, and Soil Pollution, 56, 791–803.

Vavra, CL, Kaldi JG, Sneider RM (1992). *Geological applications of capillary pressure: a review*. The American Association of Petroleum Geologist Bulletin, 76(6), 840-850.

Walvoord MA, Andraski BJ, Krabbenhoft DP, Striegl, RG (2008). *Transport of elemental mercury in the unsaturated zone from a waste disposal site in an arid region*. Applied Geochemistry, 23(3), 572-583.

Wardlaw NC, Taylor RP (1976). *Mercury capillary pressure curves and the intepretation of pore structure and capillary behaviour in reservoir rocks*. Bulletin of Canadian Petroleum Geology, 24(2), 225-262.

Warkany J, Hubbard DM (1953). *Acrodynia and mercury*. Journal of Pediatrics, 42, 365–386.

World Chlorine Council (2011). *Reduction of mercury emissions and use from the chlor-alkali sector partnership*.

Wren C (1992). *Relationship of mercury levels in sportfish with lake sediment and water quality variables*. Toronto: Ontario Environmental Research Program. Government Reports Announcements and Index (GRA&I) Issue 08.

Wu WJ, Delshad M, Oolman T, Pope GA (2000). *Remedial Options for Creosote-Contaminated Sites*. Groundwater Monitoring & Remediation, 20(2), 78-86.

Zhang L, Wright LP, Blanchard P (2009). *A review of current knowledge concerning dry deposition of atmospheric mercury*. Atmospheric Environment, 43(37), 5853-5864.

Chapter 2

The GDAn Code: Mathematical and Numerical Framework

In this chapter, GDAn (Groundwater Dynamics Analysis), the code developed entirely by the Author, is presented and described. GDAn is a 2D finite element model, based on unstructured triangular mesh, meant for the analysis of groundwater dynamics, multiphase flow and solute transport in porous media. The code, written in Visual Basic language, is made of several modules, namely: GDAn-WS (Water Saturated); GDAn-VWS (Variably Water Saturated); GDAn-ST (Solute Transport); GDAn-NAPL (NonAqueous Phase Liquid); GDAn-Hg^0 (Elemental Mercury), lately discussed in Chapter 6. The mesh is generated using EasyMesh 1.4 (Niceno, 1997), while simulation outputs are plotted using Surfer 8 (Golden Software, 2002).

The first part of the chapter is devoted to the description of the mathematical and numerical framework of each module. The shape functions and the matrices used for the numerical discretization are then presented. Finally, the procedures adopted to solve the different linear and nonlinear systems appearing in the numerical formulation are introduced.

In the second part, the code is tested by means of a series of analytical, numerical, and experimental benchmark problems taken from the scientific literature.

2.1 Steady- and Unsteady-State Water Saturated Flow

2.1.1 GDAn-WS – Governing Equations

Under the hypothesis of isothermal flow, incompressible fluid and nondeforming medium, the steady-state groundwater flow equation through water saturated porous media is written as (Bear, 1972; Istok, 1989):

$$\frac{\partial}{\partial x_i}\left[K_{w,ij}\left(\frac{\partial h_w}{\partial x_j}+u_j\right)\right]+q_w=0 \tag{2.1}$$

while the unsteady-state form is written as:

$$\frac{\partial}{\partial x_i}\left[K_{w,ij}\left(\frac{\partial h_w}{\partial x_j}+u_j\right)\right]+q_w=S_{s,w}\frac{\partial h_w}{\partial t} \tag{2.2}$$

where h_w is the water pressure head, $K_{w,ij}$ is the saturated hydraulic conductivity tensor, x_i (i = 1, 2) are the spatial coordinates, u_j is the unit vector in the direction of the x_2 coordinate (assumed to be vertically upward), t is the elapsed time, $S_{s,w}$ is the specific storage, and q_w is the water volumetric flow rate via sources (or sinks) per unit volume of the medium.

The initial conditions associated with Eq. 2.2 and the boundary conditions associated with Eqs. 2.1 and 2.2 can be expressed as:

$$h_w(x_i,0)=h_{w,0}(x_i) \tag{2.3}$$

$$h_w(x_i,t)=\tilde{h}_w \qquad \text{on } \partial_1 \tag{2.4}$$

$$v_{w,i}n_i=-v_{w,n} \qquad \text{on } \partial_2 \tag{2.5}$$

where $h_{w,0}$ is the initial water pressure head value, ∂_1 is the portion of the flow boundary where h_w is prescribed as $\tilde{h}_w$ (Dirichlet boundary condition), ∂_2 is the portion of the flow boundary where the outward water flux is prescribed as $-v_{w,n}$ (Neumann boundary condition), and n_i is the outward unit vector normal to the boundary ∂_2.

When the distribution of h_w is known, the apparent groundwater velocity components, $v_{w,i}$, are computed using Darcy's law (Bear, 1972):

$$v_{w,i}=-K_{w,ij}\left(\frac{\partial h_w}{\partial x_j}+u_j\right) \tag{2.6}$$

2.1.2 GDAn-WS – Global System of Equations

The application of Galerkin's method (Istok, 1989; Kolditz, 2002) to the equations of groundwater flow leads to systems of equations that can be written in global matrix form. In particular, for the steady-state groundwater flow through water saturated porous media, Eq. 2.1 becomes:

$$[K_w]\{h_w\} = \{F_{g,w}\} + \{F_{q,w}\} \tag{2.7}$$

where $[K_w]$ is the global conductance matrix, $\{h_w\}$ is the vector of the unknown water pressure heads, $\{F_{g,w}\}$ is the vector incorporating the gravitational forces, and $\{F_{q,w}\}$ is the vector incorporating the Neumann boundary conditions.

Conversely, the unsteady-state form, Eq. 2.2, becomes:

$$[B_w]\frac{\partial}{\partial t}\{h_w\} + [K_w]\{h_w\} = \{F_{g,w}\} + \{F_{q,w}\} \tag{2.8}$$

where $[B_w]$ is the global specific storage matrix.

By means of the backward finite difference method (backward Euler), the system of equations in Eq. 2.8 can be rearranged as follows:

$$\left(\frac{1}{\Delta t}[B_w] + [K_w]\right)\{h_w\}_{t+\Delta t} = \frac{1}{\Delta t}[B_w]\{h_w\}_t + \left(\{F_{g,w}\} + \{F_{q,w}\}\right)_{t+\Delta t} \tag{2.9}$$

where t and t + Δt denote the two different time levels.

2.2 Steady- and Unsteady-State Variably Water Saturated Flow

2.2.1 GDAn-VWS – Governing Equations

Under the hypothesis of isothermal flow, incompressible fluids and nondeforming medium, and assuming that the role of the air phase is insignificant, hence it is considered extremely mobile and its pressure field is neglected, the steady- and unsteady-state groundwater flow equations through variably water saturated porous media can be described by Richards' equation (Richards, 1931; Cooley, 1971; Braester et al., 1971, Huyakorn et al., 1984; Celia et al., 1990). In particular, the steady-state form is written as:

$$\frac{\partial}{\partial x_i}\left[K_{w,ij}k_{rw}\left(\frac{\partial h_w}{\partial x_j} + u_j\right)\right] + q_w = 0 \tag{2.10}$$

while the unsteady-state form is written as:

$$\frac{\partial}{\partial x_i}\left[K_{w,ij} k_{rw}\left(\frac{\partial h_w}{\partial x_j} + u_j\right)\right] + q_w = S_w S_{s,w}\frac{\partial h_w}{\partial t} + \phi\frac{\partial S_w}{\partial t} \tag{2.11}$$

where h_w is the water pressure head, $K_{w,ij}$ is the saturated hydraulic conductivity tensor, k_{rw} is the water relative permeability, x_i (i = 1, 2) are the spatial coordinates, u_j is the unit vector in the direction of the x_2 coordinate (assumed to be vertically upward), t is the elapsed time, S_w is the water saturation, $S_{s,w}$ is the specific storage, ϕ is the porous medium porosity, and q_w is the water volumetric flow rate via sources (or sinks) per unit volume of the medium.

Eq. 2.11 is written in mixed form (Celia et al., 1990; Rathfelder and Abriola, 1994) to ensure the mass conservation of the numerical discretization. As a matter of fact, in the conventional h-based form, mass balance errors are usually observed due to the expansion of the storage term (Aziz and Settari, 1979; Milly, 1985; Celia et al., 1990; Abriola and Rathfelder, 1993):

$$\frac{\partial S_w}{\partial t} = \frac{\partial S_w}{\partial h_w}\frac{\partial h_w}{\partial t} = C_w(S_w)\frac{\partial h_w}{\partial t} \tag{2.12}$$

While the equality shown in Eq. 2.12 holds true in mathematical terms, the discrete analogue does not, especially due to the highly nonlinear nature of the specific capacity term $C_w(S_w)$. Mass conservation is possible only when the expansion in Eq. 2.12 is equivalent to its discrete form (Aziz and Settari, 1979). Hence the choice of the mixed form (Celia et al., 1990) to overcome these difficulties.

The initial conditions associated with Eq. 2.11 and the boundary conditions associated with Eqs. 2.10 and 2.11 can be expressed as shown in Eqs. 2.3-2.5.

When the distributions of h_w and S_w are known, the apparent groundwater velocity components, $v_{w,i}$, are computed using Darcy's law (Bear, 1972):

$$v_{w,i} = -K_{w,ij} k_{rw}\left(\frac{\partial h_w}{\partial x_j} + u_j\right) \tag{2.13}$$

In Eqs. 2.10 and 2.11, the water pressure head and the water saturation are related by nonlinear constitutive relationships which depend directly on the porous medium properties. The relative permeability is also a nonlinear function, here expressed in terms

of water saturation. In particular, in the present code, the nonlinear P_c-S constitutive relationship adopted is that of van Genuchten (1980):

$$S_w = S_{w,ir} + \left(1 - S_{w,ir}\right) \cdot \overline{S_w} \tag{2.14}$$

$$\overline{S_w} = \{1 + [\alpha(h_a - h_w)]^n\}^{-m} \tag{2.15}$$

where $S_{w,ir}$ is the irreducible water saturation, $\overline{S_w}$ is the effective water saturation, h_a is the air pressure head in terms of water pressure head, α, n and m are the van Genuchten model parameters.

The k_r-S relationships, incorporated within the code, are those of Burdine and Mualem (Burdine 1953; Mualem, 1976), reported hereinafter:

- Burdine's model

$$k_{rw} = \overline{S_w}^2 \cdot \left[1 - \left(1 - \overline{S_w}^{1/m}\right)^m\right] \tag{2.16}$$

- Mualem's model

$$k_{rw} = \overline{S_w}^{1/2} \cdot \left[1 - \left(1 - \overline{S_w}^{1/m}\right)^m\right]^2 \tag{2.17}$$

where m is equal to 1-2/n, with n > 2, in the case of Burdine's model, and equal to 1-1/n, with n > 1, in the case of Mualem's model.

2.2.2 GDAn-VWS – Global System of Equations

The application of Galerkin's method (Istok, 1989; Kolditz, 2002) to the equations of groundwater flow leads to systems of equations that can be written in global matrix form. In particular, for the steady-state groundwater flow through variably water saturated porous media, Eq. 2.10 becomes:

$$[K_w(S_w)]\{h_w\} = \{F_{g,w}(S_w)\} + \{F_{q,w}\} \tag{2.18}$$

where $[K_w(S_w)]$ is the global conductance matrix, $\{h_w\}$ is the vector of the unknown water pressure heads, $\{F_{g,w}(S_w)\}$ is the vector incorporating the gravitational forces, and $\{F_{q,w}\}$ is the vector incorporating the Neumann boundary conditions.

Conversely, the unsteady-state form, Eq. 2.11, becomes:

$$\frac{\partial}{\partial t}\{S_w\} + [B_w(S_w)]\frac{\partial}{\partial t}\{h_w\} + [K_w(S_w)]\{h_w\} = \{F_{g,w}(S_w)\} + \{F_{q,w}\} \quad (2.19)$$

where $[B_w(S_w)]$ is the global specific storage matrix, and $\{S_w\}$ is the vector of the unknown water saturations.

The modified Picard iteration scheme (Celia et al., 1990), based on a fully implicit (backward Euler) time approximation, is used to discretize Eq. 2.11, thus ensuring the mass conservativeness of the solution. This discretization leads to the following scheme:

$$\left(\frac{1}{\Delta t}\left[C_w\left(S_w^{\delta+1}\right)\right] + \frac{1}{\Delta t}\left[B_w\left(S_w^{\delta+1}\right)\right] + \left[K_w\left(S_w^{\delta+1}\right)\right]\right)\{h_w\}_{t+\Delta t}^{\delta+1}$$

$$= \frac{1}{\Delta t}\left(\left[B_w\left(S_w^{\delta+1}\right)\right]\{h_w\}_t + \left[C_w\left(S_w^{\delta+1}\right)\right]\{h_w\}_{t+\Delta t}^{\delta+1} - [E]\left(S_w^{\delta+1} - S_{w,t}\right)\right) +$$

$$+\left(\left\{F_{g,w}\left(S_w^{\delta+1}\right)\right\} + \{F_{q,w}\}\right)_{t+\Delta t} \quad (2.20)$$

where t and t + Δt denote the two different time levels, δ denotes the iteration level, and $[C_w(S_w)]$ is the global capacitance matrix.

2.3 Solute Transport

2.3.1 GDAn-ST – Governing Equations

The single-species advection-dispersion equation of solutes, subjected to sorption, volatilization, decay, and interphase mass transfer occurring from NAPL dissolution, under local equilibrium transport and during transient water flow in variably water saturated nondeforming porous media, is written as (Istok, 1989; Miller et al. 1990; Šimůnek and van Genuchten, 2007):

$$\frac{\partial}{\partial t}\left(S_w\phi c + S_a\phi k_H c + \rho_b\frac{ds}{dc}c\right) = \frac{\partial}{\partial x_i}\left(S_w\phi D_{e,ij}\frac{\partial c}{\partial x_j}\right) + \frac{\partial}{\partial x_i}\left(S_a\phi D_{a,ij}\frac{\partial k_H c}{\partial x_j}\right) +$$

$$-\frac{\partial}{\partial x_i}\left(v_{w,i}c\right) - \left(\lambda_w S_w\phi c + \lambda_a S_a\phi k_H c + \lambda_s\rho_b\frac{ds}{dc}c\right) - \frac{\partial}{\partial t}\left(\rho_n S_n\phi\right) \quad (2.21)$$

where c is the solute concentration in the water phase, s is the solute concentration on the solid phase, $D_{e,ij}$ is the effective dispersion tensor in the water phase, $D_{a,ij}$ is the diffusion tensor in the air phase, S_w is the water saturation, S_a is the air saturation, S_n is the NAPL saturation, $v_{w,i}$ is the apparent groundwater velocity component, ϕ is the porous medium porosity, k_H is the Henry's constant, ρ_b is the porous medium bulk density, ρ_n is the NAPL

density, λ_w is the solute decay constant in the water phase, λ_a is the solute decay constant in the air phase, λ_s is the solute decay constant on the solid phase, x_i (i = 1, 2) are the spatial coordinates, t is the elapsed time. It is worth noticing that Eq. 2.21 holds true under the further assumption that the variation in the water phase density induced by the presence of solutes can be regarded as negligible.

The initial conditions and the boundary conditions associated with Eq. 2.21 can be expressed as:

$$c(x_i, 0) = c_0(x_i) \tag{2.22}$$

$$c(x_i, t) = \tilde{c} \qquad \text{on } \partial_1 \tag{2.23}$$

$$-S_w \phi D_{e,ij} \frac{\partial c}{\partial x_j} n_i + v_{w,i} n_i c = v_{w,i} n_i \tilde{c} \qquad \text{on } \partial_2 \tag{2.24}$$

where c_0 is the initial solute concentration in the water phase, ∂_1 is the portion of the boundary where c is prescribed as $\tilde{c}$ (Dirichlet boundary condition), ∂_2 is the portion of the boundary where the solute flux is prescribed as $v_{w,i} n_i \tilde{c}$ (Cauchy boundary condition), n_i is the outward unit vector normal to the boundary ∂_2. In those cases where the boundary can be regarded as "impermeable" or when the water flow is directed out of the region, the Cauchy boundary condition degenerates to a Neumann type boundary condition of the form:

$$S_w \phi D_{e,ij} \frac{\partial c}{\partial x_j} n_i = 0 \qquad \text{on } \partial_2 \tag{2.25}$$

For volatile solutes present in both liquid and gas phases, Eq. 2.24 must be enforced with an additional term, which allows to take into account the diffusion in the air phase through a stagnant boundary layer above the soil surface (Jury et al., 1983):

$$-S_w \phi D_{e,ij} \frac{\partial c}{\partial x_j} n_i + v_{w,i} n_i c = v_{w,i} n_i \tilde{c} + \frac{D_{0,a}}{d} (k_H c - c_{atm}) \qquad \text{on } \partial_2 \tag{2.26}$$

where $D_{0,a}$ is the molecular diffusion coefficient in the pure air phase, d is the thickness of the stagnant boundary layer, and c_{atm} is the solute concentration above the stagnant boundary layer.

Eq. 2.21 represents a general case and can be simplified by neglecting some of the terms figuring in it, depending on the groundwater flow field (steady- or unsteady-state), the water saturation field (water saturated or variably water saturated porous medium), or whether phenomena such as sorption, volatilization, decay, or NAPL dissolution must be taken into account or not.

The effects of molecular diffusion and of mechanical dispersion in the water phase are incorporated within the effective dispersion tensor for the water phase, which coefficients can be computed as follows:

$$D_{e,ij} = D_w^* + a_{ijmn} \frac{\overline{v_m} \cdot \overline{v_n}}{\sqrt{\overline{v_m}^2 + \overline{v_n}^2}} \tag{2.27}$$

where D_w^* is the solute apparent molecular diffusion coefficient, a_{ijmn} are the components of the aquifer dispersivity, i and j are the subscripts referring to the coordinate system main directions, $\overline{v_m}$ and $\overline{v_n}$ are the components of the pore water velocity and the subscripts m and n refer to the directions of the principal components of pore water velocity. Assuming the aquifer to be isotropic with respect to dispersion, all the components of the aquifer dispersivity are zero, exception made of $a_{iiii} = a_L$, $a_{jjjj} = a_T$ and $a_{ijij} = a_{ijji} = 1/2 \cdot (a_L - a_T)$, with $i \neq j$, where a_L and a_T are the longitudinal and transverse dispersivity of the aquifer, respectively.

The solute apparent molecular diffusion coefficient for the water phase, instead, can be defined as:

$$D_w^* = \tau(S_w) D_{0,w} \tag{2.28}$$

where $D_{0,w}$ is the molecular diffusion coefficient in the pure water phase, and $\tau(S_w)$ is the tortuosity factor, which is a correction factor that allows to take into account the effects of the reduced flow area and increased path length of diffusing molecules within the porous medium. The tortuosity factor is here defined by means of Millington and Quirk (1961) formula:

$$\tau(S_w) = \frac{\vartheta_w^{10/3}}{\phi^2} \tag{2.29}$$

where $\vartheta_w = S_w \cdot \phi$ is the porous medium water content.

Regarding the volatilization phenomenon, the coefficient of the diffusion tensor in the air phase, which is the only coefficient of the diffusion tensor $D_{a,ij}$, is similar to Eqs. 2.28 and 2.29, and is defined as:

$$D_a^* = \tau(S_a) D_{0,a} \tag{2.30}$$

$$\tau(S_a) = \frac{\vartheta_a^{10/3}}{\phi^2} \tag{2.31}$$

where $\vartheta_a = S_a \cdot \phi$ is the porous medium air content.

The effects of sorption are included within the term ds/dc, which represents the local slope of the adsorption isotherm. Within the code, two sorption models are implemented, namely, the linear sorption model (Batu 2006; Šimůnek and van Genuchten, 2007), which greatly simplifies the mathematical description of sorption by assuming ds/dc as a constant, namely K_d, the equilibrium distribution coefficient, and the nonlinear sorption model of Langmuir (1918), where the local slope of the adsorption isotherm becomes:

$$\frac{ds}{dc} = \frac{K_l \bar{S}}{(1+K_l c)^2} \tag{2.32}$$

where K_l is Langmuir constant and $\bar{S}$ is the total concentration of sorption sites available.

The effects of radioactive decay or biological degradation of the solute are taken into account by means of the term $-\left(\lambda_w S_w \phi c + \lambda_a S_a \phi k_H c + \lambda_s \rho_b \frac{ds}{dc} c\right)$, figuring in Eq. 2.21. This is a first-order irreversible rate reaction, where the constant λ is usually expressed in terms of the half-life time of the solute:

$$\lambda = \frac{\ln 2}{t_{1/2}} \tag{2.33}$$

where $t_{1/2}$ is the half-life time.

If a NAPL is present into the soil and its dissolution occurs, then the dissolved mass flux due to NAPL dissolution, per unit volume of porous medium, can be expressed as follows (Miller et al., 1990; Powers et al., 1992):

$$\frac{\partial}{\partial t}(\rho_n S_n \phi) = -k_{la}(c_s - c) \tag{2.34}$$

where k_{la} is the lumped mass transfer coefficient and c_s is the NAPL aqueous solubility.

2.3.2 GDAn-ST – Global System of Equations

The application of Galerkin's method (Istok, 1989; Kolditz, 2002) to the equations of solute transport leads to systems of equations that can be written in global matrix form. In particular, assuming a steady-state groundwater flow through variably water saturated porous media, Eq. 2.21 becomes:

$$[A]\frac{\partial}{\partial t}\{c\} + [D]\{c\} = \{F_{c,w}\} + \{F_{c,a}\} + \{M\} \tag{2.35}$$

while assuming an unsteady-state groundwater flow, Eq. 2.21 becomes:

$$[A(t)]\frac{\partial}{\partial t}\{c\} + [D(t)]\{c\} = \{F_{c,w}\} + \{F_{c,a}\} + \{M\} \tag{2.36}$$

where [A] and [D] are the global sorption matrix and the global advection-dispersion matrix, respectively, which can be both dependent on time t, depending whether the groundwater flow field is steady or unsteady, $\{F_{c,w}\}$ and $\{F_{c,a}\}$ are the vectors incorporating the solute and the air boundary fluxes, respectively, and {M} is the vector incorporating the effects of mass transfer.

By means of the backward finite difference method (backward Euler), the system of equations in Eq. 2.36 can be rearranged as follows (for the sake of brevity and clarity, only Eq. 2.36 is rearranged, being Eqs. 2.35 and 2.36 practically the same except for the dependency on time of the latter):

$$\left(\frac{1}{\Delta t}[A(t+\Delta t)] + [D(t+\Delta t)]\right)\{c\}_{t+\Delta t} = \frac{1}{\Delta t}[A(t)]\{c\}_t + \left(\{M\} + \{F_{c,a}\}\right)_t + \{F_{c,w}\}_{t+\Delta t} \tag{2.37}$$

where t and t + Δt denote the two different time levels.

2.4 Multiphase Flow of Immiscible Fluids

2.4.1 GDAn-NAPL – Governing Equations

Under the hypothesis of isothermal flow, incompressible fluids and nondeforming medium, and assuming that the role of the air phase is insignificant, hence it is considered extremely mobile and its pressure field is neglected, the governing equations of multiphase flow of immiscible fluids in porous media are written as follows (Abriola and Pinder, 1985; Parker et al., 1987; Parker 1989):

$$\frac{\partial}{\partial x_i}\left[K_{w,ij}k_{rw}\left(\frac{\partial h_w}{\partial x_j}+u_j\right)\right]+q_w=S_wS_{s,w}\frac{\partial h_w}{\partial t}+\phi\frac{\partial S_w}{\partial t} \tag{2.38}$$

$$\frac{\partial}{\partial x_i}\left[K_{w,ij}\frac{k_{rn}}{\eta_{rn}}\left(\frac{\partial h_n}{\partial x_j}+\rho_{rn}u_j\right)\right]+q_n=S_nS_{s,n}\frac{\partial h_n}{\partial t}+\phi\frac{\partial S_n}{\partial t} \tag{2.39}$$

where h_w is the water pressure head, h_n is the NAPL pressure head in water-equivalent head, $K_{w,ij}$ is the saturated hydraulic conductivity tensor, k_{rw} is the water relative permeability, k_{rn} is the NAPL relative permeability, η_{rn} is the dynamic viscosity ratio between NAPL and water, ρ_{rn} is the density ratio between NAPL and water, x_i (i = 1, 2) are the spatial coordinates, u_j is the unit vector in the direction of the x_2 coordinate (assumed to be vertically upward), t is the elapsed time, S_w is the water saturation, S_n is the NAPL saturation, $S_{s,w}$ is the water specific storage, $S_{s,n}$ is the NAPL specific storage, ϕ is the porous medium porosity, and q_w and q_n are the water and the NAPL volumetric flow rates via sources (or sinks) per unit volume of the medium, respectively.

Eqs. 2.38 and 2.39 are written in mixed form (Celia et al., 1990; Katyal and Parker, 1992; Rathfelder and Abriola, 1994) to ensure the mass conservation of the numerical discretization (sec. 2.2.1).

The initial and boundary conditions associated with Eq. 2.38 can be expressed as shown in Eqs. 2.3-2.5, while those associated with Eq. 2.39 can be expressed as follows:

$$h_n(x_i,0)=h_{n,0}(x_i) \tag{2.40}$$

$$h_n(x_i,t)=\tilde{h}_n \quad \text{on } \partial_1 \tag{2.41}$$

$$v_{n,i}n_i=-v_{n,n} \quad \text{on } \partial_2 \tag{2.42}$$

where $h_{n,0}$ is the initial NAPL pressure head value expressed in water-equivalent head, ∂_1 is the portion of the flow boundary where h_n is prescribed as $\tilde{h}_n$ (Dirichlet boundary condition), ∂_2 is the portion of the flow boundary where the outward NAPL flux is prescribed as $-v_{n,n}$ (Neumann boundary condition), and n_i is the outward unit vector normal to the boundary ∂_2.

When the distributions of h_w, h_n, S_w, and S_n are known, the apparent groundwater velocity components, $v_{w,i}$, are computed with Eq. 2.17, while the apparent NAPL velocity components, $v_{n,i}$, are computed by means of the extended Darcy's law (Bear, 1972):

$$v_{n,i} = -K_{w,ij}\frac{k_{rn}}{\eta_{rn}}\left(\frac{\partial h_n}{\partial x_j} + \rho_{rn}u_j\right) \tag{2.43}$$

The P_c-S and k_r-S constitutive relations used to describe the multiphase flow of a three phase system, made of air, NAPL and water (assuming a wettability hierarchy in which air phase is the nonwetting phase, the NAPL has an intermediate wetting behaviour, and the water is the wetting phase), are based on the nonhysteretic three-phase relationships introduced by Parker et al. (1987), with the extensions made by Kaluarachchi and Parker (1992) to consider hysteresis due to NAPL entrapment, Type-II hysteresis (Lenhard et al. 1989), and with the modifications made by Lenhard et al. (2004) to take into account the residual NAPL saturation. Here, according to Lenhard et al. (2004), the term entrapped refers to the NAPL saturation that occurs when the NAPL is occluded by water as water displaces the NAPL into larger pore spaces during water imbibition, while the term residual is to describe the NAPL saturation in the vadose zone that does not drain from the pore spaces when no drainage restrictions exist.

The nonlinear P_c-S constitutive relations previously introduced are briefly reported hereinafter:

$$\overline{\overline{S_w}} = \{1 + [\alpha\beta_{nw}(h_n - h_w)]^n\}^{-m} \tag{2.44}$$

$$\overline{S_t} = \{1 + [\alpha\beta_{an}(h_a - h_n)]^n\}^{-m} \tag{2.45}$$

$$\overline{\overline{S_w}} = \overline{S_w} + \overline{S_{ne}} \tag{2.46}$$

$$\overline{S_{nf}} = \overline{S_t} - \overline{S_w} \tag{2.47}$$

$$\overline{S_n} = \overline{S_{nf}} + \overline{S_{ne}} + \overline{S_{nr}} \tag{2.48}$$

$$\overline{S_{ne}} = \frac{1-\overline{S_w^{min}}}{1+R\left(1-\overline{S_w^{min}}\right)} - \frac{1-\overline{\overline{S_w}}}{1+R\left(1-\overline{\overline{S_w}}\right)} \quad \text{with } \overline{S_w} > \overline{S_w^{min}} \text{ and } R = \frac{1}{\overline{S_{ne}^{max}}} - 1 \tag{2.49}$$

$$\overline{S_{nr}} = \overline{S_{nr}^{max}}\left(\overline{S_t^{max}} - \overline{\overline{S_w}}\right)^{1/2}\left(1 - \overline{\overline{S_w}}\right)^{3/2} \tag{2.50}$$

where $\overline{\overline{S_w}}$ is the apparent water saturation, $\overline{S_t}$ is the effective total liquid saturation, $\overline{S_w}$ is the effective water saturation, $\overline{S_n}$ is the effective NAPL saturation, $\overline{S_{nf}}$ is the effective free NAPL saturation, $\overline{S_{ne}}$ is the effective entrapped NAPL saturation, $\overline{S_{nr}}$ is the effective residual NAPL saturation, R is the Land's parameter (Land, 1968), $\overline{S_{ne}^{max}}$ is the maximum

effective entrapped NAPL saturation for the main imbibition curve, $\overline{S_{nr}^{max}}$ is the maximum effective residual NAPL saturation, $\overline{S_{w}^{min}}$ is the minimum effective water saturation corresponding to the reversal from water drainage to imbibition, $\overline{S_{t}^{max}}$ is the historical maximum effective total liquid saturation, h_a is the air pressure head expressed in water-equivalent head, β_{nw} and β_{an} are fluid dependent scaling parameters (Lenhard and Parker 1987; White et al., 2004), α, n and m are the van Genuchten (1980) model parameters. Exception made of $\overline{S_w}$ (Eq. 2.14), and of $\overline{S_t} = (S_t - S_{w,ir})/(1 - S_{w,ir})$, all the other effective saturations previously introduced are computed by normalizing the respective saturations by $(1-S_{w,ir})$, where $S_{w,ir}$ is the irreducible water saturation.

The NAPL k_r-S relationships, incorporated within the code, are those of Burdine and Mualem (Burdine 1953; Mualem, 1976), properly modified according to Kaluarachchi and Parker (1992) and Lenhard et al. (2004):

- Burdine's model

$$k_{rn} = \left(\overline{S_t} - \overline{\overline{S_w}} - \overline{S_{nr}}\right)^2 \left\{\left[1 - \left(\overline{\overline{S_w}} + \overline{S_{nr}}\right)^{1/m}\right]^m - \left(1 - \overline{S_t}^{1/m}\right)^m\right\} \tag{2.51}$$

- Mualem's model

$$k_{rn} = \left(\overline{S_t} - \overline{\overline{S_w}} - \overline{S_{nr}}\right)^{1/2} \left\{\left[1 - \left(\overline{\overline{S_w}} + \overline{S_{nr}}\right)^{1/m}\right]^m - \left(1 - \overline{S_t}^{1/m}\right)^m\right\}^2 \tag{2.52}$$

where m is equal to 1-2/n, with n > 2, in the case of Burdine's model, and equal to 1-1/n, with n > 1, in the case of Mualem's model. The water k_r-S relationships are defined by either Eq. 2.15 or 2.16.

In the parts of the domain where the NAPL is absent, the governing equations, as well as the constitutive relations, reduce to those of variably water saturated flow, presented in sec. 2.2.1. To avoid numerical instabilities associated with the change from a two-phase air-water system to a three-phase air-NAPL-water system, once a location within the computational domain is classified as a three-phase node, it is not allowed anymore to revert to a two-phase air-water system (Kaluarachchi and Parker, 1989). To classify a location as a three-phase node, the following condition must be satisfied (Kaluarachchi and Parker, 1989):

$$h_n > \frac{\beta_{an} h_a + \beta_{nw} h_w}{\beta_{an} + \beta_{nw}} \tag{2.53}$$

Eq. 2.53 can be easily derived from the condition $\overline{S_t} > \overline{\overline{S_w}}$, which implies the NAPL presence within the system. Conversely, when the system is water saturated and initially pristine, the condition that implies the NAPL presence within the system is $h_n > h_w$ (Abriola and Rathfelder, 1993).

2.4.2 GDAn-NAPL – Global System of Equations

The application of Galerkin's method (Istok, 1989; Kolditz, 2002) to the equations of multiphase flow of immiscible fluids in porous media leads to a system of equations that can be written in global matrix form. In particular, Eqs. 2.38 and 2.39 become, respectively:

$$\frac{\partial}{\partial t}\{S_w\} + [B_w(S_w)]\frac{\partial}{\partial t}\{h_w\} + [K_w(S_w)]\{h_w\} = \{F_{g,w}(S_w)\} + \{F_{q,w}\} \tag{2.54}$$

$$\frac{\partial}{\partial t}\{S_n\} + [B_n(S_n)]\frac{\partial}{\partial t}\{h_n\} + [K_n(S_n)]\{h_n\} = \{F_{g,n}(S_n)\} + \{F_{q,n}\} \tag{2.55}$$

where $[K_w(S_w)]$ is the global water conductance matrix, $[K_n(S_n)]$ is the global NAPL conductance matrix, $[B_w(S_w)]$ is the global water specific storage matrix, $[B_n(S_n)]$ is the global NAPL specific storage matrix, $\{h_w\}$ is the vector of the unknown water pressure heads, $\{h_n\}$ is the vector of the unknown NAPL pressure heads, $\{S_w\}$ is the vector of the unknown water saturations, $\{S_n\}$ is the vector of the unknown NAPL saturations, $\{F_{g,w}(S_w)\}$ is the vector incorporating the gravitational forces acting on the water phase, $\{F_{g,n}(S_n)\}$ is the vector incorporating the gravitational forces acting on the NAPL, $\{F_{q,w}\}$ is the vector incorporating the Neumann boundary conditions for the water phase, and $\{F_{q,n}\}$ is the vector incorporating the Neumann boundary conditions for the NAPL.

The modified Picard iteration scheme (Celia et al., 1990), based on a fully implicit (backward Euler) time approximation, is used to discretize Eqs. 2.54 and 2.55, thus ensuring the mass conservativeness of the solution. This discretization leads to the following scheme:

$$\left(\frac{1}{\Delta t}\left[C^*\left(S^{\delta+1}\right)\right]+\frac{1}{\Delta t}\left[B^*\left(S^{\delta+1}\right)\right]+\left[K^*\left(S^{\delta+1}\right)\right]\right)\{h\}_{t+\Delta t}^{\delta+1}$$

$$=\frac{1}{\Delta t}\left(\left[B^*\left(S^{\delta+1}\right)\right]\{h\}_t+\left[C^*\left(S^{\delta+1}\right)\right]\{h\}_{t+\Delta t}^{\delta+1}-[E]\left(S^{\delta+1}-S_t\right)\right)+$$

$$+\left(\left\{F_g^*\left(S^{\delta+1}\right)\right\}+\left\{F_q^*\right\}\right)_{t+\Delta t} \tag{2.56}$$

where t and t + Δt denote the two different time levels, δ denotes the iteration level, $[B^*(S)]$ is the overall global specific storage matrix, $[C^*(S)]$ is the overall global capacitance matrix, $[K^*(S)]$ is the overall global conductance matrix, $\{F_g^*(S)\}$ is the overall vector incorporating the gravitational forces acting on the liquid phases, $\{F_q^*\} = \left\{\{F_{q,w}\}\{F_{q,n}\}\right\}^T$ is the overall vector incorporating the Neumann boundary conditions, $\{h\} = \{\{h_w\}\{h_n\}\}^T$ is the global vector of the unknown water and NAPL pressure heads, $\{S\} = \{\{S_w\}\{S_n\}\}^T$ is the global vector of the unknown water and NAPL saturations.

2.5 Shape Functions and Element Matrices

2.5.1 Influence Coefficient Matrices of the Linear Triangle Element

The application of Galerkin's method (Istok, 1989; Kolditz, 2002) to the equations presented in secs. 2.1-2.4 leads to systems of equations that can be written in global matrix form. Each global matrix results from the assembling of the respective element matrices, computed within the elements of the domain. Hence, to define the global matrices, the shape functions and the influence coefficient matrices of the generic element of the domain must be determined.

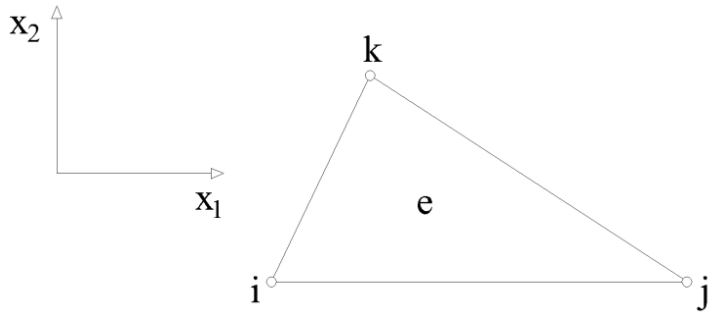

Fig. 2.1. Linear triangle element.

In the GDAn code, the 2D computational domain is discretized by means of an unstructured triangular mesh. The analytical shape functions for the general linear triangle element, Fig. 2.1, are reported hereinafter (Segerlind, 1984):

$$N_i^e(x_1, x_2) = \frac{1}{2\Omega^e}(a_i + b_i x_1 + c_i x_2) \tag{2.57}$$

$$N_j^e(x_1, x_2) = \frac{1}{2\Omega^e}(a_j + b_j x_1 + c_j x_2) \tag{2.58}$$

$$N_k^e(x_1, x_2) = \frac{1}{2\Omega^e}(a_k + b_k x_1 + c_k x_2) \tag{2.59}$$

where the subscripts i, j and k denote the element nodes, the superscript e denotes the element, x_1 and x_2 are the spatial coordinates, N_i, N_j, N_k are the shape functions, Ω is the element area, $a_{i,j,k}$, $b_{i,j,k}$, $c_{i,j,k}$ are the shape functions coefficients.
The coefficients a, b and c are computed as follows:

$$a_i = x_{1,j}x_{2,k} - x_{1,k}x_{2,j} \quad a_j = x_{1,k}x_{2,i} - x_{1,i}x_{2,k} \quad a_k = x_{1,i}x_{2,j} - x_{1,j}x_{2,i}$$

$$b_i = x_{2,j} - x_{2,k} \qquad b_j = x_{2,k} - x_{2,i} \qquad b_k = x_{2,i} - x_{2,j} \tag{2.60}$$

$$c_i = x_{1,k} - x_{1,j} \qquad c_j = x_{1,i} - x_{1,k} \qquad c_k = x_{1,j} - x_{1,i}$$

The influence coefficient matrices (Huyakorn et al., 1984, Istok, 1989) of the linear triangular element are defined hereinafter:

$$[Y_{x_1x_1}]^e = \frac{1}{4\Omega^2}\begin{bmatrix} b_i^2 & b_ib_j & b_ib_k \\ b_jb_i & b_j^2 & b_jb_k \\ b_kb_i & b_kb_j & b_k^2 \end{bmatrix} \quad [Y_{x_2x_2}]^e = \frac{1}{4\Omega^2}\begin{bmatrix} c_i^2 & c_ic_j & c_ic_k \\ c_jc_i & c_j^2 & c_jc_k \\ c_kc_i & c_kc_j & c_k^2 \end{bmatrix}$$

$$[Y_{x_1x_2}]^e = \frac{1}{4\Omega^2}\begin{bmatrix} b_ic_i & b_ic_j & b_ic_k \\ b_jc_i & b_jc_j & b_jc_k \\ b_kc_i & b_kc_j & b_kc_k \end{bmatrix} \quad [Y_{x_2x_1}]^e = \frac{1}{4\Omega^2}\begin{bmatrix} c_ib_i & c_ib_j & c_ib_k \\ c_jb_i & c_jb_j & c_jb_k \\ c_kb_i & c_kb_j & c_kb_k \end{bmatrix} \tag{2.61}$$

$$[Y_{x_1}]^e = \frac{1}{6}\begin{bmatrix} b_i & b_j & b_k \\ b_i & b_j & b_k \\ b_i & b_j & b_k \end{bmatrix} \quad [Y_{x_2}]^e = \frac{1}{6}\begin{bmatrix} c_i & c_j & c_k \\ c_i & c_j & c_k \\ c_i & c_j & c_k \end{bmatrix} \tag{2.62}$$

$$[M_{CF}]^e = \frac{1}{4}\begin{bmatrix} 2 & 1 & 1 \\ 1 & 2 & 1 \\ 1 & 1 & 2 \end{bmatrix} \quad [M_{LF}]^e = \begin{bmatrix} 1 & 0 & 0 \\ 0 & 1 & 0 \\ 0 & 0 & 1 \end{bmatrix} \tag{2.63}$$

$$\{F_{x_2}\}^e = \frac{1}{2\Omega}\begin{Bmatrix} c_i \\ c_j \\ c_k \end{Bmatrix} \tag{2.64}$$

where the subscripts CF and LF mean consistent mass formulation and lumped mass formulation, respectively.

In the following subsections, the element matrices of each global system of equations presented in secs. 2.1-2.4 are introduced. It is worth noticing that for [A] and [B] the consistent mass formulation is employed, while for [C] and [E] the lumped mass formulation is adopted. In general, for fully implicit time integration methods, the CF showed higher accuracy (Gresho et al., 1978; Huyakorn and Pinder, 1983; Sudicky, 1989; Gresho and Sani, 1998; Zienkiewicz and Taylor, 2000), exception made for variably water saturated systems or for multiphase flow problems, where the LF was superior to the CF (Milly, 1985; Kaluarachci and Parker, 1989; Celia et al., 1990).

2.5.2 GDAn-WS – Element Matrices

The element matrices of the global systems of equations shown in sec. 2.1.2 are reported hereinafter:

$$[K_w]^e = \Omega\left(K^e_{w,11}\left[Y_{x_1x_1}\right]^e + K^e_{w,22}\left[Y_{x_2x_2}\right]^e\right) \tag{2.65}$$

$$[B_w]^e = \frac{1}{3}\Omega\, S^e_{s,w}[M_{CF}]^e \tag{2.66}$$

$$\{F_{g,w}\}^e = -\Omega\left(K^e_{w,22}\{F_{x_2}\}^e\right) \tag{2.67}$$

2.5.3 GDAn-VWS – Element Matrices

The element matrices of the global systems of equations shown in sec. 2.2.2 are reported hereinafter:

$$[K_w(S_w)]^e = \Omega\, k^e_{rw}\left(K^e_{w,11}\left[Y_{x_1x_1}\right]^e + K^e_{w,22}\left[Y_{x_2x_2}\right]^e\right) \tag{2.68}$$

$$[B_w(S_w)]^e = \frac{1}{3}\Omega\, S^e_w S^e_{s,w}[M_{CF}]^e \tag{2.69}$$

$$[C_w(S_w)]^e = \frac{1}{3}\Omega\, \phi^e \left(\frac{\partial S_w}{\partial h_w}\right)^e [M_{LF}]^e \tag{2.70}$$

$$[\mathrm{E}]^{\mathrm{e}} = \frac{1}{3}\Omega\,\phi^{\mathrm{e}}[\mathrm{M_{LF}}]^{\mathrm{e}} \tag{2.71}$$

$$\left\{\mathrm{F_{g,w}(S_w)}\right\}^{\mathrm{e}} = -\Omega\left(\mathrm{K^{e}_{w,22}k^{e}_{rw}}\left\{\mathrm{F_{x_2}}\right\}^{\mathrm{e}}\right) \tag{2.72}$$

2.5.4 GDAn-ST – Element Matrices

The element matrices of the global systems of equations shown in sec. 2.3.2 are reported hereinafter:

$$[\mathrm{D}]^{\mathrm{e}} = \Omega\,\mathrm{S^{e}_w}\phi^{\mathrm{e}}\left(\mathrm{D^{e}_{11}}\left[\mathrm{Y_{x_1x_1}}\right]^{\mathrm{e}} + \mathrm{D^{e}_{22}}\left[\mathrm{Y_{x_2x_2}}\right]^{\mathrm{e}} + \mathrm{D^{e}_{12}}\left[\mathrm{Y_{x_1x_2}}\right]^{\mathrm{e}} + \mathrm{D^{e}_{21}}\left[\mathrm{Y_{x_2x_1}}\right]^{\mathrm{e}}\right) +$$

$$+ \mathrm{v^{e}_{w,1}}\left[\mathrm{Y_{x_1}}\right]^{\mathrm{e}} + \mathrm{v^{e}_{w,2}}\left[\mathrm{Y_{x_2}}\right]^{\mathrm{e}} + \frac{1}{3}\Omega\left(\lambda_{\mathrm{w}}\mathrm{S^{e}_w}\phi^{\mathrm{e}} + \lambda_{\mathrm{a}}\mathrm{S^{e}_a}\phi^{\mathrm{e}}\mathrm{k_H} + \lambda_{\mathrm{s}}\rho^{\mathrm{e}}_{\mathrm{b}}\left(\frac{\mathrm{ds}}{\mathrm{dc}}\right)^{\mathrm{e}}\right)[\mathrm{M_{CF}}]^{\mathrm{e}} +$$

$$+ \frac{1}{3}\Omega\,\mathrm{S^{e}_w}\phi^{\mathrm{e}}\mathrm{k_{la}}[\mathrm{M_{CF}}]^{\mathrm{e}} \tag{2.73}$$

$$[\mathrm{A}]^{\mathrm{e}} = \frac{1}{3}\Omega\left(\mathrm{S^{e}_w}\phi^{\mathrm{e}} + \mathrm{S^{e}_a}\phi^{\mathrm{e}}\mathrm{k_H} + \rho^{\mathrm{e}}_{\mathrm{b}}\left(\frac{\mathrm{ds}}{\mathrm{dc}}\right)^{\mathrm{e}}\right)[\mathrm{M_{CF}}]^{\mathrm{e}} \tag{2.74}$$

$$\{\mathrm{M}\}^{\mathrm{e}} = \frac{1}{3}\Omega\,\mathrm{S^{e}_w}\phi^{\mathrm{e}}\mathrm{k_{la}}\mathrm{c_s}\{\mathrm{I}\} \tag{2.75}$$

where $\mathrm{D_{ij}} = \mathrm{D_{e,ij}} + \mathrm{D_{a,ij}}$, and $\{\mathrm{I}\}$ is the identity vector.

2.5.5 GDAn-NAPL – Element Matrices

Before introducing the definition of the element matrices of the global systems of equations shown in sec. 2.4.2, the overall global matrices are reported first:

$$[\mathrm{K^{*}(S)}] = \begin{bmatrix}[\mathrm{K_w(S_w)}] & 0\\ 0 & [\mathrm{K_n(S_n)}]\end{bmatrix} \tag{2.76}$$

$$[\mathrm{B^{*}(S)}] = \begin{bmatrix}[\mathrm{B_w(S_w)}] & 0\\ 0 & [\mathrm{B_n(S_n)}]\end{bmatrix} \tag{2.77}$$

$$[\mathrm{C^{*}(S)}] = \begin{bmatrix}[\mathrm{C_w(S_w)}] & [\mathrm{C_n(S_w)}]\\ [\mathrm{C_w(S_n)}] & [\mathrm{C_n(S_n)}]\end{bmatrix} \tag{2.78}$$

$$\left\{\mathrm{F^{*}_g(S)}\right\} = \begin{Bmatrix}\left\{\mathrm{F_{g,w}(S_w)}\right\}\\ \\ \left\{\mathrm{F_{g,n}(S_n)}\right\}\end{Bmatrix} \tag{2.79}$$

The respective $[K_w(S_w)]$, $[B_w(S_w)]$, $[C_w(S_w)]$, $[E]$, and $\{F_{g,w}(S_w)\}$ element matrices are computed according to Eqs. 2.68-2.72, whereas the remaining matrices are computed as follows:

$$[K_n(S_n)]^e = \Omega \frac{k_{rn}^e}{\eta_{rn}} \left(K_{w,11}^e \left[Y_{x_1 x_1} \right]^e + K_{w,22}^e \left[Y_{x_2 x_2} \right]^e \right) \tag{2.80}$$

$$[B_n(S_n)]^e = \frac{1}{3} \Omega \, S_n^e S_{s,n}^e [M_{CF}]^e \tag{2.81}$$

$$[C_n(S_w)]^e = \frac{1}{3} \Omega \, \phi^e \left(\frac{\partial S_w}{\partial h_n} \right)^e [M_{LF}]^e \tag{2.82}$$

$$[C_w(S_n)]^e = \frac{1}{3} \Omega \, \phi^e \left(\frac{\partial S_n}{\partial h_w} \right)^e [M_{LF}]^e \tag{2.83}$$

$$[C_n(S_n)]^e = \frac{1}{3} \Omega \, \phi^e \left(\frac{\partial S_n}{\partial h_n} \right)^e [M_{LF}]^e \tag{2.84}$$

$$\{F_{g,n}(S_n)\}^e = -\Omega \frac{\rho_{rn}}{\eta_{rn}} \left(K_{w,22}^e k_{rn}^e \{F_{x_2}\}^e \right) \tag{2.85}$$

It must be noticed that when no NAPL occurs within an element of the computational domain, hence only an air-water system is present, capacity and conductivity terms related to the NAPL become zero, and the NAPL flow equation solution reduces to the identity 0 = 0. To overcome this problem, minimum cutoff values of capacities and NAPL relative permeability are assigned according to Kaluarachchi and Parker (1989).

2.6 Procedures for Solving Linear and Nonlinear Systems

2.6.1 Linear Systems

The systems of equations described in secs. 2.1 and 2.3 are linear systems of the form:

$$[G]\{X\} = \{L\} \tag{2.86}$$

where $[G]$ is the stiffness matrix, $\{X\}$ is the vector of unknown variables, and $\{L\}$ is the vector of known values.

In the case of the steady- and unsteady-state groundwater flow equations through water saturated porous media, sec. 2.1, the systems of the type showed in Eq. 2.86 are solved by means of the preconditioned conjugate gradient (PCG) method (Shewchuck 1994), where the incomplete Cholesky factorization (Kershaw 1978) is employed as preconditioning

technique. It is possible to adopt such a method thanks to the properties of symmetry and positive-definiteness satisfied by the stiffness matrix.

In the case of the solute transport equation, sec. 2.3, the resulting system of equations is linear but it does not satisfy the property of symmetry, hence, the preconditioned biconjugate gradient (PBCG) method (Press and Teukolsky, 1992) is adopted to achieve the solution, and the Jacobi preconditioner (Shewchuck, 1994) is used for the system preconditioning.

Due to the sparse nature of the matrices, all global systems are written in compressed row storage (CRS) form in order to increase the speed of calculations and, thus, the efficiency of the code.

2.6.2 Nonlinear Systems

The systems of equations described in secs. 2.2 and 2.4 are nonlinear systems of the form:

$$[G(X)]\{X\} = \{L(X)\} \tag{2.87}$$

where [G(X)] is the stiffness matrix, {X} is the vector of unknown variables, and {L(X)} is the vector of known values.

The nonlinear systems of the type showed in Eq. 2.87 are solved by means of the Picard iteration scheme based on an incremental solution procedure, also called modified Newton-Raphson method, which is more efficient for those systems where the coefficients in the stiffness matrix are particularly sensitive to small variations in X (Istok, 1989). The Picard method and its variations proved to be very effective and robust for solving nonlinear groundwater flow problems in the same way of Newton's type methods, which suffer from similar problems, like slow convergence or divergence from the true solution (Mehl, 2006). Between the advantages of the Picard scheme, its simplicity and lower computational effort per iteration (Kaluarachchi and Parker, 1989) are usually the most attracting.

The Picard method incorporated within the code is also enforced with an adaptive damping technique, in order to increase its efficiency and improve the converge behaviour of the scheme (Istok, 1989; Mehl, 2006).

The nonlinear iterative process continues until a fixed, and sufficiently small, user defined tolerance is satisfied by the solution. In particular, in the presented code, two convergence

criteria can be chosen, namely the *standard* convergence criterion (Huyakorn and Wadsworth, 1985; Celia et al., 1990) and the *empirical* convergence criterion (Kaluarachchi and Parker, 1989; Kool and van Genuchten, 1991). In the standard criterion, the solution is achieved when the difference, in absolute value, between the pressure heads of two successive iteration levels becomes less than a prescribed absolute tolerance, ε:

$$\left|h^{\eta+1,\delta+1} - h^{\eta+1,\delta}\right| \leq \varepsilon \tag{2.88}$$

where η denotes the time level and δ the iteration level.

The empirical convergence criterion, instead, introduces a relative tolerance, ε_r, with the aim of reducing the computational efforts associated with the small absolute tolerance:

$$\left|h^{\eta+1,\delta+1} - h^{\eta+1,\delta}\right| \leq \varepsilon_r \left|h^{\eta+1,\delta+1}\right| + \varepsilon \tag{2.89}$$

At each iteration level, the resulting linear systems, symmetric and positive-definite, are then solved by means of the PCG method (sec. 2.6.1). Due to the sparse nature of the matrices, all global systems are written in compressed row storage (CRS) form in order to increase the speed of calculations and, thus, the efficiency of the code.

2.7 GDAn Testing: Benchmark Problems

2.7.1 GDAn-WS: Two Pumping Wells in a Confined Aquifer

In this section, the ability of the WS module to cope with a steady-state groundwater flow field is shown. In particular, the numerical result is compared with the analytical solution given for a steady-state flow towards two fully penetrating pumping wells in a homogeneous, isotropic, confined aquifer of uniform thickness (Bear, 1972).

The horizontal spatial domain, of rectangular shape (750 m along the x-axis, 900 m along the y-axis), is discretized in 2596 nodes and 5104 unstructured triangular cells of variable size, suitably refined in proximity of the two wells. The coordinates of the two wells locations are (375 m; 375 m) and (375 m; 525 m), respectively. A Dirichlet boundary condition is chosen along all the surfaces of the outer boundary.

The simulation parameters used for this problem are listed in Tab. 2.1.

Tab. 2.1. Two Pumping Wells Problem - Parameters.

Parameter	Value
Pumping Well Rate (m^3/d)	370
Radius of Influence (m)	375
Aquifer Thickness (m)	25
Aquifer Transmissivity (m^2/s)	0.001
Specific Storage Coefficient (-)	0.001
Dirichlet Boundary Hydraulic Head (m)	35

The comparison of the results obtained with the analytical solution and with GDAn, Fig. 2.2, shows a good agreement. The piezometric profile is well captured and, with respect to the analytical solution, only a small underestimation can be noticed. The reason of this slight deviation is likely due to the mesh discretization, which is probably not fine enough. Nevertheless, the maximum error computed in the hydraulic head is of 0.74%, thus ensuring the correctness of the numerical model.

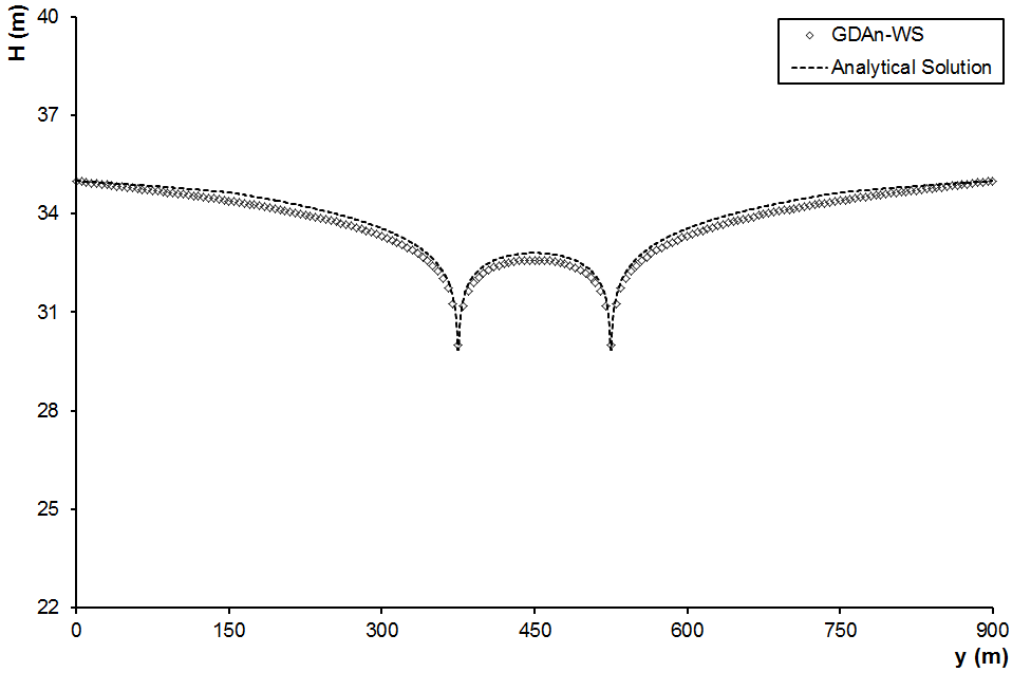

Fig. 2.2. Analytically versus numerically computed piezometric profile along the wells y-axis.

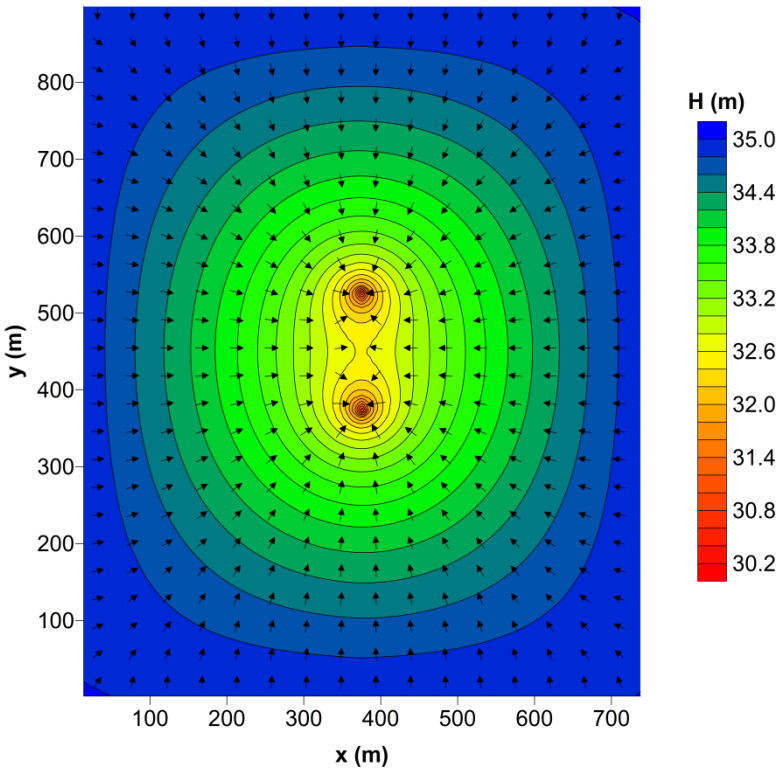

Fig. 2.3. Numerically computed piezometric surface and groundwater velocity vectors (arrows).

In Fig. 2.3, the numerically computed piezometric surface and the groundwater velocity field are shown. Here, the orthogonality between equipotential lines and flowlines is clear, thus resulting in a perfect agreement with the physics involved in the phenomenon simulated.

2.7.2 GDAn-WS: Transient Flow to a Well in a Confined Aquifer

In this section, the WS module is tested with respect to the Theis' analytical solution describing the transient groundwater flow towards a fully penetrating well into a homogeneous, isotropic, confined aquifer of uniform thickness (Theis, 1935).

The fully penetrating well is located in the center of a horizontal square domain and, due to the symmetric configuration of the problem, only one square portion of 300 m by 300 m of the domain, with origin in the well location, is taken into account for the numerical simulation. The spatial domain is discretized in 1068 nodes and 2004 unstructured triangular cells of variable size, suitably refined in proximity of the well, located in the

origin of the subdomain. A Dirichlet boundary condition is chosen along the surfaces of the outer boundary not belonging to the symmetry axis passing through the well location. The simulation parameters used for this problem are listed below in Tab. 2.2.

Tab. 2.2. Theis' Problem - Parameters.

Parameter	Value
Pumping Well Rate (m^3/d)	740
Radius of Influence (m)	300
Aquifer Thickness (m)	25
Aquifer Transmissivity (m^2/s)	0.001
Specific Storage Coefficient (-)	0.001
Dirichlet Boundary Hydraulic Head (m)	35
Initial Hydraulic Head (m)	35
Time Step Size (s)	1
Maximum Simulation Time (h)	12

Along the radial distance from the well location to the outer boundary of the domain, after 3 hours of pumping, the analytically and the numerically computed drawdowns show an excellent agreement (Fig. 2.4). Good results are clearly evident from Fig. 2.5, where the piezometric surface drawdown is plotted up to a time of 12 hours for different radial distances from the well.

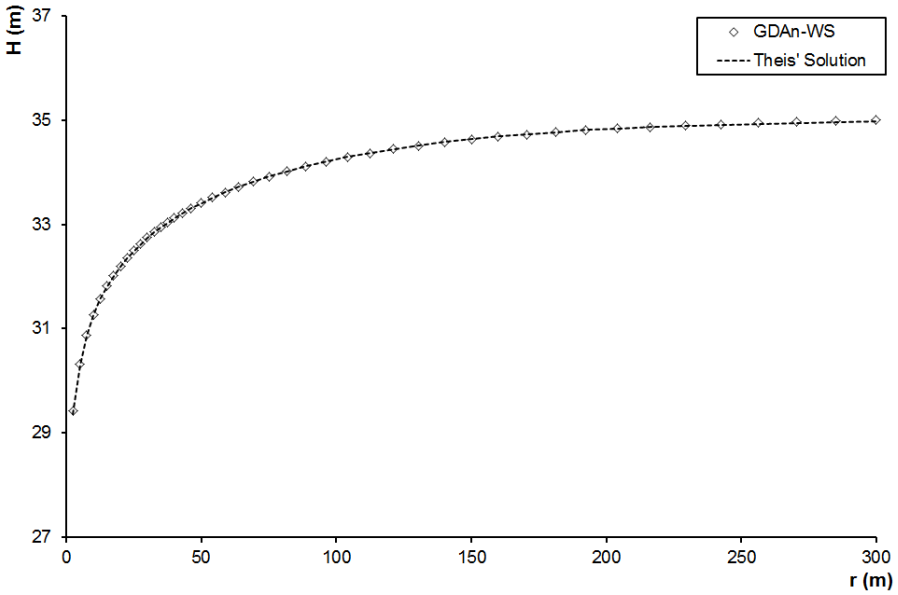

Fig. 2.4. Analytically versus numerically computed drawdown of the piezometric surface at time t = 3 h along the radial distance r from the well location.

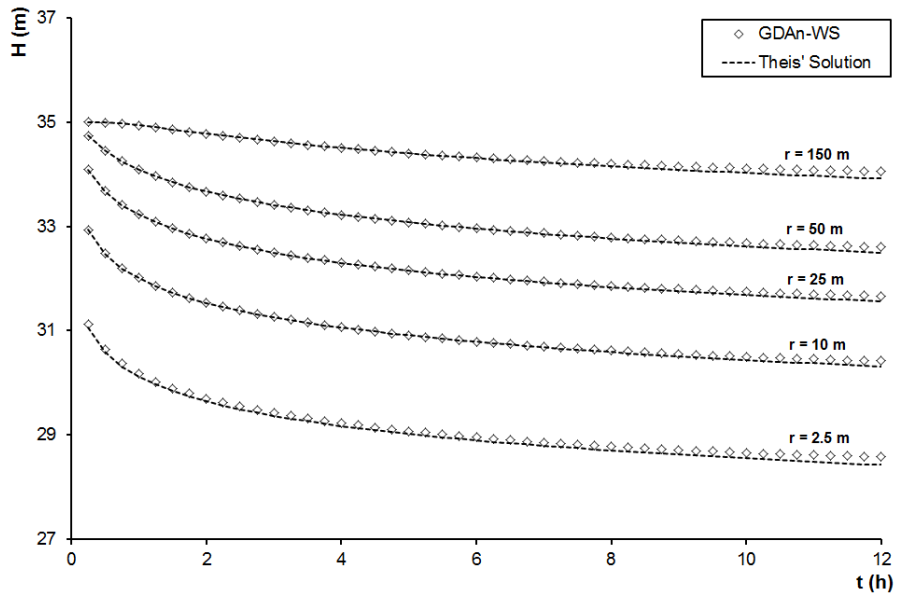

Fig. 2.5. Analytically versus numerically computed drawdown of the piezometric surface over time t at fixed radial distances r from the well location.

Nevertheless, after a certain amount of time, the numerical solution becomes affected by the constant head prescribed at the outer boundary of the subdomain, thus resulting in a slightly reduced agreement with the analytical solution. The reason of this behaviour is to be found in Theis' assumption of a constant head at infinite distance from the well. Hence, if longer simulation times are to be encountered, the domain must be enlarged to correctly evaluate the drawdowns.

2.7.3 GDAn-VWS: Transient Infiltration into a Relatively Dry Layered Soil

The ability of GDAn-VWS to cope with the transient infiltration, induced by a ponding water surface, into a relatively dry layered soil is here proved. The results are then qualitatively compared with those reported in COMSOL Multiphysics (2016), from which the benchmark test is taken.

The spatial domain is discretized in 816 nodes and 1528 unstructured triangular cells, and its geometrical configuration is shown in Fig. 2.6. The boundary conditions associated with the problem consist of a Dirichlet boundary condition of 0.01 m water pressure head in the ponding ring (Fig. 2.6), a no flow condition outside the ring on the top and along the vertical lateral surfaces, and a small outflow along the bottom surface of 0.00454 m/d. The

numerical solution is achieved with a time step of 4 min and an absolute tolerance of 10^{-4} m.

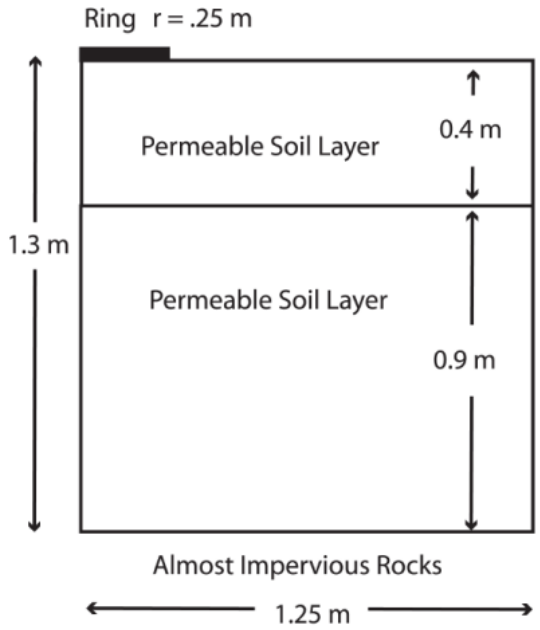

Fig. 2.6. Transient Infiltration Problem - Domain geometry (COMSOL, 2016).

The simulation parameters used for this problem are listed below in Tab. 2.3.

Tab. 2.3. Transient Infiltration Problem - Parameters.

Parameter	Upper Layer	Lower Layer
Saturated Hydraulic Conductivity (m/d)	0.298	0.454
Specific Storage (m^{-1})	0.398	0.338
Porosity (-)	0.399	0.339
Irreducible Water Content (-)	0.001	0.001
van Genuchten-Mualem - α (m^{-1})	1.74	1.39
van Genuchten-Mualem – n (-)	1.38	1.60
Initial Pressure Head (m)	-0.8 – 1.2·(z - 0.9)	0.1 - z

Note: z denotes the elevation computed from the bottom of the domain.

Even though the comparison is only qualitative, the results obtained with the GDAn code (Figs. 2.7 and 2.9) show an overall good agreement with those obtained with COMSOL (Figs. 2.8 and 2.10). In general, the physics involved in the phenomenon simulated is well captured by GDAn, which proved to be capable of coping with the infiltration process into an initially dry soil. No oscillations in the solution profiles are encountered, despite the

sharp layering of the soil, and the progression of the infiltration front over time is well captured.

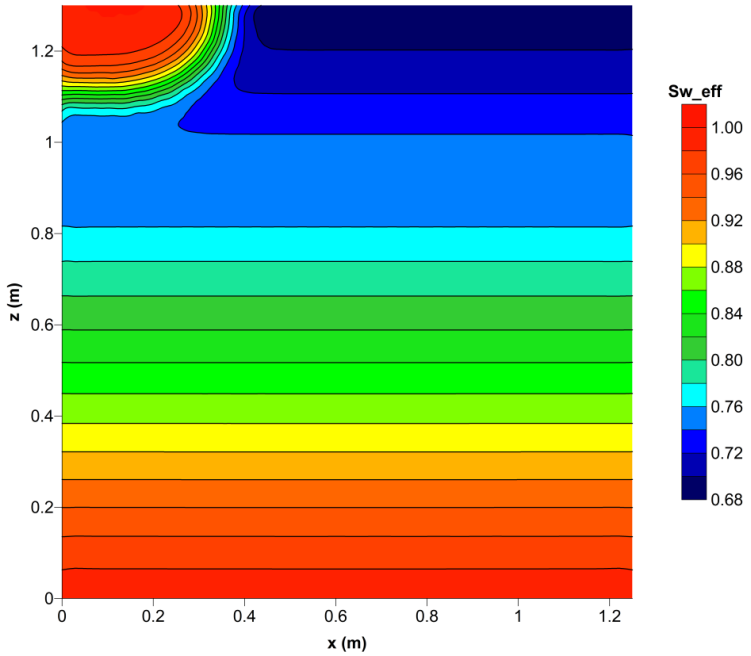

Fig. 2.7. Effective water saturation after 8 hours (GDAn-VWS).

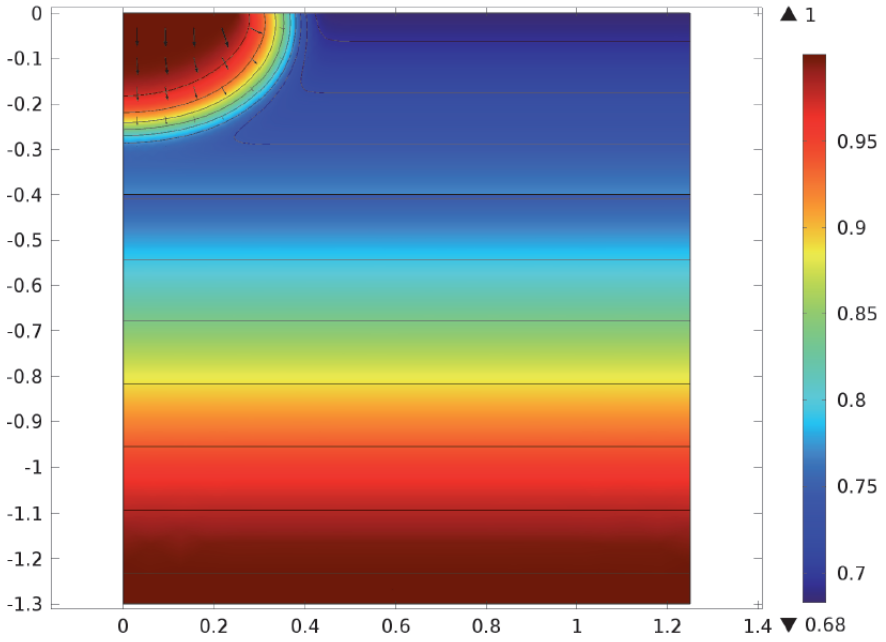

Fig. 2.8. Effective water saturation after 8 hours (extracted from COMSOL Multiphysics, 2016).

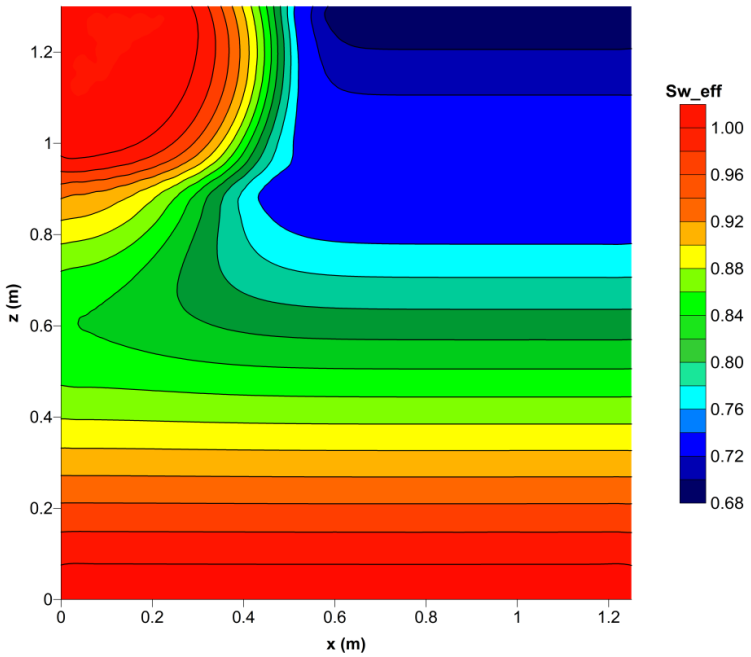

Fig. 2.9. Effective water saturation after 24 hours (GDAn-VWS).

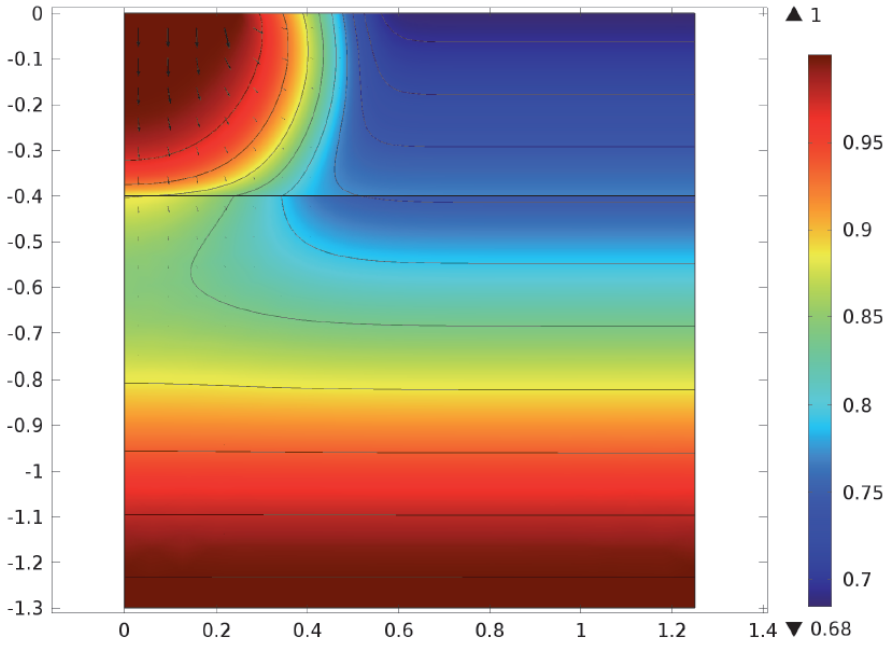

Fig. 2.10. Effective water saturation after 24 hours (extracted from COMSOL Multiphysics, 2016).

2.7.4 GDAn-VWS: Transient Water Table Recharge

The VWS module is tested against the experimental investigations of Vauclin et al. (1979), who studied the water table recharge problem in a variably water saturated sandy soil. Due to the symmetric configuration of the experiment, only half of the experimental domain is taken into account for the numerical simulation (Fig. 2.11).

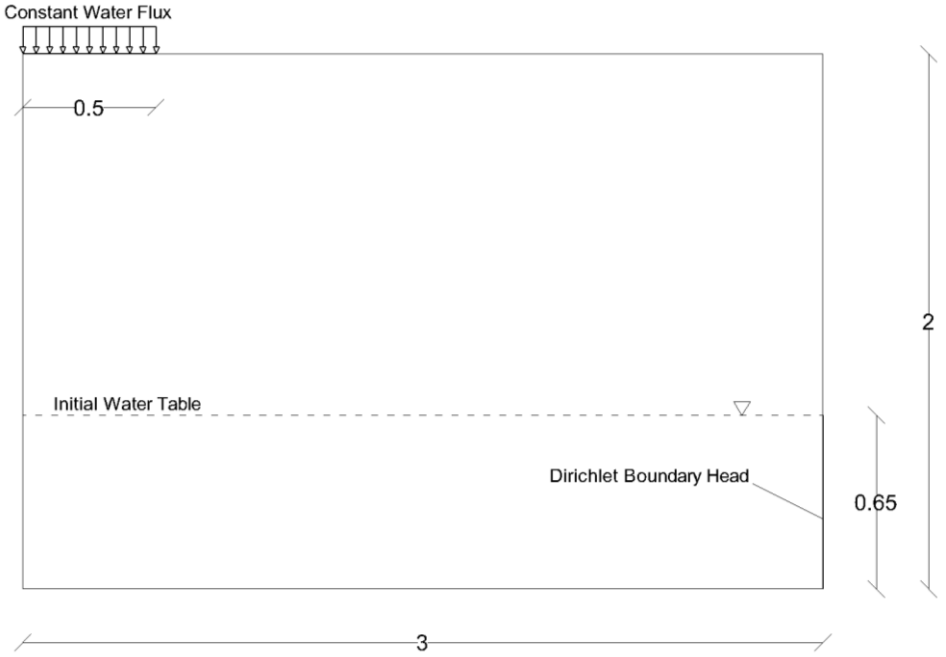

Fig. 2.11. Transient Water Table Recharge Problem - Geometrical configuration and boundary conditions (dimensions in m).

The model domain (3 m by 2 m) is discretized in 1139 nodes and 2159 unstructured triangular cells of variable dimension, suitably refined in proximity of the initial water table. Across the whole domain, the hydraulic head is set to a fixed value, and the boundary nodes on the right side are constrained to the prescribed initial water table elevation by means of a Dirichlet boundary condition. On the top of the domain, at the ground level, a constant flux is prescribed along a strip of 0.5 m starting from the left side. All the other surfaces behave as a no-flux boundary. The previous boundary conditions are fixed for the whole duration of the experiment.

The simulation parameters used for this problem are listed in Tab. 2.4.

Tab. 2.4. Transient Water Table Recharge Problem - Parameters.

Parameter	Value
Saturated Hydraulic Conductivity (m/d)	8.4
Specific Storage (m^{-1})	0.0001
Porosity (-)	0.3
Irreducible Water Saturation (-)	0.033
van Genuchten-Mualem - α (m^{-1})	3.3
van Genuchten-Mualem – n (-)	4.1
Initial Hydraulic Head (m)	0.65
Dirichlet Boundary Hydraulic Head (m)	0.65
Infiltration Rate (m/d)	3.55
Time Step Size (min)	1
Maximum Simulation Time (h)	8
Absolute Tolerance (m)	10^{-4}

The results of the simulation are presented hereinafter in Figs. 2.12 and 2.13:

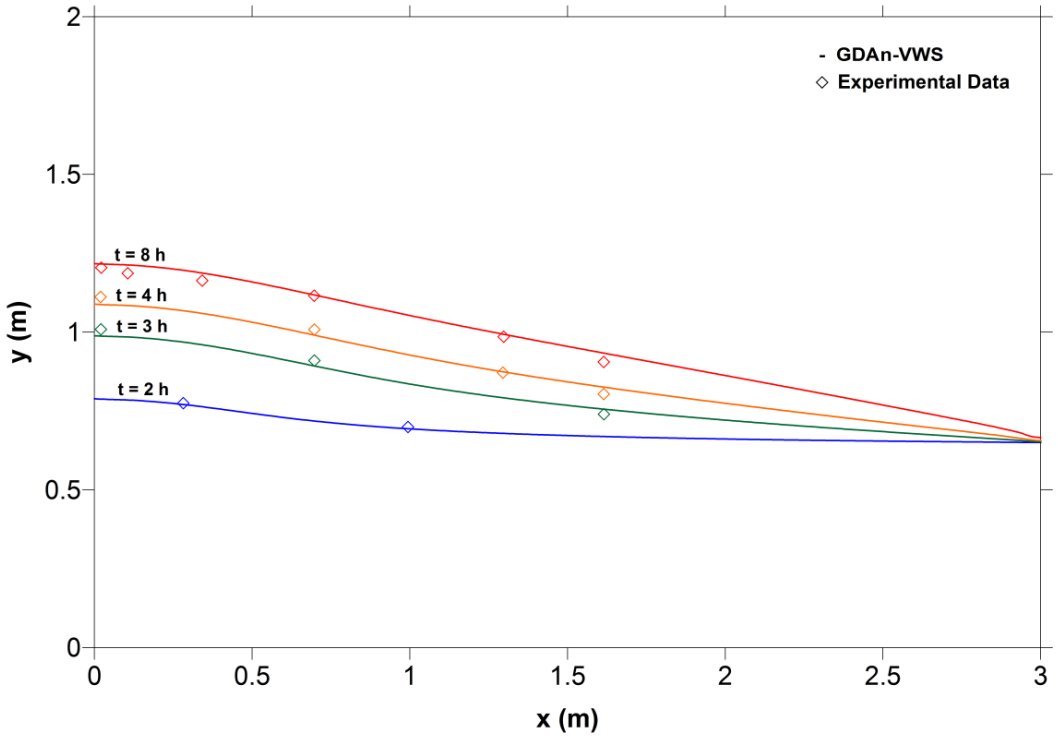

Fig. 2.12. Simulated water table elevations over time versus experimental data.

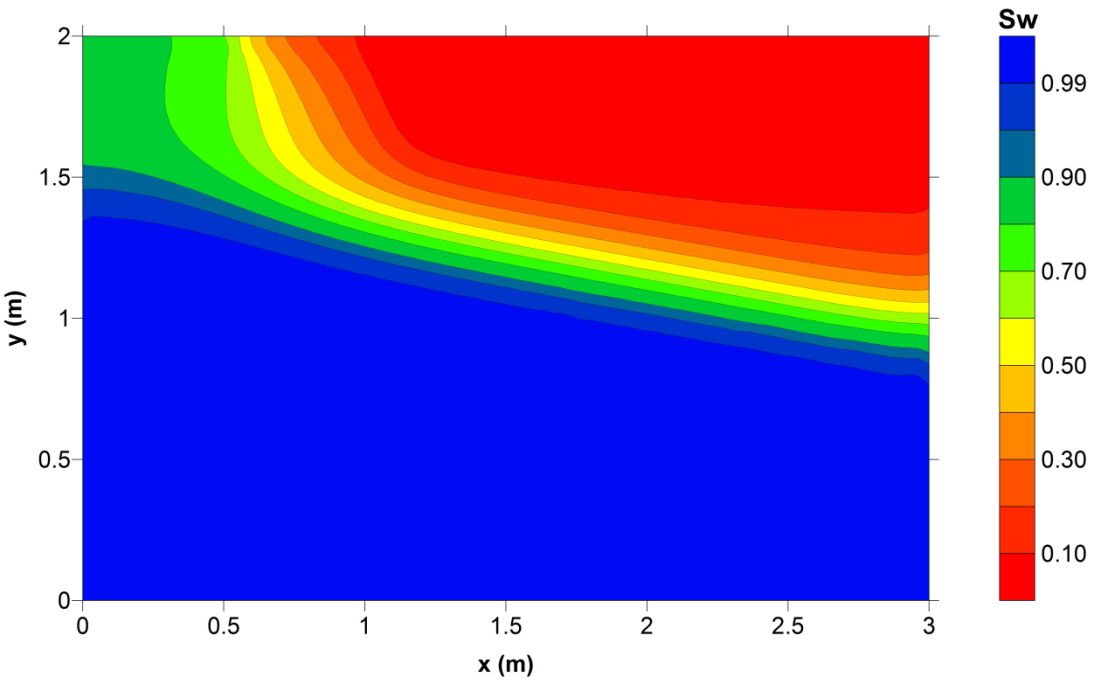

Fig. 2.13. Water saturation at t = 8 h (GDAn-VWS).

The comparison of the simulated water table elevations with the experimental results of Vauclin et al. (1979) clearly shows a good agreement (Fig. 2.12), thus confirming the ability of GDAn to capture the transient water table dynamics and to cope with real infiltration scenarios in variably water saturated soils.

2.7.5 GDAn-ST: Conservative Solute Transport

The ability of the ST module to cope with a conservative solute transport is verified by means of the analytical solution provided by Wexler (1992) for an aquifer of finite width with a finite width solute source.

The horizontal spatial domain is a rectangular of 75 m by 25 m, along the x-axis and the y-axis, respectively, discretized in 2302 nodes and 4402 unstructured triangular cells. The aquifer is initially pristine and the groundwater flow field is uniform and oriented along the x-axis. The solute source is instantaneously applied along a strip of 5 m length, located in the middle of the left side of the domain, while outside the source line, the solute concentration is constrained to 0. On the other sides, a no flux boundary condition is prescribed.

The simulation parameters used for this problem are listed below in Tab. 2.5.

Tab. 2.5. Conservative Solute Transport Problem - Parameters.

Parameter	Value
Aquifer Porosity (-)	0.35
Longitudinal Dispersivity (m)	50
Transverse Dispersivity (m)	5
Groundwater Velocity (m/d)	0.1
Dirichlet Boundary Solute Concentration (mg/l)	1
Time Step Size (d)	0.1
Maximum Simulation Time (d)	10

The comparisons between the numerical and the analytical results, at a time of 5 days and 10 days after the application of the solute source, are presented in Figs. 2.14 and 2.15. The numerical solution shows an overall good agreement with the analytical one, and the solute plume dimensions are well captured over time, thus confirming the ability of the model to cope with this phenomenon.

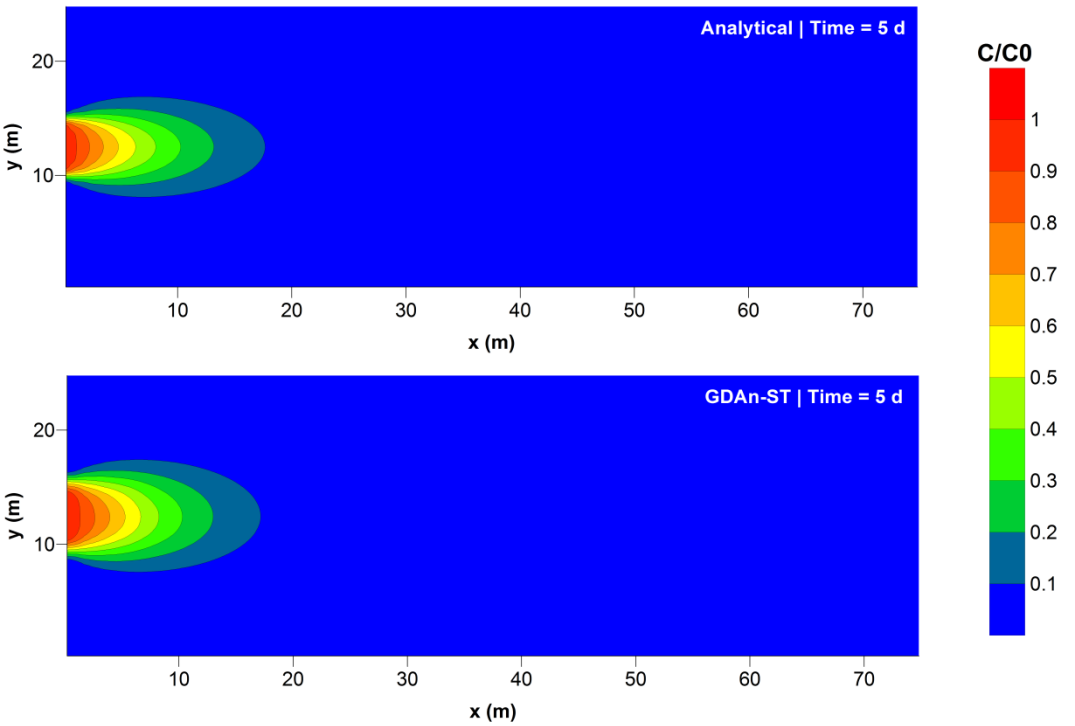

Fig. 2.14. Analytical versus numerical solute plume at t = 5 days.

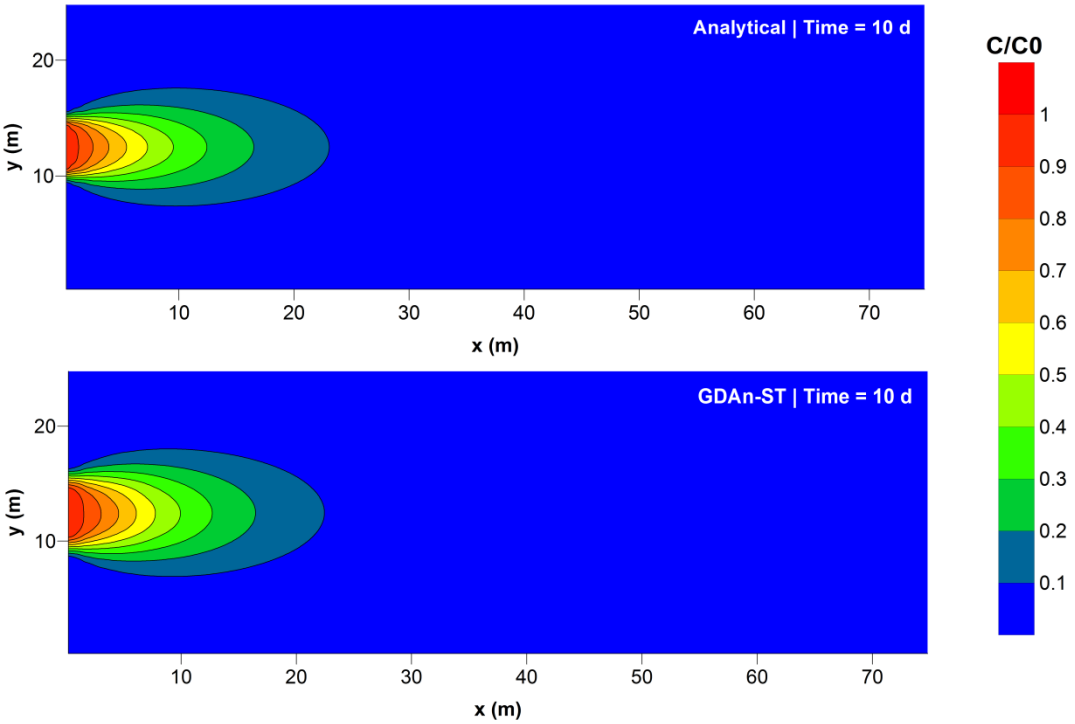

Fig. 2.15. Analytical versus numerical solute plume at t = 10 days.

2.7.6 GDAn-ST: Transport of Solute Subjected to Sorption and Decay

The ST module is tested with respect to the transport of a solute subjected to sorption and decay in a variably water saturated layered soil (COMSOL Multiphysics, 2016). Details regarding the geometrical configuration of the domain, the spatial discretization, and the flow field over time are reported in sec. 2.7.3.

The simulation parameters used for the solute transport problem are listed below in Tab. 2.6.

Tab. 2.6. Transport of Solute Problem - Parameters.

Parameter	Value
Bulk Density (kg/m^3)	1400
Equilibrium Distribution Coefficient (m^3/kg)	0.0001
Molecular Diffusion Coefficient (m^2/d)	0.00374
Longitudinal Dispersivity (m)	0.005
Transverse Dispersivity (m)	0.001
Decay Constant in the Liquid Phase (d^{-1})	0.05
Decay Constant on the Solid Phase (d^{-1})	0.01

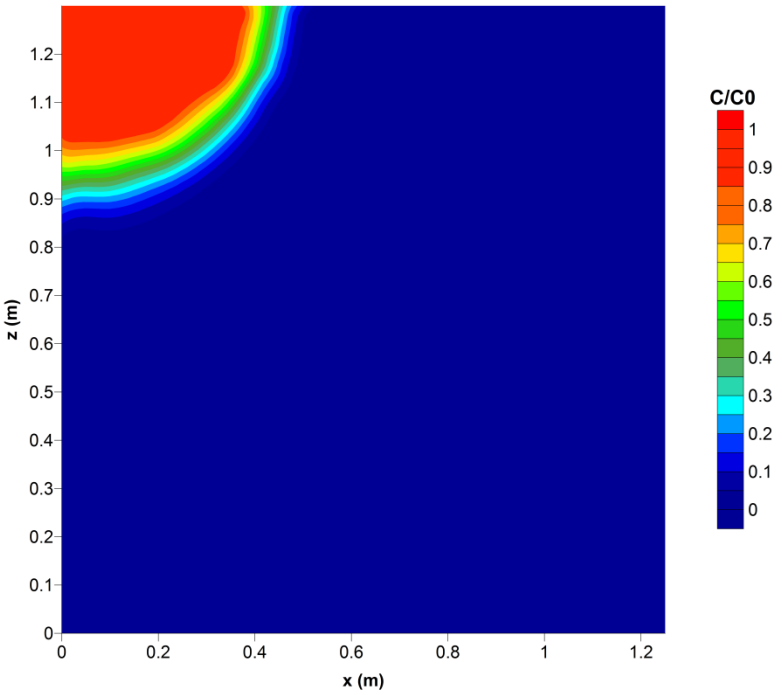

Fig. 2.16. Solute concentration after 1 day (GDAn-ST).

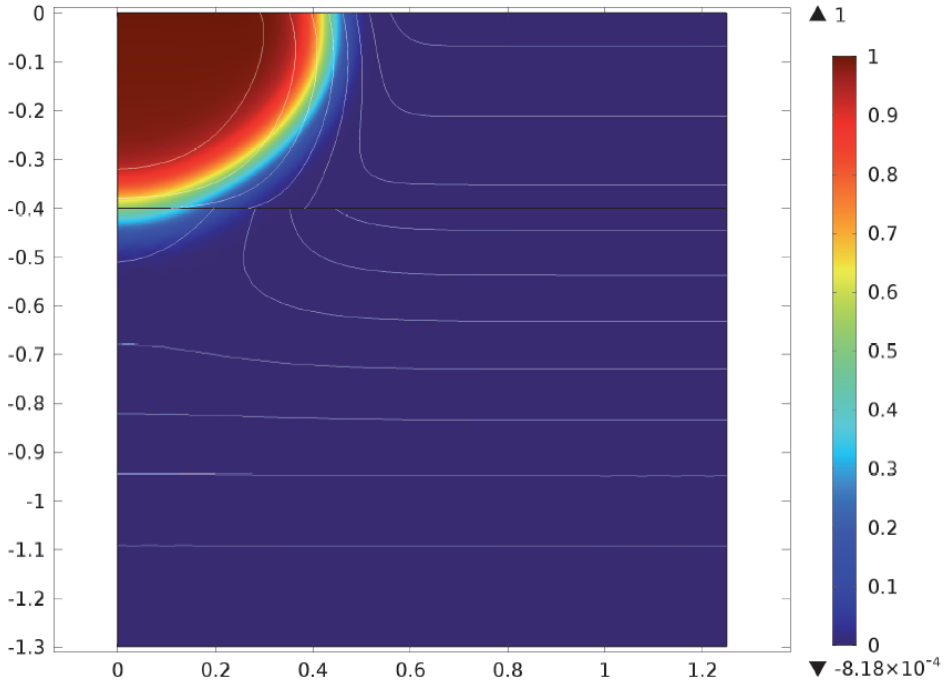

Fig. 2.17. Solute concentration after 1 day (extracted from COMSOL Multiphysics, 2016).

The soil is initially pristine and the solute is instantaneously introduced in the system by prescribing the solute concentration to 1 mg/l in the ponding ring, during the whole simulation time. A transmissive boundary is chosen for the bottom of the domain, where the solute can exit the system by pure advection. For the remaining boundaries a no solute flux condition is chosen. The solution is then advanced over time with a time step of 0.1 days.

Even though the comparison is only qualitative, the results obtained with the GDAn code, Fig. 2.16, show an overall good agreement with those obtained with COMSOL, Fig. 2.17 (extracted from COMSOL Multiphysics, 2016). In general, the physics involved in the phenomenon simulated is well captured by GDAn, which proves to be capable of coping with the transport dynamics of a solute subjected to sorption and decay in a variably water saturated soil. No oscillations in the solution profile are encountered, and the progression of the solute plume over time is well captured.

2.7.7 GDAn-NAPL: DNAPLs and LNAPLs Infiltration and Distribution

In this section, the ability of the GDAn code to cope with the infiltration and distribution phenomenon of two DNAPLs and LNAPLs in variably water saturated porous media is shown. The benchmark problem is taken from Nichols et al. (1997), where the STOMP model (White et al., 1995; White and Oostrom, 2000) is used.

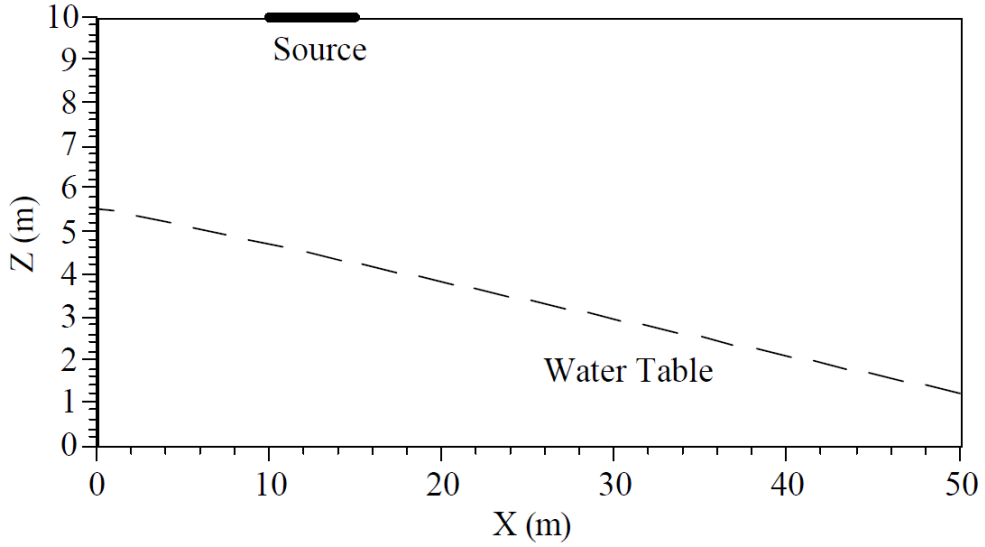

Fig. 2.18. Conceptual configuration of the flow domain (Nichols et al., 1997).

The first step of the test problem consists of the infiltration of 7.5 m^3/m of NAPL from a 5 m wide source, located on the ground surface, under a water equivalent NAPL head of 1 cm. When the source depletes, the NAPL is allowed to migrate and distribute into the subsurface up to a time of 100 days after the source application. Four different NAPLs are considered, namely two DNAPLs and two LNAPLs, respectively.

The domain (Fig. 2.18) is initially pristine and is characterised by a sloping water table with a hydraulic gradient of 2/23 (from left to right). Above the water table the domain is variably water saturated. Except for the source zone, on all other boundaries a no flow boundary condition is ensured for the NAPL, while for the water phase, on both left and right sides of the domain, the water head is constrained to the initial water table configuration.

The simulation parameters used for this problem are listed below in Tab. 2.7.

Tab. 2.7. DNAPLs and LNAPLs Infiltration and Distribution Problem - Parameters.

Parameter	Value
Saturated Hydraulic Conductivity (cm/h)	2.1
Specific Storage (m^{-1})	0.0001
Porosity (-)	0.43
Irreducible Water Saturation (-)	0.02
van Genuchten-Mualem - α (m^{-1})	0.7
van Genuchten-Mualem – n (-)	2.1
Air-NAPL Scaling Parameter	1.8
NAPL-Water Scaling Parameter	2.25
DNAPL Density (kg/m^3) – Case 1 and 2	1200
LNAPL Density (kg/m^3) – Case 3 and 4	800
Dynamical Viscosity (Pa·s) – Case 1 and 3	0.002
Dynamical Viscosity (Pa·s) – Case 2 and 4	0.0005

The vertical spatial domain is a rectangle of 50 m by 10 m, along the x-axis and the z-axis, respectively, discretized in 667 nodes and 1211 unstructured triangular cells. The solution is advanced over time with a time step of 5 min and the convergence of the solution is ensured by a relative tolerance of 0.01 (which is equivalent to an absolute tolerance varying between 10^{-5} m and 10^{-3} m). Hereinafter, to allow a qualitative comparison with STOMP, the results of the four different cases analysed are presented together with the results extracted from Nichols et al. (1997).

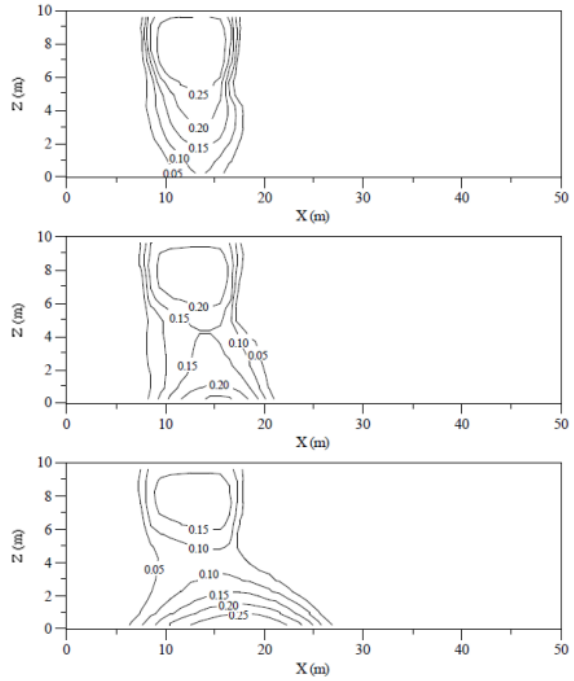

Fig. 2.19. DNAPL saturation after (from top to bottom) 25 days, 50 days and 100 days (STOMP) - Case 1.

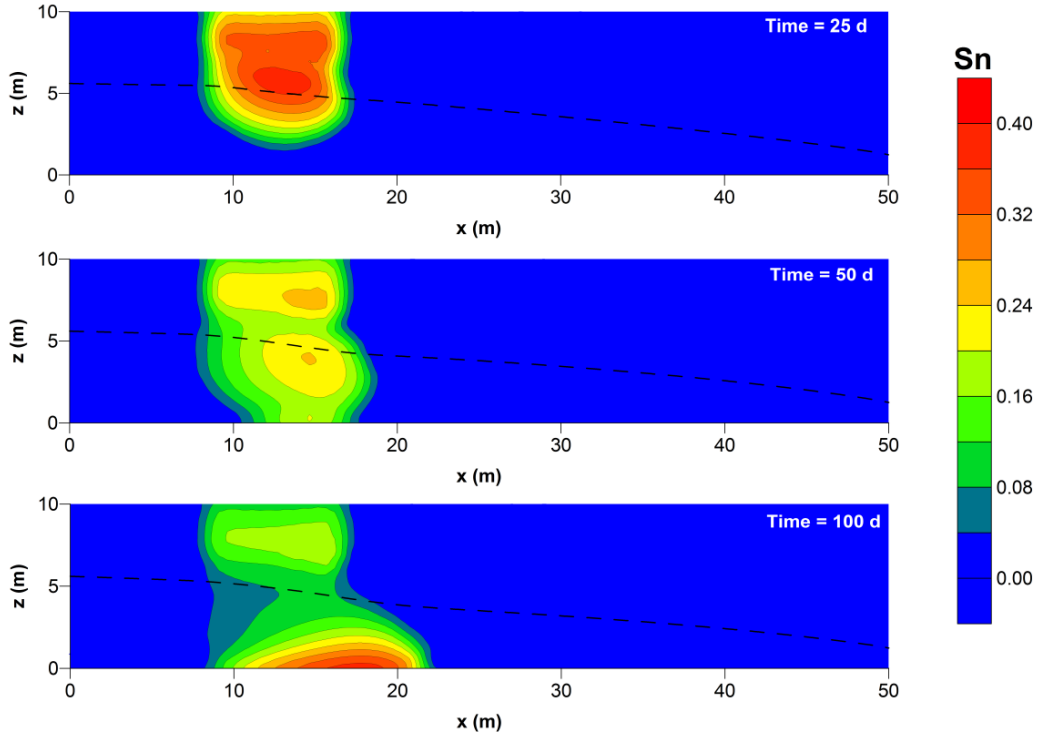

Fig. 2.20. DNAPL saturation and water table (dashed line) after 25 days, 50 days and 100 days (GDAn-NAPL) - Case 1.

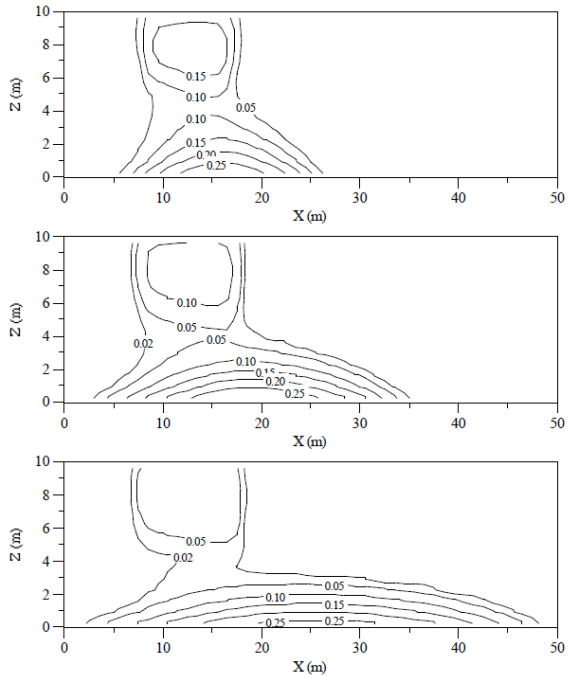

Fig. 2.21. DNAPL saturation after (from top to bottom) 25 days, 50 days and 100 days (STOMP) - Case 2.

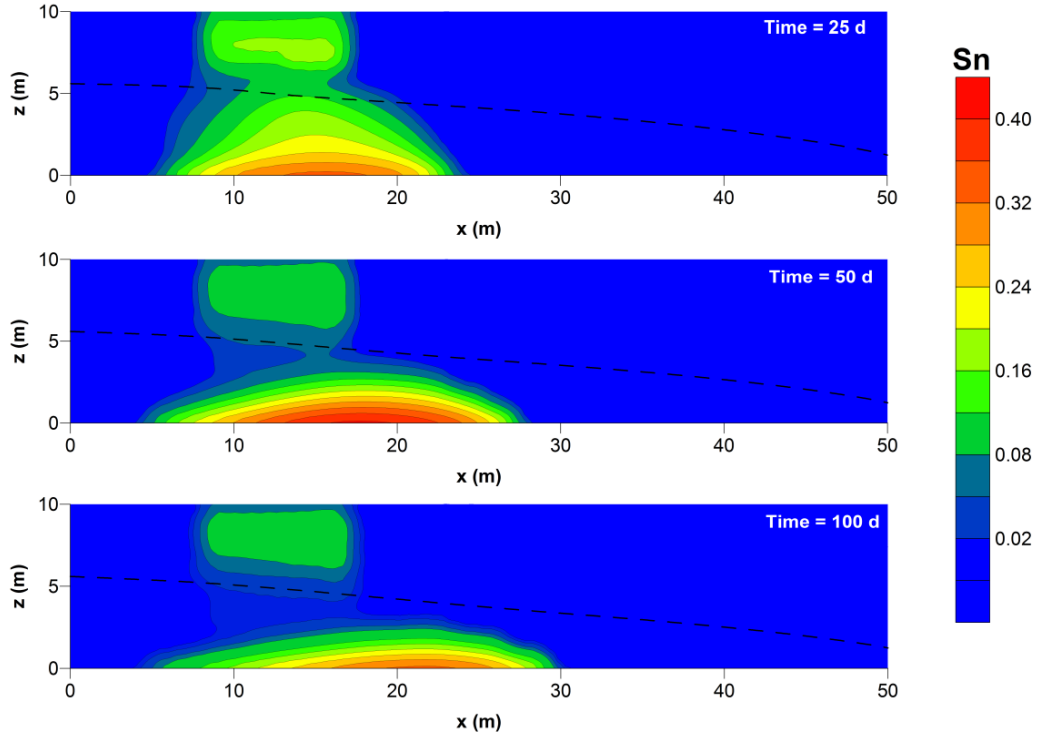

Fig. 2.22. DNAPL saturation and water table (dashed line) after 25 days, 50 days and 100 days (GDAn-NAPL) - Case 2.

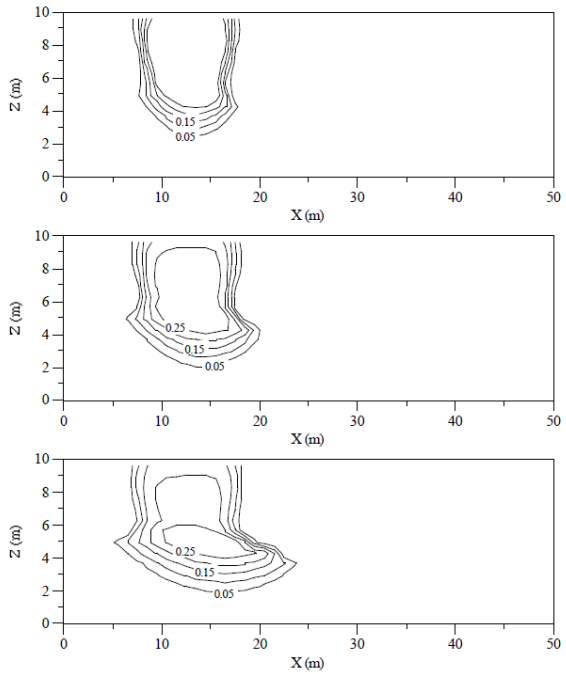

Fig. 2.23. LNAPL saturation after (from top to bottom) 25 days, 50 days and 100 days (STOMP) - Case 3.

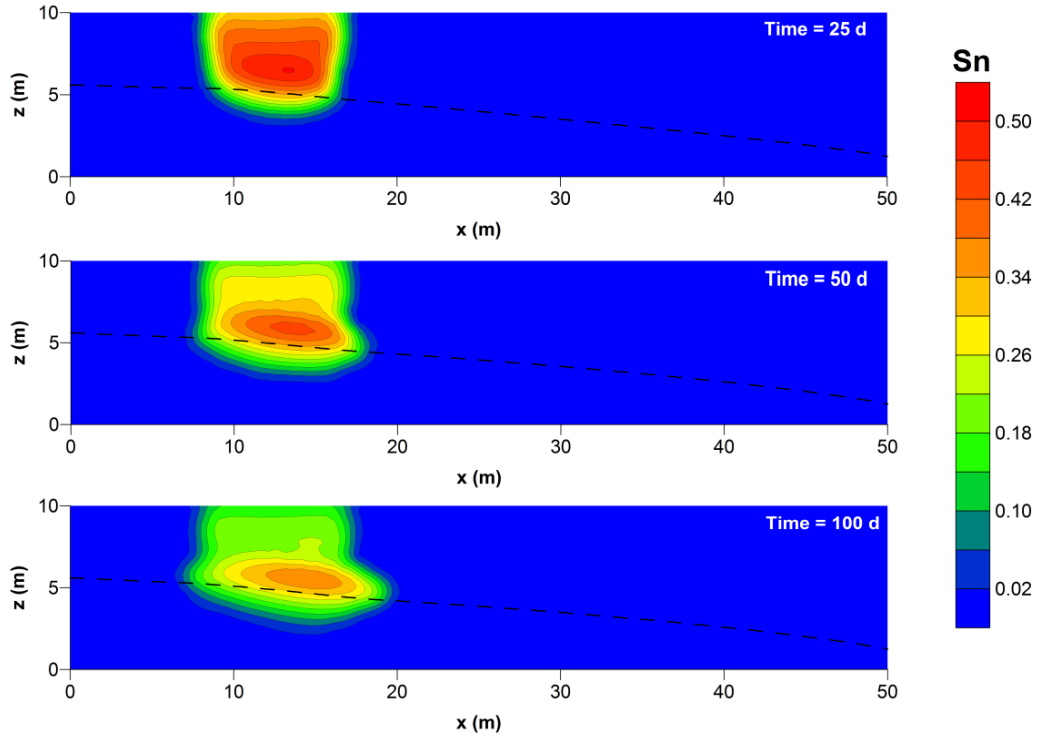

Fig. 2.24. LNAPL saturation and water table (dashed line) after 25 days, 50 days and 100 days (GDAn-NAPL) - Case 3.

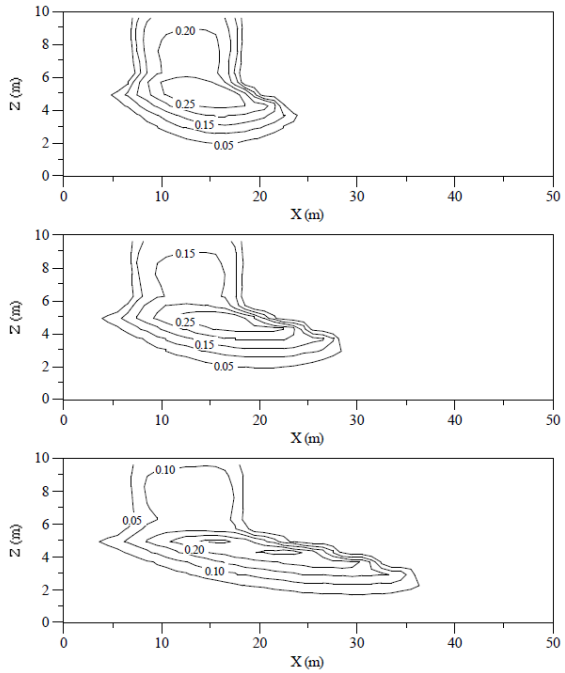

Fig. 2.25. LNAPL saturation after (from top to bottom) 25 days, 50 days and 100 days (STOMP) - Case 4.

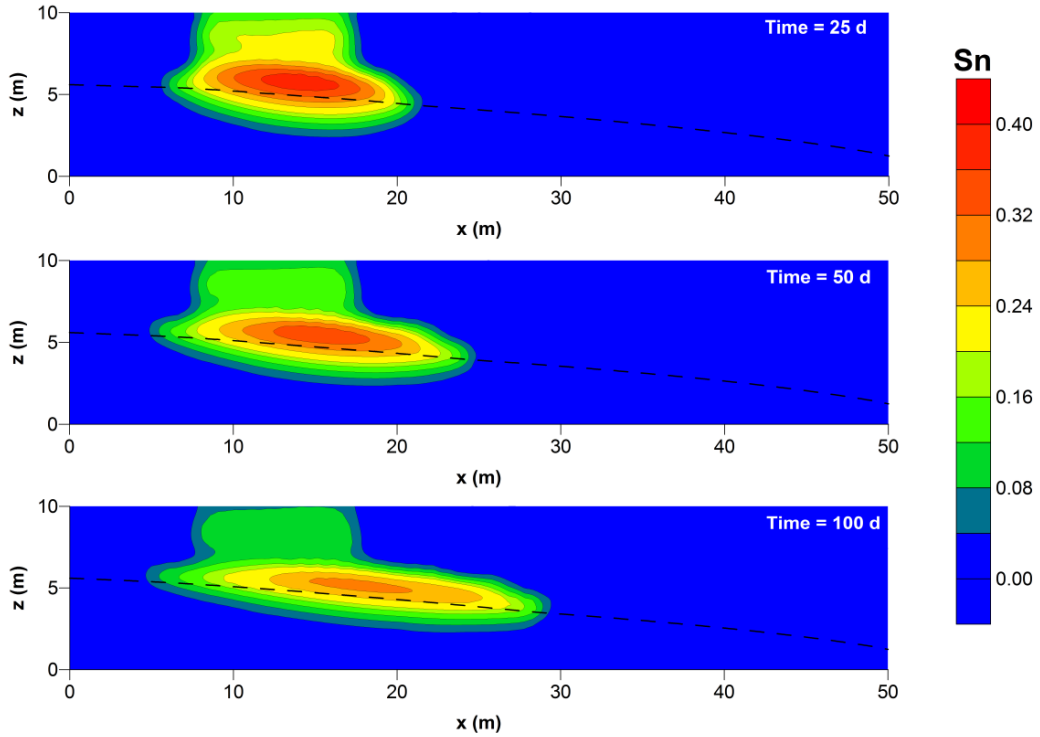

Fig. 2.26. LNAPL saturation and water table (dashed line) after 25 days, 50 days and 100 days (GDAn-NAPL) - Case 4.

The results (Figs. 2.19-2.26) show that the NAPL infiltration fronts obtained with GDAn are slower than those obtained with STOMP. The reason of this discrepancy may have multiple origins. At first, while the time marching procedure of the two models relies on the same backward Euler scheme, the spatial numerical integration is achieved in different ways. In particular, GDAn is based on a finite element discretization while STOMP is based on a finite difference scheme. Furthermore, the computational meshes used are different: GDAn uses an unstructured triangular mesh while STOMP uses a structured quadrilateral grid. In addition, some parameters are not specified in the report made by Nichols et al. (1997), like the specific storage and the minimum values adopted for the NAPL capacity terms and relative permeability in absence of NAPL within a calculation cell. In particular, these parameters (in these GDAn simulations equal to 10^{-4} m^{-1} and 10^{-6}, respectively) can affect considerably the results, and their optimal values are case dependent (Abriola and Rathfelder, 1993).

Nevertheless, the results obtained with GDAn are consistent with the physics of the phenomena involved. As a matter of fact, the results show that both DNAPLs and LNAPLs saturation fronts move predominantly in the vertical direction in the unsaturated zone. The lateral spreading, induced by capillary forces, and the water displacement in proximity of the water table are also captured. Both LNAPLs (Figs 2.24 and 2.26) reach the water table and accumulate on the capillary fringe. The volume of the two spills is large enough to allow them to build enough pressure to locally overcome the buoyancy and capillary forces, thus displacing water and partially penetrating in the saturated zone. As the NAPL source depletes, the downward vertical flow tends to cease and the LNAPLs continue their movement mainly driven by the groundwater flow, while their lenses gradually tend to become thinner. The only difference between the two LNAPLs lies in their viscosity, which considerably affects the extent of the contamination plumes. In the unsaturated zone, the behaviour of the two DNAPLs (Figs 2.20 and 2.22) is practically the same as for the LNAPLs, except for the less horizontal spreading, which is a typical feature encountered in DNAPLs migration in the subsurface. Once the DNAPLs reach the water table, they both build enough pressure to overcome the capillary pressure exerted by the water phase and to penetrate in the saturated zone, thus moving further in the downward

vertical direction. The two DNAPLs only differ from each other for their viscosity and, as for the LNAPLs, this considerably affects the extent of their contamination plumes.

References

Abriola LM, Pinder GF (1985). *A multiphase approach to the modeling of porous media contamination by organic compounds: 1. Equation development*. Water Resources Research, 21(1), 11-18.

Abriola LM, Rathfelder K (1993). *Mass balance errors in modeling two-phase immiscible flows: causes and remedies*. Advances in Water Resources, 16, 223-239.

Aziz K, Settari A (1979). *Petroleum Reservoir Simulation*. Applied Science Publishers, London.

Batu V (2006). *Applied Flow and Solute Transport Modeling in Aquifers: Fundamental Principles and Analytical and Numerical Methods*. CRC Press, Taylor & Francis Group.

Bear J (1972). *Dynamics of fluids in porous media*. Dover Publications, Inc., New York.

Braester C, Dagan G, Neuman SP, Zaslavsky D (1971). *A survey of the equations and solutions of unsaturated flow in porous media*. First Annu. Rep. Project A10-SWC-77, 176 pp, Hydraulic Engineering Laboratory, Technion, Israel.

Burdine N (1953). *Relative permeability calculations from pore size distribution data*. Journal of Petroleum Technology, 5(3), 71-78.

Celia MA, Bouloutas ET, Zarba RL (1990). *A General Mass-Conservative Numerical Solution for the Unsaturated Flow Equation*. Water Resources Research, 26(7), 1483-1496.

COMSOL Multiphysics (2016). *Variably Saturated Flow and Transport: Sorbing Solute*. Application ID: 490. https://www.comsol.it/model/variably-saturated-flow-and-transport-8212-sorbing-solute-490.

Cooley RL (1971). *A finite difference method for unsteady flow in variably saturated porous media: Application to a single pumping well*. Water Resources Research, 7(6), 1607-1625.

Golden Software (2002). *Surfer version 8: User's Guide*.

Gresho PM, Lee RL, Sani RL (1978). *Advection-dominated flows, with emphasis on the consequences of mass lumping*. Finite Elements in Fluids, 3, 335–350.

Gresho PM, Sani RL (1998). *Incompressible flow and the finite element method*. Wiley, Chichester.

Huyakorn, PS, Pinder GF (1983). *Numerical Methods in Subsurface Flow*. Academic, San Diego, Calif.

Huyakorn PS, Thomas SD, Thompson BM (1984). *Techniques for Making Finite Elements Competitve in Modeling flow in Variably Saturated Porous Media*. Water Resources Research, 20(8), 1099-1115.

Huyakorn PS, Wadsworth TD (1985). *FLAMINCO: a three-dimensional finite element code for analyzing water flow and solute transport in saturated-unsaturated porous media*. Inc., Herndon, VA.

Istok JD (1989). *Groundwater modelling by the finite element method*. Water Resources Monograph, 13, American Geophysical Union, 2000 Florida Avenue, NW, Washington, DC 2000.

Jury WA, Spencer WF, Farmer W (1983). *Behavior Assessment Model for Trace Organics in Soil: I. Model Description*. Journal of Environmental Quality, 12(4), 558-564.

Kaluarachchi JJ, Parker JC (1989). *An Efficient Finite Element Method for Modeling Multiphase Flow*. Water Resources Research, 25(1), 43-54.

Kaluarachchi JJ, Parker JC (1992). *Multiphase Flow with a Simplified Model for Oil Entrapment*. Transport in Porous Media, 7(1), 1-14.

Katyal AK, Parker JC (1992). *An adaptive solution domain algorithm for solving multiphase flow equations*. Computers & Geosciences, 18(1), 1-9.

Kershaw DS (1978). *The incomplete Cholesky-conjugate gradient method for the iterative solution of systems of linear equations*. Journal of Computational Physics, 26(1), 43-65.

Kolditz O (2002). *Computational Methods in Environmental Fluid Mechanics*. Springer-Verlag Berlin Heidelberg GmbH.

Kool JB, van Genuchten MT (1991). *HYDRUS: One-dimensional Variably Saturated Flow and Transport Model, Including Hysteresis and Root Water Uptake, Version 3.31*. Riverside, CA: US Salinity Laboratory.

Land CS (1968). *Calculation of imbibition relative permeability for two- and three-phase flow from rock properties*. Society of Petroleum Engineers Journal, 8(02), 149-156.

Langmuir I (1918). *The adsorption of gases on plane surfaces of glass, mica and platinum*. Journal of the American Chemical Society, 40(9), 1361-1403.

Lenhard RJ, Parker JC (1987). *Measurement and prediction of saturation-pressure relationships in three-phase porous media systems*. Journal of Contaminant Hydrology, 1, 407–424.

Lenhard RJ, Parker JC, Kaluarachchi JJ (1989). *A Model for Hysteretic Constitutive Relations Governing Multiphase Flow 3. Refinements and Numerical Simulations*. Water Resources Research, 25(7), 1727-1736.

Lenhard RJ, Oostrom M, Dane JH (2004). *A constitutive model for air–NAPL–water flow in the vadose zone accounting for immobile, non-occluded (residual) NAPL in strongly water-wet porous media*. Journal of Contaminant Hydrology, 71, 261-282.

Mehl S (2006). *Use of Picard and Newton Iteration for Solving Nonlinear Ground Water Flow Equations*. Ground Water, 44(4), 583-594.

Miller CT, Poirier-McNeil MM, Mayer AS (1990). *Dissolution of Trapped Nonaqueous Phase Liquids: Mass Transfer Characteristics*. Water Resources Research, 26(11), 2783-2796.

Millington RJ, Quirk JP (1961). *Permeability of porous solids*. Transactions of the Faraday Society, 57, 1200-1207.

Milly PCD (1985). *A mass-conservative procedure for time-stepping in models of unsaturated flow*. Advances in Water Resources, 8(1), 32-36.

Mualem Y (1976). *A new model for predicting the hydraulic conductivity of unsaturated porous media*. Water Resources Research, 12(3), 513-522.

Niceno B (1997). *EasyMesh version 1.4: A Two-Dimensional Quality Mesh Generator*.

Nichols WE, Aimo NJ, Oostrom M, White MD (1997). *STOMP Subsurface Transport Over Multiple Phases: Application Guide*. Pacific Northwest Laboratory, Richland, WA (United States), No. PNNL-11216.

Parker JC, Lenhard RJ, Kuppusamy T (1987). *A Parametric Model for Constitutive Properties Governing Multiphase Flow in Porous Media*. Water Resources Research, 23(4), 618-624.

Parker JC (1989). *Multiphase flow and transport in porous media*. Reviews of Geophysics, 27(3), 311-328.

Powers SE, Abriola LM, Weber WJ (1992). *An Experimental Investigation of Nonaqueous Phase Liquid Dissolution in Saturated Subsurface Systems: Steady State Mass Transfer Rates*. Water Resources Research, 28(10), 2691-2705.

Press WH, Teukolsky SA (1992). *Biconjugate Gradient Method for Sparse Linear Systems*. Computers in Physics, 6(4), 400-403.

Rathfelder K, Abriola LM (1994). *Mass conservative numerical solutions of the head-based Richards equation*. Water Resources Research, 30(9), 2579-2586.

Richards LA (1931). *Capillary conduction of liquids through porous mediums*. Journal of Applied Physics, 1(5), 318-333.

Segerlind LJ (1984). *Applied finite element methods*. John Wiley & Sons, New York.

Shewchuck JR (1994). *An Introduction to the Conjugate Gradient Method Without the Agonizing Pain*. School of Computer Science, Carnegie Mellon University, Pittsburgh.

Šimůnek J, van Genuchten MT (2007). *Contaminant Transport in the Unsaturated Zone: Theory and Modelling*. The Handbook of Groundwater Engineering, 22, 22-38.

Sudicky EA (1989). *The Laplace Transform Galerkin Technique: A Time-Continuous Finite Element Theory and Application to Mass Transport in Groundwater*. Water Resources Research, 25(8), 1833-1846.

Theis CV (1935). *The relation between the lowering of the piezometric surface and the rate and duration of discharge of a well using ground-water storage*. Eos, Transactions American Geophysical Union, 16(2), 519-524.

van Genuchten MT (1980). *A closed form equation for predicting the hydraulic conductivity of unsaturated soils*. Soil Science Society of American Journal, 44, 892–898.

Vauclin M, Khanji D, Vachaud G (1979). *Experimental and numerical study of a transient, two-dimensional unsaturated-saturated water table recharge problem*. Water Resources Research, 15(5), 1089-1101.

Wexler EJ (1992). *Analytical solutions for one-, two-, and three-dimensional solute transport in ground-water systems with uniform flow*. US Government Printing Office.

White MD, Oostrom M, Lenhard RJ (1995). *Modeling fluid flow and transport in variably saturated porous media with the STOMP simulator. 1. Nonvolatile three-phase model description*. Advances in Water Resources, 18(6), 353-364.

White MD, Oostrom M (2000). *STOMP Subsurface Transport Over Multiple Phases Version 2.0: Theory Guide*. Pacific Northwest National Laboratory, Richland, WA (United States), No. PNNL-12030.

White MD, Oostrom M, Lenhard RJ (2004). *A Practical Model for Mobile, Residual, and Entrapped NAPL in Water-Wet Porous Media*. Ground Water, 42(5), 734-746.

Zienkiewicz O, Taylor R (2000). *The Finite Element Method. Volume 1: The Basis*. 5th edn Butterworth-Heinemann, Oxford.

Notation

Greek Symbols

α	van Genuchten model parameter
β_{an}	air-NAPL system scaling parameter
β_{nw}	NAPL-water system scaling parameter
δ	iteration level
ε	absolute tolerance
ε_r	relative tolerance
η	time level
η_{rn}	dynamic viscosity ratio between NAPL and water
θ_a	air content
θ_w	water content
λ	decay constant
λ_a	decay constant in the air phase
λ_s	decay constant on the solid phase
λ_w	decay constant in the water phase
ρ_{bulk}	bulk density
ρ_n	NAPL density
ρ_{rn}	density ratio between NAPL and water
τ	tortuosity factor
ϕ	porosity
Ω	element area

Latin Symbols

$a_{i,j,k}$, $b_{i,j,k}$, $c_{i,j,k}$	shape functions coefficients
a_{ijmn}	components of the aquifer dispersivity
a_L	longitudinal dispersivity of the aquifer
a_T	transverse dispersivity of the aquifer
c	solute concentration in the water phase
c_{atm}	solute concentration above the stagnant boundary layer
c_0	initial solute concentration in the water phase
$\tilde{c}$	prescribed water pressure head in the water phase
C_n	specific NAPL capacity term
c_s	NAPL aqueous solubility
C_w	specific water capacity term
d	thickness of the stagnant boundary layer
$D_{a,ij}$	diffusion tensor in the air phase
$D_{e,ij}$	effective dispersion tensor in the water phase
$D_{0,a}$	molecular diffusion coefficient in the pure air phase
$D_{0,w}$	molecular diffusion coefficient in the pure water phase
D_w^*	solute apparent molecular diffusion coefficient
h_n	NAPL pressure head
$h_{n,0}$	initial NAPL pressure head
$\tilde{h}_n$	prescribed NAPL pressure head
h_w	water pressure head
$h_{w,0}$	initial water pressure head
$\tilde{h}_w$	prescribed water pressure head
k_r	relative permeability
K_d	equilibrium distribution coefficient
k_H	Henry's constant
k_{la}	lumped mass transfer coefficient
k_{rn}	NAPL relative permeability
k_{rw}	water relative permeability
$K_{w,ij}$	saturated hydraulic conductivity tensor
m	van Genuchten model parameter
n	van Genuchten model parameter
n_i	outward unit vector
N_i, N_j, N_k	shape functions
P_c	capillary pressure
q_n	NAPL volumetric flow rate
q_w	water volumetric flow rate
R	Land's parameter

s	solute concentration on the solid phase
S	saturation
S_a	air saturation
S_n	NAPL saturation
$S_{s,w}$	water specific storage
$S_{s,n}$	NAPL specific storage
S_w	water saturation
$S_{w,ir}$	irreducible water saturation
$\overline{S_n}$	effective NAPL saturation
$\overline{S_{ne}}$	effective entrapped NAPL saturation
$\overline{S_{nf}}$	effective free NAPL saturation
$\overline{S_{nr}}$	effective residual NAPL saturation
$\overline{S_t}$	effective total liquid saturation
$\overline{S_w}$	effective water saturation
$\overline{\overline{S_w}}$	apparent water saturation
$\overline{S_{ne}^{max}}$	maximum effective entrapped NAPL saturation
$\overline{S_{nr}^{max}}$	maximum effective residual NAPL saturation
$\overline{S_w^{min}}$	historical minimum effective water saturation
$\overline{S_t^{max}}$	historical maximum effective total liquid saturation
t	elapsed time
$t_{1/2}$	half-life time
u_j	unit vector in the direction of the x_2 coordinate
$\overline{v_m}$, $\overline{v_n}$	components of the pore water velocity
$v_{n,i}$	apparent NAPL velocity component
$v_{n,n}$	outward NAPL flux
$v_{w,i}$	apparent groundwater velocity component
$v_{w,n}$	outward water flux
x_i, x_j	spatial coordinates
z	elevation

Other Symbols

∂_1, ∂_2	flow boundaries
$[A]$	global sorption matrix
$[B^*]$	overall global specific storage matrix
$[B_n]$	global NAPL specific storage matrix
$[B_w]$	global water specific storage matrix
$[C^*]$	overall global capacitance matrix
$[C_n]$	global NAPL capacitance matrix
$[C_w]$	global water capacitance matrix
$[D]$	global advection-dispersion matrix

$[E]$	global element matrix
$[G]$	stiffness matrix
$[K^*]$	overall global conductance matrix
$[K_n]$	global NAPL conductance matrix
$[K_w]$	global water conductance matrix
$[M_{CF}]$	influence coefficient matrix – consistent mass formulation
$[M_{LF}]$	influence coefficient matrix – lumped mass formulation
$\left[Y_{x_i x_j}\right]$	influence coefficient matrices
$\left[Y_{x_i}\right]$	influence coefficient matrices
$\{F_{c,a}\}$	air boundary flux vector
$\{F_{c,w}\}$	solute boundary flux vector
$\{F_g^*\}$	overall vector incorporating the gravitational forces acting on the liquid phases
$\{F_{g,n}\}$	vector incorporating the gravitational forces acting on the NAPL
$\{F_{g,w}\}$	vector incorporating the gravitational forces acting on the water phase
$\{F_q^*\}$	overall vector incorporating the Neumann boundary conditions
$\{F_{q,n}\}$	vector incorporating the Neumann boundary conditions for the NAPL
$\{F_{q,w}\}$	vector incorporating the Neumann boundary conditions for the water phase
$\{F_{x_2}\}$	influence coefficient matrix
$\{h\}$	global vector of the unknown pressure heads
$\{h_n\}$	vector of the unknown NAPL pressure heads
$\{h_w\}$	vector of the unknown water pressure heads
$\{I\}$	identity vector
$\{L\}$	vector of known values
$\{M\}$	mass transfer vector
$\{S\}$	global vector of the unknown saturations
$\{S_n\}$	vector of the unknown NAPL saturations
$\{S_w\}$	vector of the unknown water saturations
$\{X\}$	vector of unknown variables

Chapter 3

Dual Gamma System Calibration and Liquid Hg^0 Attenuation Potential of Gamma Rays

The chapter is devoted to the description of the calibration process of the dual gamma ray system employed at Utrecht University laboratories. The first part focuses on the theoretical framework of gamma radiation and on the operating principles of the dual gamma system. The calibration process is then described. Furthermore, the analysis of the attenuation behaviour of gamma radiation exhibited by the substances and the materials used within this research (Chapter 4) is presented, with particular emphasis on liquid Hg^0. In the end, the mathematical description of Beer-Lambert law for porosity and liquid phases saturation measurements is introduced.

3.1 Dual Gamma System

3.1.1 Gamma Ray Attenuation Technique

In recent years, gamma rays have been successfully employed for non-destructive measurements of porosity and fluid saturations in several porous systems (Ferrand et al., 1986; Hofstee et al. 1998a; Hofstee et al. 1998b; Barataud et al., 1999; Johnson et al. 1999; Baytaş and Akbal, 2002; Pires et al., 2005; Pires and Bereira, 2014). Conventionally, a gamma ray is a photon with a specific wave length, which corresponds to a specific energy. A photon is an elementary particle, massless and stable, with no electric charge,

and it is regarded as the quantum of energy of electromagnetic radiation, exhibiting properties of waves and particles at the same time.

The Gamma Ray Attenuation (GRA) technique is essentially based on the interaction of radiation with matter. Depending on how the radiation travels through the sample and, in particular, on how the radiation gets absorbed (hence attenuated), it is possible to determine, in a non-invasive way, properties related to the structure of the porous medium and fluid saturations within the pores.

The attenuation of gamma rays, induced by the absorption of a medium, can be described by Beer-Lambert law:

$$I = I_0 \cdot e^{(-\mu \cdot x)} \tag{3.1}$$

where I_0 is the incident intensity of gamma rays, I is the intensity of gamma rays after attenuation through a medium of length x (path length), and μ is the linear attenuation coefficient of the material. The attenuation coefficient, which is dependent on the physical density of the material, measures the probability per unit length of a photon to be absorbed or scattered while interacting with a sample. In the case where the sample is shielded from the gamma radiation by the presence of the additional thickness of a container, the incident intensity is called background intensity, and it must be measured in advance.

3.1.2 Dual Gamma Ray Setup and Operating Principles

The dual gamma ray system consists of two radioactive sources, namely Americium 241 (^{241}Am) and Cesium 137 (^{137}Cs), which emit gamma rays, and a sodium iodide (NaI) detector (Figs. 3.1 and 3.2).

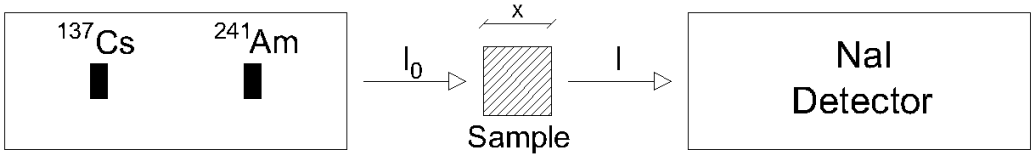

Fig. 3.1. Schematic illustration of the dual gamma ray setup.

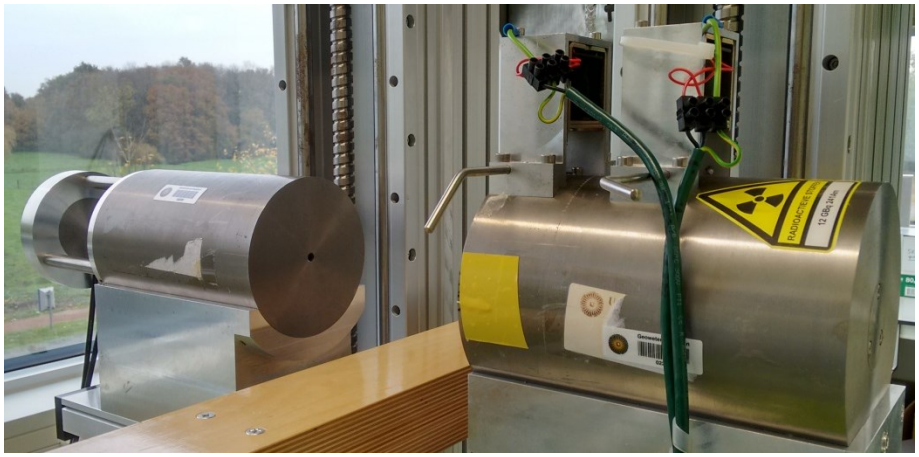

Fig. 3.2. Detail of the dual gamma ray setup.

The NaI detector measures an average value, over the beam cross section (6 mm diameter) and the path length, of the number of arriving photons (counts) over their energy, rather than intensities. Intensities are determined by first summing up the count rates of the peak areas, from 40.4 keV to 82 keV for ^{241}Am, and from 623.5 keV to 740.9 keV for ^{137}Cs, and then by dividing them by the measurement time. The detector cannot process and measure simultaneously more photons at the same location, and the measurement time is affected by dead times (between 8% and 15%, depending on the sample thickness and properties), which are automatically taken into account within the measurements by a real time procedure incorporated in the setup.

The detector is one of the most sensitive components, being particularly susceptible to temperature and moisture variations. The voltage itself has a great influence on the spectrum of measured energies. As a matter of fact, the spectrum decreases with increasing voltage, thus resulting in an increase in accuracy due to the sharper resolution of the energies. Nevertheless, if the voltage is too high, it could be not possible to detect the Cesium peak.

The determination of the energies is affected by uncertainties, and the signal reproduced by the detector mainly consists of a Gaussian distributed curve rather than of two straight lines, which would appear only under ideal conditions, namely at 59 keV for ^{241}Am and at 662 keV for ^{137}Cs, respectively. The two main peaks, namely the Americium and the Cesium peaks, can be clearly observed in Fig. 3.3, where a typical signal reproduced by the dual gamma ray system is depicted. One of the aspects to notice is the high elevation of the

Americium peak due to the Compton Scattering. This phenomenon is induced by the energy transfer caused by the collision of Cesium photons with electrons. The highest loss of energy occurs if the scattering angle due to the collision is of 180°, and the electron entering the detector under such condition has an energy of about 477 keV (Compton Edge). The Escape peak, instead, can be found on the left of the Americium peak, and it takes form due to the photon absorption by the deepest electronic layer of the detector.

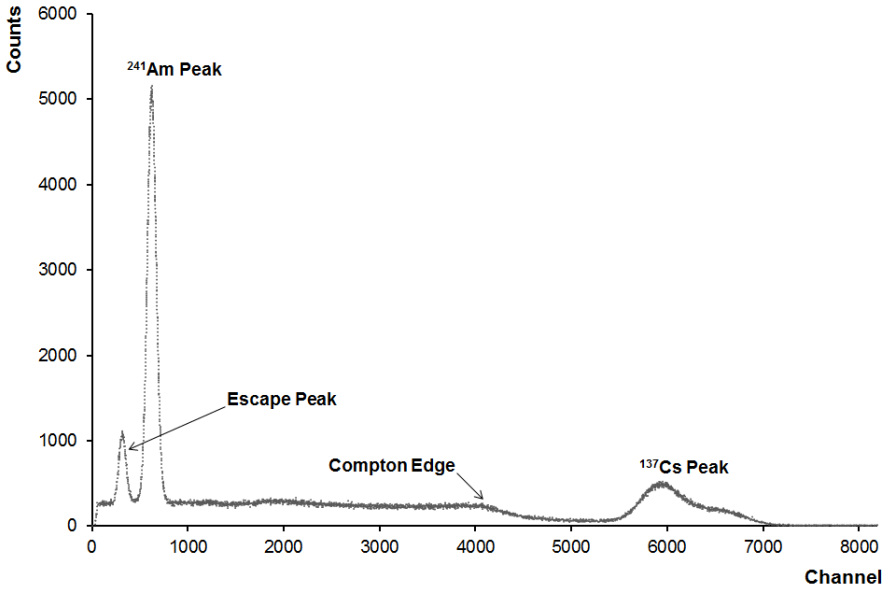

Fig. 3.3. Typical signal reproduced by the dual gamma ray system.

3.2 System Calibration

3.2.1 System Warmup

To stabilize the NaI detector, before every round of measurements, the dual gamma system was subjected to a warmup. The warmup mainly consisted of a constant bombing of the detector with gamma radiation for a fixed time. After a proper amount of time, several trial runs were performed on a reference sample to verify the stability of the signal. Each trial run was performed for the same measurement time and under the same operative conditions employed for the subsequent measurements.

This procedure was fundamental especially due to the Cesium source instability. As a matter of fact, while ^{241}Am was particularly stable as its channel range was affected by negligible variations, the ^{137}Cs source, instead, was affected by a horizontal shift in the

channel range. Hence, a daily calibration was performed to correctly evaluate the detected intensities (Fig. 3.4). Nevertheless, even if the channel range was shifted, measurements taken during different days could be compared between each other because the width of the channel range was fixed a priori, according to the peaks energy ranges.

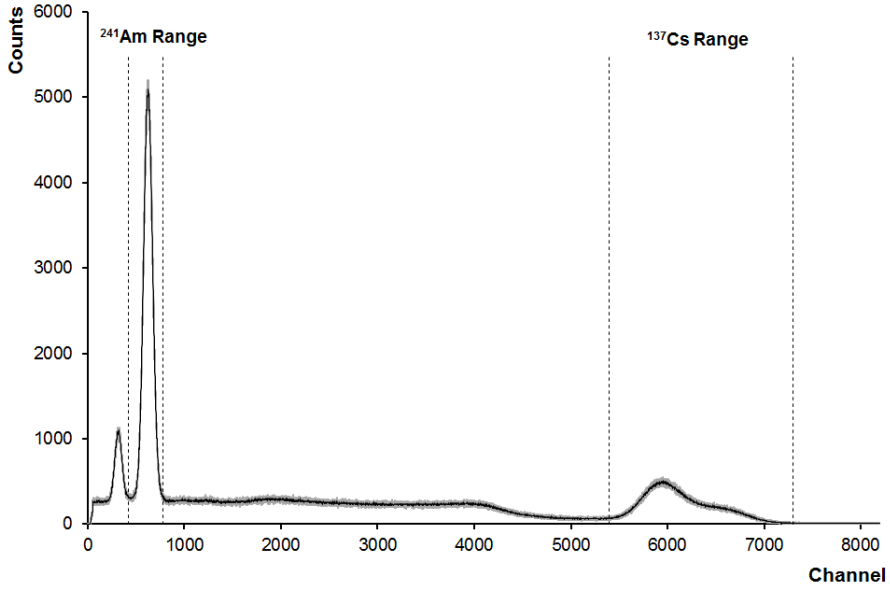

Fig. 3.4. Typical daily calibration signals (mean value as black line) and radioactive sources channel ranges.

3.2.2 Time and Accuracy Measurements

The choice of the measurement time was based on the measurements to be performed on the flow container samples (lately discussed in Chapters 5 and 6). The limiting factor was mainly represented by the presence of liquid elemental mercury within the porous samples. Because of liquid Hg^0 high attenuation potential (sec. 3.3.3), the determination of the measurement time was based on it. To this aim, the thicknesses of the materials used in the calibration procedure were in the same range of those of the experimental setup reported in Chapters 5 and 6.

Two different rounds of measurements were performed: the first one, on a single Hg^0 filled cuvette, while, the second one, on a row of four Hg^0 filled cuvettes (Fig. 3.5). This choice was dictated by the need of a set of measurements based on a range of path lengths, induced by the fact that Hg^0 would have been present in samples characterized by heterogeneous porosity fields. Therefore, its path length would have been subjected to non-

negligible variations. Hence, according to the setup dimensions (Chapter 5) and the cuvettes size (each polystyrene squared cuvette had a thickness of 1 cm and a nominal volume of 4 ml), the two limits taken into account were 1 cm and 4 cm, respectively.

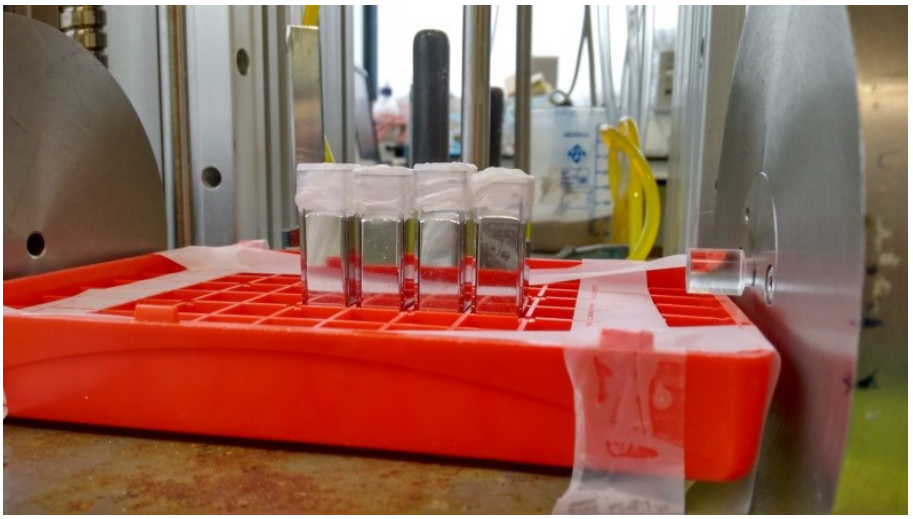

Fig. 3.5. Illustration of the four Hg^0 filled cuvettes – Time and accuracy measurements.

For each measurement time, a set of 12 runs was performed at the same location, and, afterwards, arithmetic means and standard deviations of the measured intensities were calculated. The choice of the measurement time is usually a compromise between desired intensities, accuracy, and speed, hence, the tested range of measurement times was fixed between 20 s and 120 s, with a step of 20 s. In particular, the right limit was chosen as the limit after which it would have not been feasible to carry out several measurements in a single round.

Because of the complete attenuation of ^{241}Am radiation exerted by elemental mercury, the data are reported in terms of ^{137}Cs intensity. When working with Hg^0 the only possibility is to use a source emitting high energy radiation, as Cesium.

The results of the round of measurements performed for the single Hg^0 filled cuvette (Fig. 3.6) do not show any preferable measurement time among the selected ones. Intensities are practically the same, while their standard deviations are affected by slight variations. Increasing the number of cuvettes, hence increasing Hg^0 path length, the intensities drop dramatically, thus showing the remarkable shielding potential of elemental mercury, even with respect to high energy radiation.

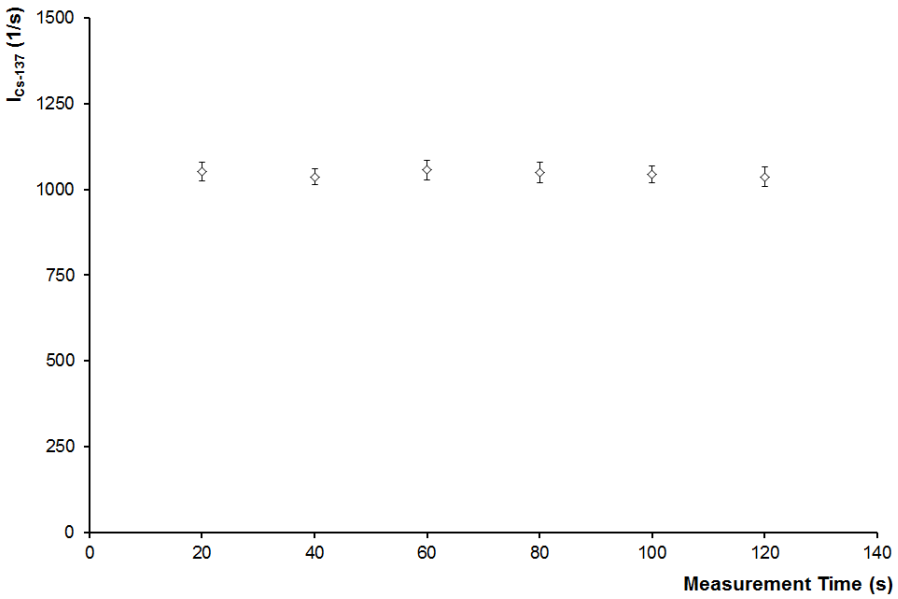

Fig. 3.6. Mean values and standard deviation bars of Cesium intensities versus measurement time (1 cuvette).

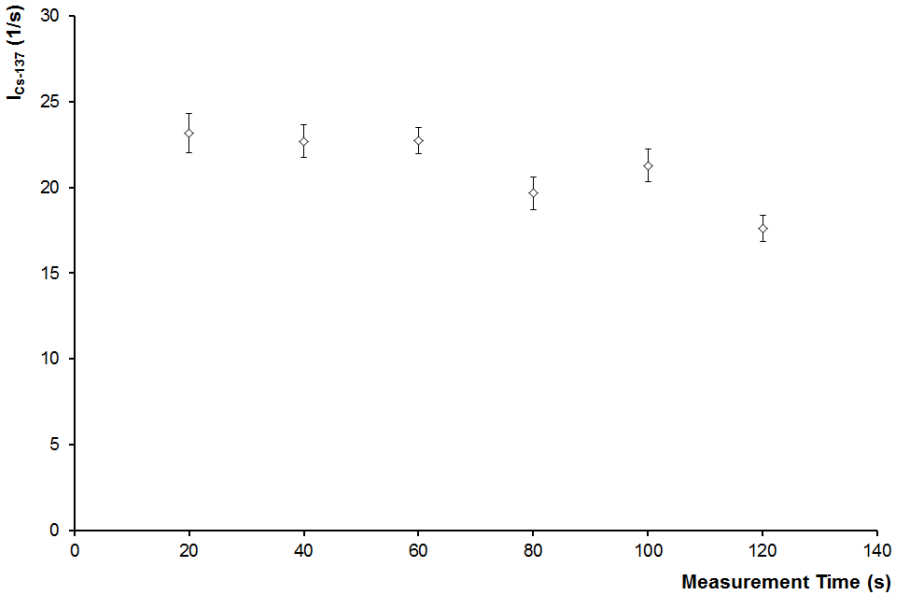

Fig. 3.7. Mean values and standard deviation bars of Cesium intensities versus measurement time (4 cuvettes).

The measurement time was then fixed to 120 s according to the results showed by the 4 cuvettes round of measurements (Fig. 3.7), aiming to cope with the most critical condition (namely, the longest path length). Even though the standard deviation associated with the

chosen time was of 4%, this choice was dictated by the fact that longer measurement times would not have been feasible for numerous sequential rounds of measurements.

3.2.3 Compton Scattering Coefficients

The Compton Scattering induces an increase in Americium intensity (sec. 3.1.2), therefore, to properly compute Americium intensities, a correction is needed. The correction is performed as follows:

$$I_{Am,cor} = a \cdot I_{Cs} + b \tag{3.2}$$

$$I_{Am} = I_{Am,0} - I_{Am,cor} \tag{3.3}$$

To determine the coefficients a and b, several measurements were taken over the height of a PMMA (Poly-Methyl Methacrylate) prism of triangular shape (so that to have a wide range of intensities, thanks to the variation of thickness with the height) shielded with brass plates of 0.5 mm each. Brass was chosen because of its high absorption potential with respect to Americium and, conversely, only to a small extent with respect to Cesium.

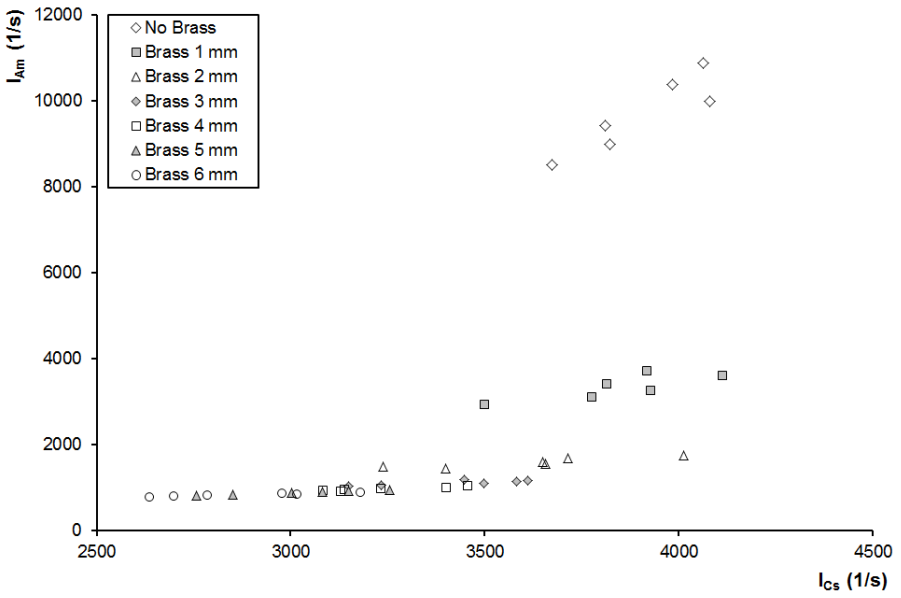

Fig. 3.8. Distribution of Americium intensities over Cesium intensities.

Several brass thicknesses were tested (Fig. 3.8), and a thickness of 6 mm was found to be the most appropriate to be taken into account due to its stronger shielding potential. In this way, thanks to the almost complete attenuation of Americium, it was possible to measure

the number of incoming photons induced by the Compton Scattering in the Americium energy range. In particular, the resulting Americium intensities linearly increase with increasing Cesium intensities (Fig. 3.8).

The Compton Scattering coefficients were then evaluated by means of a linear interpolation, which returned the following values of 0.1928 and of 279.41 s^{-1} for a and b, respectively.

3.3 Attenuation Coefficients

The attenuation coefficients were measured by placing different amounts of cuvettes in a row, thus leading to different thicknesses (path lengths, Eq. 3.1). To establish the background intensity, the cuvettes were measured empty first and then, with the aim of determining the intensity measurements, each cuvette was filled with the substance/material to analyse. Polystyrene (PS) squared cuvettes, of 1 cm thickness and 4 ml volume, were used for most of the measurements, with the exception of those carried out for tetrachloroethylene, where PMMA was used, due to the almost null resistance of PS to PCE. Then, on the basis of Beer-Lambert equation (Eq. 3.1), the attenuation coefficients were determined by means of a least square fitting technique over the measurement points. The resulting attenuation coefficients are reported in Tab. 3.1, while the analysis performed are described in the subsequent sections.

Tab. 3.1. Attenuation Coefficients.

Substance	μ_{Am} (cm^{-1})	μ_{Cs} (cm^{-1})	R^2_{Am}	R^2_{Cs}
Demineralized Water (DW)	0.186	0.075	0.997	0.934
DW + Bromophenol	0.185	0.072	0.997	0.940
DW (Medium Sand 1) + Bromophenol	0.187	0.084	0.997	0.952
DW (Medium Sand 2) + Bromophenol	0.185	0.070	0.997	0.916
PCE	0.633	0.113	0.993	0.970
Hg^0	-	1.280	-	0.990
Medium Sand 1	0.680	0.195	0.999	0.990
Medium Sand 2	0.645	0.191	0.998	0.975

In particular, the results reported in Tab. 3.1 are consistent with the experimental results reported in literature (Hubbell and Seltzer, 1989; Pires et al., 2005; Fritz, 2012; Pires and Bereira, 2014).

3.3.1 Demineralized Water Attenuation

In Fig. 3.9, the experimental determinations of the measured intensities passing through different path lengths of demineralized water are shown.

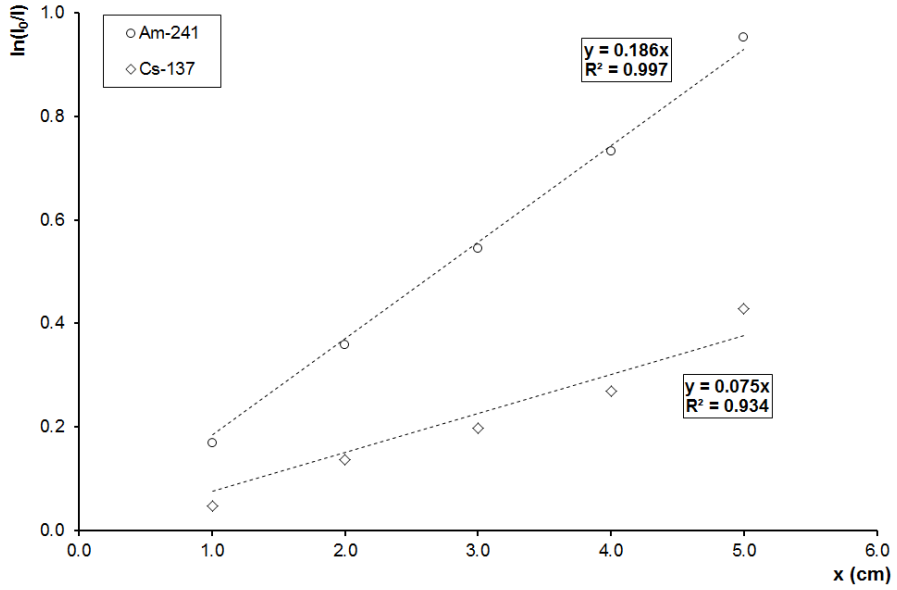

Fig. 3.9. Linear attenuation coefficients of demineralized water.

Besides of the demineralized water measurements, other measurements were carried out to determine whether the use of a colour agent could have exerted an effect on water attenuation coefficients or not. In particular, as will be shown in Chapter 5, Bromophenol Blue, a pH indicator, was used in a concentration of 1 g/l. Two different set of samples were dyed: in the first set, bromophenol was added to pure demineralized water, while, in the second one, the pH indicator was added to demineralized water after having allowed water to stay in contact with Medium Sand 1 and Medium Sand 2 (Chapter 4), respectively, for at least one hour, to see whether the sand could affect considerably both pH and attenuation coefficients of water.

The results (Tab. 3.1) show that there are no considerable changes between the samples if compared to the pure demineralized water, and that the deviations found are just to be imputed to the natural oscillations in the gamma ray signal and to the less accuracy of the Cesium source (Fritz, 2012). The colour itself of the different samples did not change, thus

remaining blue and confirming that if any pH change occurred, it was not in the range detectable by the pH indicator.

3.3.2 Tetrachloroethylene Attenuation

In Fig. 3.10, the experimental determinations of the measured intensities passing through different path lengths of PCE are shown.

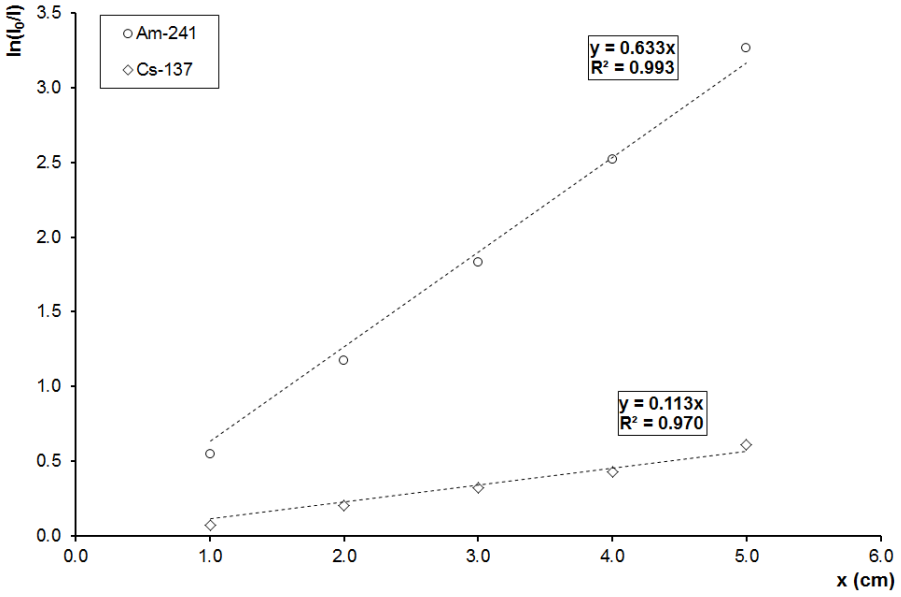

Fig. 3.10. Linear attenuation coefficients of PCE.

3.3.3 Liquid Elemental Mercury Attenuation

Liquid elemental mercury showed to completely shield ^{241}Am radiation for path lengths of the order of the centimetres. Hence, to completely investigate elemental mercury attenuation potential, further measurements were carried out for 0.5 cm and 1 mm, respectively. For the half centimetre path length, a squared cuvette, of half centimetre thickness, was used. Instead, for the 1 mm path length, the desired Hg^0 thickness was obtained by joining together three square glass plates, of 1 mm thickness each, and creating a circular hole of 2 cm diameter into the middle plate (Fig. 3.11). The hole was connected to the top by a channel of 2 mm width to allow the filling with Hg^0. Then, the top port was sealed with super glue.

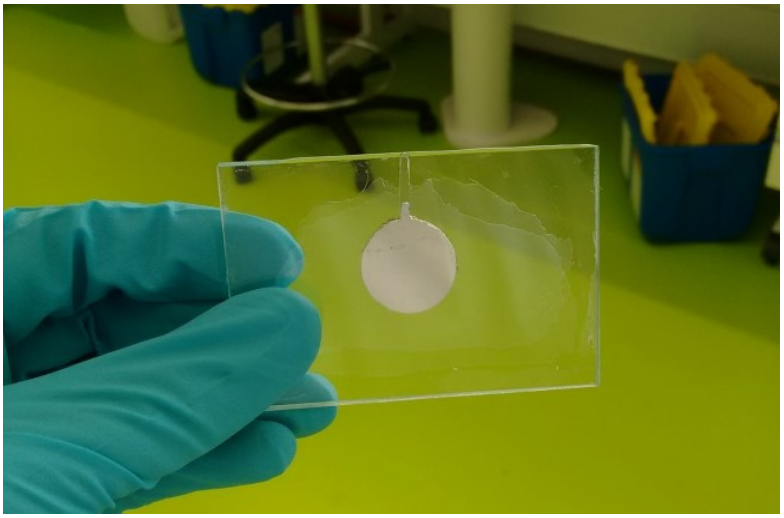

Fig. 3.11. Detail of the 1 mm thickness Hg^0 sample.

The measurements performed on the additional 1 mm sample (Fig. 3.12) showed a complete attenuation of Americium radiation as well.

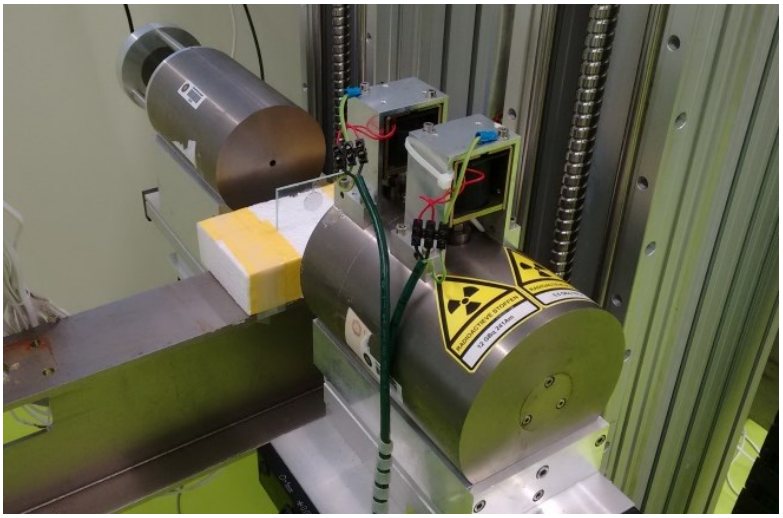

Fig. 3.12. Illustration of the measurements performed on the 1 mm thickness Hg^0 sample.

As clearly shown in Fig. 3.13, the Americium peak is extremely reduced and is slightly visible only due to Compton Scattering, the Escape peak is not visible anymore, and only Cesium radiation is able to pass through liquid Hg^0. Even though Cesium has a stronger capacity to penetrate matter than Americium, liquid Hg^0 shows a remarkably high attenuation coefficient with respect to this gamma radiation, about 17 times higher than

water (Tab. 3.1). According to Eq. 3.1, this implies that 0.5 cm of liquid Hg^0 are sufficient to attenuate Cesium radiation of about 47%, whereas 2 cm can induce an attenuation of 92%. However, according to the thickness (4-5 cm) and average porosity (0.363-0.380) of the porous samples used for the Hg^0 flow container experiments (Chapters 5 and 6), at 100% of mercury saturation, liquid Hg^0 can reach a maximum thickness of about 2 cm within the samples, thus enabling the use of the Cesium source to determine its complete range of saturation.

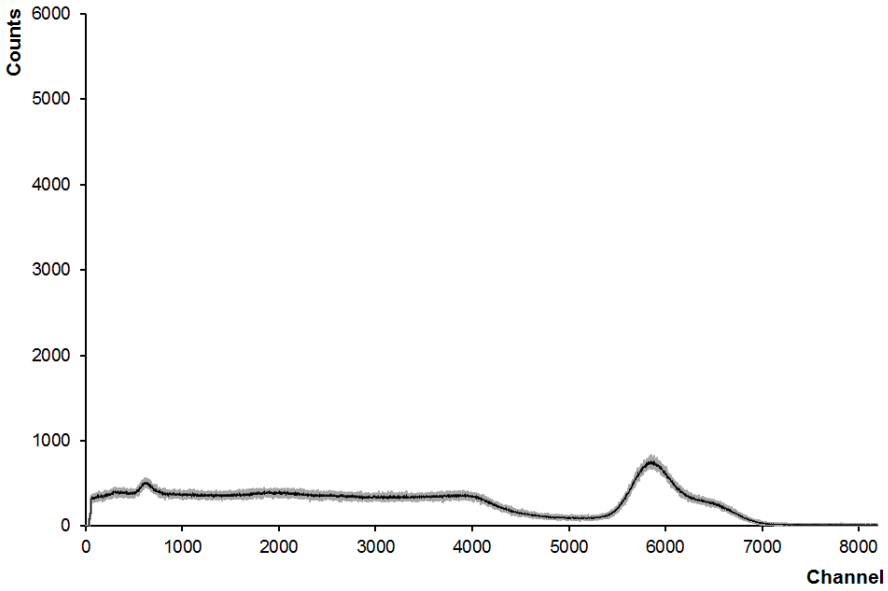

Fig. 3.13. Detected signals (mean value as black line) for the 1 mm thickness Hg^0 sample.

These experimental results highlight that, when analysing Hg^0 DNAPL flow behaviour in porous media by means of non-intrusive techniques as GRA, attention must be paid in the choice of the sources of radiation. In particular, the sources should be strong enough to penetrate liquid Hg^0 to at least some extent, and the sample thickness should not exceed a certain path length to allow a correct characterization of Hg^0 DNAPL saturation range within the porous medium.

In Fig. 3.14, the experimental determinations of the measured Cesium intensities passing through different path lengths of Hg^0, namely from 1 mm to 4 cm, are shown. Due to liquid Hg^0 complete attenuation of ^{241}Am radiation, only ^{137}Cs attenuation coefficient was determined.

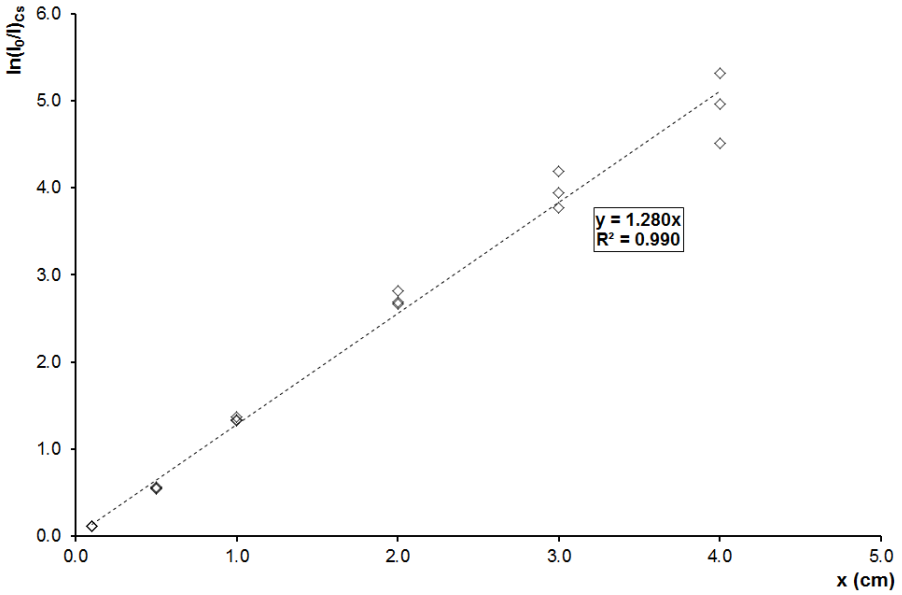

Fig. 3.14. Linear attenuation coefficient of Hg^0.

3.3.4 Dry Sands Attenuation

In Figs. 3.15 and 3.16, the experimental determinations of the measured intensities passing through different path lengths of Medium Sand 1 and Medium Sand 2 are shown, respectively.

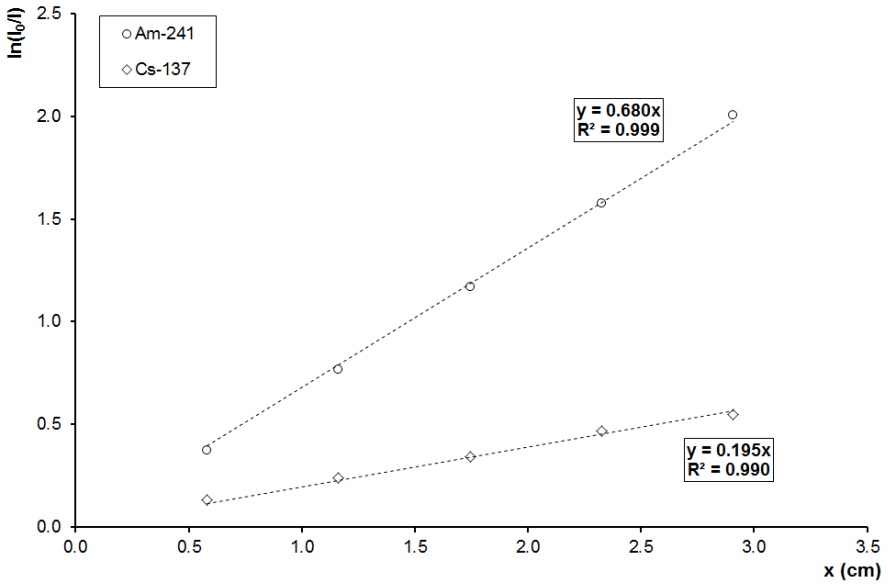

Fig. 3.15. Linear attenuation coefficients of Medium Sand 1.

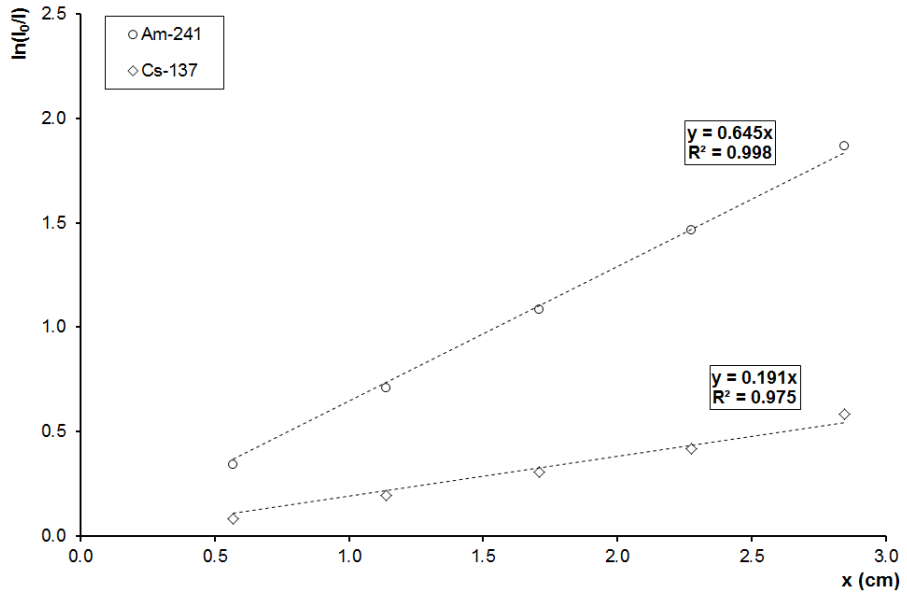

Fig. 3.16. Linear attenuation coefficients of Medium Sand 2.

After having completely filled the cuvettes with dry sand, the effective path lengths were determined by evaluating the theoretical sample porosity (by knowing the mass of the sand used, the particle density, and the total volume occupied), equal to 0.582 for Medium Sand 1 and to 0.569 for Medium Sand 2, and then multiplying it for the thickness of the cuvettes row.

3.4 Mathematical Description of Beer-Lambert Law for Two- and Three-Phase Flows

3.4.1 Porosity

In the case of a water saturated porous medium, Eq. 3.1 becomes:

$$I^{\alpha} = I_0^{\alpha} \cdot e^{(-\mu_w^{\alpha} \cdot x_w - \mu_s^{\alpha} \cdot x_s)} \tag{3.4}$$

where α = Am, Cs, I_0 is the background intensity of the gamma rays passing through the walls of a hypothetical container in which the porous medium is located, μ_w and μ_s are the attenuation coefficients for water and for the dry porous medium, respectively, $x_w = \phi \cdot l$ and $x_s = (1 - \phi) \cdot l$ are the path lengths for water and the dry porous medium, respectively, with *l* the thickness of the sample.

Hence, by simply expanding the terms in Eq. 3.4, after few manipulations, the porosity, ϕ, can be determined as follows:

$$\phi = \frac{\ln\left(I^{\alpha}/I_0^{\alpha}\right)+\mu_s^{\alpha}\cdot l}{l\cdot(\mu_s^{\alpha}-\mu_w^{\alpha})} \tag{3.5}$$

3.4.2 Water Saturation

In the case of a partially water saturated porous medium, if the porosity field is derived from the measurements taken in the water saturated sample, the background intensity must be evaluated first. In particular, it corresponds to the attenuation exerted by the walls of the hypothetical container, in which the porous medium is located, and by the dry porous medium. Hence, the background intensity can be defined by reducing the measured intensity passing through the water saturated sample by the attenuation of the water phase:

$$I_0^{\alpha} = \frac{I^{\alpha}}{e^{(-\mu_w^{\alpha}\cdot\phi\cdot l)}} \tag{3.6}$$

The water saturation, S_w, is then calculated with simple manipulations of Eq. 3.4, written in terms of water attenuation:

$$S_w = \frac{\ln\left(I_0^{\alpha}/I^{\alpha}\right)}{\mu_w^{\alpha}\cdot\phi\cdot l} \tag{3.7}$$

being $x_w = S_w \cdot \phi \cdot l$ the path length.

3.4.3 NAPL Saturation – Two-Phase Flow

Assuming a two-phase flow of NAPL and water within the pores, the NAPL saturation, S_n, can be determined by extending Eq. 3.1 as follows:

$$I^{\alpha} = I_0^{\alpha} \cdot e^{(-\mu_n^{\alpha}\cdot x_n-\mu_w^{\alpha}\cdot x_w)} \tag{3.8}$$

where the subscript n refers to the NAPL, I_0 is evaluated according to Eq. 3.6, and the path lengths are $x_w = S_w \cdot \phi \cdot l$ and $x_n = S_n \cdot \phi \cdot l$, respectively

Because of $x_w + x_n = \phi \cdot l$, simple manipulations of Eq. 3.8 lead to the following expression of the NAPL saturation:

$$S_n = \frac{\ln\left(I^{\alpha}/I_0^{\alpha}\right)+\mu_w^{\alpha}\cdot\phi\cdot l}{(\mu_w^{\alpha}-\mu_n^{\alpha})\cdot\phi\cdot l} \tag{3.9}$$

which, theoretically, reduces to 0 in absence of NAPL.

3.4.4 Water and NAPL Saturations – Three-Phase Flow

When a three-phase system of air, NAPL and water is encountered, the determination of the liquid phases saturations within the pores is performed by solving simultaneously Eq. 3.8 for both radioactive sources, with background intensities evaluated with Eq. 3.6. With simple calculations, the two equations can be rearranged, thus giving the desired expressions of the liquid saturations.

For example, Eq. 3.8, written in terms of ^{241}Am intensities, gives the water saturation:

$$S_w = \left[\ln\left(\frac{I_0^{Am}}{I^{Am}}\right) - \mu_n^{Am} \cdot S_n \cdot \phi \cdot l\right] / \left(\mu_w^{Am} \cdot \phi \cdot l\right) \tag{3.10}$$

After substitution of Eq. 3.8, written in terms of ^{137}Cs intensities, into Eq. 3.10, the resulting NAPL saturation can be expressed as follows:

$$S_n = \left[\ln\left(\frac{I_0^{Cs}}{I^{Cs}}\right) - \frac{\mu_w^{Cs}}{\mu_w^{Am}} \cdot \ln\left(\frac{I_0^{Am}}{I^{Am}}\right)\right] \Big/ \left[\left(\mu_n^{Cs} - \frac{\mu_w^{Cs}}{\mu_w^{Am}} \cdot \mu_n^{Am}\right) \cdot \phi \cdot l\right] \tag{3.11}$$

References

Barataud F, Moyne C, Stemmelen D (1999). *Measurement of soil water diffusivity of an undisturbed forest soil using dual-energy gamma radiation technique*. Soil Science, 164(7), 493-502.

Baytaş AF, Akbal A (2002). *Determination of soil parameters by gamma-ray transmission*. Radiation Measurements, 35(1), 17-21.

Ferrand LA, Milly PCD, Pinder GF (1986). *Dual-Gamma Attenuation for the Determination of Porous Medium Saturation with Respect to Three Fluids*. Water Resources Research, 22(12), 1657-1663.

Fritz S (2012). *Experimental Investigations of Water Infiltration into Unsaturated Soil - Analysis of Dynamic Capillarity Effects*. Universität Stuttgart, Germany.

Hofstee C, Dane JH, Walker RC (1998a). *Infiltration and redistribution of perchloroethylene in stratified water-saturated porous media*. Soil Science Society of America Journal, 62(1), 13-22.

Hofstee C, Oostrom M, Dane JH, Walker RC (1998b). *Infiltration and redistribution of perchloroethylene in partially saturated, stratified porous media*. Journal of Contaminant Hydrology, 34(4), 293-313.

Hubbell JH, Seltzer SM (1989). *Tables of X-ray Mass Attenuation Coefficients and Mass Energy-Absorption Coefficients from 1 keV to 20MeV for Elements Z=1 to 92 and 48 Additional Substances of Dosimetric Interest*. NIST Physical Measurement Laboratory, Radiation Physics Division. US Secretary of Commerce, USA.

Johnson JC, Sun S, Jaffé PR (1999). *Surfactant Enhanced Perchloroethylene Dissolution in Porous Media: The Effect on Mass Transfer Rate Coefficients*. Environmental Science & Technology, 33(8), 1286-1292.

Pires LF, Bacchi OOS, Reichardt K (2005). *Soil water retention curve determined by gamma-ray beam attenuation*. Soil & Tillage Research, 82(2005), 89-97.

Pires LF, Pereira AB (2014). *Gamma-Ray Attenuation to Evaluate Soil Porosity: An Analysis of Methods*. The Scientific World Journal, 2014, ID 723041.

Notation

Greek Symbols

μ	linear attenuation coefficient
μ_n	NAPL linear attenuation coefficient
$\mu_{n,Am}$	NAPL linear attenuation coefficient of Americium gamma rays
$\mu_{n,Cs}$	NAPL linear attenuation coefficient of Cesium gamma rays
μ_s	dry porous medium linear attenuation coefficient
μ_w	water linear attenuation coefficient
$\mu_{w,Am}$	water linear attenuation coefficient of Americium gamma rays

$\mu_{w,Cs}$	water linear attenuation coefficient of Cesium gamma rays
ϕ	porosity

Latin Symbols

a	Compton Scattering correction coefficient
b	Compton Scattering correction coefficient
I_0	incident\background intensity of gamma rays
$I_{0,Am}$	incident\background intensity of Americium gamma rays
$I_{0,Cs}$	incident\background intensity of Cesium gamma rays
I	intensity of gamma rays after attenuation
I_{Am}	intensity of Americium gamma rays after attenuation
$I_{Am,cor}$	intensity of Americium gamma rays after attenuation, Compton Scattering correction
I_{Cs}	intensity of Cesium gamma rays after attenuation
l	sample thickness
R^2_{Am}	coefficient of determination of Americium measurements
R^2_{Cs}	coefficient of determination of Cesium measurements
S_n	NAPL saturation
S_w	water saturation
x	path length
x_n	NAPL path length
x_s	dry porous medium path length
x_w	water path length

Chapter 4

Infiltration Behaviour of Hg^0 DNAPL in Variably Water Saturated Porous Media

In this chapter, the analysis of the properties affecting the constitutive relations governing Hg^0 DNAPL infiltration behaviour in different granular porous media is described. Porous media and fluids properties are described together with the setup and the methods used for the capillary pressure-saturation, $P_c(S)$, measurements. The retention curves, obtained under stable flow behaviour, are then presented for different two-phase and three-phase systems. The results are compared and discussed at the end of the chapter.

4.1 Materials and Methods

4.1.1 Porous Media

Three types of glass beads, *coarse* (d_{50} = 1 mm), *medium* (d_{50} = 0.375 mm), and *fine* (d_{50} = 0.175 mm), (Glaswarenfabrik Karl Hecht; Retsch), and two different medium sands, Filtersand 0.2-0.5 mm and Silversand S60 (FILCOM-Sibelco Group), were used as porous media (Tab. 4.1). The two medium sands will be referred to *medium sand 1* (MS1) and *medium sand 2* (MS2), respectively. The particle size distribution of MS1 (d_{50} = 0.39 mm) is wider (Fig. 1; Tab. 1) than MS2 (d_{50} = 0.26 mm), and the particle sizes mainly fall in the range of 0.200-0.500 mm and 0.125-0.355 mm for MS1 and MS2, respectively. For each

granular porous medium, information regarding hydraulic conductivity and intrinsic permeability were obtained experimentally using the falling head method (Bear, 1972).

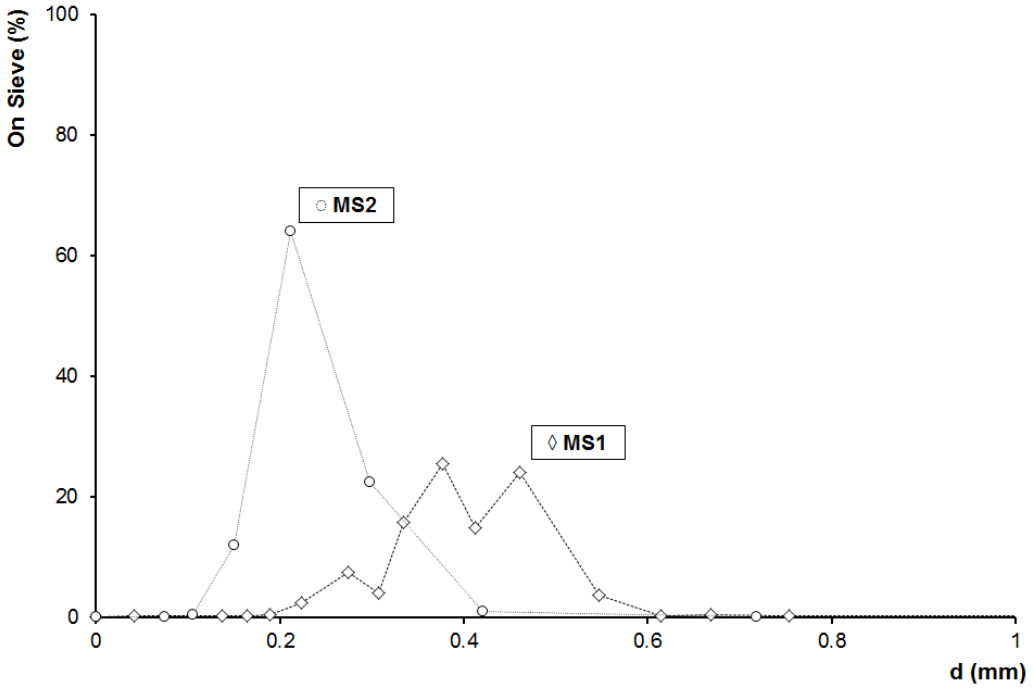

Fig. 4.1. Particle size frequencies of the medium sand samples (MS1 and MS2). Data from FILCOM (2015).

Tab. 4.1. Porous Media Properties.

Porous Medium	ρ_s (g/cm^3)	d_{50} (mm)	Size Range (mm)
Coarse Glass Beads[a]	2.65	1	-
Medium Glass Beads[b]	2.65	0.375	0.200-0.500
Fine Glass Beads[b]	2.65	0.175	0.100-0.250
Medium Sand 1[c]	2.67	0.39	0.200-0.500
Medium Sand 2[c]	2.65	0.26	0.125-0.355

[a]Glaswarenfabrik Karl Hecht (2013); [b]Retsch (2013); [c]FILCOM (2015). Particle size classification based on Wentworth classification (1922).

4.1.2 Fluids

Demineralized water was used as the wetting fluid, while laboratory grade ($\geq$ 99%) tetrachloroethylene (PCE), (Acros Organics), and 99.9% $\pm$ 1% redistilled liquid elemental mercury (Hg^0), (Alfa Aesar), were used as the nonwetting fluids for the $P_c(S)$ measurements (Tab. 4.2).

Tab. 4.2. Fluids Properties.

Parameter	Unit	Hg^0	PCE	Water
Density	g/cm^3	13.500[a]	1.630[b]	0.998
Dynamic Viscosity	10^{-3} Pa·s	1.55[c]	0.89[b]	0.98
Surface Tension	Dynes/cm	485[c]	32.6[b]	72
Interfacial Tension with Water	Dynes/cm	375[c]	47.8[b]	-
Vapour Pressure	Pa	0.07[a,d]	1867[b]	-
Aqueous Solubility	mg/l	0.06-0.08[a]	225[e]	-

[a]CRC (2014); [b]Schwille (1988); [c]US DOE (2001) and references therein; [d]At 10 °C; [e]Imhoff et al. (1995).

4.1.3 Columns

Column experiments were performed to determine the intrinsic permeability and the $P_c(S)$ curves for different two- and three-phase systems under stable flow behaviour. Two cylindrical columns with identical dimensions (42 mm diameter by 51 mm length) were used. One column was made of PMMA (Poly-Methyl Methacrylate) and was used for all the experiments except those involving PCE, as it is wetting with respect to PMMA. Hence, to prevent preferential flow along the column wall, a stainless steel column was used. The two columns were closed by two caps, each of them provided with a rubber ring to ensure water and air tightness.

The packing of the porous media was performed under water saturated conditions to avoid any presence of entrapped air within the grains. The column was initially filled halfway with water and then, after having thoroughly mixed the grains with water in another container, the solid particles were gradually poured into it. In order to maintain a fully water saturated system, attention was paid to constantly ensure a water head over the top layer of the porous medium. At each filling step, each layer was subjected to the same degree of tamping. A nylon filter, with coarse mesh size, was put at the inflow and the outflow ports of the column to prevent loss of solid particles. This filter acted as a water wet membrane and had a sufficiently coarse mesh size to not affect the measurements. At the end of the packing procedure, the porosity was analytically derived based on the volume and the weight of the filled column, and the densities of both water and the solid particles.

4.1.4 Capillary Pressure-Saturation Measurements

After filling the columns with the porous media, they were used to determine the $P_c(S)$ retention curves (Fig. 4.2).

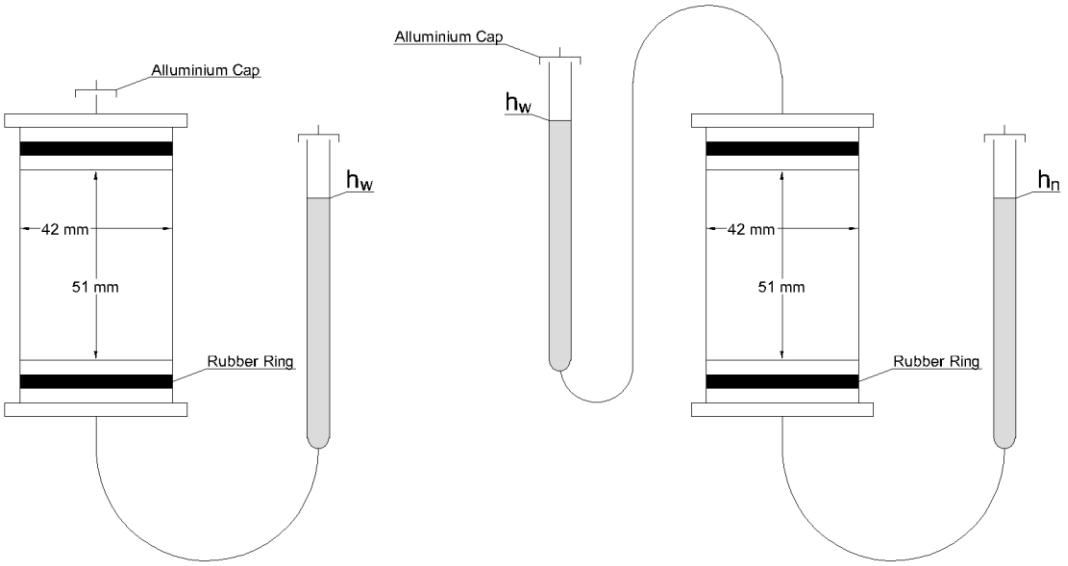

Fig. 4.2. Air-Water (left) and NAPL-Water (right) $P_c(S)$ setups.

Glass burettes were used to host the wetting and the nonwetting fluids, and both top ports of the burettes were covered with an aluminium foil cap, to prevent any liquid loss through volatilisation. The columns and the burettes were connected by Tygon tubes, while, for the PCE experiments, they were connected using a combination of Viton and Teflon tubes. Bottom and top valves of the columns had a three way configuration, which allowed the removal of any entrapped air in the tubes connecting the columns to the glass burettes. Valves were made of PS (Polystyrene), exception for the bottom valve used for the PCE experiments, where stainless steel was used. The choice of different materials for valves and connections was dictated by: i) the incompatibility of PS and Tygon to PCE, and ii) by the tendency of elemental mercury to adsorb to metallic surfaces, such as stainless steel components.

In the Air-Water experiments, the column was connected at the bottom to a burette filled with water, while the top of the column was left in contact with air and covered with an aluminium foil cap to prevent water loss through evaporation. In the two-phase NAPL-

Water experiments (Fig. 4.3), the columns were connected at the top to a burette filled with water, while, at the bottom, to a burette filled with NAPL. An additional nylon filter (10 μm mesh size) was placed on the top of the porous sample as a water wet membrane, to allow the flow of water and not of the NAPL. The NAPL was passed from below in order to maintain a stable interface with water, thus avoiding the triggering of gravity induced instability phenomena, such as fingering (Mayer and Hassanizadeh, 2005).

Fig. 4.3. Illustrations of the Hg^0–Water $P_c(S)$ experiments (MS1 and MS2 from left to right).

In the Hg^0-Air-Water experiments, the top of the column was connected to an empty burette, in contact with air. These three-phase retention curves were determined after having obtained, for each sample, the drainage branch of the retention curve for the Air-Water system. Hence, the sample structure (porosity and intrinsic permeability) was the same between the two couples of experiments. Within each sample, the air phase was continuous, thus giving the possibility to determine whether Hg^0 was able to infiltrate into a partially water saturated porous medium or not, and, in particular, to evaluate the head required to overcome the resistance exerted by the presence of air within the pores.

The drainage branch of the retention curves was explored by subjecting the columns to stepwise increments in capillary pressure. In the Air-Water experiments, this was achieved by gradually lowering the water filled burette, whereas, in the other experiments, by

gradually elevating the NAPL filled burette. At each step, the levels in the burettes were allowed to equilibrate until no further changes were observed. At each step, the water saturation was calculated based on the initial water volume in the sample and the volume increments in the water filled burette. Only in the Hg^0-Air-Water experiments, the Hg^0 saturation was calculated at each step based on the volume decrements in the Hg^0 filled burette. In the Air-Water experiments, the stepwise procedure was continued until the water in the bottom tube became disconnected due to the presence of air, symptom that the air phase became continuous within the sample. In the other experiments, the procedure was continued until the breakthrough of NAPL from the top of the columns.

The experimental determinations were fitted by means of SWRC fit (Seki, 2007), adopting van Genuchten-Mualem model (Mualem, 1976; van Genuchten, 1980):

$$S = S_{w,ir} + \left(1 - S_{w,ir}\right) \cdot \bar{S} \tag{4.1}$$

$$\bar{S} = [1 + (\alpha h_c)^n]^{-m} \tag{4.2}$$

where S is the wetting phase saturation, $S_{w,ir}$ is the irreducible water saturation, $\bar{S}$ is the effective wetting phase saturation, h_c is the capillary head between nonwetting and wetting phases, α, n and m are the van Genuchten model parameters, with m equal to 1-1/n (n > 1). The parameters taken into account in the fitting procedure were α and n, whereas the irreducible water saturation was assumed to be zero due to the lack of measured data in the last branch of the $P_c(S)$ curves. The nonwetting phase entry head was derived as the intersection of two straight lines (Sillers et al., 2001; Pasha et al. 2015): the first line, horizontal and asymptotic to the $P_c(S)$ data at zero capillary head, is representative of the zone prior to the nonwetting phase infiltration, while the second line, tangent to the inflection point and obtained by fitting the central branch of the $P_c(S)$ data, is representative of the zone when the nonwetting phase becomes connected within the pores.

4.2 Results

4.2.1 Hydraulic Conductivity Measurements

Results showed that the intrinsic permeability (Tab. 4.3) of the glass beads decreased with decreasing particle size, with small variation in porosity. An analogous behaviour is found

between the two sand types. For the medium sands, both porosity and intrinsic permeability of MS1 were slightly lower than MS2.

Tab. 4.3. Determined porosity and intrinsic permeability of the porous media used.

Porous Medium	ϕ	k_{mean} ($10^{-7}cm^2$)	$k_{st.dev}$ ($10^{-7}cm^2$)
Coarse Glass Beads*	0.410	45.15	0.30
Medium Glass Beads*	0.440	9.43	0.14
Fine Glass Beads*	0.440	1.91	0.07
Medium Sand 1	0.368	1.61	0.06
Medium Sand 2	0.391	1.79	0.01

*Sweijen (2013).

4.2.2 Capillary Pressure-Saturation Curves

Detailed $P_c(S)$ curves were obtained for Hg^0-Water in the three types of glass beads (Fig. 4.4), and for MS1 and MS2 for Air-Water (Figs. 4.5 and 4.6), PCE-Water (Fig. 4.7), Hg^0-Water (Fig. 4.8), and Hg^0-Air-Water (Figs. 4.9 and 4.10).

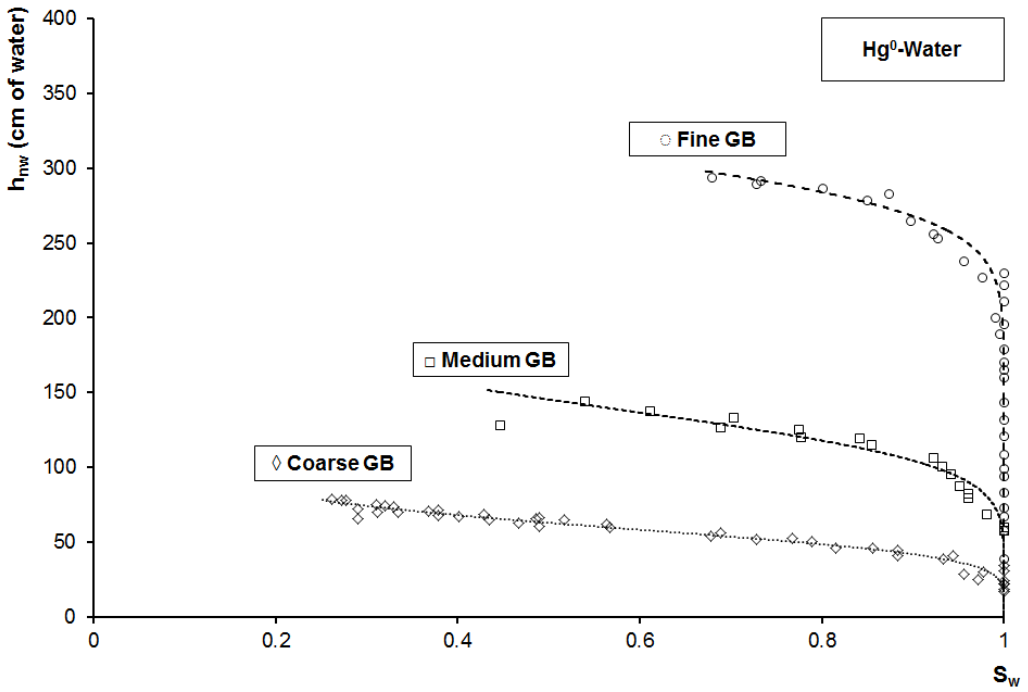

Fig. 4.4. Observed (symbols) and fitted (dashed lines) Hg^0–Water $P_c(S)$ curves (Glass Beads).

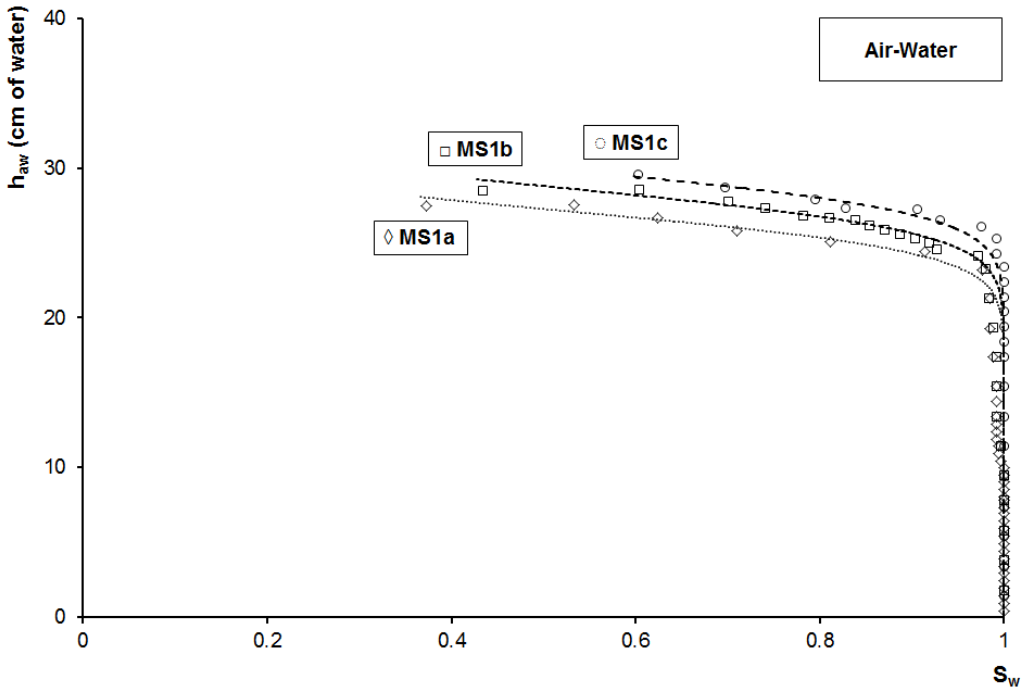

Fig. 4.5. Observed (symbols) and fitted (dashed lines) Air–Water $P_c(S)$ curves (MS1).

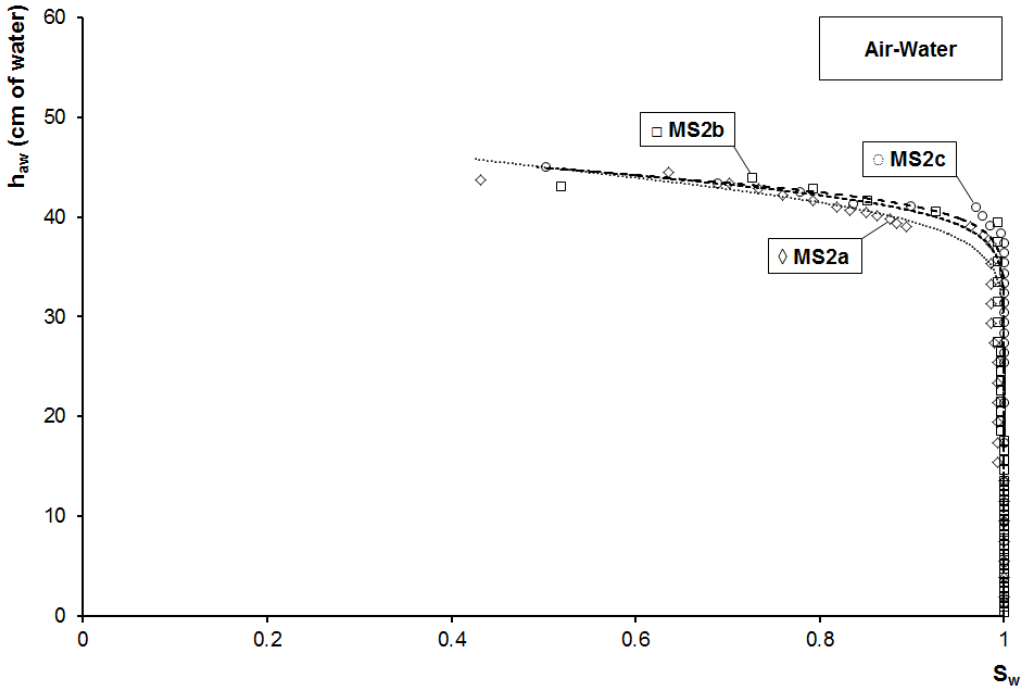

Fig. 4.6. Observed (symbols) and fitted (dashed lines) Air–Water $P_c(S)$ curves (MS2).

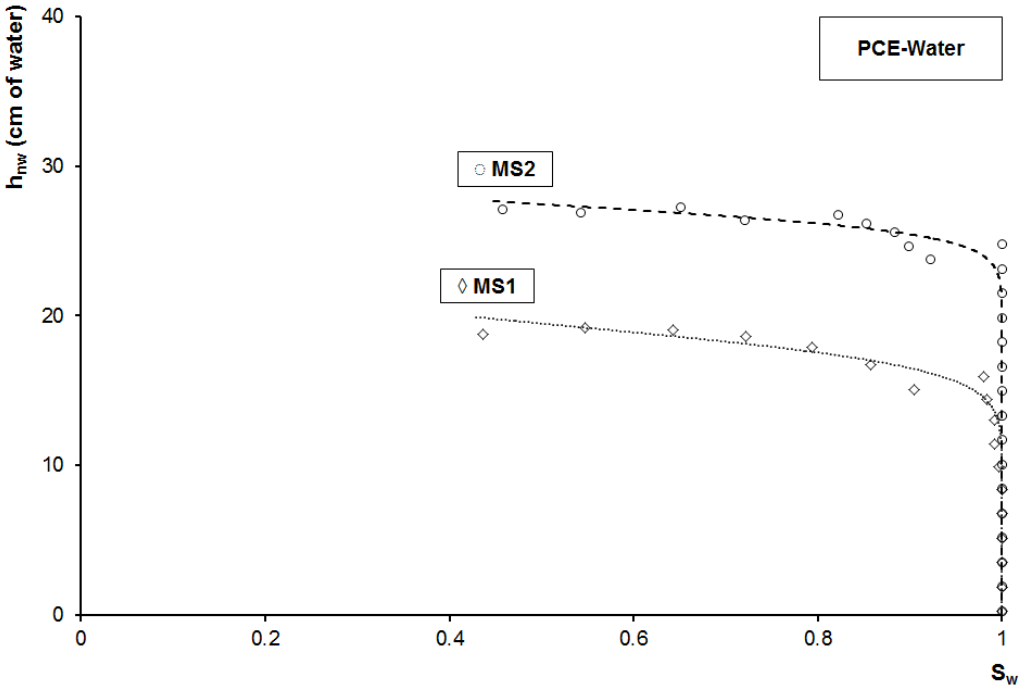

Fig. 4.7. Observed (symbols) and fitted (dashed lines) PCE–Water $P_c(S)$ curves (MS1 and MS2).

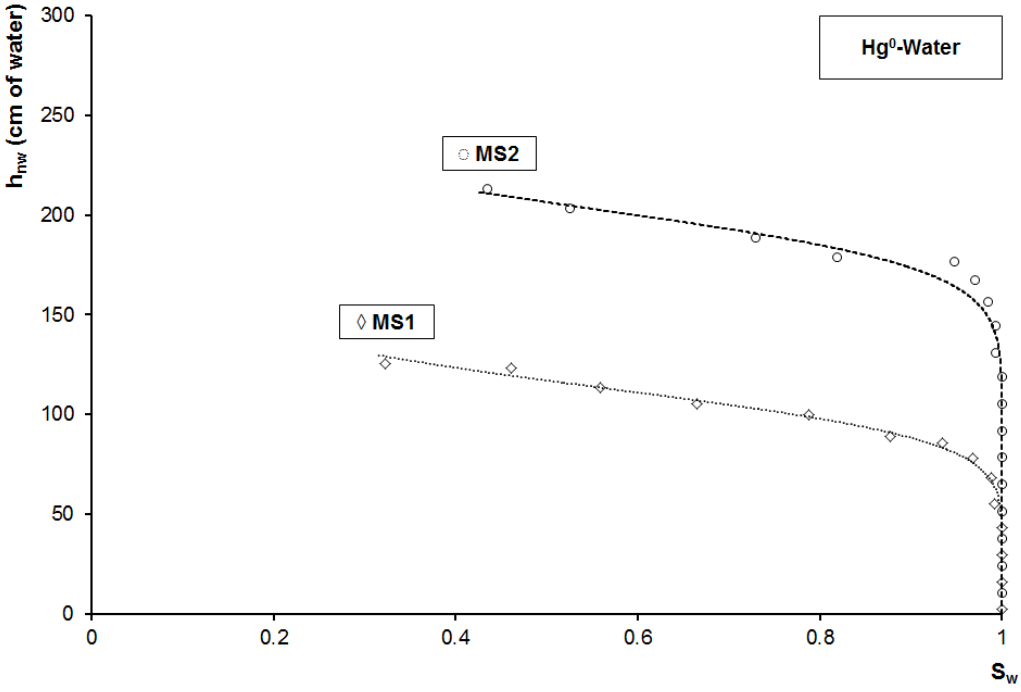

Fig. 4.8. Observed (symbols) and fitted (dashed lines) Hg^0–Water $P_c(S)$ curves (MS1 and MS2).

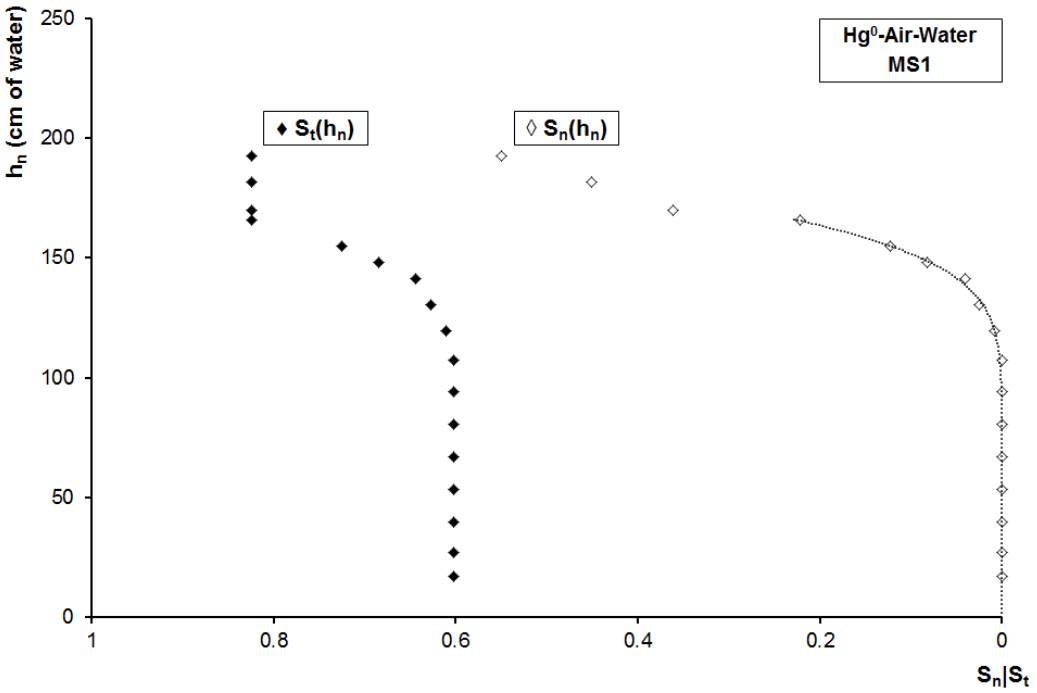

Fig. 4.9. Observed (symbols) and fitted (dashed line) Hg^0–Air–Water $P_c(S)$ curves (MS1).

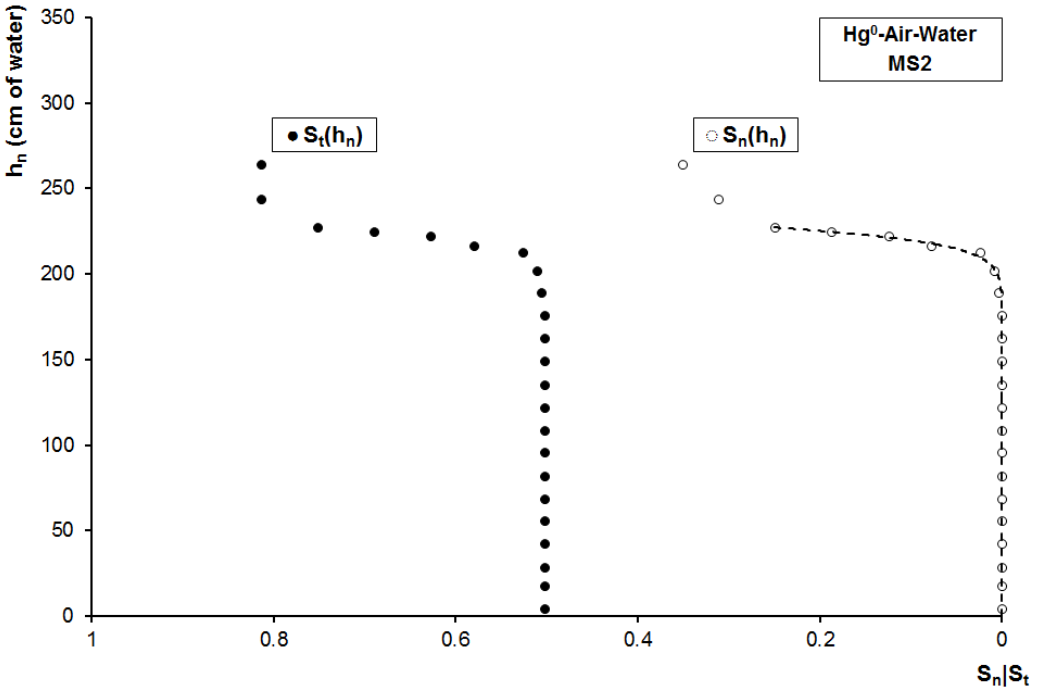

Fig. 4.10. Observed (symbols) and fitted (dashed line) Hg^0–Air–Water $P_c(S)$ curves (MS2).

In Figs. 4.9 and 4.10, the Hg^0 head (h_n) is plotted versus the nonwetting Hg^0 saturation (S_n) and the total liquid saturation (S_t) for MS1 and MS2, respectively. In contrast with other DNAPLs, elemental mercury had to overcome an entry head to infiltrate and migrate into the partially water saturated samples. As elemental mercury infiltrated, S_n increased, and, at a certain point, the rise in the Hg^0 head no longer induced any increase in the total liquid saturation. At this point, the infiltration of mercury resulted in the expulsion of an equal volume of water from the top of the sand column, and in the entrapment of discontinuous air of about the 20% of the pore volume.

On the basis of the experimental observations previously shown, in partially water saturated porous media, the Hg^0 infiltration is also affected by the presence of water in the pores. Once mercury overcomes the resistance exerted by continuous air and infiltrates within the sample, it also displaces water. Prior to Hg^0 infiltration, the air phase is expected to be present in higher saturations in bigger pores, hence, as elemental mercury infiltrates, it is likely to find a preferential pathway through smaller pores, mostly filled with water. Even though the pores are smaller, elemental mercury displaces the water phase easier than air due to the lower interfacial tension with water (Tab. 4.2). To further enforce this, the comparison of the entry heads required by mercury to infiltrate in fully and partially water saturated sands (Tab. 4.4) clearly shows that Hg^0 entry heads considerably increase in presence of air. As mercury infiltration continues, the air phase becomes discontinuous and entrapped within both liquid phases, and most of the elemental mercury comes in contact with water. At this point, a further infiltration of mercury induces the displacement of an equal amount of water, as shown in the last branch of the $P_c(S_t)$ curves in Figs. 4.9 and 4.10, until the breakthrough of Hg^0 in the outflow port of the column. These experimental evidences confirm that the conventional wettability hierarchy, in which the NAPL has an intermediate wetting state between the air and the water phases, is not valid for liquid elemental mercury. Therefore, a new formulation for the constitutive relations governing elemental mercury flow behaviour in variably water saturated porous media is required.

The results obtained from the $P_c(S)$ experiments for each two- and three phase system are summarized in Tab. 4.4.

Tab. 4.4. $P_c(S)$ Experiments - Results.

Sample	System	ϕ	$S_{w,0}$	α (cm^{-1})	n	h_e (cm of water)	h_e (cm of NAPL)
Coarse GB*	Hg^0-Water	0.410#	1	0.0167	5.58	38.40	2.84
Medium GB*	Hg^0-Water	0.440#	1	0.0071	6.83	113.03	8.36
Fine GB*	Hg^0-Water	0.440#	1	0.0032	14.04	262.71	19.42
MS1a	Air-Water	0.365	1	0.0368	19.17	24.02	-
MS1b	Air-Water	0.363	1	0.0349	19.04	25.13	-
MS1c	Air-Water	0.359	1	0.0334	19.95	26.10	-
MS2a	Air-Water	0.385	1	0.0223	17.17	39.58	-
MS2b	Air-Water	0.383	1	0.0223	21.58	40.04	-
MS2c	Air-Water	0.373	1	0.0223	24.95	40.32	-
MS1d	PCE-Water	0.353	1	0.0517	13.41	16.17	9.90
MS2d	PCE-Water	0.375	1	0.0365	28.99	25.75	15.77
MS1e	Hg^0-Water	0.354	1	0.0087	7.97	83.69	6.19
MS2e	Hg^0-Water	0.375	1	0.0049	12.83	169.19	12.51
MS1c_bis	Hg^0-Air-Water	0.359	0.602	0.0054	10.85	141.33	10.45
MS2c_bis	Hg^0-Air-Water	0.373	0.502	0.0043	32.62	212.90	15.74

*GB - Glass Beads; #Sweijen (2013).

In Tab. 4.4, $S_{w,0}$ is the initial water saturation of the porous sample, while h_e denotes the entry head required by the nonwetting phase to infiltrate into the granular porous medium.

4.3 Discussion

Based on the results, the infiltration behaviour of Hg^0 in granular porous media is analysed and discussed. First, the results of the two- and three-phase $P_c(S)$ experiments are discussed in relation to the samples intrinsic permeability and porosity to assess the role played by porous media characteristics on Hg^0 infiltration behaviour. Then, the infiltration behaviour of elemental mercury in water saturated systems is compared with that of PCE, aiming to verify the applicability of the traditional scaling theory. The Hg^0 infiltration behaviour and the scaling of its retention properties in variably water saturated systems are finally addressed.

4.3.1 Hg^0 Infiltration Behaviour and Porous Media Characteristics

Pore structure is a key aspect that affects the infiltration behaviour of elemental mercury, as illustrated by the correlation of entry head with intrinsic permeability (Fig. 4.11) found

in the two-phase glass beads systems analysed. A power law results in the best fit of the data, thus showing a general tendency of the entry head to be higher in samples with lower intrinsic permeability, but not necessarily with lower porosity (Tabs. 4.3 and 4.4). Although intrinsic permeability is a bulk parameter affected by the combined inner pore structure characteristics of a porous medium, it related with the more locally expressed entry head for the glass beads samples. However, within the small range in intrinsic permeability of the medium sand samples used, the correlation did not hold. Despite the somewhat (11%) higher intrinsic permeability of MS2 (Tab. 4.3), the entry head is higher than for MS1 (Fig. 4.12). Likely, this is the result of the smaller particle size and narrow range in MS2 than MS1 (Fig. 4.1), which limit the potential for locally present larger pores.

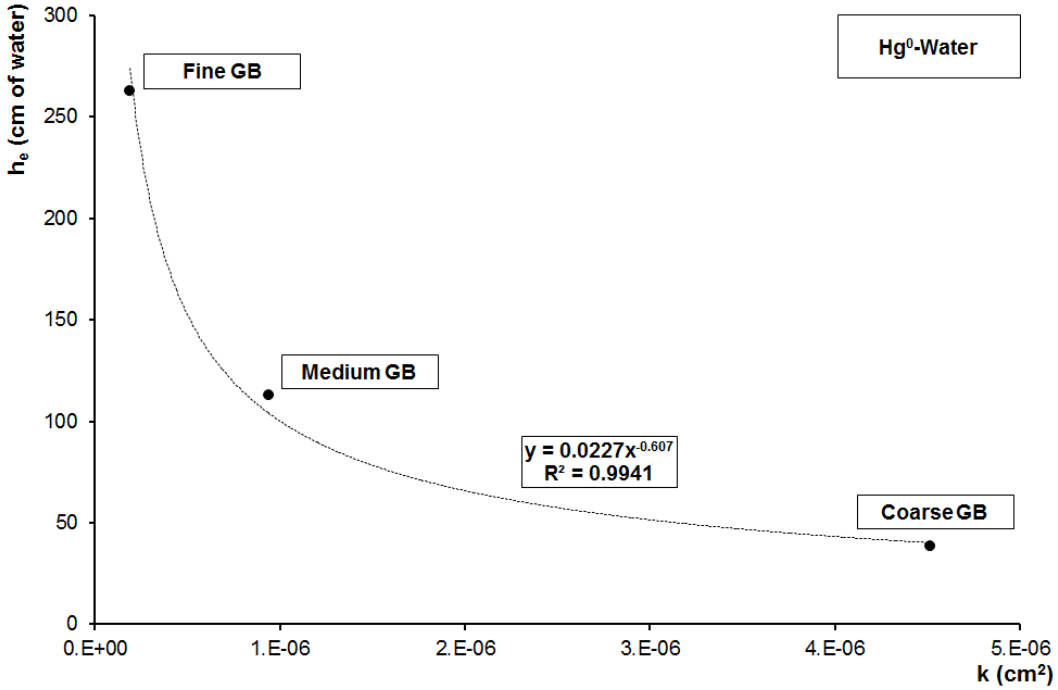

Fig. 4.11. Nonwetting phase entry head (h_e) versus intrinsic permeability (k) in glass beads (Hg^0-Water).

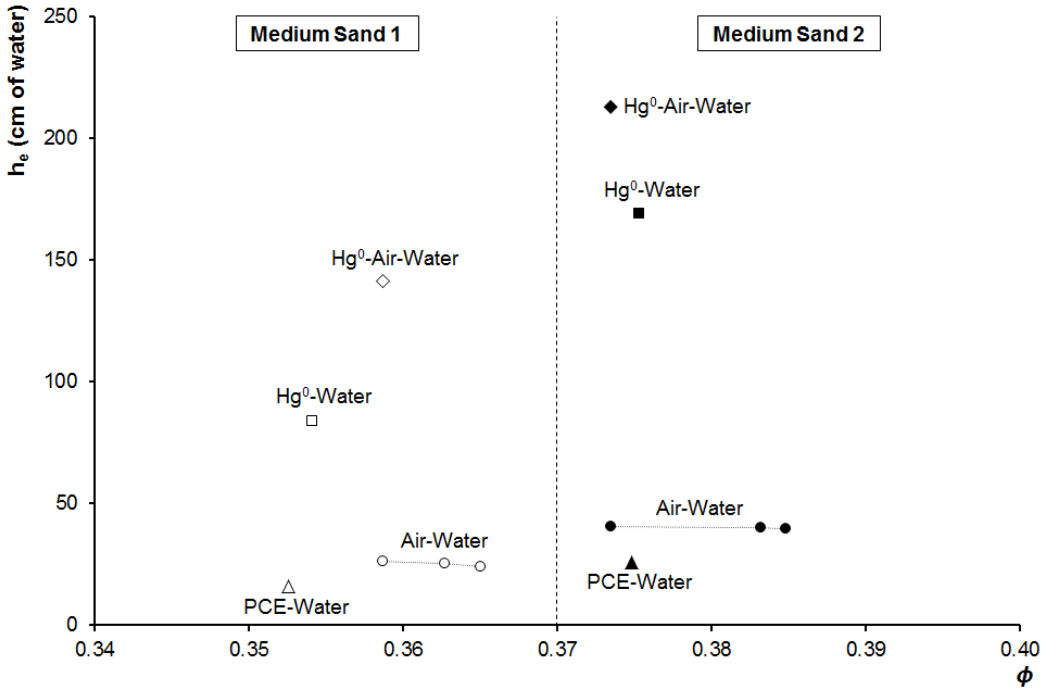

Fig. 4.12. Nonwetting phase entry head (h_e) versus porosity (ϕ) in MS1 and MS2 (all fluid systems).

4.3.2 Leverett Scaling in PCE-Water and Hg^0-Water Systems

As the fluid properties of PCE and elemental mercury strongly differ (Tab. 4.2), their infiltration behaviour is expected to differ as well. As for each sand type the couples of samples studied have practically the same porosity (Fig. 4.12; Tab. 4.4), this allows the evaluation of the use of Leverett scaling (Leverett, 1941) between the two-phase systems analysed. The α parameter, typically used for scaling purposes in numerical modelling (Parker et al., 1987), for elemental mercury is lower than for PCE (Tab. 4.4) and, conversely, the entry heads are higher if expressed in terms of water head. However, in terms of the respective DNAPL heads, PCE requires to overcome an entry head of about 60% higher than Hg^0 for MS1, while of about 26% for MS2. This is considerably more than when assuming Leverett scaling to be applicable (Devasena and Nambi, 2010). Under the hypothesis of no flow, hydrostatic pressure distribution, and assuming the pore structure to be identical for the two systems, the relation between Hg^0 and PCE entry heads can be defined as follows:

$$h_e^{Hg} = h_e^{PCE} \cdot \left(\rho_{PCE}/\rho_{Hg}\right) \cdot \left(\sigma_{Hg\text{-}W}/\sigma_{PCE\text{-}W}\right) \tag{4.3}$$

where ρ denotes the fluid density and σ the fluid pair interfacial tension.

Using the fluids properties reported in Tab. 4.2, Eq. 4.3 yields that $h_e^{Hg} = 0.947 \cdot h_e^{PCE}$, hence, according to Leverett scaling, PCE should require to overcome an entry head of about 5.6% higher than Hg^0 to infiltrate in the same porous medium. Although Leverett scaling is able to reproduce the natural tendency of Hg^0 to be more prone than PCE to infiltrate in water saturated porous media, it considerably underestimates Hg^0 infiltration capacity in comparison with the experimental results.

4.3.3 Experimental Scaling Parameters for PCE-Water and Hg^0-Water Systems

In Fig. 4.13, the observed PCE-Water scaling parameters (β_{nw}), defined as the ratio (α_{nw}/α_{aw}) between the DNAPL-Water and the three Air-Water α parameters (Lenhard and Parker, 1987), are plotted versus the samples porosity ratio (ϕ_{nw}/ϕ_{aw}), the ratio between the DNAPL-Water and the three Air-Water samples porosity, for MS1 and MS2, respectively.

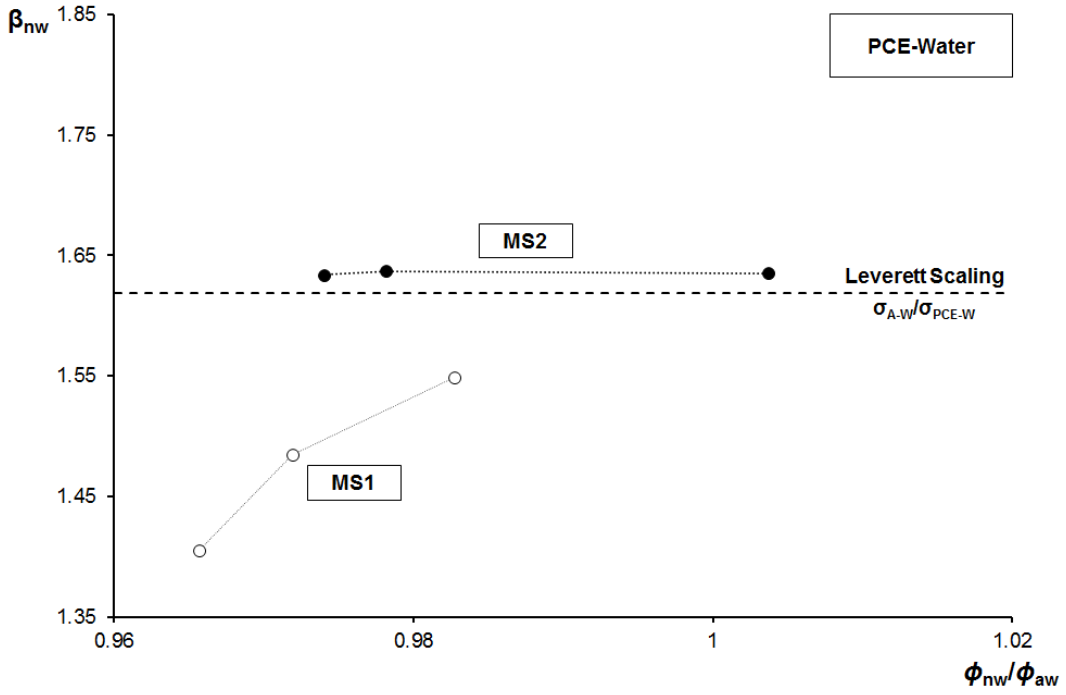

Fig. 4.13. Experimental PCE-Water scaling parameters (β_{nw}) versus samples porosity ratio (ϕ_{nw}/ϕ_{aw}).

To verify the ability of the scaling theory to cope with PCE behaviour, the Leverett scaling parameter, given as the ratio between the water surface tension ($\sigma_{A\text{-}W}$) and the DNAPL interfacial tension with water ($\sigma_{PCE\text{-}W}$), Tab. 4.2, (Lenhard and Parker, 1987), calculated

taking into account the non-spreading behaviour of PCE (White et al., 2004), is also plotted.

For MS1, the observed scaling parameters get closer to the value based on the fluids properties (1.618), with underestimations ranging from 15% to 4.5% as the porosity ratio approaches unity, and the pore structure likely becomes more similar between the couples of samples analysed. For MS2, instead, the agreement between the experimental determinations and the Leverett scaled value is definitely good, with only a slight overestimation of about 1%. These results show that the scaling procedure is applicable for the two-phase PCE-Water system, congruently with the experimental evidence found in sands for other NAPLs, like benzene, p-cymene, o-xylene, and benzyl alcohol (Lenhard and Parker, 1987), Soltrol 170®, toluene, and TCE (Busby et al., 1995). In particular, for these studies, the reported deviations between Leverett and experimental scaling parameters are 12%, 5.2%, 5.8%, 5%, 1.8%, 15%, and 5%, respectively.

The agreement found for PCE between Leverett and experimental scaling parameters was less for elemental mercury (Fig. 4.14).

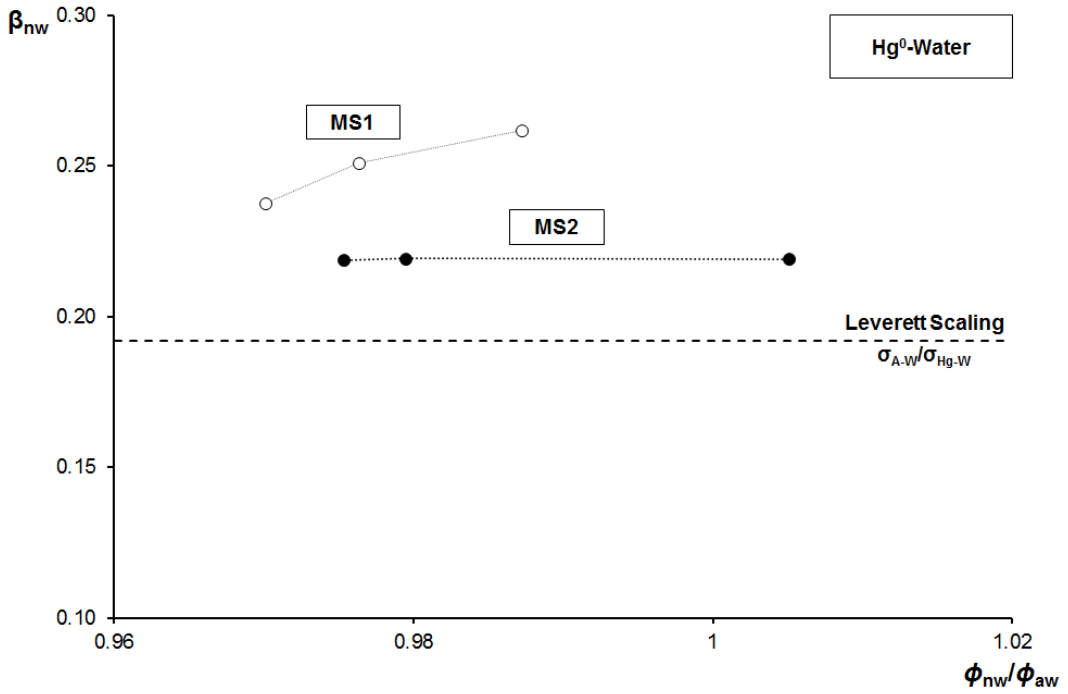

Fig. 4.14. Experimental Hg^0-Water scaling parameters (β_{nw}) versus samples porosity ratio (ϕ_{nw}/ϕ_{aw}).

For MS2, the differences between the experimentally determined values are negligible, and the deviation from the value based on the fluids properties (0.192), given as the ratio between the water surface tension and the Hg^0 interfacial tension with water ($\sigma_{Hg\text{-}W}$), Tab. 4.2, remains practically constant. Even when the porosity ratio slightly deviates from unity, the scaling parameter underestimates by 14%, similar to the largest deviations observed in literature for other NAPLs. In MS1, the agreement with the Leverett scaled value does not improve as the porosity ratio approaches unity but rather worsens, with overestimations ranging from 23.8% to 36.4%.

4.3.4 Hg^0 Infiltration in Variably Water Saturated Systems

Based on the required DNAPL heads, the capacity of Hg^0 to infiltrate in partially water saturated porous media is lower than PCE and Hg^0 in fully water saturated systems (Fig. 4.12; Tab. 4.4). The elemental mercury entry head in a partially water saturated system was 5.6% higher than for PCE in fully water saturated conditions for MS1, while it was practically the same of PCE for MS2. For the partially water saturated MS1 sample, Hg^0 required to overcome an entry head 68.9% higher than required in the fully water saturated counterpart. Also for MS2, the entry head in the partially water saturated system was higher than for the fully water saturated counterpart, by 25.8%.

The mercury entry heads were determined at residual water saturations, and it could be expected that entry heads would increase further at lower partial water contents. Therefore, assuming Leverett scaling to be applicable (sec. 4.3.2), the Hg^0 entry head at zero water saturation (namely 100% air saturation) was estimated, for both sands, based on the measured Hg^0 and PCE entry heads in water saturated media (Tab. 4.4). By substituting the elemental mercury surface tension (Tab. 4.2) in lieu of its interfacial tension with water in Eq. 4.3, and assuming the Hg^0-Water and PCE-Water systems to be the two respective references for the scaling of the Hg^0-Air retention properties, two different estimates of the Hg^0 entry head values can be derived at zero water saturation for both sands. This results in two estimated entry head values of fictitious completely dry MS1 and MS2 samples.

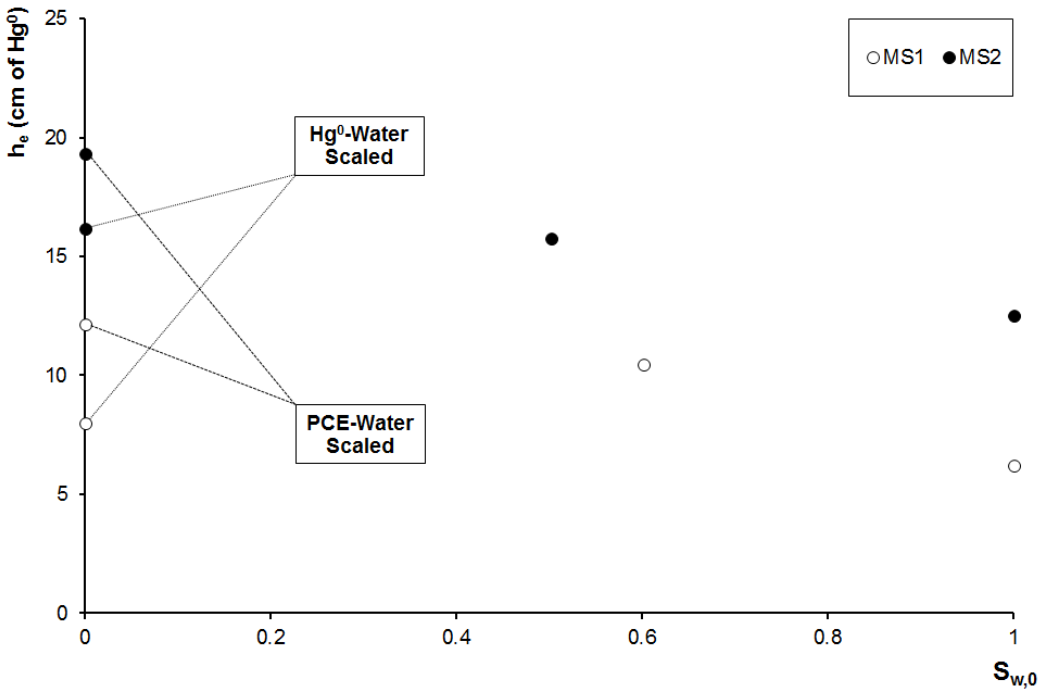

Fig. 4.15. Hg^0 entry head (h_e) versus initial water saturation ($S_{w,0}$) for MS1 and MS2 (measured and scaled values).

The Leverett scaled PCE-Water values of the Hg^0 entry head at zero water saturation (Fig. 4.15) are 16.1% and 22.7% higher than the experimental observations for the partially water saturated samples, for MS1 and MS2, respectively. For the Hg^0-Water scaled values (Fig. 4.15), only the scaled entry head in MS2 is higher, 2.8%, than for the partially water saturated sample. Conversely, for MS1 the scaled value of the Hg^0 entry head at zero water saturation is 23.4% lower. Nevertheless, in both cases, the scaled values are higher than the measured Hg^0 entry heads for the water saturated conditions, 29.3% for the Hg^0-Water scaled values, and 96% and 54.4% for the PCE-Water scaled values, for MS1 and MS2, respectively. How entry head develops in more detail with decreasing water content remains to be explored. However, considering the spread in the scaled estimates for the entry head at zero water saturation, the entry head in the partially water saturated (residual) conditions is possibly already controlled by the larger, air filled, pores.

4.3.5 Experimental Scaling Parameters for Hg^0-Air-Water Systems

In Tab. 4.5, the observed Hg^0-Air-Water scaling parameter (β_{naw}), defined as the ratio (α_{naw}/α_{aw}) between the Hg^0-Air-Water and the Air-Water α parameter, is reported together

with the Leverett scaled value (0.148), given as the ratio ($\sigma_{A\text{-}W}/\sigma_{Hg\text{-}A}$) between the water and the DNAPL surface tensions, Tab. 4.2, (Lenhard and Parker, 1987), for MS1 and MS2, respectively. In particular, the scaling procedure is limited to the experimental set of MS1c-MS1c_bis and MS2c-MS2c_bis because the respective Air-Water and Hg^0-Air-Water $P_c(S)$ curves were determined on the same porous sample (sec. 4.1.4), and thus on identical pore structure, ideal for an accurate and reliable scaling.

Tab. 4.5. Hg^0-Air-Water Scaling Parameter (β_{naw}).

Sample	Leverett ($\sigma_{A\text{-}W}/\sigma_{Hg\text{-}A}$)	Experimental (α_{naw}/α_{aw})
MS1c_bis	0.148	0.163
MS2c_bis	0.148	0.191

As for the Hg^0-Water system (sec. 4.3.3), there is a poor agreement between experimental and Leverett determinations for the Hg^0-Air-Water system. Even though the pore structure is exactly the same, the experimentally derived scaling parameter is 9.6% higher than the scaled value for MS1, and 28.6% higher for MS2.

The deviations found in both two- and three-phase systems may suggest that the classical scaling theory is less able to cope with Hg^0 retention properties than for other NAPLs. Still, the order of magnitude of the experimental scaling parameters is similar to that of the determinations based solely on the fluids properties, thus not excluding its application to elemental mercury DNAPL. Among the reasons for the observed discrepancies is probably that, if the porous medium is partially water saturated to a degree that allows air to be continuous within the pores, the Hg^0 that tries to infiltrate is expected to be predominantly in contact with air. However, as the sample is water wet, it is also in contact with water, hence the Leverett scaling parameter, defined as the ratio of water and Hg^0 surface tensions, may not be accurate, and the effect induced by the Hg^0 interfacial tension with water could be relevant. Furthermore, once infiltration occurs in a partially water saturated porous medium, elemental mercury displaces both air and water (sec. 4.2.2), depending on the initial water distribution within the pores, thus further enhancing the difficulty to cope with its particular behaviour.

References

Busby RD, Lenhard RJ, Rolston DE (1995). *An Investigation of Saturation-Capillary Pressure Relations in Two-and Three-Fluid Systems for Several NAPLS in Different Porous Media*. Ground Water, 33(4), 570-578.

CRC (2014). *Handbook of Chemistry and Physics*. 94th ed. (Internet Version 2014).

Devasena M, Nambi IM (2010). *Migration and entrapment of mercury in porous media*. Journal of Contaminant Hydrology, 117, 60–70.

FILCOM (2015). *Technical Datasheet Filtersand 0.2-0.5 mm and Silversand S60*.

Glaswarenfabrik Karl Hecht (2013). *Technical Datasheet 1 mm Glass Beads.*

Imhoff PT, Gleyzer SN, McBride JF, Vancho LA, Okuda I, Miller CT (1995). *Cosolvent-Enhanced Remediation of Residual Dense Nonaqueous Phase Liquids: Experimental Investigation*. Environmental Science & Technology, 29(8), 1966-1976.

Lenhard RJ, Parker JC (1987). *Measurement and prediction of saturation-pressure relationships in three-phase porous media systems*. Journal of Contaminant Hydrology, 1, 407–424.

Leverett M (1941). *Capillary behavior in porous solids*. Transactions of the AIME, 142(01), 152-169.

Mayer A, Hassanizadeh SM (2005). *Soil and Groundwater Contamination: Nonaqueous Phase Liquids, Principles and Observations*. American Geophysical Union.

Mualem Y (1976). *A new model for predicting the hydraulic conductivity of unsaturated porous media*. Water Resources Research, 12(3), 513-522.

Parker JC, Lenhard RJ, Kuppusamy T (1987). *A parametric model for constitutive properties governing multiphase flow in porous media*. Water Resources Research, 23(4), 618-624.

Pasha AY, Khoshghalb A, Khalili N (2015). *Pitfalls in interpretation of gravimetric water content-based soil-water characteristic curve for deformable porous media*. International Journal of Geomechanics, 16(6), D4015004.

Retsch (2013). *Technical Datasheet 0.10-0.25 mm and 0.20-0.50 mm Glass Beads*.

Schwille F (1988). *Dense Chlorinated Solvents in Porous and Fractured Media - Model Experiments*. Lewis Publishers, Chelsea, MI.

Seki K (2007). *SWRC fit - a nonlinear fitting program with a water retention curve for soils having unimodal and bimodal pore structure*. Hydrology and Earth System Sciences Discussions, 4, 407-437.

Sillers WS, Fredlund DG, Zakerzadeh N (2001). *Mathematical attributes of some soil-water characteristic curve models*. In Unsaturated soil concepts and their application in geotechnical practice (pp. 243-283). Springer Netherlands.

Sweijen T (2013). *Experiments on the physical behaviour of elemental mercury in saturated porous media*. Universiteit Utrecht, The Netherlands.

US DOE (2001). *Mercury Contaminated Material Decontamination Methods: Investigation and Assessment*. DE-FG21-95EW55094.

van Genuchten MT (1980). *A closed form equation for predicting the hydraulic conductivity of unsaturated soils*. Soil Science Society of American Journal, 44, 892–898.

Wentworth CK (1922). *A scale of grade and class terms for clastic sediments*. The Journal of Geology, 30(5), 377-392.

White MD, Oostrom M, Lenhard RJ (2004). *A Practical Model for Mobile, Residual, and Entrapped NAPL in Water-Wet Porous Media*. Ground Water, 42(5), 734-746.

Notation

Greek Symbols

α	van Genuchten model parameter
α_{naw}/α_{aw}	ratio between Hg^0-Air-Water and Air-Water α parameters
α_{nw}/α_{aw}	ratio between DNAPL-Water and Air-Water α parameters
β_{naw}	Hg^0-Air-Water system scaling parameter
β_{nw}	DNAPL-Water system scaling parameter
ρ_{Hg}	elemental mercury density
ρ_{PCE}	tetrachloroethylene density
ρ_s	particle density
$\sigma_{A\text{-}W}$	water surface tension
$\sigma_{Hg\text{-}A}$	elemental mercury surface tension
$\sigma_{Hg\text{-}W}$	interfacial tension between elemental mercury and water
$\sigma_{PCE\text{-}W}$	interfacial tension between tetrachloroethylene and water
ϕ	porosity
ϕ_{nw}/ϕ_{aw}	ratio between DNAPL-Water and Air-Water samples porosity

Latin Symbols

d_{50}	median particle diameter
h_{aw}	capillary head between air and water
h_c	capillary head
h_e	nonwetting phase entry head
h_n	NAPL head
h_{nw}	capillary head between NAPL and water
k_{mean}	intrinsic permeability, arithmetic mean value
$k_{st.dev}$	intrinsic permeability, standard deviation value
n	van Genuchten model parameter

P_c	capillary pressure
S	wetting phase saturation
$\overline{S}$	effective wetting phase saturation
S_n	NAPL saturation
S_t	total liquid saturation
S_w	water saturation
$S_{w,ir}$	irreducible water saturation
$S_{w,0}$	initial water saturation

Chapter 5

Infiltration and Distribution of Hg^0 DNAPL in Water Saturated Porous Media

Within this chapter, the infiltration and distribution behaviour of Hg^0 DNAPL in water saturated stratified granular porous media is analysed and compared to that of PCE by means of two-dimensional flow container experiments. To allow a quantitative comparison of the flow behaviours of the two DNAPLs, non-intrusive measurements of porosity fields and DNAPLs saturation profiles were performed with the dual gamma ray system (Chapter 3). These results are then discussed together with the experimental results found for Hg^0 DNAPL in a stratified glass beads system. Finally, to assess to what extent numerical modelling can predict elemental mercury migration in water saturated porous media, a selected flow container experiment was simulated using GDAn (Chapter 2).

5.1 Materials and Methods

5.1.1 Porous Media and Fluids

Porous media and fluids used within the current study are reported in Chapter 4 (secs. 4.1.1 and 4.1.2) together with their respective properties. Briefly, two medium sands, namely MS1 (d_{50} = 0.39 mm) and MS2 (d_{50} = 0.26 mm), and two types of glass beads, namely coarse (d_{50} = 1 mm) and medium (d_{50} = 0.375 mm), were used as porous media, while demineralized water, tetrachloroethylene (PCE), and liquid elemental mercury (Hg^0) were

used as fluids. Information regarding intrinsic permeability and $P_c(S)$ curves are reported in sec. 4.2.

5.1.2 Flow Container Experiments with Sands

A detailed illustration of the flow container used for the sands experiments is shown in Fig. 5.1.

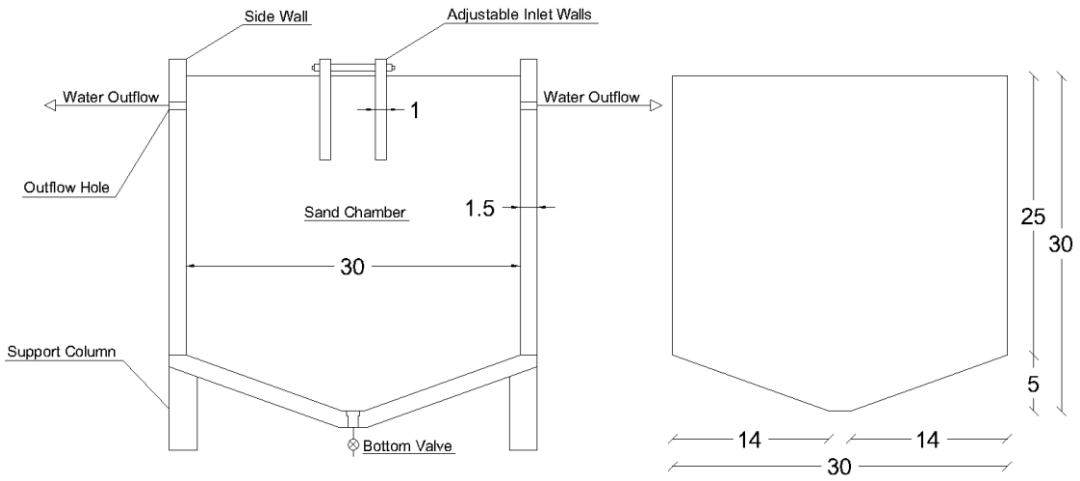

Fig. 5.1. Flow container details (left) and inner dimensions (right) reported in cm.

The core of the setup was the sand chamber, which hosted the porous sample. The main part had a rectangular shape, while the lowest part presented an inclined bottom to facilitate DNAPLs flow towards the bottom valve. The container consisted of two front walls and two side walls, made of PMMA (Poly-Methyl Methacrylate). The walls thickness was specifically designed and set to 1.5 cm to prevent deformations induced by the thrusts exerted by both water and sand. Due to the preferential wettability of PCE to PMMA, the two front walls were layered with a glass plate of 0.5 cm, thus resulting in an inner thickness of the sand chamber of 3.95 cm. Conversely, the two side walls, sufficiently far from the DNAPL source, were not expected to come in contact with PCE and were not covered with glass. For the same reason of the front walls, the two PMMA inlet walls, of 1 cm thickness each, were layered with a glass plate of 1 mm. The main aim of these walls was to create an undisturbed location for the DNAPLs reservoir. To avoid relative displacements between the two screens and to fix them at the desired distance, the inlet walls were hooked on the front walls of the container and were equipped with a series

of adjustable screws. To maintain a prescribed water table over the sand sample, the two side walls had an outflow to remove any excess water. The flow container was covered on top with a PMMA cap of rectangular shape, provided with a ventilation hole to maintain the air phase within the container at atmospheric pressure.

The flow container was mainly filled with the medium sand 1 (MS1) and, to study the effects of macro heterogeneities on PCE and Hg^0 migration, a rectangular lens of 10 cm length by 5 cm height of medium sand 2 (MS2) was located in the middle of the container, at 9 cm from the bottom (Fig. 5.2). The water table was fixed at 1 cm from the top layer of MS1, located at 25 cm from the bottom. The two inlet walls were placed 2.5 cm deep from the top of the MS1 layer, in the middle of the container, with a spacing of 1.5 cm between each other. For each experiment, a fixed amount of DNAPL was carefully added between the inlet walls, thus allowing the DNAPL to build enough head to infiltrate and migrate in the porous sample. During the whole infiltration process, the DNAPL head was tracked using a camera to determine the DNAPL infiltration rate over time.

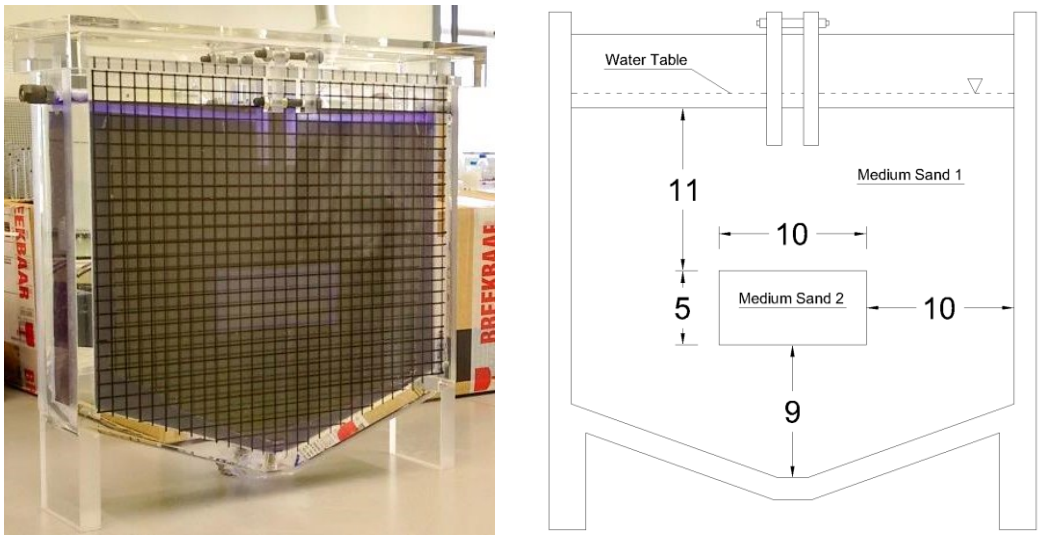

Fig. 5.2. Illustration (left) and schematic representation (right) of a flow container sample (dimensions in cm).

The sand in the container was packed under water saturated conditions to avoid any entrapped air between the sand particles. The flow container was initially filled halfway with water and then, after having thoroughly mixed the sand with water in another container, the sand was gradually poured into it. To maintain a fully water saturated

system, a water head over the top layer of the sand was kept at all times. At each filling step, each sand layer was tamped in the same manner to compact the porous medium. To prevent accumulation of sand in the bottom valve, a nylon filter was put in the bottom hole.

The packing procedure described above was the same for the PCE experiment, except that, to visualize the PCE infiltration front over time, the water was dyed. For this, a water soluble pH indicator, Bromophenol Blue (Acros Organics), was used in a concentration of 1 g/l, equal to 1/4 of bromophenol solubility in water (O'Neil, 2006). As a result, the water in the container showed a dark blue colour. To avoid any presence of bromophenol granular residuals, after several rounds of mechanical mixing, the water was filtered using a 10 μm mesh nylon filter. The choice of dying water rather than PCE was dictated by the fact that oil soluble dyes like Sudan III, Sudan IV, and Oil Red, generally used to dye PCE (Schwille, 1988; Hofstee et al., 1998a; Hofstee et al., 1998b), proved to influence PCE interfacial properties (Tuck et al., 2003), reducing its entry pressure and affecting its spreading behaviour, thus enhancing its mobility. Moreover, in the case of Sudan IV, residuals can be left on the sediments as a result of PCE dilution (Hartog et al., 2010), thus affecting the porous medium characteristics and, potentially, PCE flow behaviour. Hence the choice to dye water with Bromophenol Blue, generally used for conservative tracer tests (Cirpka et al., 2006; Rockhold et al., 2007; Chiogna, 2010). Furthermore, as shown is sec. 3.3.1 (Chapter 3), adding bromophenol to demineralized water does not result in any appreciable change in the water phase gamma ray attenuation.

5.1.3 Porosity and DNAPL Saturation Measurements

The packing of the flow container samples was followed by non-intrusive measurements of the porosity field. These measurements were performed over the whole samples by means of the dual gamma ray system (Chapter 3), on the basis of a regular grid consisting of 632 points with 1 cm spacing. DNAPLs saturation profiles were measured 24 hours after the end of the infiltration process, established when there was no further change of DNAPL level in the inlet. For this set of measurements, the grid was locally refined with additional 459 points, located in between the points of the first grid, with the same spacing. Porosity and background intensity of the refinement grid were derived from interpolation of the

values measured for the first grid. Details on the working principles of the dual gamma ray system, and on the analytical derivation of porosity and of DNAPL saturation from the gamma ray measurements, are reported in Chapter 3.

5.1.4 Flow Container Experiment with Glass Beads

The experiment (Sweijen, 2013) was carried out in a water saturated stratified glass beads system, consisting of two layers of coarse glass beads with a medium glass beads layer of 6 cm height in between, located at 8 cm from the bottom of the container (Fig. 5.3).

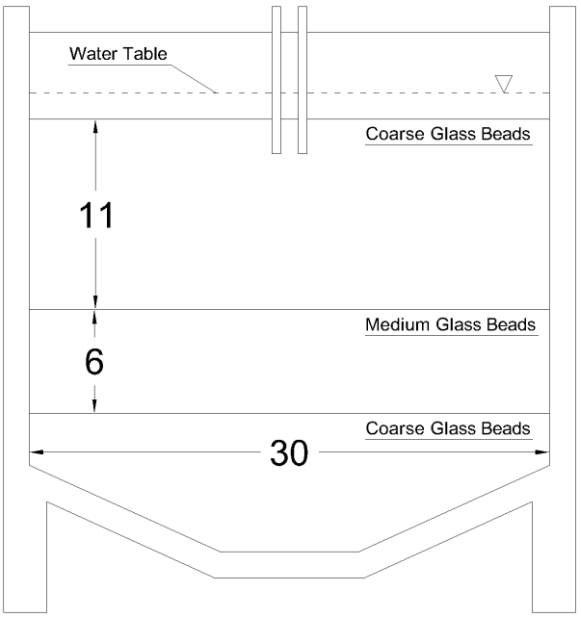

Fig. 5.3. Schematic representation of the glass beads flow container sample (dimensions in cm) used by Sweijen (2013).

The experimental procedure and the setup were slightly different from those described previously (sec. 5.1.2). In particular, glass beads were simply poured in the container, hence the porous sample was not subjected to any additional compaction besides of the one induced by its own weight. As the experiment was only carried out for elemental mercury, the flow container was not equipped with glass plates and was entirely in PMMA, thus resulting in an inner thickness of the sand chamber of 5 cm. The two inlet walls, located 2 cm deep from the top of the coarse glass beads layer, had a thickness of 0.5 cm, and the spacing between the two was of 1 cm. The horizontal part of the bottom of the container

was of 8 cm rather than of 2 cm, as described previously. The water table was fixed at 1.5 cm from the top layer of the coarse glass beads, located at 25 cm from the bottom.

5.1.5 Numerical Modelling: Hg^0 Infiltration and Distribution in Glass Beads

To assess to what extent numerical modelling can describe elemental mercury DNAPL infiltration and distribution in water saturated porous media, the glass beads flow container experiment was simulated with GDAn (Chapter 2). The input parameters of the numerical simulations were mostly taken from Tabs. 4.1-4.4. In addition to these data, the irreducible water saturation was set to 0.05, while the maximum entrapped NAPL saturation to 0.10, (Sweijen, 2013). Specific storage coefficients were determined assuming a compressibility of 4.6e-10 Pa^{-1} and of 3.7e-11 Pa^{-1} for water and Hg^0 (Young et al., 2012), respectively, of 1.4e-11 Pa^{-1} for glass beads (Luo et al., 2015), and an average porosity of 0.380, based on dual gamma ray measurements. In absence of any information regarding the air-water $P_c(S)$ measurements for glass beads, the scaling parameter β_{nw} was assumed equal to the ratio between water surface tension and Hg^0 interfacial tension with water, on the basis of Lenhard and Parker (1987) scaling theory, thus resulting in a value of 0.192. To describe the P_c-S and k_r-S relationships between elemental mercury and water, the van Genuchten-Mualem model (Mualem, 1976; van Genuchten, 1980) was used.

To describe the variability of intrinsic permeability with porosity and of capillary retention parameters with intrinsic permeability, the Kozeny-Carman formula (Kozeny, 1927; Carman, 1938, 1956; Bear, 1972; Fitts, 2002) and the Leverett function (Leverett, 1941) were applied. In this way, each cell of the numerical domain was set to different values for porosity, intrinsic permeability, and the van Genuchten α parameter. The van Genuchten n parameter was assumed constant within the same glass beads type.

With the information derived from the gamma ray measurements, the porosity field (Fig. 5.8) was deduced for the whole domain and the Kozeny-Carman formula (Eq. 5.1) was used to determine the intrinsic permeability (k) in each cell:

$$k = \frac{d_{50}^2}{SF^2} \frac{\phi^3}{(1-\phi)^2} \tag{5.1}$$

with ϕ the porosity, and SF the particles shape factor, (SF = 20.7), determined as the best fit with the data reported in Tab. 4.3. Then, the generalized form of the Leverett function

(Kueper and Frind, 1991; Dekker and Abriola, 2000) was used to determine the van Genuchten α parameter in each cell. In particular, for any pair of permeability values, the van Genuchten α parameter can be scaled as:

$$\alpha_2 = \alpha_1 \left(\frac{k_2}{k_1}\right)^{\gamma} \tag{5.2}$$

where α_1 and k_1 are the van Genuchten parameter and the intrinsic permeability of the reference samples (Tabs. 4.3 and 4.4), respectively, α_2 and k_2 are the values to be determined in each cell, while γ is a fitting parameter, equal to 0.5 for the conventional Leverett function. To verify to what extent the spatial variability of intrinsic permeability plays a significant role in the numerical prediction of Hg^0 DNAPL infiltration and distribution, the γ parameter was subjected to a sensitivity analysis, assuming the value of 0.5 of the conventional Leverett function, and the very large values of 0.75 and 0.95, thus considering three different numerical scenarios.

The spatial domain was discretized in 1273 nodes and 2413 unstructured triangular cells, suitably refined in proximity of the DNAPL reservoir and of the top part of the medium glass beads layer. Across the whole domain, the water hydraulic head was set to 26.5 cm, and the boundary nodes on the top of the domain, outside the inlet, were constrained to this value assuming a Dirichlet boundary condition. Between the inlet walls, a volume of 10 ml of liquid Hg^0 was injected into the domain with an average infiltration rate of 0.099 ml/s, over a time of 101 s. On all other boundaries a no flux boundary condition was assumed for both water and elemental mercury. The solution was advanced over time with a variable time step ranging from 0.1 s to 2 s depending on convergence history, while convergence of the solution was ensured by an absolute tolerance of 10^{-5} m.

5.2 Results and Discussion

5.2.1 PCE and Hg^0 Flow Container Experiments with Sands

The main difference between the two PCE and Hg^0 infiltration experiments was found in the early stage of the infiltration process. While PCE infiltrated and distributed within the water saturated porous sample, liquid Hg^0 did not. When elemental mercury was poured between the inlet walls, the sand particles of the top layer were displaced and started floating over the top of Hg^0 surface, due to their lack of cohesion and lower density. More

mercury was added to build a sufficient head to overcome the sand entry head but, rather than infiltrating in the porous sample, Hg^0 found a preferential pathway between the inlet walls and the front walls of the container, thus spreading over the top surface of MS1. Then the experiment was stopped. Conversely, 12 ml of PCE infiltrated over a time of 436 s, under an initial head of 2.16 cm. Unfortunately, Bromophenol Blue did not allow the visualization of the PCE infiltration front within the stratified porous medium, hence no track of it over time is available. Nevertheless, PCE inflow rate and head variation over time (Fig. 5.4) were successfully measured.

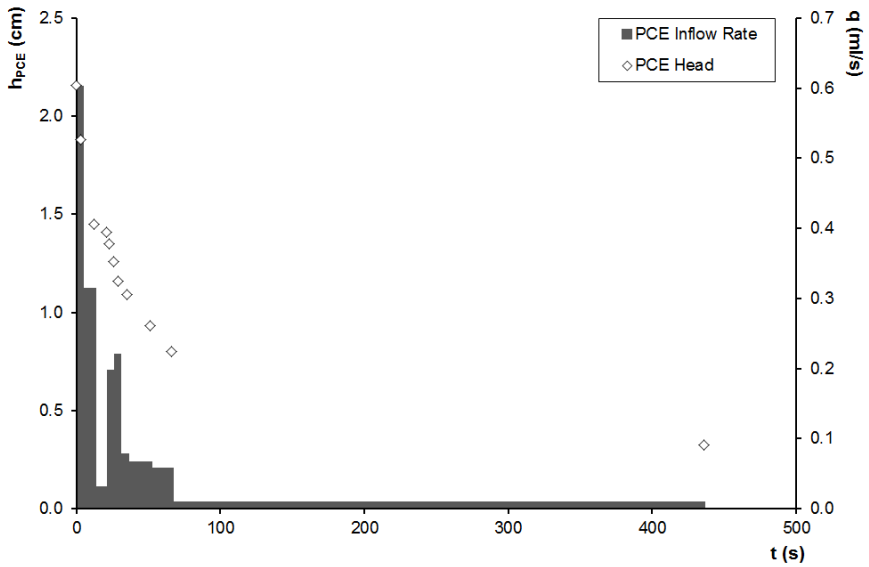

Fig. 5.4. Measured PCE inflow rate and head over time.

The $P_c(S)$ experiments (Chapter 4) showed that, in water saturated porous media, for the same sands, elemental mercury behaves like other DNAPLs, thus requiring to overcome an entry head to infiltrate. In terms of respective DNAPL heads, Hg^0 entry head was lower than that of PCE (6.19 cm in MS1 and 12.51 cm in MS2 for Hg^0, and 9.90 cm in MS1 and 15.77 in MS2 for PCE), thus enhancing elemental mercury natural tendency to be more prone than PCE to infiltrate in water saturated porous media. Hence, the reason of such a sharp difference in the infiltration behaviour exhibited by the two DNAPLs in the flow container experiments is not immediately clear. Most probably, the difference in the intrinsic permeability field of the two flow container samples played a major role.

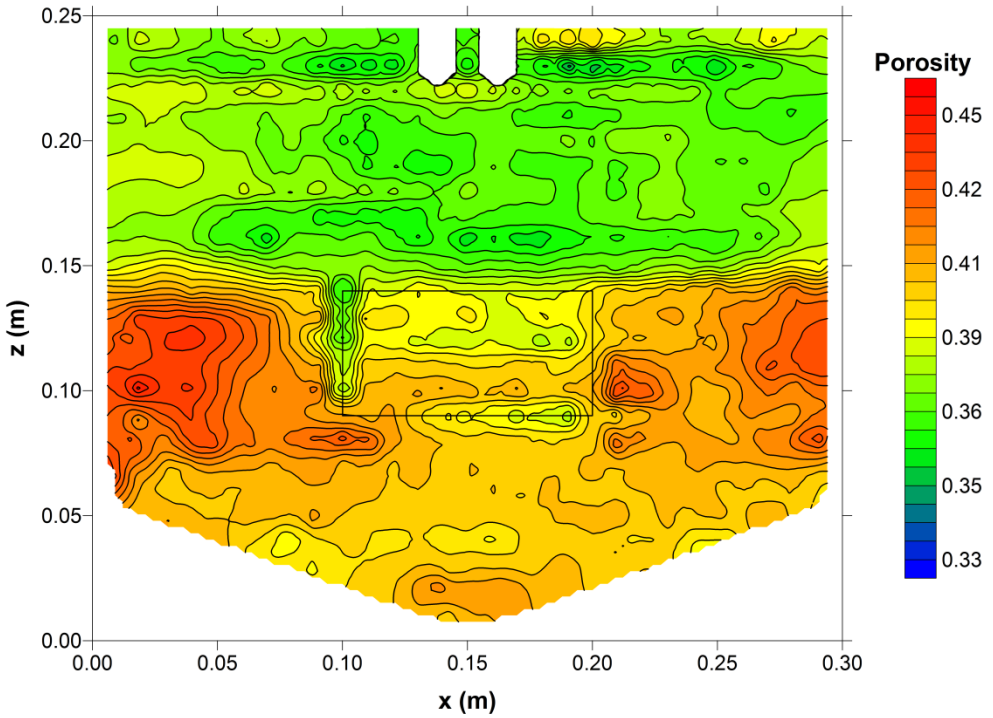

Fig. 5.5. PCE flow container sample: measured porosity field.

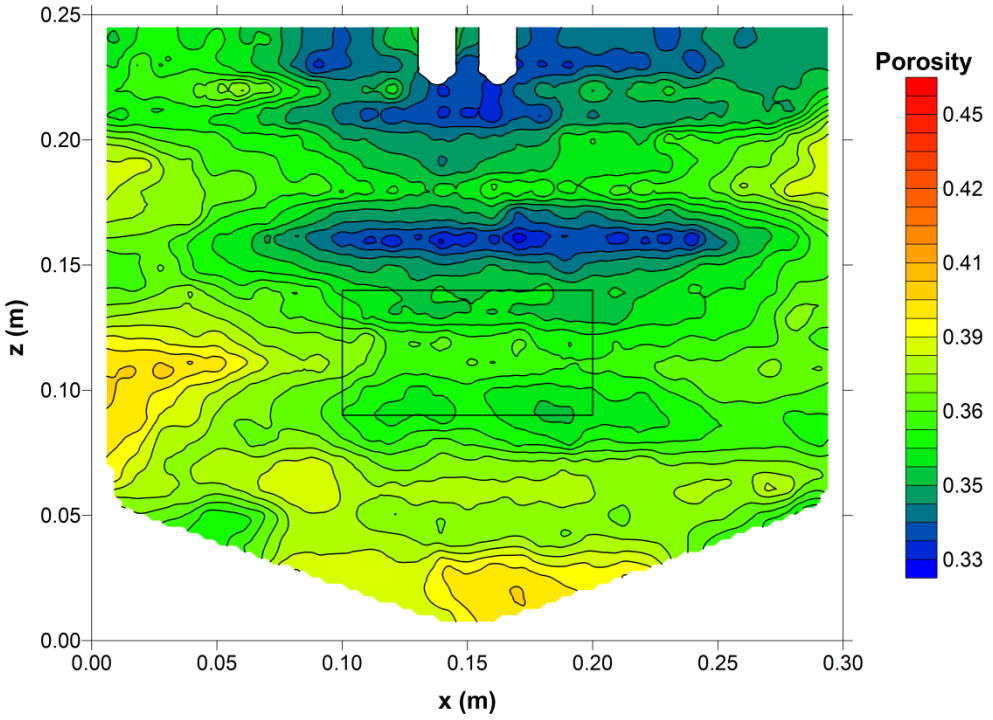

Fig. 5.6. Hg^0 flow container sample: measured porosity field.

Dual gamma ray measurements of the porosity field (Figs. 5.5 and 5.6) revealed significant differences among the two samples. As a matter of fact, the sample used for the Hg^0 flow container experiment showed a porosity remarkably lower than the one used for the infiltration of PCE. Such a strong difference in porosity likely resulted in a sharp difference in intrinsic permeability, thus inducing differences in entry head. In particular, this difference in porosity was more pronounced in proximity of the inlet, namely where the infiltration should have occurred. Therefore, Hg^0 did not infiltrate because it was unable to build a sufficient head to overcome the higher entry head induced by a locally lower intrinsic permeability. Hence, the increase in DNAPL pressure, following the further addition of Hg^0, resulted in the overcome of the resistance exerted by water between the inlet and the front walls rather than that of water in the sand, thus inducing the Hg^0 escape through a preferential pathway.

The heterogeneity in the intrinsic permeability field played an important role also for the migration of PCE. This influence can be first noticed in Fig. 5.4, where the PCE inflow rate is depicted. Its maximum value occurred at the early stages of the infiltration, when the DNAPL head was at its maximum level and when the PCE front encountered the top layer of MS1, where porosity and intrinsic permeability were higher than the layers immediately underneath the inlet. Subsequently, for a short time interval, the inflow rate dropped dramatically, symptom of the fact that a small lower permeability lens was encountered. Then, it increased again and gradually reduced, with no particular variations, until the end of the infiltration process.

The discontinuity observed in the PCE saturation profile (Fig. 5.7) illustrates the dependency of the migration pattern with intrinsic permeability. The dual gamma ray detected the presence of PCE everywhere in the lowest part of the sample, with a maximum saturation of 0.094, while almost no PCE was detected in the top part. Most likely, the effect of micro heterogeneities was even more pronounced than macro heterogeneities. As a result, PCE migration probably developed under a gravitational instability regime, enhanced by the micro heterogeneities present within the sample, thus resulting in fingers formation (Poulsen and Kueper, 1992; Illangasekare, 1998). This would explain why the dual gamma ray system was not able to perform a continuous

measurement of the PCE front, in spite of the fine measurement grid adopted, and why PCE was found in the finer sand.

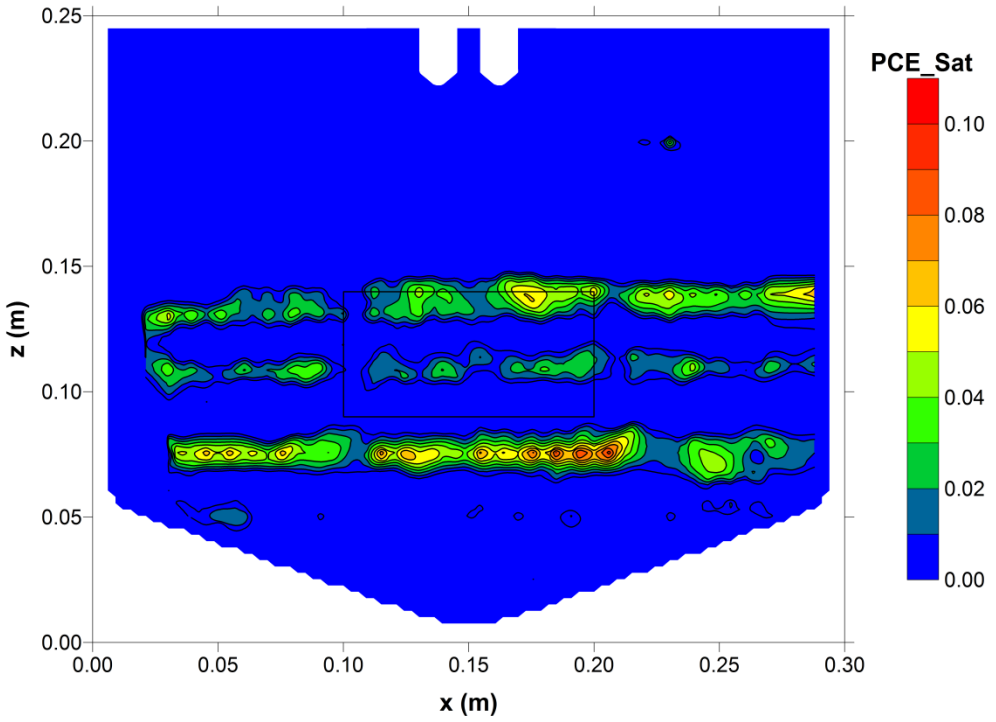

Fig. 5.7. Measured PCE saturation profile.

Fingers are expected to be thin, of the order of the pore sizes, hence, most probably, the dual gamma ray beam had locally either missed the fingers or smeared the saturation value through the whole thickness of the porous medium, thus resulting in an overall negligible measured PCE saturation in the top part of the sample. Fingers develop through preferential pathways dictated by the micro heterogeneities found during the migration (Mayer and Hassanizadeh, 2005). Therefore, under this flow regime and given the heterogeneity exhibited by the stratified sand sample, it is realistic to find PCE within the MS2 lens, despite the high entry head (15.77 cm of PCE) exhibited in the $P_c(S)$ measurements (Chapter 4).

5.2.2 Hg^0 Flow Container Experiment with Glass Beads

The porosity field and the elemental mercury saturation profile of the glass beads flow container experiment are depicted in Figs. 5.8 and 5.9.

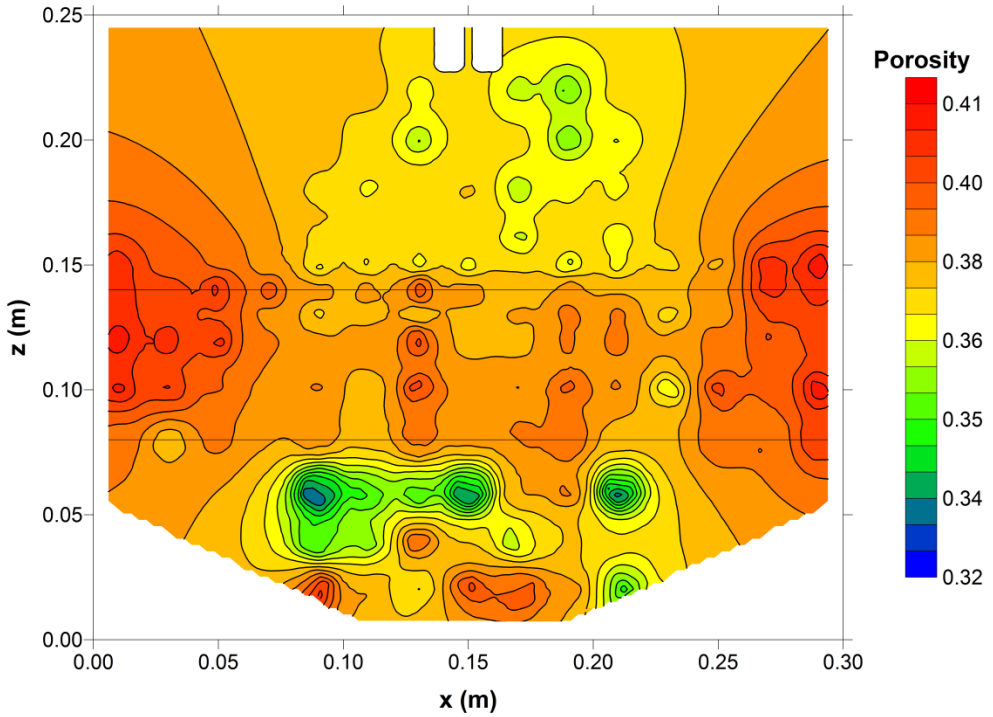

Fig. 5.8. Glass beads flow container sample: measured porosity field.

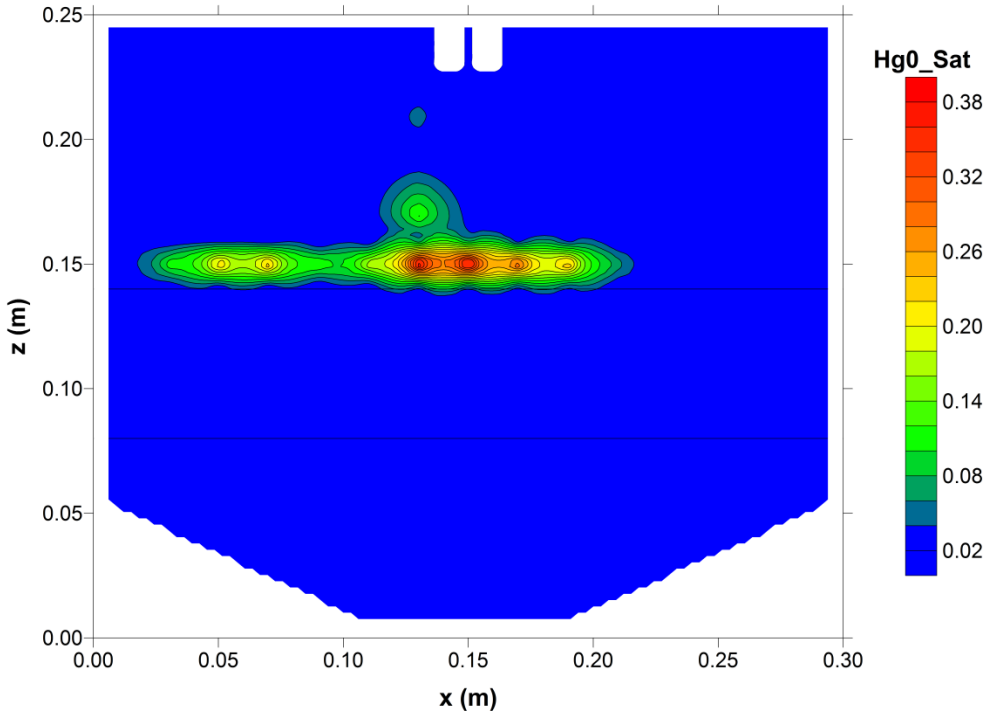

Fig. 5.9. Measured Hg^0 saturation profile in glass beads.

The final distribution of elemental mercury (Fig. 5.9) in the highest porosity zone (Fig. 5.8) shows that its infiltration and distribution were largely affected by the heterogeneities present within the sample. The infiltration front was fast and reached the top of the medium glass beads layer in 31 s. After 101 s the elemental mercury source was depleted and the distribution occurred. No elemental mercury was able to penetrate the medium glass beads, and a flat pool, of about 1 cm height, formed on top of this layer. Steady state was visually observed after 112 s from the beginning of the infiltration process. The maximum DNAPL saturation measured at the end of the experiment was of 0.368, where the Hg^0 pool was formed.

Numerical simulations, performed with GDAn (Chapter 2), showed an overall good agreement with the experimental results. The main features of Hg^0 DNAPL migration, such as the magnitude of the infiltration time, the stretched shape of the infiltration front along the vertical axis as a result of the predominance of gravity over capillary forces, and the spreading above the medium glass beads layer without penetrating it, were well captured.

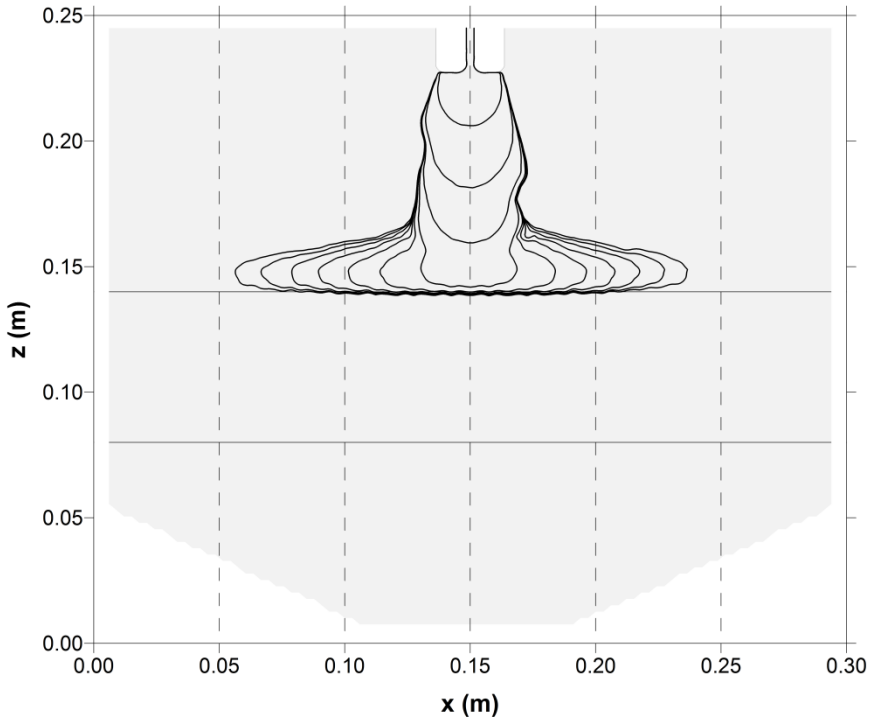

Fig. 5.10. $\gamma = 0.50$ - Simulated Hg^0 infiltration front ($S_n = 0.03$) over time (10 s – 100 s) every 10 s.

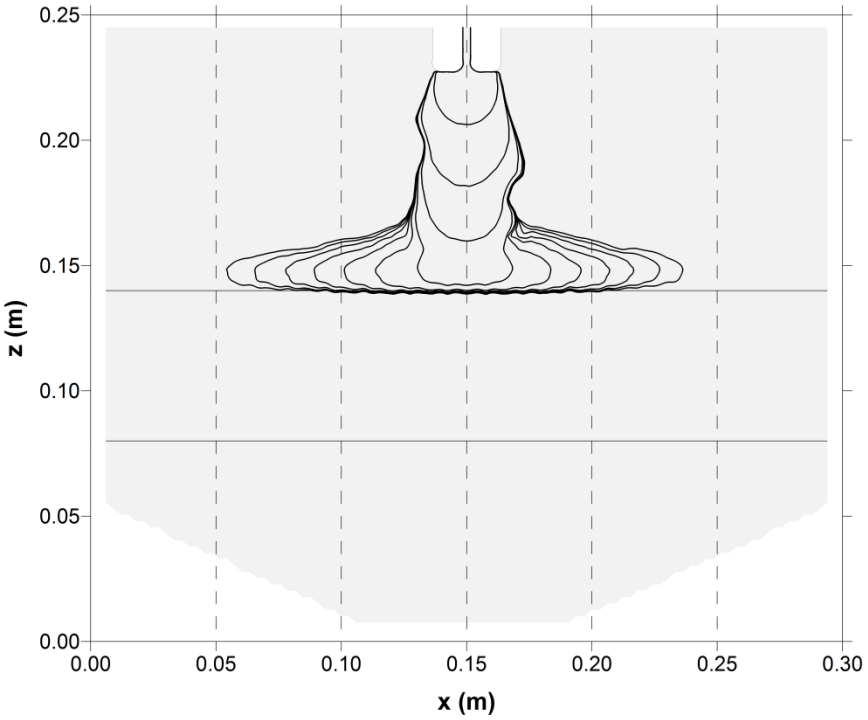

Fig. 5.11. $\gamma = 0.75$ - Simulated Hg^0 infiltration front ($S_n = 0.03$) over time (10 s – 100 s) every 10 s.

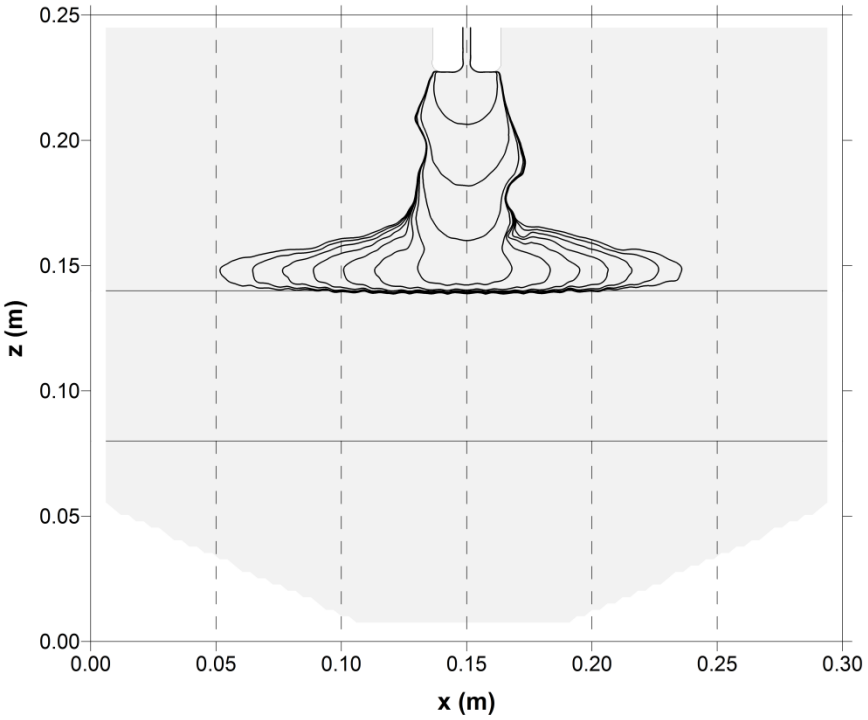

Fig. 5.12. $\gamma = 0.95$ - Simulated Hg^0 infiltration front ($S_n = 0.03$) over time (10 s – 100 s) every 10 s.

The inspection of Figs. 5.10-5.12, where, for each permeability scenario, the progression of the Hg^0 infiltration front is reported over time, shows that the more the γ parameter (Eq. 5.2) increases, the sharper becomes the variation of the van Genuchten α parameter with intrinsic permeability, thus resulting in a more realistic prediction of the infiltration and distribution phenomena. As a matter of fact, with increasing γ, the shape of the infiltration front becomes less symmetric, moving towards areas with higher porosity and intrinsic permeability, as observed in the experiment (Fig. 5.9), where Hg^0 mainly migrated in the left part of the container once the medium glass beads layer was reached. However, numerical simulations were not able to perfectly replicate the experimental observations. As a matter of fact, the simulated infiltration front was slower than the observed one, reaching the medium glass beads layer in about 40 s rather than 31 s, and achieving the steady state in about 180 s rather than 112 s. Furthermore, due to the more pronounced lateral spreading of the simulated Hg^0 infiltration front above the medium glass beads layer, the resulting maximum saturations (Figs. 5.13-5.15) were definitely lower than the measured one, ranging between 0.114 and 0.128 with γ ranging from 0.95 to 0.5.

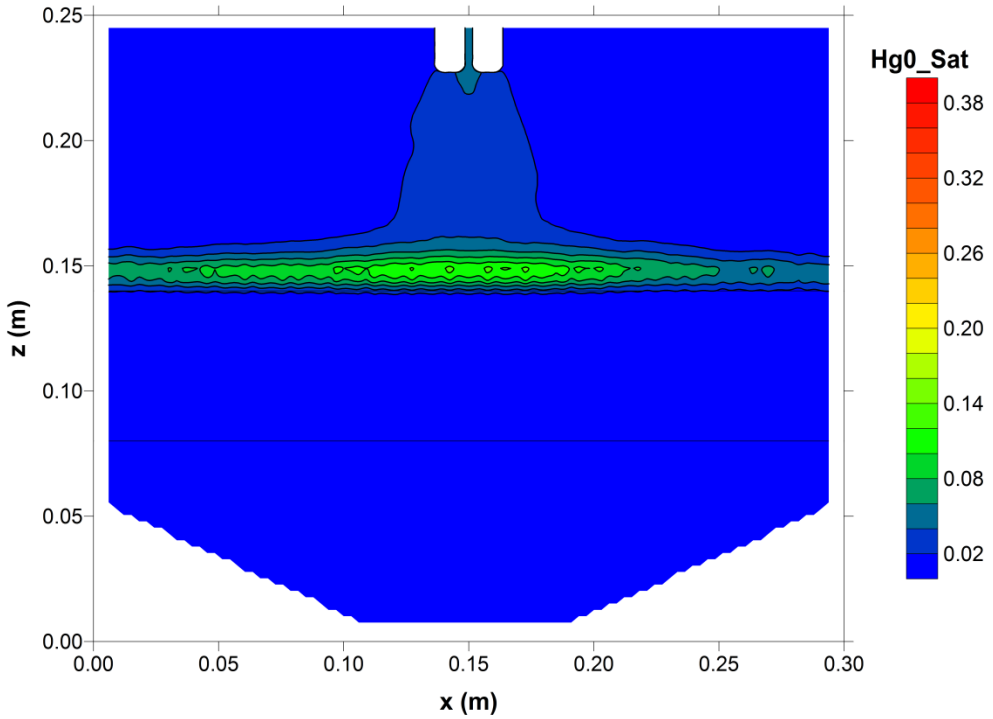

Fig. 5.13. γ = 0.50 - Simulated Hg^0 saturation at 180 s.

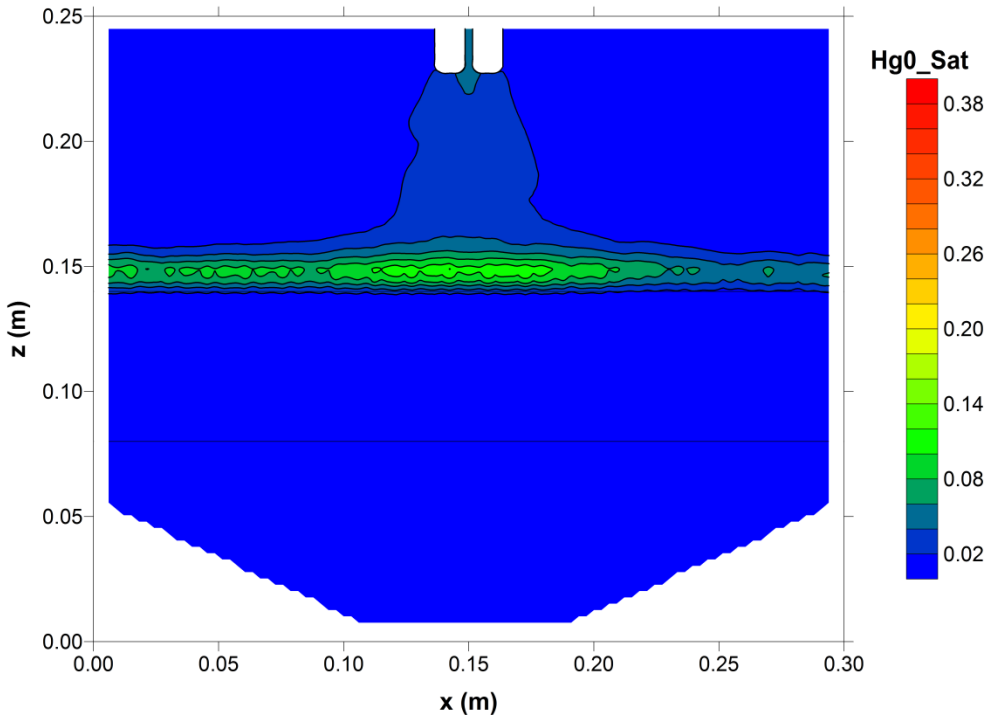

Fig. 5.14. $\gamma = 0.75$ - Simulated Hg^0 saturation at 180 s.

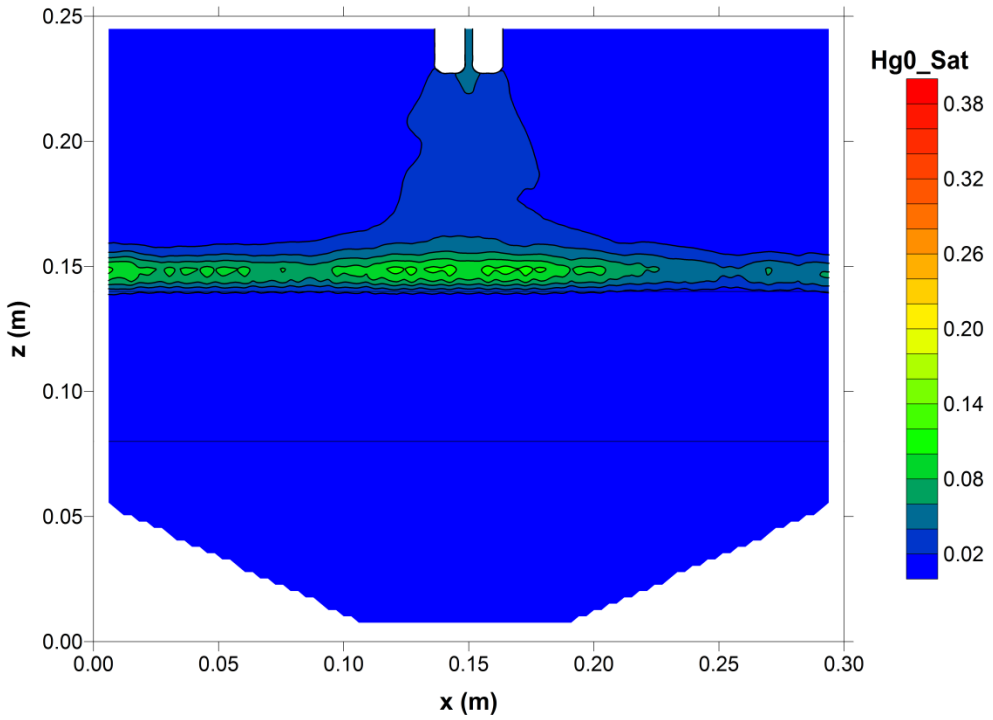

Fig. 5.15. $\gamma = 0.95$ - Simulated Hg^0 saturation at 180 s.

Taking into account the heterogeneity of the intrinsic permeability field across the whole domain played an important role also in assessing the final distribution of elemental mercury, even though, in the numerical simulations, Hg^0 spread completely over the top of the medium glass beads layer, reaching the lateral boundaries of the domain. As a matter of fact, with increasing γ, elemental mercury was found at higher saturations in the left part of the container, while it reached lower saturations in the right part, where the Hg^0 pool became thinner.

The discrepancies found between the experimental results and the numerical predictions are probably due to the lack of knowledge of the Hg^0 inflow rate and to the low agreement of the correlation between the measured porosity field with the estimated intrinsic permeability and retention properties. As a matter of fact, considering an average value of the inflow rate makes it practically impossible to predict the position of the infiltration front over time, and it may leads to substantial overestimations of the extent of Hg^0 migration. In absence of any measurement, the prediction of the inflow rate in a specific porous system requires a detailed knowledge of the locations of varying permeability lenses in the proximity of the DNAPL source (Kueper and Gerhard, 1995). Even though the non-intrusive measurements performed with the dual gamma ray system allowed a detailed description of the porosity field, the correlation of porosity with intrinsic permeability, as well as with the retention properties, would have required more experimental determinations to guarantee a more reliable estimation. The information based on Kozeny-Carman formula and on the modified Leverett function proved to be not sufficient outside the porosity range defined with the hydraulic conductivity and $P_c(S)$ experiments on glass beads (Sweijen, 2013). Nevertheless, the three scenarios showed improvements with increasing γ, thus confirming numerical predictions dependency on the correlation between intrinsic permeability and retention properties.

These evidences found for Hg^0 are in agreement with those found in the scientific literature for organic DNAPLs, like PCE. Dekker and Abriola (2000) suggested that, among the factors influencing the prediction of organic liquid migration and entrapment in porous media, the most critical were (i) the inflow rate, (ii) the reliable estimation of the porous formation permeability, and (iii) the accurate representation of the correlation between $P_c(S)$ curves and intrinsic permeability. This is exactly what was found for Hg^0 within the

current study, thus confirming the similarity with other DNAPLs of its infiltration and distribution behaviour in water saturated porous media.

References

Bear J (1972). *Dynamics of fluids in porous media*. Dover Publications, Inc., New York.

Carman PC (1938). *The determination of the specific surface of powders*. Journal of the Society of Chemical Industry, 57, 225.

Carman PC (1956). *Flow of gases through porous media*. Butterworths Scientific Publications, London.

Chiogna G (2010). *Transverse mixing of conservative and reactive tracers in porous media*. Doctoral dissertation, Universität Tübingen.

Cirpka OA, Olsson Å, Ju Q, Rahman MD, Grathwohl, P (2006). *Determination of transverse dispersion coefficients from reactive plume lengths*. Ground Water, 44(2), 212-221.

Dekker TJ, Abriola LM (2000). *The influence of field-scale heterogeneity on the infiltration and entrapment of dense nonaqueous phase liquids in saturated formations*. Journal of Contaminant Hydrology, 42(2), 187-218.

Fitts CR (2002). *Groundwater science*. Academic Press.

Hartog N, Cho J, Parker BL, Annable, MD (2010). *Characterization of a heterogeneous DNAPL source zone in the Borden aquifer using partitioning and interfacial tracers: residual morphologies and background sorption*. Journal of Contaminant Hydrology, 115(1), 79-89.

Hofstee C, Dane JH, Walker RC (1998a). *Infiltration and redistribution of perchloroethylene in stratified water-saturated porous media*. Soil Science Society of America Journal, 62(1), 13-22.

Hofstee C, Oostrom M, Dane JH, Walker RC (1998b). *Infiltration and redistribution of perchloroethylene in partially saturated, stratified porous media*. Journal of Contaminant Hydrology, 34(4), 293-313.

Illangasekare TH (1998). *Flow and entrapment of nonaqueous phase liquids in heterogeneous soil formations*, in Physical Non-equilibrium in Soil. Ann Arbor Press, Chelsea, Michigan, 417-423.

Kozeny J (1927). *Ueber kapillare Leitung des Wassers im Boden*. Akademie der Wissenschaften in Wien, 136 (2a), 271.

Kueper BH, Frind EO (1991). *Two-phase flow in heterogeneous porous media: 2. Model application*. Water Resources Research, 27(6), 1059-1070.

Kueper BH, Gerhard JI (1995). *Variability of point source infiltration rates for two-phase flow in heterogeneous porous media*. Water Resources Research, 31(12), 2971-2980.

Lenhard RJ, Parker JC (1987). *Measurement and prediction of saturation-pressure relationships in three-phase porous media systems*. Journal of Contaminant Hydrology, 1, 407–424.

Leverett M (1941). *Capillary behavior in porous solids*. Transactions of the AIME, 142(01), 152-169.

Luo H, Du Y, Hu Z, Cooper WL, Lu H (2015). *High-Strain Rate Compressive Behavior of Glass Beads Under Confinement*. Experimental Mechanics, 55(5), 935-950.

Mayer A, Hassanizadeh SM (2005). *Soil and Groundwater Contamination: Nonaqueous Phase Liquids, Principles and Observations*. American Geophysical Union.

Mualem Y (1976). *A new model for predicting the hydraulic conductivity of unsaturated porous media*. Water Resources Research, 12(3), 513-522.

O'Neil MJ (2006). *The Merck Index: An Encyclopedia of Chemicals, Drugs, and Biologicals*. Whitehouse Station, NJ, Merck and Co. Inc.

Poulsen MM, Kueper BH (1992). *A field experiment to study the behavior of tetrachloroethylene in unsaturated porous media*. Environmental Science & Technology, 26(5), 889-895.

Rockhold ML, Yarwood RR, Niemet MR, Bottomley PJ, Brockman FJ, Selker JS (2007). *Visualization and modeling of the colonization dynamics of a bioluminescent bacterium in variably saturated, translucent quartz sand*. Advances in Water Resources, 30(6), 1593-1607.

Schwille F (1988). *Dense Chlorinated Solvents in Porous and Fractured Media - Model Experiments*. Lewis Publishers, Chelsea, MI.

Sweijen T (2013). *Experiments on the physical behaviour of elemental mercury in saturated porous media*. Universiteit Utrecht, The Netherlands.

Tuck DM, Iversen GM, Pirkle WA (2003). *Organic dye effects on dense nonaqueous phase liquids (DNAPL) entry pressure in water saturated porous media*. Water Resources Research, 39(8).

van Genuchten MT (1980). *A closed form equation for predicting the hydraulic conductivity of unsaturated soils*. Soil Science Society of American Journal, 44, 892–898.

Young HD, Freedman RA, Ford AL (2012). *Sears and Zemansky's University Physics with Modern Physics*. Addison-Wesley, ISBN 978-0321696861.

Notation

Greek Symbols

α	van Genuchten model parameter
γ	Leverett function fitting parameter
ϕ	porosity

Latin Symbols

d_{50}	median particle diameter

h_{PCE}	PCE head
k	intrinsic permeability
k_r	relative permeability
n	van Genuchten model parameter
P_c	capillary pressure
q	inflow rate
SF	particles shape factor
S_n	NAPL saturation
t	time

Chapter 6

Infiltration and (Re)Distribution of Hg^0 DNAPL in Variably Water Saturated Porous Media

This chapter deals with the analysis of Hg^0 DNAPL infiltration and (re)distribution behaviour in variably water saturated porous media. First, a new theoretical formulation of elemental mercury retention properties is presented, and the new constitutive relationship is enforced within the GDAn code (Chapter 2). Then, a two-dimensional flow container experiment in a variably water saturated stratified granular porous medium is described and analysed. To allow a quantitative analysis of the flow behaviour of elemental mercury, non-intrusive measurements of porosity, water and Hg^0 saturations were performed with the dual gamma ray system (Chapter 3). Finally, to assess to what extent the new constitutive formulation is able to cope with elemental mercury migration in variably water saturated porous media, the flow container experiment was simulated with the modified GDAn code.

6.1 A New Constitutive Model of Hg^0 DNAPL Flow Behaviour in Variably Water Saturated Porous Media

6.1.1 Theoretical Framework

The experimental results reported in Chapter 4 show that liquid Hg^0 requires a smaller head to infiltrate into fully water saturated porous media than other DNAPLs, such as PCE. Conversely, in partially water saturated porous systems, in contrast with well-known NAPLs, elemental mercury requires to overcome an entry head to infiltrate. This head is considerably higher than those required for both PCE and Hg^0 in fully water saturated systems. Therefore, the conventional wettability hierarchy, in which the NAPL has an intermediate wetting state between the air and the water phases, is not valid for elemental mercury.

In absence of a suitable formulation, the only way to model elemental mercury DNAPL migration in partially water saturated systems, although not physically consistent, would be to apply the conventional constitutive relations governing multiphase flow in porous media (Parker et al., 1987). However, due to the values assumed by the Hg^0 scaling parameters, these relations give unsatisfactory results. This is shown hereinafter with an example, where the conventional theory is applied to both PCE and Hg^0. Assuming the same porous medium, the scaling parameters β_{an} and β_{nw} are equal to 2.617 and 1.618 for PCE, 0.148 and 0.192 for Hg^0, respectively. The scaling parameters were derived as the ratios between the water surface tension and the DNAPL interfacial tensions with air and water (Lenhard and Parker, 1987), and, in the case of PCE, taking into account its non-spreading behaviour (White et al., 2004). Adopting the van Genuchten model (van Genuchten, 1980), to have NAPL infiltration in a partially water saturated system, the following condition must be satisfied (Kaluarachchi and Parker, 1992):

$$h_n > \frac{\beta_{an} h_a + \beta_{nw} h_w}{\beta_{an} + \beta_{nw}} \tag{6.1}$$

derived from the condition $\overline{S_t} > \overline{S_w}$ ($\overline{S_n} > 0$), where $\overline{S_t}$ is the effective total liquid saturation, $\overline{S_w}$ is the effective water saturation, $\overline{S_n}$ is the effective NAPL saturation, h_a, h_n, and h_w are the pressure heads of air, NAPL, and water, respectively. Assuming the air pressure field to be equal to the atmospheric value ($h_a = 0$), this implies that the air-NAPL capillary head

(h_{an}) and the NAPL-water capillary head (h_{nw}) are lower than the air-water capillary head (h_{aw}). In the case of well-known NAPLs, like PCE, when infiltration occurs, the total liquid saturation increases, $\overline{S_t}(h_{an}) > \overline{S_w}(h_{aw})$, while the water saturation decreases, $\overline{S_w}(h_{nw}) < \overline{S_w}(h_{aw})$, Fig. 6.1.

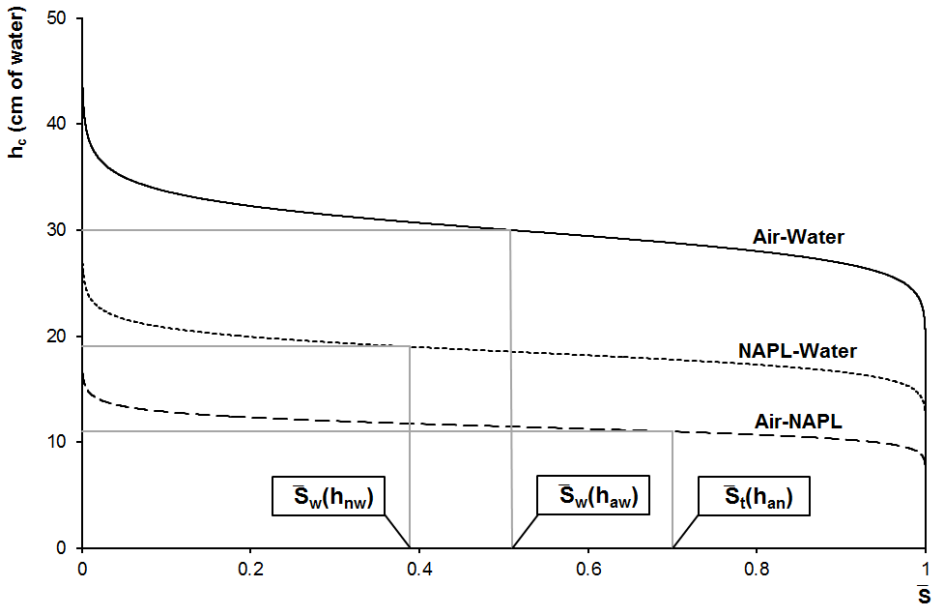

Fig. 6.1. Air-Water, scaled Air-PCE and scaled PCE-Water $P_c(S)$ curves.

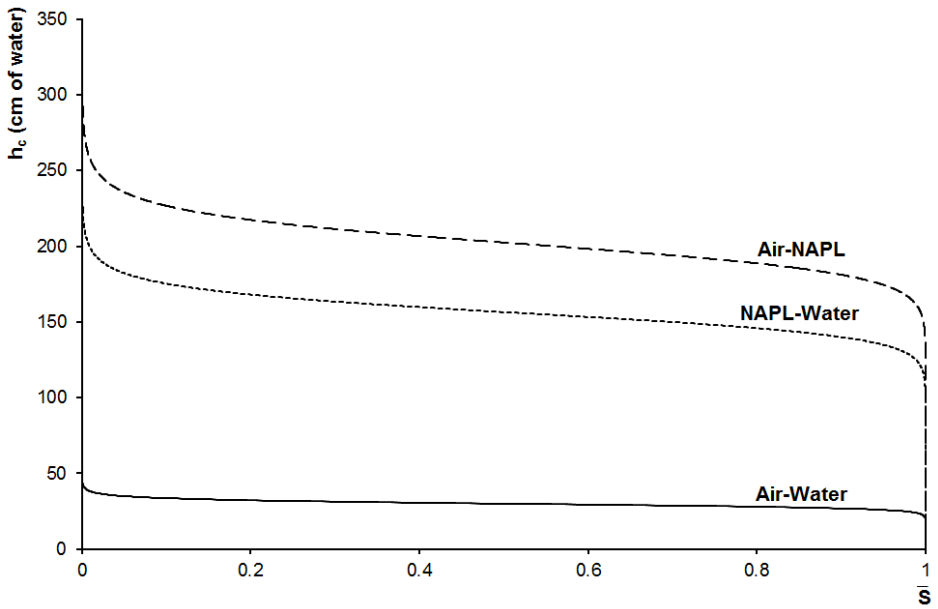

Fig. 6.2. Air-Water, scaled Air-Hg^0 and scaled Hg^0-Water $P_c(S)$ curves.

According to Eq. 6.1, to have elemental mercury infiltration, the air-Hg^0 and the Hg^0-water capillary heads should be lower than the air-water capillary head, but, due to the fact that the Hg^0 scaling parameters are much lower than unity, as confirmed by experimental results (Chapter 4), the Hg^0 scaled curves are higher than the air-water curve (Fig. 6.2), and $\overline{S_t} = \overline{S_t}(h_{an})$ and $\overline{S_w} = \overline{S_w}(h_{nw})$ would be equal to unity. This would imply an unphysical water imbibition, $\overline{S_w}(h_{nw}) > \overline{S_w}(h_{aw})$, and no NAPL infiltration, $\overline{S_n} = 0$. This makes the classical procedure not applicable for elemental mercury, and the same conclusions hold true for any other conventional P_c-S model. Hence the need of a new formulation for the constitutive relations governing elemental mercury DNAPL flow behaviour in variably water saturated porous media.

The crucial assumption of the proposed formulation, based on the experimental observations reported in sec. 4.2.2, is that, when liquid Hg^0, air, and water coexist within the pores of a water wet porous medium, the solid particles are expected to "like" elemental mercury less than air and water, due to its remarkably high surface tension (Tab. 4.2). Moreover, air is assumed to be continuous and extremely mobile within the porous medium, thus neglecting its compressibility as well as any variation in its pressure field, equal to the atmospheric value. Hence, under this condition, elemental mercury infiltration occurs when it has sufficient head to overcome the entry head dictated by the presence of air within the pores. If it is so, its infiltration is followed by a displacement of air and water. When liquid elemental mercury invades a partially water saturated pore, it first displaces air that, in turn, does not displace water, and leaves the pore due to its lower wettability than water with the water wet solid particles. As most of the air abandons the pore due to a further infiltration of mercury, the air phase is locally not continuous anymore, and most of the Hg^0 comes in contact with water. At this point, a further infiltration of elemental mercury causes the Hg^0 front to displace the water phase together with entrapped air. Hence, during elemental mercury infiltration in a partially water saturated pore, the water saturation does not change until most of the air comes out of the pore. Once it happens and the elemental mercury infiltration continues, the water saturation locally changes, and the water pressure in the pore, and in the surrounding pores, changes accordingly to the induced saturation variation.

6.1.2 Mathematical Framework

The governing equations of multiphase flow of immiscible fluids in porous media (Abriola and Pinder, 1985; Parker et al., 1987; Parker 1989) can be used to describe Hg^0 DNAPL flow behaviour (Sweijen et al., 2014), as also confirmed by the experimental and numerical results described in Chapters 4 and 5. Hence, the hypothesis of isothermal flow of incompressible fluids into a water wet nondeforming medium, with continuity of the air phase within the porous medium and negligibility of its pressure field, hold true. In the same manner, the k_r-S constitutive relations (Burdine, 1953; Mualem, 1976; Parker et al., 1987), and the extensions made by Kaluarachchi and Parker (1992) to consider hysteresis due to NAPL entrapment, Type-II hysteresis (Lenhard et al. 1989), can be used.

The fundamental assumption of the new model is the modification of the conventional wettability hierarchy (Parker et al., 1987), in which air is the nonwetting phase, the NAPL is intermediate wetting, and water is the wetting phase. With the new postulated wettability hierarchy, Hg^0 is the nonwetting phase, air is intermediate wetting, and water is the wetting phase. Hence, the major change involves the modification of the P_c-S constitutive relationships when a three phase system of liquid Hg^0, air, and water is encountered. In the new constitutive model is first defined a new variable, $S_{taw}(h_{ma})$, which is the total air-water saturation, function of h_{ma}, namely the capillary head between elemental mercury (m) and air (a):

$$S_{taw} = S_a + S_w \tag{6.2}$$

$$\overline{S_{taw}} = \overline{S}_a + \overline{S_w} \tag{6.3}$$

$$\overline{S}_a = S_a/(1 - S_{w,ir}) \tag{6.4}$$

$$\overline{S_w} = (S_w - S_{w,ir})/(1 - S_{w,ir}) \tag{6.5}$$

where S_a and S_w are the air and the water saturation, respectively, $S_{w,ir}$ is the irreducible water saturation, and the variables denoted with the overbar are the effective saturations. The application of the van Genuchten model (van Genuchten, 1980) leads to the following expression of the effective total air-water saturation, $\overline{S_{taw}}$:

$$\overline{S_{taw}} = \{1 + [\alpha\beta_{ma}(h_m - h_a)]^n\}^{-m} \tag{6.6}$$

where h_m is the elemental mercury pressure head, expressed in water equivalent head, α, n and m are the van Genuchten model parameters, and β_{ma} is a fluid dependent scaling parameter, either defined experimentally (Chapter 4) or through scaling as the ratio between the water and the Hg^0 surface tensions (Lenhard and Parker, 1987). Here, $\overline{S_{taw}}$ assumes the role of an overall effective wetting phase saturation which changes according to the pressure exerted by liquid Hg^0, the nonwetting phase.

Therefore, the proposed P_c-S constitutive model is structured as follows:

1) <u>Hg^0 absence in the system</u> ($h_m - h_w \leq 0$)

1.a) $h_a - h_w \leq 0$ (Fully Water Saturated System)

$$\overline{S_w} = 1 \tag{6.7a}$$

1.b) $h_a - h_w > 0$ (Partially Water Saturated System)

$$\overline{S_w} = \{1 + [\alpha(h_a - h_w)]^n\}^{-m} \tag{6.7b}$$

2) <u>Hg^0 may infiltrate in the system</u> ($h_m - h_w > 0$)

2.a) $h_a - h_w \leq 0$ (Two-Phase Flow, Hg^0-Water)

$$\begin{cases} \overline{\overline{S_w}} = \{1 + [\alpha\beta_{mw}(h_m - h_w)]^n\}^{-m} \\ \overline{S_w} = \overline{\overline{S_w}} - \overline{S_{me}} \\ \overline{S_t} = 1 \\ \overline{S_{mf}} = \overline{S_t} - \overline{S_w} \end{cases} \tag{6.8a}$$

2.b) $h_a - h_w > 0$ and $h_m - h_a > 0$ (Three-Phase Flow, Hg^0-Air-Water)

$$\begin{cases} \overline{S_{taw}} = \{1 + [\alpha\beta_{ma}(h_m - h_a)]^n\}^{-m} \\ \overline{S_w} = \{1 + [\alpha(h_a - h_w)]^n\}^{-m} \\ \overline{S_a} = \overline{S_{taw}} - \overline{S_w} \\ \overline{S_{mf}} = 1 - \overline{S_{taw}} \end{cases} \tag{6.8b}$$

- 2.b.1) $\bar{S}_a > 0$

$$\begin{cases} \overline{\overline{S_w}} = \overline{S_w} \\ \bar{S}_t = \overline{S_{mf}} + \overline{S_w} \end{cases} \tag{6.8c}$$

- 2.b.2) $\bar{S}_a \leq 0$

$$\begin{cases} \bar{S}_a = 0 \\ \overline{S_w} = \overline{S_{taw}} \\ \overline{\overline{S_w}} = \overline{S_w} \\ \bar{S}_t = 1 \end{cases} \tag{6.8d}$$

The additional variables present in the above equations are $\overline{\overline{S_w}}$, the apparent water saturation, $\overline{S_{mf}}$, the effective free Hg^0 saturation, $\overline{S_{me}}$, the effective entrapped Hg^0 saturation, and β_{mw}, a fluid dependent scaling parameter, either defined experimentally (Chapter 4) or as the ratio between the water surface tension and the Hg^0 interfacial tension with water (Lenhard and Parker, 1987). It follows that the effective total elemental mercury saturation is defined as $\overline{S_m} = \overline{S_{mf}} + \overline{S_{me}}$. Except for $\overline{S_w}$ (Eq. 6.5) and $\bar{S}_t = \left(S_t - S_{w,ir}\right)/\left(1 - S_{w,ir}\right)$, all the other effective saturations previously introduced are computed by normalizing the respective saturations by $(1\text{-}S_{w,ir})$.

From the inspection of Eqs. 6.7 and 6.8, the novelty of the proposed formulation emerges in 2.b), when Hg^0 tries to infiltrate in a partially water saturated porous medium. In this case, once Hg^0 overcomes the entry head required by Eq. 6.6 to infiltrate, a decrease in S_{taw} follows. As described in sec. 6.1.1, two cases can arise: i) the air phase is still present and continuous within the pores ($\bar{S}_a > 0$), hence the elemental mercury saturation increases and the air saturation decreases accordingly, while no change in water saturation occurs as a result of Hg^0 infiltration, $\overline{S_w} = \overline{S_w}(h_{aw})$; ii) the decrease in the effective total air-water saturation implies either an unphysical value of the effective air saturation ($\bar{S}_a < 0$) or its depletion in continuous form ($\bar{S}_a = 0$), hence air becomes discontinuous and the Hg^0 front can displace the water phase. Therefore, the effective air saturation is set to zero and water is displaced, and its change in saturation depends only on the elemental mercury head,

$\overline{S_w} = \overline{S_{taw}}(h_{ma})$, until the water pressure head becomes positive due to the water imbibition of the surrounding pore spaces. At this point, the model reverses to a two-phase flow of Hg^0 and water (Eq. 6.8a). As shown in Chapter 4 (sec. 4.2.2), when elemental mercury infiltrated in the sand column, the elemental mercury saturation increased, and, at a certain point, the rise in the Hg^0 head no longer induced any increase in the total liquid saturation. At this point, the infiltration of mercury resulted in the expulsion of an equal volume of water from the top of the column, and in the entrapment of discontinuous air, but the increase in Hg^0 saturation was still dictated by the capillary head between mercury and air.

Traditional models (Lenhard, 1992; White et al., 2004) regard air entrapment as a result of wetting phases (NAPL and water) imbibition. Actually, in the case of elemental mercury infiltration, air entrapment is likely to be induced by both nonwetting (Hg^0) and wetting (water) phases simultaneously. In absence of microscale evidence about the wettability hierarchy postulated, no formulation for the air entrapment induced by mercury imbibition was developed within the current model, and air entrapment is disregarded.

In the presented constitutive model, the first condition to satisfy to have liquid Hg^0 infiltration in a partially water saturated porous medium is that $h_m - h_w > 0$. However, this condition, even though necessary, is not sufficient to guarantee elemental mercury infiltration. The moving assumption is based on the experimental observations described in Chapter 4, where liquid Hg^0 entry head showed to be higher in partially than in fully water saturated porous media. Hence, having assumed the air pressure field to be negligible, the only variable that can discriminate the presence of elemental mercury within the system is h_w, the water pressure head. Therefore, to infiltrate in a partially water saturated system, the elemental mercury head should be at least bigger than that of water. This condition, if satisfied, does not imply Hg^0 infiltration, but only that it may infiltrate in the system. To effectively infiltrate in a partially water saturated porous medium, Hg^0 pressure head must be sufficiently high to guarantee $\overline{S_{taw}} < 1$ (Eq. 6.6), otherwise, no infiltration occurs and the model degenerates to Eq. 6.7.

The last changes introduced by the new formulation concern the analytical derivatives of the fluid saturations, used for the definition of the capacity terms figuring in the multiphase flow governing equations. The modification is applied at the 2.b) level, when a three-phase flow effectively occurs:

2.b) Three-Phase Flow, Hg^0-Air-Water

- Burdine's model

$$\begin{cases} \partial S_w/\partial h_w = \alpha \cdot (n-2) \cdot (1 - S_{w,ir}) \cdot \overline{S_w}^{1/m} \cdot \left(1 - \overline{S_w}^{1/m}\right)^m \cdot \left(\overline{S_w}^{-1/m} - 1\right)^{1/n} \\ \partial S_w/\partial h_n = 0 \\ \partial S_n/\partial h_w = 0 \\ \partial S_n/\partial h_n = \alpha \cdot \beta_{ma} \cdot (n-2) \cdot (1 - S_{w,ir}) \cdot \overline{S_{taw}}^{1/m} \cdot \left(1 - \overline{S_{taw}}^{1/m}\right)^m \cdot \left(\overline{S_{taw}}^{-1/m} - 1\right)^{1/n} \end{cases} \quad (6.9a)$$

- Mualem's model

$$\begin{cases} \partial S_w/\partial h_w = \alpha \cdot (n-1) \cdot (1 - S_{w,ir}) \cdot \overline{S_w}^{1/m} \cdot \left(1 - \overline{S_w}^{1/m}\right)^m \\ \partial S_w/\partial h_n = 0 \\ \partial S_n/\partial h_w = 0 \\ \partial S_n/\partial h_n = \alpha \cdot \beta_{ma} \cdot (n-1) \cdot (1 - S_{w,ir}) \cdot \overline{S_{taw}}^{1/m} \cdot \left(1 - \overline{S_{taw}}^{1/m}\right)^m \end{cases} \quad (6.9b)$$

where m is equal to 1-2/n, with n > 2, in the case of Burdine's model (Burdine, 1953), and equal to 1-1/n, with n > 1, in the case of Mualem's model (Mualem, 1976).

6.1.3 Numerical Implementation: GDAn-Hg^0

The main structure of the Hg^0 module of GDAn is essentially the same as the NAPL module (Chapter 2), except for the new formulation of the P_c-S relationships. Hence, to successfully implement the new procedure in conventional multiphase flow programs, only few modifications (sec. 6.1.2) must be performed. Moreover, to circumvent the numerical errors associated to null capacity terms induced by null mixed derivatives (Eq. 6.9), the mixed derivatives are set to a case dependent minimum value as for the minimum values adopted for the NAPL capacity terms in absence of NAPL (Abriola and Rathfelder, 1993).
In addition to these, a further minor change is required when defining the pressure field of liquid Hg^0 when is absent in the system. When the porous medium is water saturated, the initial condition to adopt is $h_m = h_w$, which implies a null capillary pressure head, hence no elemental mercury infiltration. In conventional two-phase flow modelling of NAPL and

water, this condition already proved to be the best choice to prevent the insurgence of large mass balance errors (Abriola and Rathfelder, 1993). Conversely, when a three-phase flow field condition can be triggered, the modification of the initial condition proposed by Kaluarachchi and Parker (1989) cannot stand anymore due to the change in the wettability hierarchy proposed in the new model. Therefore, when the porous medium is partially water saturated and liquid Hg^0 is initially absent, following the approach of Abriola and Rathfelder (1993), the elemental mercury pressure head is set to maintain the capillary pressure head to 0, hence the initial condition is $h_m = h_a$.

6.2 Materials and Methods

6.2.1 Porous Media and Fluids

Porous media and fluids used within the current study are reported in Chapter 4 (secs. 4.1.1 and 4.1.2) together with their respective properties. Briefly, two medium sands, namely MS1 (d_{50} = 0.39 mm) and MS2 (d_{50} = 0.26 mm), were used as porous media, while demineralized water and liquid elemental mercury (Hg^0) were used as fluids. Information about intrinsic permeability and $P_c(S)$ curves are reported in sec. 4.2.

6.2.2 Flow Container Experiment

The flow container (sec. 5.1.2) was mainly filled with MS1 and, to study the effects of macro heterogeneities on Hg^0 migration, a layer of 5 cm height of MS2 was located 11 cm from the bottom (Fig. 6.3). The water table was fixed at 2 cm from the top layer of MS1, located at 25 cm from the bottom. The two inlet walls were placed 2.5 cm deep from the top of the MS1 layer, in the middle of the container, with a spacing of 1.5 cm between each other. The packing of the sample was performed under water saturated conditions as described in sec. 5.1.2. To establish a partially water saturated condition within the sample, a drainage was performed from the bottom. A volume of about 380 ml of water was removed from the container, and 160 ml of it were directly coming from the porous sample.

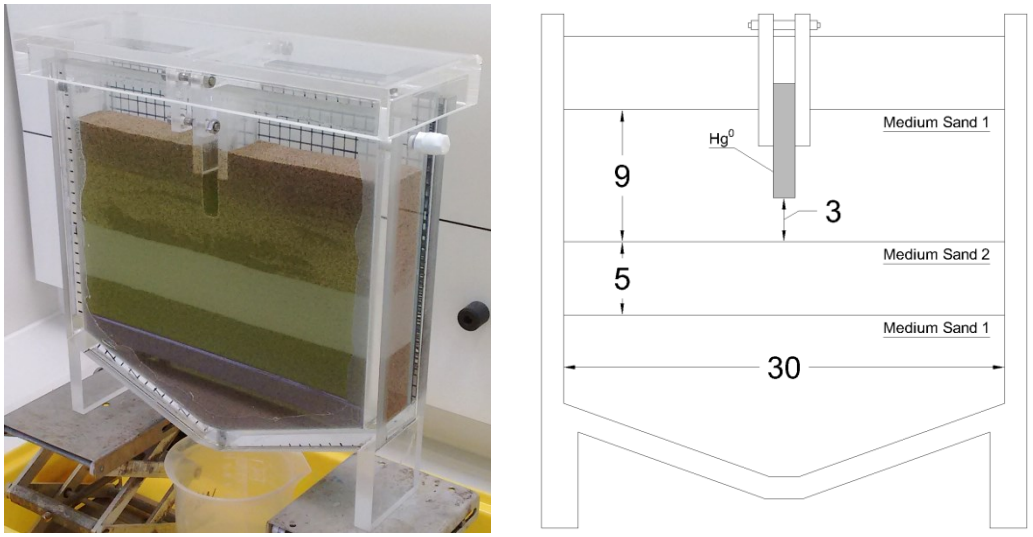

Fig. 6.3. Illustration (left) and schematic representation (right) of the flow container sample (dimensions in cm).

On the basis of the experimental results reported in Chapter 4, the entry head required by liquid elemental mercury to infiltrate into the partially water saturated sample was expected to be higher than the height available between the two inlet walls. Hence, after having allowed the water phase to achieve a steady state configuration, 24 hours after the partial drainage of the sample, a trench of 1.5 cm width and 6 cm depth, with vertical walls, was carefully excavated between the inlet screens, thus creating additional space for the Hg^0 DNAPL source.

In the first stage of the experiment, a fixed amount of liquid Hg^0 was carefully added in the trench in five steps, of about 9.2 ml each, thus allowing the DNAPL to build enough head to infiltrate and migrate within the partially water saturated sample. The second stage of the experiment consisted of the simulation of a "rain event" to assess whether the elemental mercury already infiltrated within the sample could be mobilized due to the local increase in water saturation. The rain event lasted 40 min and was performed by pouring water, at a rate of 5 ml/min, on top of the MS1 layer, with two sources placed in the middle of each portion outside the inlet walls. During the whole experiment, the Hg^0 head and its infiltration front were tracked with a camera to determine its infiltration rate and its position over time within the sample.

6.2.3 Porosity and Fluid Saturations Measurements

Non-intrusive measurements of porosity, water and Hg^0 saturations were performed over the whole sample with the dual gamma ray system (Chapter 3), on the basis of a regular grid consisting of 632 points with 1 cm spacing. The porosity field was measured first, at the end of the packing procedure, when the sample was fully water saturated. Then, when the sample was partially water saturated, after the trench excavation, the initial water saturation distribution was determined. Liquid Hg^0 and water saturation profiles were measured 24 hours after the end of each experimental stage (sec. 6.2.2), established when there was no further change of liquid Hg^0 level in the trench. Details on the working principles of the dual gamma ray system, and on the analytical derivation of porosity and of fluid saturations from the gamma ray measurements, are reported in Chapter 3.

In the locations where elemental mercury was found, the analytical formulation usually adopted to derive the fluid saturations in presence of three different phases (sec. 3.4.4) could not be used due to the complete attenuation of the Americium source exerted by liquid Hg^0 (sec. 3.3.3). To circumvent this problem, in these measuring points, the water saturation was initially assumed to be constant and Hg^0 saturation was derived according to it, based on Cesium intensities. If the sum of the resulting fluid saturations was found to be bigger than the total saturation, namely bigger than 1, the Hg^0 saturation was computed again assuming a water saturated condition. Through this approximation, it was found that the Cesium signal was only slightly affected by the presence of water. Hence, when deriving Hg^0 saturation, considering the location water saturated or not leads to negligible variations, thus ensuring the quality of the measurement. Conversely, when elemental mercury was encountered by the dual gamma ray in a specific location, it was impossible to measure the water saturation, and its value could only be determined by analysing the behaviour of the water phase in the surrounding measuring points, where liquid Hg^0 was not present.

6.2.4 Numerical Modelling: Hg^0 Infiltration and Distribution

To assess to what extent the proposed model can predict elemental mercury infiltration and distribution in partially water saturated porous media, the first stage of the flow container experiment was simulated with the modified version of GDAn (sec. 6.1). The input

parameters of the numerical simulations were mostly taken from Tabs. 4.1-4.4. In addition to these data, the irreducible water saturation was set to 0.075, while the maximum entrapped NAPL saturation to 0.024, based on the minimum values detected with the dual gamma ray system. Specific storage coefficients were determined assuming a compressibility of 4.6e-10 Pa^{-1} and of 3.7e-11 Pa^{-1} for water and Hg^0 (Young et al., 2012), respectively, of 1.4e-11 Pa^{-1} for sand, (Domenico and Mifflin, 1965), and an average porosity of 0.363, based on dual gamma ray measurements. The scaling parameters β_{mw} and β_{ma} were assumed equal to 0.262 and 0.163, respectively, based on the experimental observations reported in Chapter 4. To describe the modified P_c-S and k_r-S relationships, the van Genuchten-Mualem model (Mualem, 1976; van Genuchten, 1980) was chosen.

To relate the variability of measured porosities with intrinsic permeability and capillary retention parameters, the Kozeny-Carman formula (Kozeny, 1927; Carman, 1938, 1956; Bear, 1972; Fitts, 2002) and the generalized form of the Leverett function (Leverett, 1941; Kueper and Frind, 1991; Dekker and Abriola, 2000) were applied. In this way, each cell of the numerical domain was set to different values of porosity, intrinsic permeability, and of the van Genuchten α parameter. The van Genuchten n parameter, instead, was assumed constant within the same sand type, namely equal to 19.4 and 21.2 for MS1 and MS2, respectively, as a result of the averaging of the values obtained for the Air-Water retention curves reported in Chapter 4.

With the information derived from the gamma ray measurements, the porosity field (Fig. 6.7) was deduced for the whole domain, and the Kozeny-Carman formula (Eq. 5.1) was used to determine the intrinsic permeability, assuming particles shape factors (SF) of 34.2 and 24.2 for MS1 and MS2, respectively, determined as the best fit with the data reported in Tab. 4.3.

Within the porosity ranges defined by the Air-Water $P_c(S)$ measurements (sec. 4.2.2), based on the fitted results (Tab. 4.4), for MS1 the van Genuchten α parameter was determined in each cell by the following linear regression $\alpha = 0.518\phi - 0.153$ ($R^2 = 0.945$), in cm^{-1}, while for MS2 the value was assumed to be constant (Tab. 4.4) as no variations were observed. Outside these ranges, based on the intrinsic permeability field derived with the Kozeny-Carman formula, the generalized form of the Leverett function (Eq. 5.2) was used to determine the van Genuchten α parameter in each cell, assuming the

γ parameter to be equal to 0.125. The reference values of α and k were based on the values assumed at the limits of the porosity ranges of the Air-Water $P_c(S)$ samples (Tab. 4.4).
The spatial domain was discretized in 625 nodes and 1149 unstructured triangular cells, suitably refined in proximity of the inlet and of the top part of the MS2 layer. Across the whole domain, the water hydraulic head was set to - 12.5 cm, which resulted in the best fit of the initial water saturation distribution. At the bottom of the trench, liquid Hg^0 was injected into the domain on the basis of the inflow rate reported in sec. 6.3.1 (Figs. 6.4 and 6.5). On all other boundaries a no flux boundary condition was assumed for both water and elemental mercury. The solution was advanced over time with a variable time step ranging from 1 s to 120 s depending on convergence history, while convergence of the solution was ensured by an absolute tolerance of 10^{-8} m.

6.3 Results and Discussion

6.3.1 Flow Container Experiment: Stage 1

During the first stage of the flow container experiment, infiltration and distribution of Hg^0 DNAPL occurred in a partially water saturated stratified sand sample. A volume of 16.3 ml of elemental mercury was allowed to infiltrate within the sample under an initial DNAPL head of 7.76 cm. Steady state was achieved 3054 min (50.9 h) after the beginning of the infiltration, and the Hg^0 head reached the final value of 5 cm. The Hg^0 inflow rate did not show a clear trend over time (Figs. 6.4 and 6.5), other than highest infiltration rates occurring initially. Conversely, the Hg^0 head (Figs. 6.4 and 6.5) decreased smoothly with time. As observed for other DNAPLs, the fluctuations reported in the elemental mercury inflow rate were likely induced by the heterogeneities present within the porous formation (Kueper and Gerhard, 1995). Another factor that probably increased these variations was the spatial and temporal variability of the water saturation field as Hg^0 infiltrated and distributed within the porous sample.

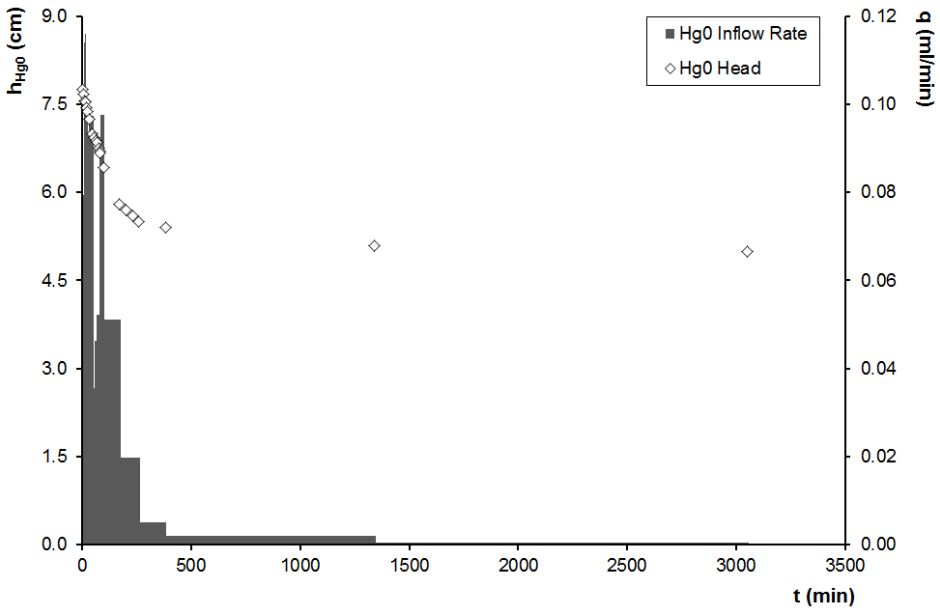

Fig. 6.4. Measured Hg^0 inflow rate and head over time - Stage 1.

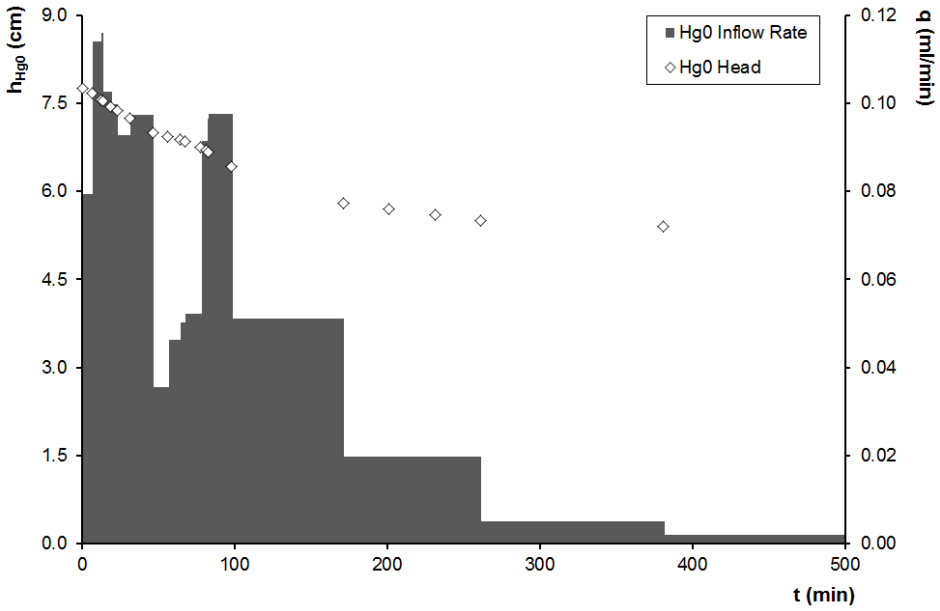

Fig. 6.5. Measured Hg^0 inflow rate and head over time (first 500 min) - Stage 1.

As found in the experiments reported in Chapter 4, Hg^0 migration in partially water saturated porous media was followed by a redistribution of water within the pores, hence of air, which in turn affected the elemental mercury migration itself. Elemental mercury

proved to be nonwetting with respect to air (Chapter 4), hence, the air presence within the pores, in different saturations, probably affected Hg^0 migration as well as its infiltration pattern.

The Hg^0 head under which the infiltration occurred was much lower than the one that could be predicted on the basis of the $P_c(S)$ measurements (Chapter 4). The start of DNAPL infiltration into the MS1 layer occurred when raising the Hg^0 head from 6.21 cm to 7.76 cm. This is significantly lower than the DNAPL entry head of 10.45 cm (Tab. 4.4) observed for the Hg^0-Air-Water $P_c(S)$ experiment in MS1. This about 25.7-40.6% lower entry head occurred despite both average porosity (0.344) and water saturation (0.240), in the first centimeter beneath the trench, being about 4% and 2.5 times lower than measured in the $P_c(S)$ experiment. This appears to be in contrast with the experimental results presented in Chapter 4, since a reduction in both porosity and water saturation would be expected to yield higher rather than lower entry heads. Such a strong deviation was probably induced by the fact that the entry heads obtained with the $P_c(S)$ measurements were derived under stable flow behaviour, while the infiltration in the flow container was likely unstable. Consequently, the effect of gravity might have been predominant in the first stages of the infiltration. Moreover, in the $P_c(S)$ samples, porosity was averaged over the whole sand column (42 mm diameter by 51 mm length), hence it was likely lower than average in proximity of the Hg^0 inflow (namely the bottom of the sand column).

As shown in Fig. 6.6, the infiltration of Hg^0 took place directly at the bottom of the trench, with no evidence of lateral spreading until the MS2 layer was encountered, and fingering might have occurred. Visual observations indicated that at least two fingers developed (Fig. 6.6) and, since lateral spreading occurred above MS2, elemental mercury was likely continuous beneath the reservoir, thus providing a connection with the DNAPL source in the trench. Hence, fingers were probably the main flow paths through which elemental mercury reached MS2 and started distributing over it.

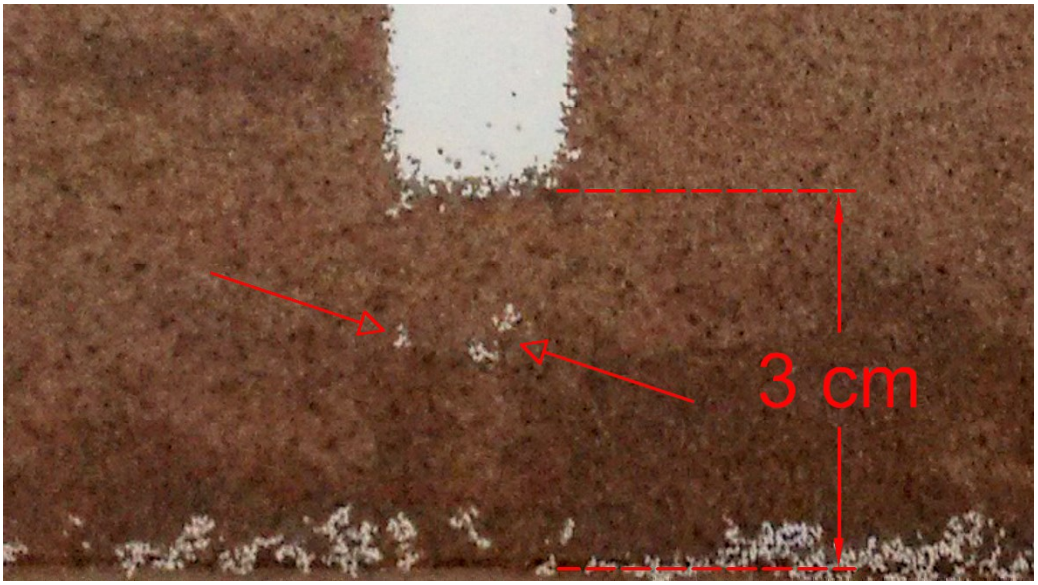

Fig. 6.6. Detail of the Hg^0 distribution below the reservoir with red arrows indicating the two fingers - End of stage 1.

Elemental mercury reached the top layer of MS2 in about 9 min, when a volume of 0.79 ml of liquid Hg^0 had infiltrated, based on the measured inflow rate (Figs. 6.4 and 6.5). This is in keeping with the integration of dual gamma ray measurements (Figs. 6.7 and 6.11), indicating that 0.69 ml of liquid Hg^0 infiltrated. Hence, in the first 3 cm beneath the trench, most of the elemental mercury occurred in the first minutes of the experiment, and no relevant change was observed over time. This suggests that, once mercury found a pathway, from the DNAPL source in the trench to the top layer of MS2, all the additional infiltrated Hg^0 probably migrated through this pathway before distributing above MS2.

Including the 3 cm of DNAPL head below the bottom of the infiltration reservoir (Fig. 6.6), the total liquid Hg^0 head on top of the MS2 layer was at maximum 10.5 cm, according to the head measurements over time (Figs. 6.4 and 6.5). In agreement with the $P_c(S)$ measurements (Chapter 4), this head was not sufficient to allow liquid Hg^0 to penetrate MS2, for which higher entry heads were observed (12.51 cm and 15.74 cm of Hg^0 in fully and partially water saturated samples, respectively).

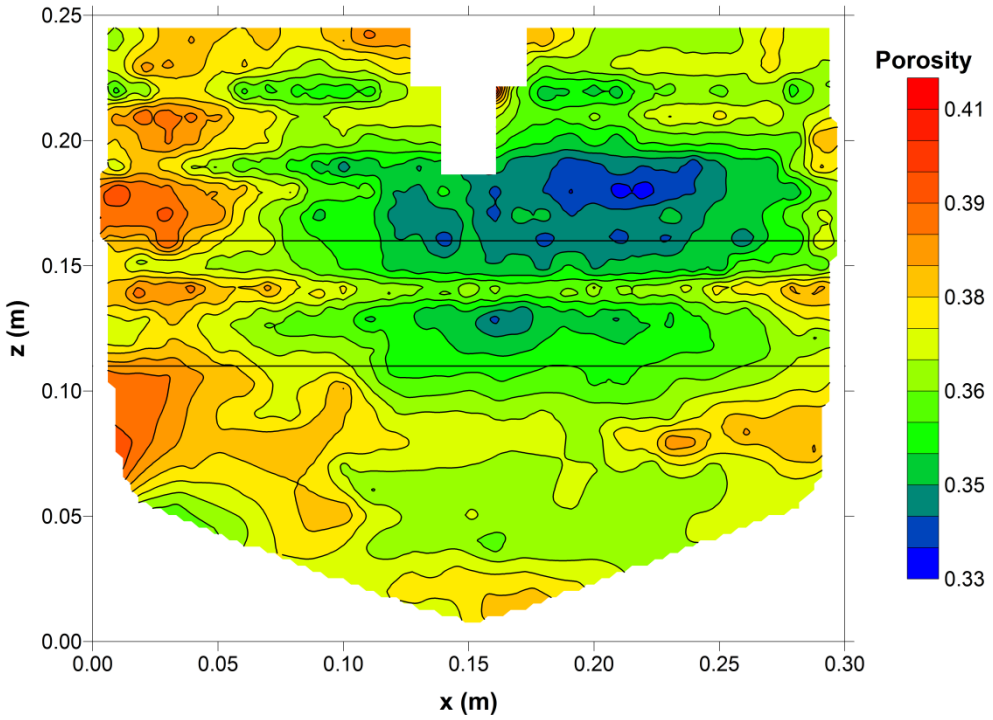

Fig. 6.7. Measured porosity field.

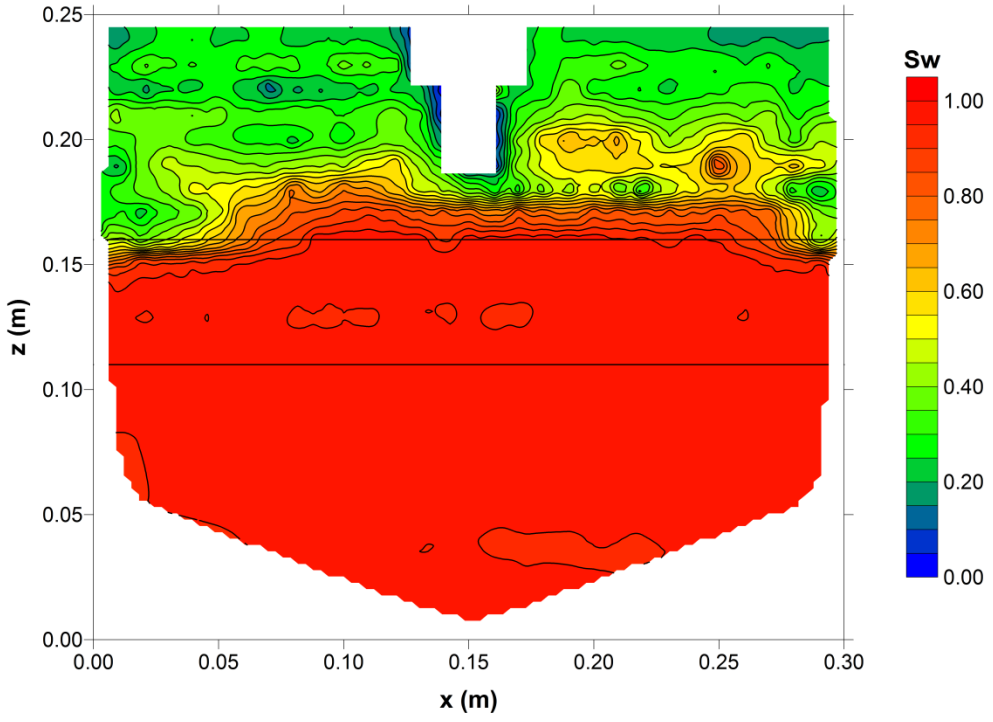

Fig. 6.8. Measured initial water saturation (S_w) profile.

Once the top layer of MS2 was reached, the DNAPL distributed above it, thus creating a pool of about 1 cm height. Elemental mercury distribution over MS2 was not symmetric, probably as a result of the variability of both porosity field (Fig. 6.7) and initial water saturation distribution (Fig. 6.8). This emerges clearly from Fig. 6.10, where the liquid Hg^0 lateral spreading above the MS2 layer, on both left and right sides of the sample (Fig. 6.9), is reported with respect to the vertical symmetry axis of the sample over a time of 60 min.

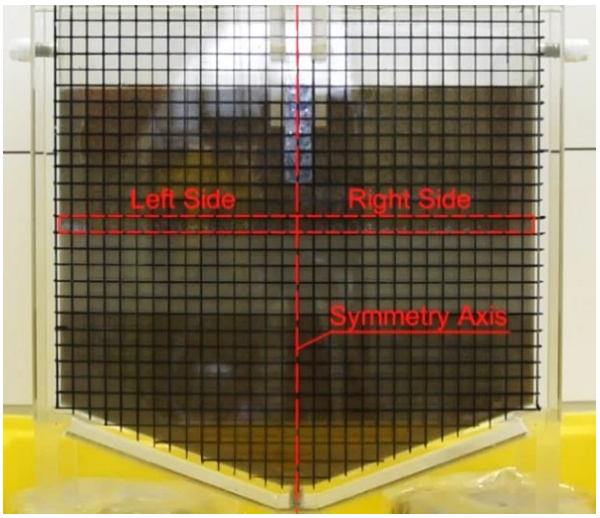

Fig. 6.9. Detail of the Hg^0 lateral spreading zone (dashed rectangular box).

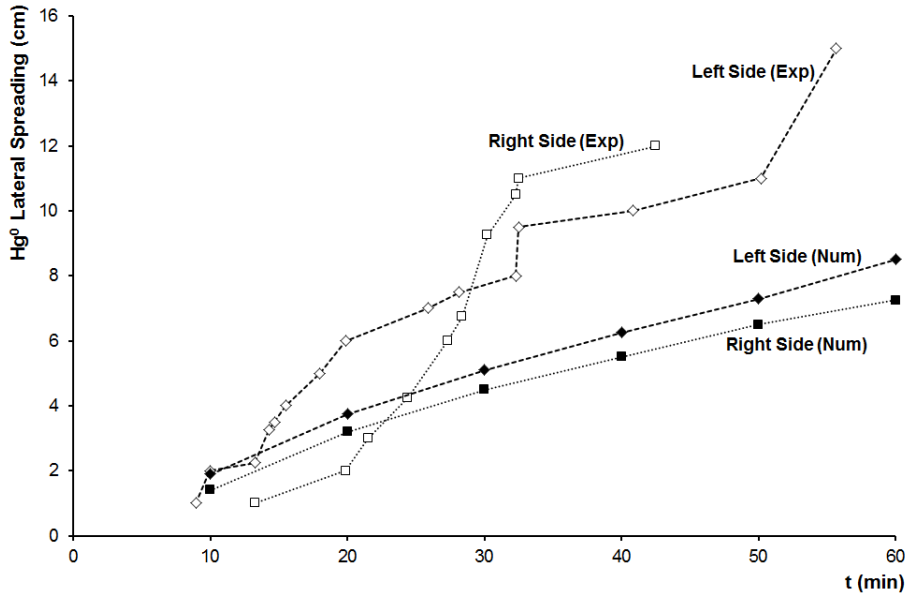

Fig. 6.10. Hg^0 lateral spreading above the MS2 layer on both left and right sides (experimental and numerical results).

Initially, the infiltration front was faster on the left side but, after a time of about 30 minutes, the trend reversed. Then, the infiltration temporarily ceased on the right side and continued on the left side, where elemental mercury rapidly reached the side wall of the container. This may be explained by the higher porosity, hence higher intrinsic permeability, found at the left side of the sample (Fig. 6.7), thus resulting in a preferential pathway for elemental mercury migration and distribution. Actually, the inspection of Fig. 6.11 confirms the tendency of liquid Hg^0 to migrate towards the left side of the container, where porosity was the highest (0.392) above the MS2 layer. As a matter of fact, the highest Hg^0 saturation (0.615) was found in proximity of the left side wall, where the height of the DNAPL pool increased to 2 cm. Nevertheless, at the left side, the initial water saturation was lower than at the right side. Actually, the bigger the pores, the lower the entry head, hence, it is reasonable to think that, when a higher permeability zone is encountered, the easier air and water are displaced towards it as a result of elemental mercury infiltration.

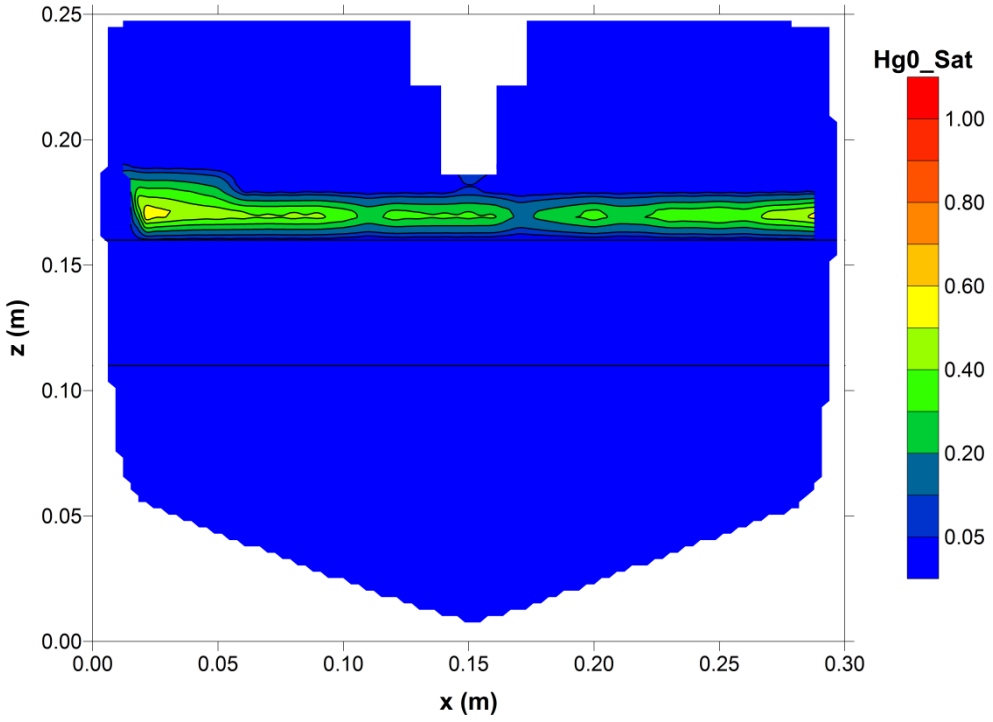

Fig. 6.11. Measured Hg^0 saturation profile - End of stage 1.

Therefore, even though the initial water saturation was lower in the left side of the sample, the effect of a higher intrinsic permeability probably prevailed in determining a preferential pathway for liquid Hg^0 migration.

This is confirmed by the overall increase of the water saturation above the Hg^0 front (Fig. 6.12), as consequence of the redistribution of the water phase induced by elemental mercury infiltration in the partially water saturated part of the sample. This is in agreement with what found in the $P_c(S)$ experiments (Chapter 4), thus strengthening the theoretical assumptions made in sec. 6.1.1 on liquid Hg^0 migration in partially water saturated porous media.

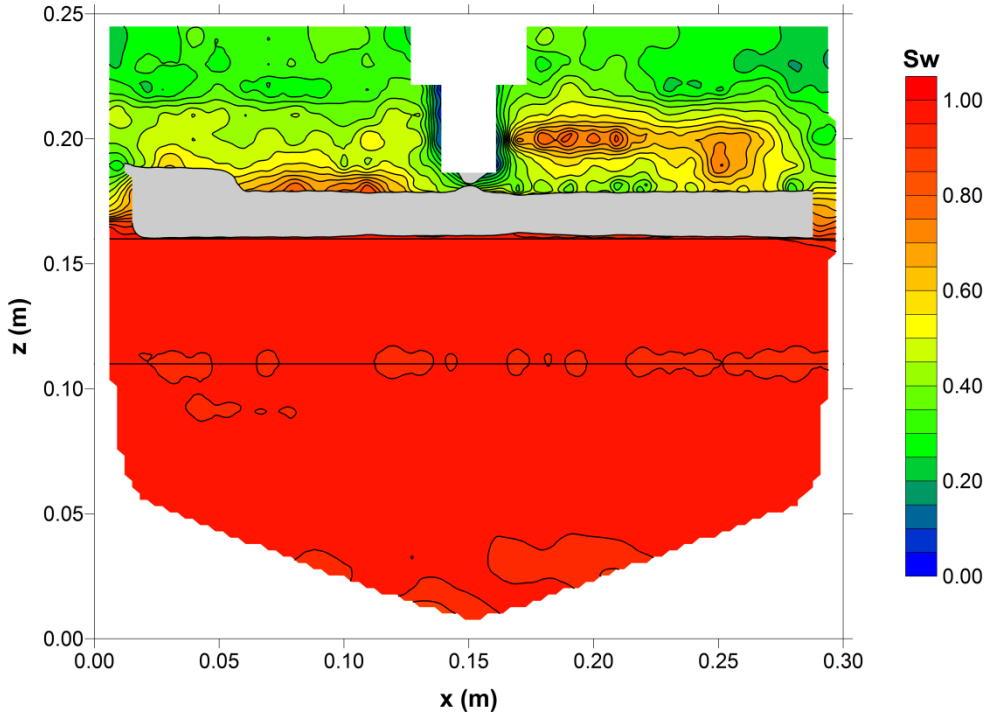

Fig. 6.12. Measured water saturation (S_w) profile (in grey the Hg^0 distribution) - End of stage 1.

6.3.2 Flow Container Experiment: Stage 2 - "Rain Event"

The second stage of the flow container experiment consisted of the simulation of a "rain event", to test whether redistribution of liquid Hg^0 present within the sample could be induced by local increases in water saturation. The increase in water saturation of the sample induced the infiltration of an additional volume of 4.7 ml of elemental mercury, to a total of 21 ml. Steady state was achieved in 2100 min (35 h) and the Hg^0 level in the

trench reached the final value of 4.2 cm. The mobilization of the liquid Hg^0 present within the sample occurred at the end of the rain event (Figs. 6.13 and 6.14), namely after 40 min, when the additional water, infiltrated from the top, almost completely saturated the MS1 layer above MS2.

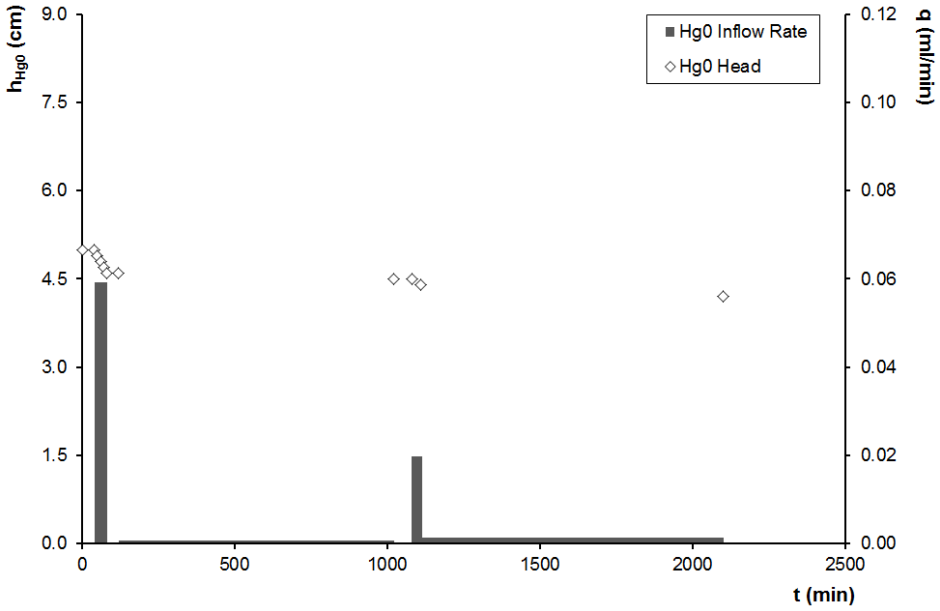

Fig. 6.13. Measured Hg^0 inflow rate and head over time - Stage 2.

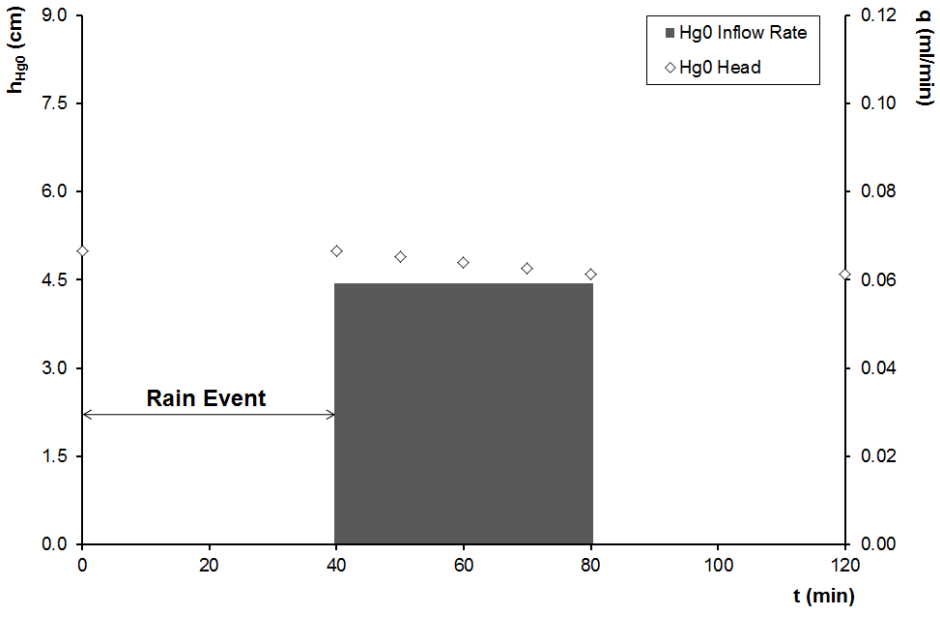

Fig. 6.14. Measured Hg^0 inflow rate and head over time (first 120 min) - Stage 2.

During stage 2, the infiltration of elemental mercury mostly occurred in the first 40 min following the end of the rain event (Figs. 6.13 and 6.14). The maximum Hg^0 inflow rate (Figs. 6.13 and 6.14) was half of the maximum value measured during stage 1 (Figs. 6.4 and 6.5). Both inflow rate and head assumed a stepwise pattern over time (Fig. 6.13), with large time intervals where no (or negligible) liquid Hg^0 infiltration occurred. This may be explained based on the times required by water to redistribute within the sample. Probably, as water slowly imbibed the pores, a displacement of air occurred, allowing further elemental mercury infiltration.

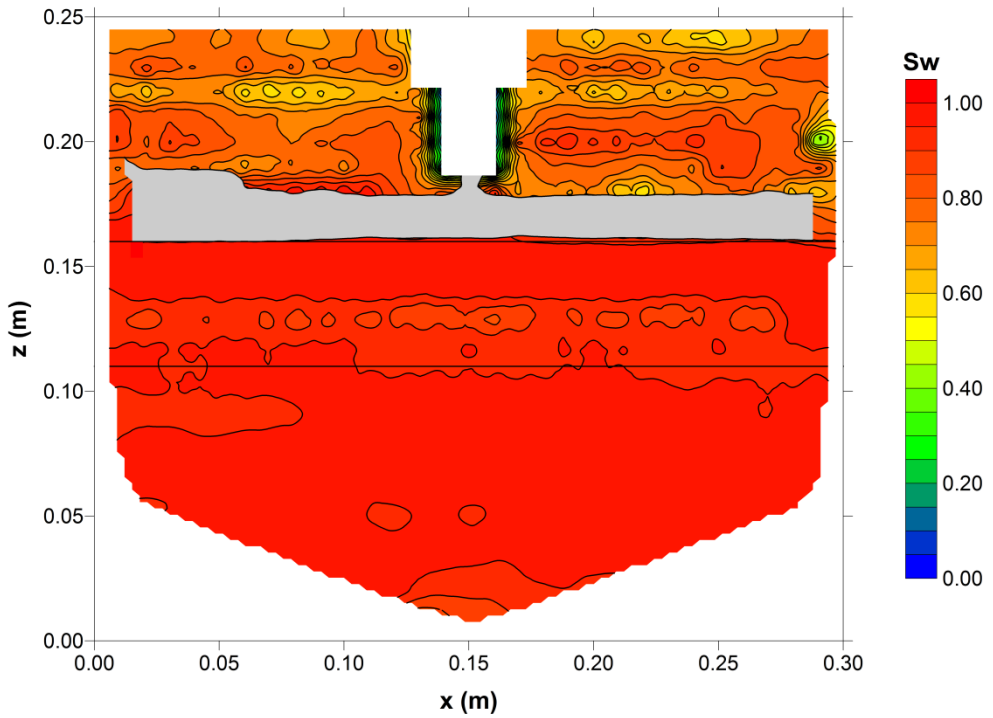

Fig. 6.15. Measured water saturation (S_w) profile (in grey the Hg^0 distribution) - End of stage 2.

Hence, the mobilization of elemental mercury was probably dictated by the local increase of the water saturation up to values close to unity (Fig. 6.15), since the Hg^0 entry head is lower in a fully rather than in a partially water saturated porous medium (Chapter 4).

During stage 2, no considerable changes in the shape of the Hg^0 front were noticed (Fig. 6.16), indicating that the additional volume of elemental mercury mainly moved within the areas of the sample where it was already present, thus locally increasing the DNAPL saturation.

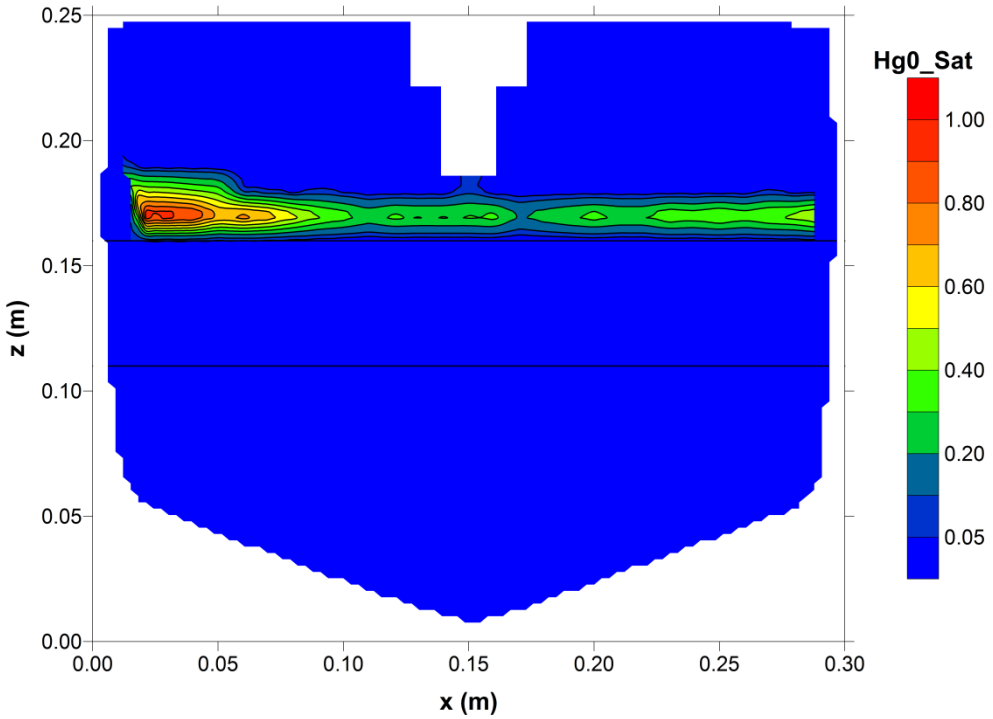

Fig. 6.16. Measured Hg^0 saturation profile - End of stage 2.

In particular, most of the additional liquid Hg^0 preferentially migrated towards the left side of the container, according to the presence of a higher permeability zone (sec. 6.3.1), thus reaching almost complete DNAPL saturation. Furthermore, in proximity of the left side wall, the Hg^0 presence showed a local thickening of its redistribution front (Fig. 6.17).

The second stage of the flow container experiment further strengthens the theoretical assumptions postulated in sec. 6.1.1, giving additional insight into the flow behaviour of elemental mercury DNAPL in variably water saturated porous media. These last experimental results provide an evidence that, if liquid Hg^0 infiltration occurs within a partially water saturated system, the extent and the magnitude of its migration can considerably increase when the water saturation increases and reaches values close to unity, especially if the mercury DNAPL is still connected within the porous formation with the original source of contamination. For example, if Hg^0 DNAPL is present in a ditch or in wastes buried in the unsaturated zone, an increase in the water saturation, induced by a groundwater table rise, prolonged and intense rains, or flooding, may cause elemental mercury to remobilize and infiltrate deeper in the subsurface.

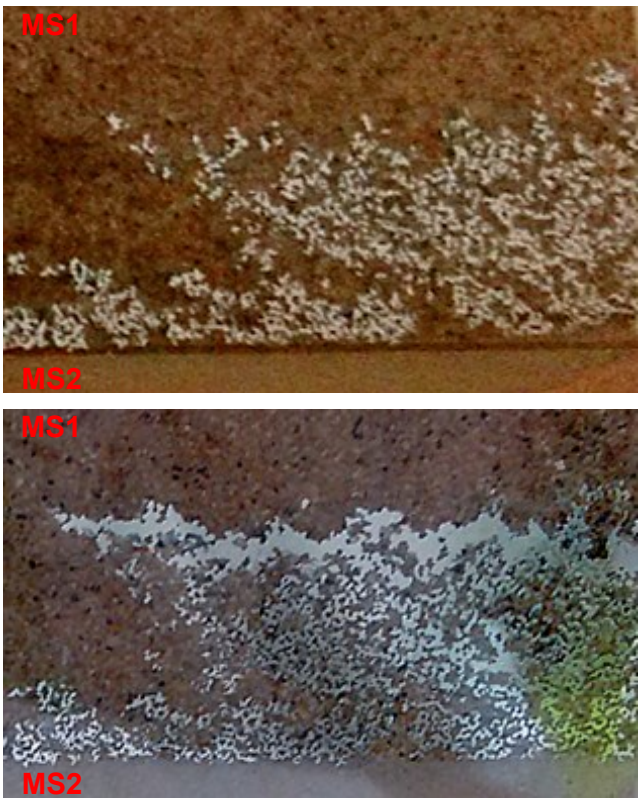

Fig. 6.17. Detail of the Hg^0 (re)distribution front at the end of stage 1 (top) and stage 2 (bottom).

6.3.3 Flow Container Experiment: Numerical Modelling

Hereinafter, the results of the numerical simulation of the first stage of the flow container experiment, performed with the modified version of GDAn (sec. 6.1), are presented. The results are reported up to a time of 261 min (4.35 h) because, after this time, the model showed high mass balance errors, and therefore the simulation was stopped. The reason of these errors is not clear yet and could be either induced by the new formulation of the P_c-S relationships (sec. 6.1.2) or by its numerical implementation (sec. 6.1.3). Among the causes likely responsible of these errors, the postulated transition from a three-phase system (Eq. 6.8c) to a pseudo two-phase system (Eq. 6.8d), and the analytical treatment of the capacity terms (Eq. 6.9), might have a major role. Moreover, another source of error might be found in the definition of the Hg^0 pressure field when mercury is initially absent in the porous medium (sec. 6.1.3), and the jump condition associated to the transition from the pristine configuration (two-phase air-water system) to the Hg^0 DNAPL presence within

the porous medium (three-phase Hg^0-air-water system) might lead to numerical errors. Hence, further analytical and numerical investigation is required. However, until 261 min, the numerical results showed a reasonable agreement with the experiment (sec. 6.3.1). Therefore, keeping in mind the limitations of the new model, these results are discussed hereinafter.

During the simulation, in accordance with the experimental results (sec. 6.3.1), the infiltration of liquid Hg^0 occurred at the bottom of the trench, with no evidence of lateral spreading until the MS2 layer was encountered. Furthermore, no infiltration of elemental mercury occurred in MS2 due to the higher entry head exhibited by the finer sand (Tab. 4.4). As a matter of fact, elemental mercury was not able to build enough head to penetrate within the overall smaller pores of MS2, thus preferentially migrating on top of it.

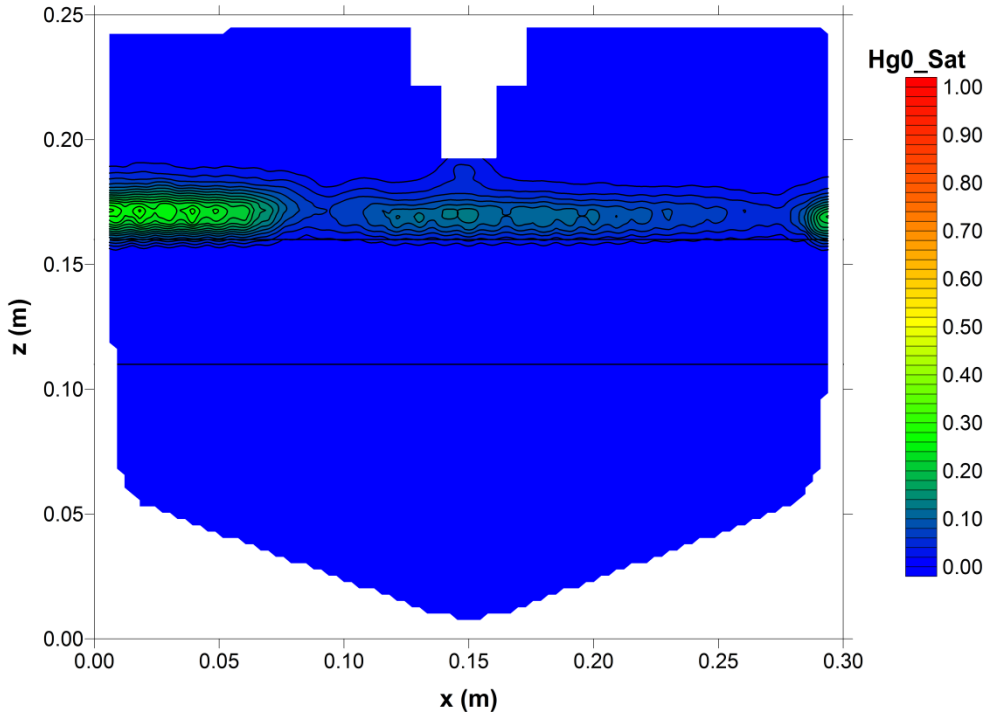

Fig. 6.18. Simulated Hg^0 saturation at 261 min (4.35 h).

Similar to the experimental observations, Hg^0 was found in higher saturations (Fig. 6.18) in proximity of the side walls of the container, where porosity was locally higher (Fig. 6.7). As a result of the predominance of gravity over capillary forces, the shape of the Hg^0 pool

appeared to be narrow, with heights ranging between 1 cm and 2 cm, thus not exceeding the values observed in the flow container experiment (sec. 6.3.1).

Taking into account the heterogeneity of porosity, intrinsic permeability, and P_c-S parameters, across the whole domain, played an important role in describing the transient infiltration of elemental mercury (Fig. 6.19).

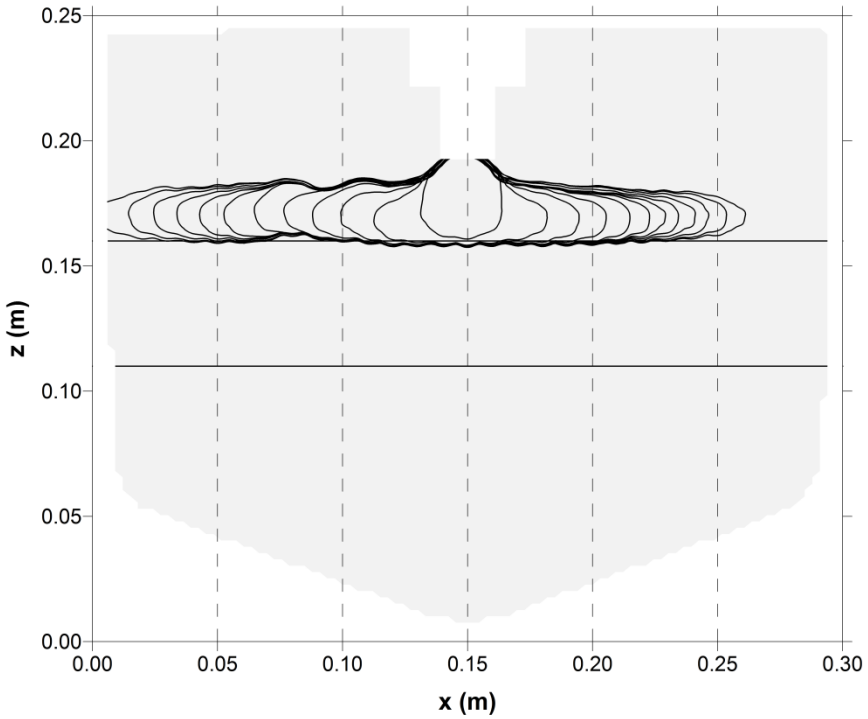

Fig. 6.19. Simulated Hg^0 infiltration front (S_n = 0.03) over time (10 min – 120 min) every 10 min.

As a result, according to the experimental observations (sec. 6.3.1), once Hg^0 reached the MS2 layer, it spread over it, and the shape of its infiltration front was asymmetric and markedly shifted towards the left part of the sample, which exhibited higher porosity (Fig. 6.7), hence higher intrinsic permeability and lower entry heads. Nevertheless, as the simulation progressed, the positions of the infiltration front over time, on both left and right sides of the sample, were affected by a lag. The comparison with the experimental observations (Fig. 6.10) shows that the position of the Hg^0 front was correctly predicted only on the left side and in the first 10 minutes of the infiltration, and the lag increased as the simulation advanced over time. While in the experiment the infiltration front reached

the left side wall of the container in approximately 60 min (1 h), the simulated Hg^0 front came in contact with the left side boundary only after 120 min (2 h).

Among the reasons of the discrepancies found between the experimental results and the numerical simulation, the uncertainty related to the correlation of porosity with both intrinsic permeability and retention properties probably played an important role. Even though the non-intrusive measurements performed with the dual gamma ray system allowed a detailed description of the porosity field, the information derived with the Kozeny-Carman formula and the modified Leverett function were probably not sufficient for a reliable estimation of the parameters used in the numerical simulation. Moreover, as reported in sec. 6.3.1, the knowledge of the $P_c(S)$ curves under stable flow behaviour (Chapter 4) was not sufficient for the correct prediction of realistic liquid Hg^0 infiltration scenarios like that described previously. Especially in the first stage of the infiltration, elemental mercury, due to its remarkably high density (Tab. 4.2), proved to be dominated by gravitational forces, hence the need of a characterization of its retention properties under unstable flow behaviour. To this must be also added the uncertainty related to the scaling of liquid Hg^0 retention properties in partially water saturated systems (Chapter 4).

Even though some of the key features of Hg^0 DNAPL infiltration and distribution in variably water saturated porous media were captured by the model, the proposed theoretical and mathematical framework (sec. 6.1), as well as its numerical implementation, needs further validation and verification, and more physical knowledge is required. In particular, experimental investigations at the pore level would be beneficial to assess whether the postulated wettability hierarchy, between liquid Hg^0, air, and water, effectively reproduces what happens when these three phases interact between each other within a porous medium. A better understanding and a quantification of the air entrapment, induced by the combined effect of liquid Hg^0 imbibition and subsequent water displacement, would also give additional insight into the elemental mercury infiltration dynamics. A further hypothesis to verify is whether neglecting the air phase compressibility and its pressure field is a good approximation or not when liquid Hg^0 infiltrates within a partially water saturated pore. In the end, the new formulation is far from being exhaustive of elemental mercury flow behaviour in variably water saturated

porous media, nevertheless, it represents a first step towards the definition of a new comprehensive formulation, thus laying the groundwork for future research.

References

Abriola LM, Pinder GF (1985). *A multiphase approach to the modeling of porous media contamination by organic compounds: 1. Equation development*. Water Resources Research, 21(1), 11-18.

Abriola LM, Rathfelder K (1993). *Mass balance errors in modeling two-phase immiscible flows: causes and remedies*. Advances in Water Resources, 16, 223-239.

Bear J (1972). *Dynamics of fluids in porous media*. Dover Publications, Inc., New York.

Burdine N (1953). *Relative permeability calculations from pore size distribution data*. Journal of Petroleum Technology, 5(3), 71-78.

Carman PC (1938). *The determination of the specific surface of powders*. Journal of the Society of Chemical Industry, 57, 225.

Carman PC (1956). *Flow of gases through porous media*. Butterworths Scientific Publications, London.

Dekker TJ, Abriola LM (2000). *The influence of field-scale heterogeneity on the infiltration and entrapment of dense nonaqueous phase liquids in saturated formations*. Journal of Contaminant Hydrology, 42(2), 187-218.

Domenico PA, Mifflin MD (1965). *Water from low-permeability sediments and land subsidence*. Water Resources Research, 1(4), 563-576.

Fitts CR (2002). *Groundwater science*. Academic Press.

Kaluarachchi JJ, Parker JC (1989). *An Efficient Finite Element Method for Modeling Multiphase Flow*. Water Resources Research, 25(1), 43-54.

Kaluarachchi JJ, Parker JC (1992). *Multiphase Flow with a Simplified Model for Oil Entrapment*. Transport in Porous Media, 7(1), 1-14.

Kozeny J (1927). *Ueber kapillare Leitung des Wassers im Boden*. Akademie der Wissenschaften in Wien, 136 (2a), 271.

Kueper BH, Frind EO (1991). *Two-phase flow in heterogeneous porous media: 2. Model application*. Water Resources Research, 27(6), 1059-1070.

Kueper BH, Gerhard JI (1995). *Variability of point source infiltration rates for two-phase flow in heterogeneous porous media*. Water Resources Research, 31(12), 2971-2980.

Lenhard RJ, Parker JC (1987). *Measurement and prediction of saturation-pressure relationships in three-phase porous media systems*. Journal of Contaminant Hydrology, 1, 407–424.

Lenhard RJ, Parker JC, Kaluarachchi JJ (1989). *A Model for Hysteretic Constitutive Relations Governing Multiphase Flow 3. Refinements and Numerical Simulations*. Water Resources Research, 25(7), 1727-1736.

Lenhard RJ (1992). *Measurement and modeling of three-phase saturation-pressure hysteresis*. Journal of Contaminant Hydrology, 9(3), 243-269.

Leverett M (1941). *Capillary behavior in porous solids*. Transactions of the AIME, 142(01), 152-169.

Mualem Y (1976). *A new model for predicting the hydraulic conductivity of unsaturated porous media*. Water Resources Research, 12(3), 513-522.

Parker JC, Lenhard RJ, Kuppusamy T (1987). *A Parametric Model for Constitutive Properties Governing Multiphase Flow in Porous Media*. Water Resources Research, 23(4), 618-624.

Parker JC (1989). *Multiphase flow and transport in porous media*. Reviews of Geophysics, 27(3), 311-328.

Sweijen T, Hartog N, Marsman A, Keijzer TJ (2014). *The transport behaviour of elemental mercury DNAPL in saturated porous media: Analysis of field observations and two-phase flow modelling*. Journal of Contaminant Hydrology, 161, 24-34.

van Genuchten MT (1980). *A closed form equation for predicting the hydraulic conductivity of unsaturated soils*. Soil Science Society of American Journal, 44, 892–898.

White MD, Oostrom M, Lenhard RJ (2004). *A Practical Model for Mobile, Residual, and Entrapped NAPL in Water-Wet Porous Media*. Ground Water, 42(5), 734-746.

Young HD, Freedman RA, Ford AL (2012). *Sears and Zemansky's University Physics with Modern Physics*. Addison-Wesley, ISBN 978-0321696861.

Notation

Greek Symbols

α	van Genuchten model parameter
β_{an}	Air-NAPL system scaling parameter
β_{ma}	Hg^0-Air system scaling parameter
β_{mw}	Hg^0-Water system scaling parameter
β_{nw}	NAPL-Water system scaling parameter
ϕ	porosity

Latin Symbols

d_{50}	median particle diameter
h_a	air pressure head
h_{an}	Air-NAPL capillary pressure head
h_{aw}	Air-Water capillary pressure head
h_c	capillary pressure head
h_e	nonwetting phase entry head
h_m	Hg^0 pressure head
h_{ma}	Hg^0-Air capillary pressure head
h_n	NAPL pressure head

h_{nw}	NAPL-Water pressure head
h_w	water pressure head
k	intrinsic permeability
k_r	relative permeability
m	van Genuchten model parameter
n	van Genuchten model parameter
P_c	capillary pressure
S	saturation
$\bar{S}$	effective wetting phase saturation
S_a	air saturation
S_m	Hg^0 saturation
S_t	total liquid saturation
S_{taw}	total air-water saturation
S_w	water saturation
$S_{w,ir}$	irreducible water saturation
$\overline{S_a}$	effective air saturation
$\overline{S_m}$	effective Hg^0 saturation
$\overline{S_{me}}$	effective entrapped Hg^0 saturation
$\overline{S_{mf}}$	effective free Hg^0 saturation
$\overline{S_n}$	effective NAPL saturation
$\overline{S_t}$	effective total liquid saturation
$\overline{S_{taw}}$	effective total air-water saturation
$\overline{S_w}$	effective water saturation
$\overline{\overline{S_w}}$	apparent water saturation
SF	particles shape factor
t	time

Chapter 7

Synthesis and Conclusions

The aim of this research was to give additional insight into the flow behaviour of elemental mercury DNAPL in porous media. As shown in Chapter 1, Hg^0 DNAPL can act as a long lasting source of contamination in the subsurface, causing detrimental consequences for the human health and the environment (US EPA, 2007; World Chlorine Council, 2011). Therefore, insight into the flow behaviour of liquid elemental mercury in porous media is needed and is critical in assessing the control of contaminant spreading as well as remediation approaches. However, the scientific literature on Hg^0 DNAPL is still very limited (Chapter 1) and, to date, it was unclear to what extent the validity of the classical constitutive relations (Parker et al., 1987), used to describe DNAPLs flow behaviour, as well as the scaling theory (Lenhard and Parker, 1987), held for elemental mercury. These issues become crucial in partially water saturated porous media, where liquid Hg^0 behaves as a nonwetting phase with respect to both air and water (Chapters 4 and 6). To address these knowledge gaps, experimental and numerical analysis were performed within the current research. Hereinafter, the main findings of the research activity are highlighted and discussed together with the implications for future research.

7.1 Liquid Hg^0 Attenuation Potential of Gamma Rays

Liquid Hg^0 showed a strong attenuation potential of gamma rays if compared to demineralized water and PCE (Chapter 3). As a matter of fact, for all the path lengths considered (from 0.1 cm to 4 cm), liquid Hg^0 shielded Americium radiation completely.

The Americium peak practically disappears even with 1 mm thickness of elemental mercury between the radioactive source and the detector, and only Cesium radiation is able to pass through liquid Hg^0. Even though Cesium has a stronger capacity to penetrate matter than Americium, liquid Hg^0 shows a remarkably high attenuation coefficient with respect to this gamma radiation, about 17 times higher than water. According to Beer-Lambert law, this implies that 0.5 cm of liquid Hg^0 are sufficient to attenuate Cesium radiation of about 47%, whereas 2 cm can induce an attenuation of 92%. However, according to the thickness (4-5 cm) and average porosity (0.363-0.380) of the porous samples used for the Hg^0 flow container experiments (Chapters 5 and 6), at 100% of mercury saturation, liquid Hg^0 could reach a maximum thickness of about 2 cm within the samples, thus enabling the use of the Cesium source to determine its complete range of saturation.

Furthermore, with the current dual gamma ray system, elemental mercury saturation can be correctly derived from Beer-Lambert law only when the porous medium is completely dry or water saturated. As a matter of fact, when a three-phase system of air, NAPL, and water is encountered within a porous medium, the determination of the liquid phases saturation is usually performed by solving simultaneously Beer-Lambert equation for both radioactive sources, but, in the case of liquid mercury, this is not possible because of the complete attenuation of Americium. Therefore, to perform a quantitative analysis of elemental mercury DNAPL flow behaviour in partially water saturated porous media, an approximate procedure was developed (Chapter 6).

These experimental results highlight that, when analysing Hg^0 DNAPL flow behaviour in porous media by means of non-intrusive techniques as GRA (Gamma Ray Attenuation), attention must be paid in the choice of the sources of radiation. In particular, the sources should be strong enough to penetrate liquid Hg^0 to at least some extent, and the sample thickness should not exceed a certain path length to allow a correct characterization of Hg^0 DNAPL saturation range within the porous medium.

7.2 Infiltration Behaviour of Hg^0 DNAPL in Variably Water Saturated Porous Media

In Chapter 4, the infiltration behaviour of Hg^0 DNAPL was studied using $P_c(S)$ experiments of two- and three-phase fluid systems, in two types of medium sand (MS1 and

MS2) and three types of glass beads (coarse, medium and fine) with different particle size distribution characteristics.

Two-phase flow experiments of liquid Hg^0 and water in glass beads revealed the importance of pore structure on elemental mercury DNAPL infiltration behaviour. Elemental mercury entry heads were higher in samples with lower intrinsic permeability, but not necessarily with lower porosity. Although intrinsic permeability is a bulk parameter affected by the combined inner pore structure characteristics of a porous medium, it related with the more locally expressed entry head for the glass beads samples. However, within the small range in intrinsic permeability of the medium sand samples used, the correlation did not hold. Despite the somewhat higher intrinsic permeability of MS2, the entry head is higher than for MS1. Likely, this is the result of the smaller particle size and narrow range in MS2 than MS1, which limit the potential for locally present larger pores.

In water saturated porous media, elemental mercury behaves like other DNAPLs, such as PCE, thus requiring to overcome an entry head to infiltrate. The results of the PCE-Water and the Hg^0-Water $P_c(S)$ experiments in sands showed that liquid Hg^0 capacity to infiltrate is higher than that of PCE. In terms of the respective DNAPL heads, PCE required to overcome an entry head of about 60% higher than Hg^0 for MS1, while of about 26% for MS2. Conversely, according to Leverett scaling (Leverett, 1941), PCE should have required to overcome an entry head of about 5.6% higher than liquid Hg^0 to infiltrate in the same porous medium. Although Leverett scaling was able to reproduce the natural tendency of liquid Hg^0 to be more prone than PCE to infiltrate in water saturated porous media, it considerably underestimated Hg^0 infiltration capacity in comparison with the experimental results.

In contrast with other NAPLs, elemental mercury is a nonwetting fluid in partially water saturated porous media. Hence, to infiltrate, it requires to overcome an entry head, and its migration is affected by the presence of water in the pores. As shown in the experiments, once liquid mercury overcame the resistance exerted by the presence of continuous air and infiltrated within the samples, it also displaced water. Prior to liquid Hg^0 infiltration, the air phase is expected to be present in higher saturations in bigger pores, hence, as elemental mercury infiltrates, it is likely to find a preferential pathway through smaller pores, mostly filled with water. Even though the pores are smaller, elemental mercury displaces water

easier than air, due to the lower interfacial tension with water. As mercury infiltration continued, the air phase became discontinuous and entrapped within both liquid phases, and most of the elemental mercury came in contact with water. At this point, the further infiltration of mercury induced the displacement of an equal amount of water.

Based on the required DNAPL heads, the capacity of Hg^0 to infiltrate in partially water saturated porous media was lower than PCE and Hg^0 in fully water saturated systems. The elemental mercury entry head in a partially water saturated system was 5.6% higher than for PCE in fully water saturated conditions for MS1, while it was practically the same of PCE for MS2. The comparison of Hg^0 entry heads in partially and fully water saturated systems showed differences more pronounced. As a matter of fact, for the partially water saturated MS1 sample, Hg^0 required to overcome an entry head 68.9% higher than required in the fully water saturated counterpart. Also for MS2, the entry head in the partially water saturated system was higher than for the fully water saturated counterpart, by 25.8%.

In the partially water saturated samples, the mercury entry heads were determined at residual water saturations and it could be expected that entry heads would increase further at lower partial water contents. Therefore, assuming Leverett scaling to be applicable, the Hg^0 entry head at zero water saturation (namely 100% air saturation) was estimated, for both sands, based on the measured Hg^0 and PCE entry heads in water saturated media. The Leverett scaled PCE-Water values of the Hg^0 entry head at zero water saturation were 16.1% and 22.7% higher than the experimental observations for the partially water saturated samples, for MS1 and MS2, respectively. For the Hg^0-Water scaled values, only the scaled entry head in MS2 was higher, 2.8%, than for the partially water saturated sample. Conversely, for MS1 the scaled value of the Hg^0 entry head at zero water saturation was 23.4% lower. Nevertheless, in both cases, the scaled values were higher than the measured Hg^0 entry heads for the water saturated conditions, 29.3% for the Hg^0-Water scaled values, and 96% and 54.4% for the PCE-Water scaled values, for MS1 and MS2, respectively. How entry head develops in more detail with decreasing water content remains to be explored. However, considering the spread in the scaled estimates for the entry head at zero water saturation, the entry head in the partially water saturated (residual) conditions is possibly already controlled by the larger, air filled, pores.

Liquid Hg^0 infiltration behaviour in porous media is unique with respect to well-known DNAPLs, such as PCE. As a matter of fact, both theory and experiments confirmed that elemental mercury behaves as a nonwetting fluid in both fully and partially water saturated porous media, thus requiring to overcome an entry head to infiltrate, while PCE, like other DNAPLs, exhibits an entry head only when the porous medium is fully water saturated. Hence, the conventional wettability hierarchy, in which the NAPL has an intermediate wetting state between the air and the water phases, is not valid for elemental mercury. Therefore, a new formulation of the constitutive relations governing elemental mercury flow behaviour in variably water saturated porous media was proposed in Chapter 6.

An attempt of scaling liquid Hg^0 constitutive relations was also made for both fully and partially water saturated systems. The deviations found in both two- and three-phase systems may suggest that the classical scaling theory is less able to cope with Hg^0 retention properties than for other NAPLs. Still, the order of magnitude of the experimental scaling parameters is similar to that of the determinations based solely on the fluids properties, thus not excluding its application to elemental mercury DNAPL. Among the reasons for the observed discrepancies is probably that, if the porous medium is partially water saturated to a degree that allows air to be continuous within the pores, the Hg^0 that tries to infiltrate is expected to be predominantly in contact with air. However, as the sample is water wet, it is also in contact with water, hence the Leverett scaling parameter, defined as the ratio of water and Hg^0 surface tensions, may not be accurate, and the effect induced by the Hg^0 interfacial tension with water could be relevant. Furthermore, once infiltration occurs in a partially water saturated porous medium, elemental mercury displaces both air and water, depending on the initial water distribution within the pores, thus further enhancing the difficulty to cope with its particular behaviour.

7.3 Infiltration and Distribution of Hg^0 DNAPL in Water Saturated Porous media

In Chapter 5, the infiltration and distribution behaviour of Hg^0 DNAPL in water saturated stratified granular porous media was analysed by means of two-dimensional flow container experiments. Non-intrusive measurements of porosity fields and DNAPLs saturation profiles, performed with the dual gamma ray system (Chapter 3), allowed a quantitative

evaluation of elemental mercury infiltration and distribution behaviour. Moreover, to assess to what extent numerical modelling can predict elemental mercury migration in water saturated porous media, a selected flow container experiment was simulated using GDAn (Chapter 2).

The first set of experiments consisted of the comparison of Hg^0 DNAPL infiltration and distribution behaviour in sands with that of PCE. The main difference between the two PCE and Hg^0 infiltration experiments was found in the early stage of the infiltration process. While PCE infiltrated and distributed within the water saturated porous sample, liquid Hg^0 did not. When elemental mercury was poured between the inlet walls, the sand particles of the top layer were displaced and started floating over the top of Hg^0 surface, due to their lack of cohesion and lower density. More mercury was added to build a sufficient head to overcome the sand entry head but, rather than infiltrating in the porous sample, liquid Hg^0 found a preferential pathway between the inlet walls and the front walls of the container, thus spreading over the top surface of the sand.

The $P_c(S)$ experiments (Chapter 4) showed that, in water saturated porous media, for the same sands, elemental mercury behaves like other DNAPLs, thus requiring to overcome an entry head to infiltrate. In terms of respective DNAPL heads, Hg^0 entry head was lower than that of PCE, thus enhancing elemental mercury natural tendency to be more prone than PCE to infiltrate in water saturated porous media. Hence, the reason of such a sharp difference in the infiltration behaviour exhibited by the two DNAPLs in the flow container experiments was not immediately clear. Most probably, the difference in the intrinsic permeability field of the two flow container samples played a major role. Dual gamma ray measurements of the porosity field confirmed this, revealing significant differences among the two samples. As a matter of fact, the sample used for the Hg^0 flow container experiment showed a porosity remarkably lower than the one used for the infiltration of PCE. Such a strong difference in porosity likely resulted in a sharp difference in intrinsic permeability, thus inducing differences in entry head. In particular, this difference in porosity was more pronounced in proximity of the inlet, namely where the infiltration should have occurred. Therefore, Hg^0 did not infiltrate because it was unable to build a sufficient head to overcome the higher entry head induced by a locally lower intrinsic permeability.

The flow container experiment with glass beads showed that infiltration and distribution of Hg^0 DNAPL are affected by the heterogeneities present within the porous formation as for other DNAPLs, such as PCE. The infiltration was fast and the finer horizontal glass beads layer was rapidly reached by the heavy DNAPL. Then, elemental mercury distributed over the top of the horizontal layer of finer material, migrating towards the highest porosity zone of the sample. Finally, no elemental mercury was able to penetrate this horizontal layer, and a flat pool, of about 1 cm height, formed on top of it.

Numerical simulations, performed with GDAn (Chapter 2), showed an overall good agreement with the experimental results in glass beads, thus showing that conventional multiphase flow models can cope with Hg^0 DNAPL migration in water saturated porous media. The main features of Hg^0 DNAPL migration, such as the magnitude of the infiltration time, the stretched shape of the infiltration front along the vertical axis as a result of the predominance of gravity over capillary forces, and the spreading above the finer glass beads layer without penetrating it, were well captured.

However, numerical simulations were not able to perfectly replicate the experimental observations. The discrepancies found between the experimental results and the numerical predictions were most probably due to the lack of knowledge of the Hg^0 inflow rate and to the low agreement of the correlation between the measured porosity field with the estimated intrinsic permeability and retention properties. Even though the non-intrusive measurements performed with the dual gamma ray system allowed a detailed description of the porosity field, the correlation of porosity with intrinsic permeability, as well as with the retention properties, would have required more experimental determinations to guarantee a more reliable estimation. The information based on Kozeny-Carman formula (Kozeny, 1927; Carman, 1938, 1956; Bear, 1972; Fitts, 2002) and on the generalized Leverett function (Kueper and Frind, 1991; Dekker and Abriola, 2000) proved to be not sufficient outside the porosity range defined with the hydraulic conductivity and $P_c(S)$ experiments on glass beads (Chapter 4). Nevertheless, the sensitivity analysis performed on the modified Leverett function confirmed numerical predictions dependency on the correlation between intrinsic permeability and retention properties, showing improvements in the numerical results as this correlation was strengthened.

In the end, as found for organic DNAPLs, like PCE, by Dekker and Abriola (2000), this study showed that (i) the knowledge of the inflow rate, (ii) the reliable estimation of the porous formation permeability, and (iii) the accurate representation of the correlation between $P_c(S)$ curves and intrinsic permeability are critical for the prediction of liquid Hg^0 migration in porous media as well, thus confirming the similarity with other DNAPLs of its infiltration and distribution behaviour in water saturated porous media.

7.4 Infiltration and (Re)Distribution of Hg^0 DNAPL in Variably Water Saturated Porous Media

Chapter 6 dealt with the analysis of Hg^0 DNAPL infiltration and (re)distribution behaviour in variably water saturated porous media. From the experimental analysis described in Chapter 4, the need of a new theoretical formulation of liquid elemental mercury retention properties in variably water saturated porous media clearly emerged. To further enforce this, in Chapter 6, the inapplicability of the conventional constitutive relations governing multiphase flow in partially water saturated porous media (Parker et al., 1987) was demonstrated with an example. As a matter of fact, due to the values assumed by the Hg^0 scaling parameters (Chapter 4), these relations do not give satisfactory results.

A new theoretical formulation was then proposed. The crucial assumption is that, when liquid Hg^0, air, and water coexist within the pores of a water wet porous medium, the solid particles are expected to "like" elemental mercury less than air and water, due to its remarkably high surface tension. Moreover, air is assumed to be continuous and extremely mobile within the porous medium, thus neglecting its compressibility as well as any variation in its pressure field, equal to the atmospheric value. Hence, under this condition, elemental mercury infiltration occurs when it has sufficient head to overcome the entry head dictated by the presence of air within the pores. If it is so, its infiltration is followed by a displacement of air and water.

The new constitutive relationship was also enforced within the GDAn code (Chapter 2), thus proving that only few modifications must be performed to successfully implement the new procedure in conventional multiphase flow programs.

Then, a two-dimensional flow container experiment in a variably water saturated stratified granular porous medium was described and analysed. The first stage of the experiment

consisted of the Hg^0 DNAPL infiltration and distribution in a partially water saturated system. When elemental mercury infiltration stopped and the distribution front reached the steady state, the second stage of the experiment started. In particular, this stage consisted of the simulation of a "rain event" to assess whether the elemental mercury already infiltrated within the sample could be mobilized due to the local increase in water saturation. To perform a quantitative analysis of elemental mercury DNAPL flow behaviour, non-intrusive measurements of porosity, water and liquid Hg^0 saturations were performed over the whole sample with the dual gamma ray system (Chapter 3). In the locations where elemental mercury was found, the analytical formulation usually adopted to derive the fluid saturations in presence of three different phases could not be used due to the complete attenuation of the Americium source exerted by liquid Hg^0 (Chapter 3). To circumvent this problem, an approximate procedure was developed.

During the first stage of the flow container experiment, Hg^0 DNAPL infiltration took place directly at the bottom of the DNAPL reservoir, with no evidence of lateral spreading until the horizontal finer layer (MS2) was encountered. The Hg^0 head under which the infiltration occurred in MS1 was much lower than the one that could be predicted on the basis of the $P_c(S)$ measurements (Chapter 4). This about 25.7-40.6% lower entry head occurred despite both average porosity and water saturation, in the first centimeter beneath the inlet, being about 4% and 2.5 times lower than measured in the $P_c(S)$ experiment. This appears to be in contrast with the experimental results presented in Chapter 4, since a reduction in both porosity and water saturation would be expected to yield higher rather than lower entry heads. Such a strong deviation was probably induced by the fact that the entry heads obtained with the $P_c(S)$ measurements were derived under stable flow behaviour, while the infiltration in the flow container was likely unstable. Consequently, the effect of gravity might have been predominant in the first stages of the infiltration. In particular, visual observations indicated that at least two fingers developed and, since lateral spreading occurred above MS2, elemental mercury was likely continuous beneath the reservoir, thus providing a connection with the DNAPL source in the inlet, as suggested by the inflow rate and the dual gamma ray measurements.

Once the top layer of MS2 was reached, the DNAPL distributed above it, thus creating a pool of about 1 cm height. Elemental mercury distribution over MS2 was not symmetric,

probably as a result of the variability of both porosity field and initial water saturation distribution.

Above the Hg^0 front, an overall increase of the water saturation was noticed as a consequence of the redistribution of the water phase, induced by elemental mercury infiltration in the partially water saturated part of the sample. This was in agreement with what found in the $P_c(S)$ experiments (Chapter 4), thus strengthening the theoretical assumptions made on Hg^0 migration in partially water saturated porous media.

The second stage of the flow container experiment showed that mobilization of the liquid Hg^0 present within the sample occurred at the end of the rain event, when the additional water, infiltrated from the top, almost completely saturated the MS1 layer above MS2. Hence, the mobilization of elemental mercury was probably dictated by the local increase of the water saturation up to values close to unity, since the Hg^0 entry head is lower in a fully rather than in a partially water saturated porous medium (Chapter 4). During stage 2, no considerable changes in the shape of the Hg^0 front were noticed, indicating that the additional volume of elemental mercury mainly moved within the areas of the sample where it was already present, thus locally increasing the DNAPL saturation.

The second stage of the flow container experiment further strengthens the theoretical assumptions postulated in this work, giving additional insight into the flow behaviour of elemental mercury DNAPL in variably water saturated porous media. These last experimental results provide an evidence that, if liquid Hg^0 infiltration occurs within a partially water saturated system, the extent and the magnitude of its migration can considerably increase when the water saturation increases and reaches values close to unity, especially if the mercury DNAPL is still connected within the porous formation with the original source of contamination. For example, if Hg^0 DNAPL is present in a ditch or in wastes buried in the unsaturated zone, an increase in the water saturation, induced by a groundwater table rise, prolonged and intense rains, or flooding, may cause elemental mercury to remobilize and infiltrate deeper in the subsurface.

To assess to what extent the proposed model can predict elemental mercury infiltration and distribution in partially water saturated porous media, the first stage of the flow container experiment was simulated with the modified version of GDAn. However, the results were reported up to a time of 261 min (4.35 h) because, after this time, the model showed high

mass balance errors, and therefore the simulation was stopped. The reason of these errors is not clear yet and could be either induced by the new formulation of the P_c-S relationships or by its numerical implementation. Among the causes likely responsible of these errors, the postulated transition from a three-phase system to a pseudo two-phase system, and the analytical treatment of the capacity terms, might have a major role. Moreover, another source of error might be found in the definition of the Hg^0 pressure field when mercury is initially absent in the porous medium, and the jump condition associated to the transition from the pristine configuration (two-phase air-water system) to the Hg^0 DNAPL presence within the porous medium (three-phase Hg^0-air-water system) might lead to numerical errors. Hence, further analytical and numerical investigation is required.

However, until 261 min, the numerical results showed a reasonable agreement with the experiment. As a matter of fact, in accordance with the experimental results, the infiltration of liquid Hg^0 occurred at the bottom of the inlet, with no evidence of lateral spreading until the MS2 layer was encountered. Furthermore, no infiltration of elemental mercury occurred in MS2 due to the higher entry heads exhibited by the finer sand. Similar to the experimental observations, Hg^0 was found in higher saturations in proximity of the side walls of the container, where porosity was locally higher. Nevertheless, as the simulation progressed, the positions of the infiltration front over time, on both left and right sides of the sample, were affected by a lag.

Among the reasons of the discrepancies found between the experimental results and the numerical simulation, the uncertainty related to the correlation of porosity with both intrinsic permeability and retention properties probably played an important role. Even though the non-intrusive measurements performed with the dual gamma ray system allowed a detailed description of the porosity field, the information derived with the Kozeny-Carman formula and the modified Leverett function were probably not sufficient for a reliable estimation of the parameters used in the numerical simulation. Moreover, as previously shown, the knowledge of the $P_c(S)$ curves under stable flow behaviour was not sufficient. In the end, to this must be also added the uncertainty related to the scaling of liquid Hg^0 retention properties in partially water saturated systems (Chapter 4).

7.5 Implications for Future Research

Liquid elemental mercury showed a unique infiltration and distribution behaviour in porous media with respect to well-known DNAPLs, such as PCE. Through experiments and modelling, this research confirmed that Hg^0 DNAPL behaves as a nonwetting fluid in both fully and partially water saturated porous media, thus highlighting that the conventional wettability hierarchy, in which the NAPL has an intermediate wetting state between the air and the water phases, is not valid for elemental mercury. Furthermore, the deviations found in both two- and three-phase systems suggested that the classical scaling theory is less able to cope with liquid Hg^0 retention properties than for other NAPLs.

Conventional multiphase flow modelling proved to be able to cope with Hg^0 DNAPL infiltration and distribution behaviour in water saturated porous media, showing similarities with well-known DNAPLs. However, the same results were not obtained in partially water saturated porous media. Even though some of the key features of Hg^0 DNAPL infiltration and distribution in partially water saturated porous media were captured by the model, the proposed theoretical and mathematical framework, as well as its numerical implementation, needs further validation and verification, and more physical knowledge is required.

Experimental investigations at the pore level would be beneficial to assess whether the postulated wettability hierarchy, between liquid Hg^0, air, and water, effectively reproduces what happens when these three phases interact between each other within a porous medium. A better understanding and a quantification of the air entrapment, induced by the combined effect of liquid Hg^0 imbibition and subsequent water displacement, would also give additional insight into the elemental mercury infiltration dynamics. A further hypothesis to verify is whether neglecting the air phase compressibility and its pressure field is a good approximation or not when liquid Hg^0 infiltrates within a partially water saturated pore.

In the end, this research is far from being exhaustive of elemental mercury DNAPL flow behaviour in variably water saturated porous media, nevertheless, it represents a first step towards the definition of a new comprehensive formulation, thus laying the groundwork for future research.

References

Bear J (1972). *Dynamics of fluids in porous media*. Dover Publications, Inc., New York.

Carman PC (1938). *The determination of the specific surface of powders*. Journal of the Society of Chemical Industry, 57, 225.

Carman PC (1956). *Flow of gases through porous media*. Butterworths Scientific Publications, London.

Dekker TJ, Abriola LM (2000). *The influence of field-scale heterogeneity on the infiltration and entrapment of dense nonaqueous phase liquids in saturated formations*. Journal of Contaminant Hydrology, 42(2), 187-218.

Fitts CR (2002). *Groundwater science*. Academic Press.

Kueper BH, Frind EO (1991). *Two-phase flow in heterogeneous porous media: 2. Model application*. Water Resources Research, 27(6), 1059-1070.

Kozeny J (1927). *Ueber kapillare Leitung des Wassers im Boden*. Akademie der Wissenschaften in Wien, 136 (2a), 271.

Lenhard RJ, Parker JC (1987). *Measurement and prediction of saturation-pressure relationships in three-phase porous media systems*. Journal of Contaminant Hydrology, 1, 407–424.

Leverett M (1941). *Capillary behavior in porous solids*. Transactions of the AIME, 142(01), 152-169.

Parker JC, Lenhard RJ, Kuppusamy T (1987). *A Parametric Model for Constitutive Properties Governing Multiphase Flow in Porous Media*. Water Resources Research, 23(4), 618-624.

US EPA (2007). *Treatment Technologies for Mercury in Soil, Waste, and Water*. EPA Report 542-R-07-003. US Environmental Protection Agency, Office of Superfund Remediation and Technology Innovation.

World Chlorine Council (2011). *Reduction of mercury emissions and use from the chlor-alkali sector partnership*.